Above barrier narrow resonances in fluorine-15

Valerian Girard-Alcindor

Normandie Université

THÈSE

Pour obtenir le diplôme de doctorat

Spécialité PHYSIQUE

Préparée au sein de l'Université de Caen Normandie

Above barrier narrow resonances in fluorine-15

Présentée et soutenue par
Valerian GIRARD ALCINDOR

Thèse soutenue publiquement le 30/09/2020 devant le jury composé de		
Mme SANDRINE COURTIN	Professeur des universités, Institut Hubert Curien	Rapporteur du jury
M. JEROME GIOVINAZZO	Directeur de recherche au CNRS, Centre d'Etudes Nucléaires de Bordeaux	Rapporteur du jury
Mme FRANCESCA GULMINELLI	Professeur des universités, Université Caen Normandie	Président du jury
Mme IOLANDA MATEA	Maître de conférences, Université Paris-Saclay	Membre du jury
M. ALEXANDRE OBERTELLI	Professeur des universités, GSI Darmstadt - Allemagne	Membre du jury
M. IULIAN STEFAN	Chargé de recherche au CNRS, Université Paris-Saclay	Membre du jury
Mme FAIROUZ HAMMACHE	Chargé de recherche au CNRS, Université Paris 11 Paris-Sud	Co-directeur de thèse

Thèse dirigée par FRANCOIS DE OLIVEIRA SANTOS et FAIROUZ HAMMACHE, Grand accélérateur national d'ions lourds

UNIVERSITÉ CAEN NORMANDIE

ED 591 PSIME

GANIL laboratoire commun CEA/DRF spiral2 CNRS/IN2P3

Above barrier narrow resonances in the unbound nucleus ^{15}F.

Valérian Girard-Alcindor

GANIL/IJCLAB

Remerciements

Alors que je n'avais que trois ans, en passant devant le GANIL, j'ai dit à ma mère: "Plus tard je travaillerai là..." Si à cette époque j'étais plus intéressé par le nombre impressionnant de lapins qui couraient dans le parc que par la physique voilà que, 20 ans plus tard, j'ai finalement la chance d'y travailler et d'y faire ma thèse...

Trois ans de thèse ce sont trois ans remplis de bons moments, de voyages, de découvertes, mais aussi de galères... C'est aussi une période qui permet de se réinventer, de changer et de se réaliser... Bien entendu c'est surtout l'occasion de se former au métier de chercheur et comme on ne se forme que très difficilement tout seul, je tiens à remercier tout ceux qui m'ont accompagné durant ces trois années.

Tout d'abord, je voudrais commencer par remercier mon jury d'avoir pris le temps de lire mon manuscrit ainsi que pour leurs questions et remarques qui m'ont données, et me donnent toujours, pour certaines d'entre-elles, matière à réfléchir. Je voudrais tout particulièrement remercier Sandrine et Jérôme pour avoir accepté d'être les rapporteurs de ce manuscrit ainsi que Iolanda et Alexandre, que je remercie en particulier de m'avoir pris en postdoc, et finalement Francesca que j'étais heureux de retrouver comme présidente du Jury.

Je voudrais aussi remercier les laboratoires du GANIL et de l'IJCLAB pour leur accueil pendant ces trois années. Je voudrais en particulier remercier les personnels techniques, avec qui j'ai eu la chance de travailler au cours des différentes expériences auxquelles j'ai participé. Je pense bien entendu à Vincent qui arrive toujours à vous faire sourire même après une nuit blanche sur LISE à attendre du faisceau... Mais aussi à Johan, Arnaud, Laurent, Sébastien...

Je souhaite aussi remercier mes encadrants François et Iulian, avec qui j'ai eu la chance de travailler pendant ces trois ans. François pour ton calme, ta gentillesse et ta capacité à toujours trouver les mots... et Iulian pour ton efficacité, tes conseils, et ta bonne humeur... Je voudrais aussi remercier Faïrouz d'avoir joué le rôle de directrice officielle

à Orsay. Je voudrais aussi en profiter pour remercier les chercheurs avec qui j'ai eu la chance d'apprendre, de travailler ou de discuter: Antoine, Emmanuel, Olivier, Thomas, Beyhan, Dieter, Jean-Charles, Christelle, Piet, Laurent, Pierre, Bertrand, Marek, Maurycy, Samuel, Julien, Yves, François, Olivier, Thomas, Valérie, Nicolas, Didier, Yorick, Daisuke, Mihai, Florine... Et bien d'autres que j'oublie sûrement... Je voudrais aussi particulièrement remercier Marlène pour son investissement durant les deux campagnes expérimentales dont mes expériences de thèse ont faites parties. Je voudrais aussi dire un grand merci à Adrien et Freddy, merci pour tout, merci pour les conseils, merci pour nos discussions, merci pour les fous-rires et merci pour la motivation que ce soit au CrossFit ou en manip!

Une thèse c'est aussi des rencontres et des bons moments autour d'un verre ou en missions entre thésards ou postdocs, je voudrais tout d'abord remercier mon premier "co-bureau", Simon avec qui on j'ai partagé de bons moments, des pistes de ski en Autriche, aux lacs Finlandais. Je pense aussi à Benoît et Pierre mes partenaires de pauses café pendant un peu plus de deux ans. Je remercie aussi Sylvain de nous avoir permis de garder un groupe soudé et motivé, Joël et sa fascination étrange pour les chauves, mais aussi les postdocs: Diego, Pedja, Panos, Franco, Phil... ceux qui ont soutenus avant moi: Aldric, Quentin, Bartholomé, Belen, Alexandre... et ceux qui soutiendront après: Julien, Ablaihan, Armel, Cyril, Nishu, Jekabs, Alejandro, Alexandre, Louis... et particulièrement Chloé avec qui j'ai partagé mon bureau pendant un an et Blaise-Maël qui sera le prochain à soutenir, bon courage à vous deux! Je remercie aussi ceux que j'ai oublié de citer... J'espère qu'ils m'en excuseront. Je voudrais aussi remercier Thomas mon compagnon de toujours qui m'a supporté pendant ces huit années de la licence au doctorat... Je n'aurai pas pu espérer meilleur binôme, ni meilleur ami!

Je veux aussi finalement remercier ma famille pour son soutien de tous les instants, je pense particulièrement à mes grands-parents qui ont su être toujours présent pour moi quand j'en avais besoin et a ma mère qui m'a élevée, qui s'est toujours battue pour que je ne manque jamais de rien et sans qui je n'aurai pas pu en arriver là, merci Maman. Mes derniers mots iront à Marie, celle qui est devenue ma femme seulement deux jours après avoir rendu mon manuscrit de thèse. Merci pour ton investissement, merci pour ta patience, merci de me suivre jusqu'en Allemagne. À toi qui me soutien depuis maintenant plus de 6 ans et ce tous les jours, les bons comme les mauvais, à toi qui as vécu la thèse au même rythme que moi, encore une fois, merci.

Introduction

Since its discovery in 1911 by Ernest Rutherford [FRS11], the atomic nucleus has been studied extensively to better understand the forces keeping its constituents, namely neutrons and protons, bonded to each others. For this purpose, experiments involving nuclear collisions were performed between accelerated ions and target nuclei. For decades, most of them were done using stable beams, leading to the discovery of ∼300 nuclei. To better understand the structure of the nucleus and the interactions between its nucleons, physicists had to test the nuclear forces under extreme conditions. It motivated the development, in the 90's, of new radioactive beam facilities which accelerated the discovery of new nuclei from 300 to more than 3000 known particle-bound nuclei today.

Those new radioactive beams gave the physicists the tool they needed to reach new regions of the nuclear chart, further and further away from what is known as the valley of stability. The further they went the more exotic (unstable) the nuclei were. They kept experimenting until they reached the edge of the nuclear chart to regions called the drip-lines. There are two drip-lines one for the proton-rich side and one for the neutron-rich side. They correspond to the limit where it is not possible to add a proton or a neutron to the nucleus, any added nucleon will immediately make the nucleus unbound and emit a nucleon. Nuclei that lie beyond the drip-lines are called particle-unbound nuclei, they exist only as resonances and can generally be studied indirectly by measuring their decay products.

Particle-unbound nuclei are the perfect candidates to test theories and challenge the limit of our knowledge of the nuclear forces. The study of those highly unstable nuclei lead for example to the questioning of one the most successful nuclear structure theory: the shell model. Derived in 1949 by M. Goeppert Mayer, E. P. Wigner, and J. Hans D. Jensen, the nuclear shell model mimics the atomic shell model with an added spin-orbit term to describe the arrangement of the nucleons in the nucleus. Developed with stable nuclei in mind, one of its most successful feature was its reproduction of the experimentally observed magic numbers (2, 8, 20, 28, 50, 82, 126). Those numbers correspond to the number of protons or neutrons for which over-stability was observed. Those magic (or

doubly-magic) nuclei are often characterized by an important binding energy, as well as a low probability of excitation from the ground state to their first excited state. While the magic numbers were considered immutable for several decades [Sor08], for highly unstable nuclei that lie close or beyond the drip-lines mutliple experiments have demonstrated the disappearance of the neutron magic numbers: N=20 [Gui84] [Mot95] or N=28 [Sor93] and the appearance of the new neutron magic numbers: N=16 [Oza00] or N=32 [Huc85].

The study of nuclei at the drip-lines also challenges our representation of the nucleus. For decades, the nucleus was considered to be perfectly spherical but it is not rare for unstable nuclei to have deformed shapes or complex structures. An extreme example of such complex structure, observed at the drip-lines is the halo phenomena. Halo nuclei are composed of a core surrounded by one or more orbiting nucleons. When they have a three-body structure, they are called borromean nuclei as a reference to the borromean rings, where three rings are linked together in such way that if a ring is removed the two other rings will no longer be linked. By comparison, for such nuclei removing one particle will leave the remaining two-body system unbound leading to its separation. This is the case of ^{11}Li for example [Tan85] (see Fig. 1).

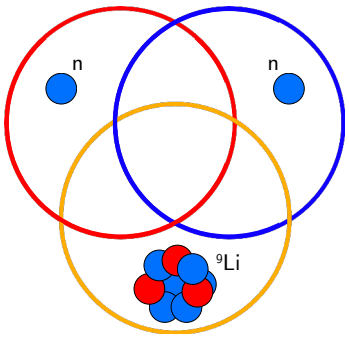

Figure 1: *Schematic representation of the borromean structure of* ^{11}*Li.*

This thesis will focus on the study of above barrier narrow resonances in the unbound nucleus ^{15}F. In the first chapter the motivations and experimental methods used in this work will be described. Then, in the second and third chapter two experiments performed at GANIL and focusing on the negative parity states of ^{15}F will be detailed. The results from those experiments will be discussed in the fourth chapter where we will present our interpretations. Finally the last chapter will conclude this work and present several outlooks.

Summary

1

Motivations and experimental methods

Contents

1.1 Motivations

1.1.1 Proton-rich nucleus at the drip-lines

This work will focus on the study of ^{15}F, an unbound nucleus located two-neutron away from the proton drip-line. As it can be observed on Fig. 1.1, compared to the neutron drip-line, the proton drip-line is reached by removing only two neutrons compared to the stable isotope ^{19}F. This can mostly be explained by the Coulomb repulsion.

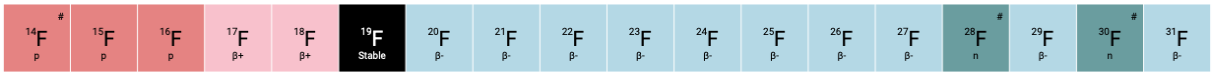

Figure 1.1: *Fluorine isotopic chain, in black is drawn the stable isotope of fluorine:* ^{19}F*, in blue are drawn the neutron rich nuclei, and in red the proton rich one. Darker shades corresponds to the particle unbound nuclei.*

The impact of the Coulomb repulsion for proton rich nuclei can be qualitatively understood considering the semi-empirical mass formula [Kra88]:

$$E_{Binding}(A,Z) = a_{vol}A - a_{surf}A^{2/3} - a_{Coul}\frac{Z^2}{A^{1/3}} - a_{asy}\frac{(N-Z)^2}{A} \tag{1.1}$$

The different terms of Eq. 1.1 are fitted on the experimental data and are called respectively the volume, surface, Coulomb and symmetry energies. Equation 1.1 shows the importance of the Coulomb term in reducing the binding energy of the nucleons due to its dependence in Z^2. Equation 1.1 also illustrates that the binding energy will be the strongest for an equal number of protons and neutrons, showing the impact of the proton-neutron symmetry. Considering the shell model representation, increasing the asymmetry will change the mean field felt by the nucleons. As we move toward the proton drip-line, the number of neutrons decreases. This will change the nuclei binding energy, thus the proton mean field will become shallower while the neutron mean field will become deeper. This is illustrated for different Fluorine isotopes in Fig. 1.2.

As the proton mean field becomes shallower, more of the excited states will be in the continuum, above the proton emission threshold (S_p). Those states are unbound for

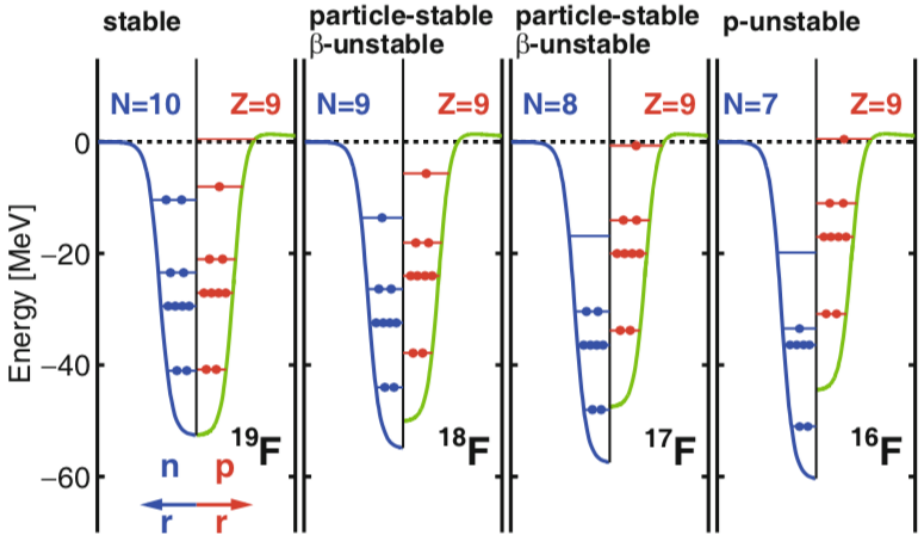

Figure 1.2: *Schematic representation of the evolution of neutron and proton energy levels as a function of their mass number for different fluorine isotopes. [Cha16]*

the proton emission with a finite lifetime (of the order of 10^{-21}s). From the time-energy uncertainty principle, it can be derived that: $\Delta E \Delta t \sim \hbar$, a state with a finite lifetime will not have a perfectly defined energy. Those states will then be observed as resonances characterized by their width (Γ). The measurement of those widths thus gives information about their lifetime (τ): $\Gamma \approx \hbar\tau$. The larger the width of the state, the shorter lived it will be and conversely. For more details on the determination of widths and the treatment of resonances see section 1.3.

As it can be observed on Fig. 1.2, with the increased proton/neutron asymmetry, ^{16}F ground state is already unbound. Removing another neutron can then lead to the formation of an even more unbound nucleus. For example, ^{15}F is more proton unbound than ^{16}F with a ground state ∼1.3 MeV above the proton separation energy (S_p) compared to ^{16}F whose ground state is ∼ 500 keV above S_p. This increased instability compared to ^{16}F translates to a ground state width an order of magnitude larger ($\Gamma_{^{15}F} \sim 500keV$ and $\Gamma_{^{16}F} \sim 40keV$) [**iulan16F**; Gra16].

1.1.2 Mirror asymmetry

Except for their charge difference, neutrons and protons have very similar characteristics, so much so, that they are often treated as a single particle, the nucleon. It was shown in

different experiments that nuclear force has charge symmetry (neutron-neutron interaction = proton-proton interaction) and charge independence (neutron-neutron interaction = proton-proton interaction = neutron-proton interaction). Thus, nuclei with the same number of nucleons but with exchanged number of neutrons and protons, the so-called mirror nuclei, are expected to have an almost identical level scheme. It is interesting to compare the level schemes in extreme conditions, for mirror pair of bound and unbound nucleus for instance.

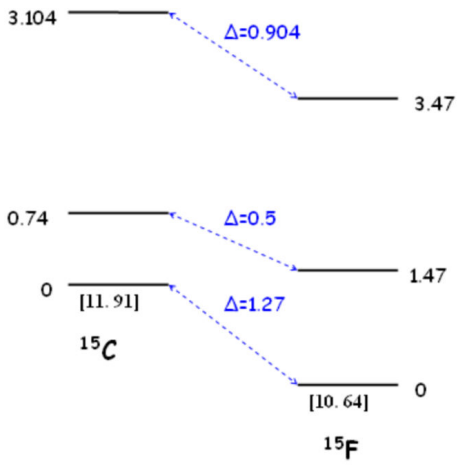

Figure 1.3: *Level scheme of* ^{15}C *and* ^{15}F*. The energy in MeV between square brackets corresponds to the nuclear energy difference relative to* ^{15}N *[Gra09].*

The naive understanding of mirror symmetry was proven to be broken for nuclei near the drip-lines. This asymmetry translates sometimes to large shifts in energy between states of pair of mirror nucleus. This was first studied in the 50's by R. G. Thomas [Tho52] and J. B. Ehrman [Ehr51], those shifts in energy were then observed multiple times and were named the Thomas-Ehrman shifts after them. Such differences between pair of mirror nuclei can be explained by the fact that when the proton-rich nucleus is unbound, or weakly bound, the probability for the proton to be located further away from the nucleus is larger, thus reducing the Coulomb barrier and consequently shifting down the states of the proton-rich nuclei. This effect is stronger when the centrifugal barrier is smaller, making it more visible for protons in the s shell.

A striking example of such shifts in energy was measured between ^{16}N and ^{16}F [Ste14] where large differences between their level schemes were measured. Indeed, the ground state of ^{16}F is a 0^- while the one of ^{16}N is a 2^- and the 0^- and 1^- states of ^{16}F are

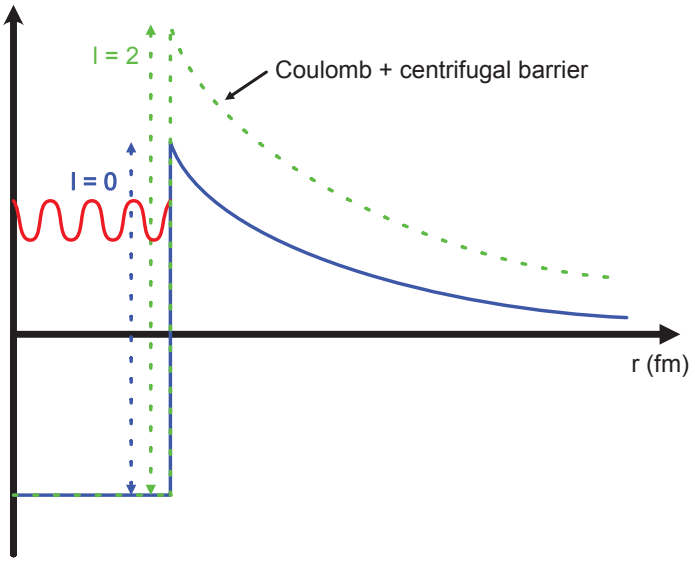

Figure 1.4: *Schematic representation of the Coulomb barrier for l = 0 and Coulomb + centrifugal barrier for l = 2.*

more than 500 keV lower than in ^{16}N compared to other states. Other examples were observed between ^{13}N and ^{13}C [Tho52; Ehr51] where they found shifts of more than 700 keV between the two mirror nuclei, or between the neutron halo nuclei ^{11}Be and its mirror ^{11}N [Aoy98].

Large shifts were also measured between ^{15}F and ^{15}C (Fig. 1.3), where the ground state shows a Thomas-Ehrman shift of 1.27 MeV, one of the strongest known values. Looking at the other known excited states of ^{15}F much smaller shifts were observed. The explanation is that the ground state is interpreted as a $^{14}O_{g.s.}$ core plus an unbound proton in the 1s1/2 shell with no centrifugal barrier (angular momentum l = 0), while, on the other hand, the first excited state is interpreted as a $^{14}O_{g.s.}$ core with a proton in the 1d5/2 shell with an angular momentum l = 2 and thus sensitive to the centrifugal barrier which limits the spatial distribution of the proton (Fig. 1.4). Concerning the second excited state, the shift is large, but still much smaller than the one of the ^{15}F ground state, it is considered to be a consequence of the different structure of this state viewed mostly as a $^{13}N_{g.s.}$ core surrounded by two protons ([Gra09]).

1.1.3 Near-threshold clusterisation

Hoyle state

The ≈ 1200 published articles referring to the Hoyle state make this state one of the most studied state in nuclear physics. Its existence was predicted by F. Hoyle in 1953 to account for the stellar abundance of carbon [Hoy54] and the state observed the same year [Dun53]. The so-called Hoyle state is the second excited state in ^{12}C (Fig.1.5).

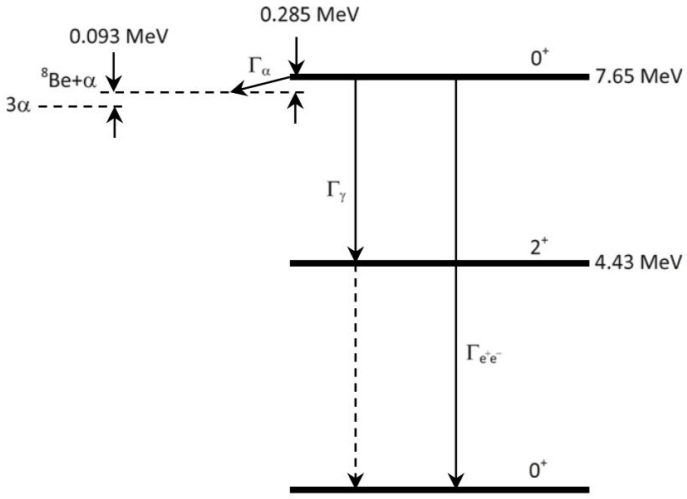

Figure 1.5: *Level scheme representing the capture process by which ^{12}C is formed from the radiative ^8Be + α capture [Fre14].*

The synthesis of ^{12}C in stars is a two step process where two α particles fuse together to form ^{8}Be whose ground state is 93 keV above the α decay threshold. Then, the capture of another α particle leads to the formation of ^{12}C in the Hoyle state located only 285 keV above the ^{8}Be + α decay threshold or equivalently 378 keV above the 3α decay threshold. It can either decay back to ^{8}Be + α or electromagnetically decay to ^{12}C ground state. The existence of the Hoyle state just above the ^{8}Be + α threshold boosts the capture of an α by ^{8}Be by a factor of 10-100 million [Fre14], making much more efficient the formation of ^{12}C in the universe and subsequently the existence of life.

The Hoyle state is described as a 3α-cluster structure while ^{8}Be ground state is described as a 2α-cluster. Those observations lead to an obvious question concerning the link between the structure of such states and their proximity to α decay thresholds. To

understand if this is a general feature of the nucleus, other examples of such near threshold α clustering had to be found. Clustering should, then, be studied to determine if it is more energetically favorable for the nucleus to form a system composed of smaller composite subsystems, rather than to keep all of his nucleonic degrees of freedom. Due to its large binding energy the α particle makes it a rather perfect subsystem.

Ikeda's conjecture

Previous attempts at developing molecular nuclear models with α particles were based on the assumption that α particles stayed bound in the nucleus. They were mostly abandoned due to the fact that α particles could easily dissolve into their constituents in the nucleus. The nucleus ^{16}O is an interesting test case to study α-clustering. Its ground state is well described from the particle independent point of view [May49; Hax49; Wig37], but traces of four-α correlations that are not predicted by the shell model were still highlighted by different theoretical studies [Den54; Kam56; Wil58; Tan78]. However, those studies showed that the correlations are not sufficiently strong to change the structure of ^{16}O into a 4α-cluster.

Ikeda et al. then proposed [Ike68] a different model to explain the alpha clustering. Their hypothesis is that α particles, do dissolve inside the compact nucleus, but, they keep some of their correlated characteristics such as it was observed in ^{16}O. When the compactness of the whole system is released (such as in ^{8}Be), the correlated α particles should reappear leading to the formation of molecular-like system. The compactness of the nucleus will depend on its mass number as well as its excitation energy. Ikeda explains the possibility of a diatomic-like (2α) structure, as observed for ^{8}Be ground state, for two reasons :

- Alpha particles are tightly bound.
- The interaction between α particles is weak. Strong enough to trap the particles in a quasi-bound state, but not sufficient for the two alpha particles to collapse in a compact nucleus.

For those reasons, the binding energy of ^{8}Be is just a little smaller than the sum of the binding energies of two α particles. This diatomic behavior should then be observed for other nuclei, and based on the observations made for ^{8}Be, the energy of such states should be close to α-decay thresholds. This study was performed first for nuclei with a diatomic-like structure : α + Core. But it was then generalized for other polyatomic-like structure, a summary of such hypothetical molecular structure is found in Fig. 1.6.

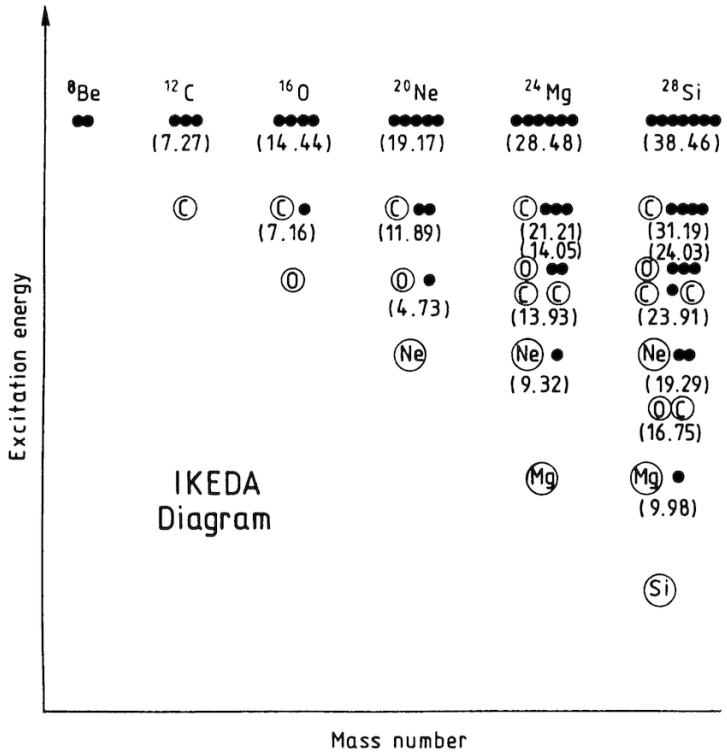

Figure 1.6: *Ikeda's threshold diagram. Energy in parenthesis are given in MeV and correspond to the threshold energy of each decay mode. This diagram gives the hypothetical molecular structure expected at each energy for different nuclei. [Von02]*

Ikeda's conjecture that the structure of states near their Nα decay thresholds should lead to the formation of Nα-cluster states has been validated multiple times experimentally by studying the rotational band of such states. The above mentioned Hoyle state is a good example of such near-threshold phenomenon.

Generalization to two-nucleon cluster

Following Ikeda's work on α clustering, Okolowicz et al. [Oko12; Oko13] proposed to generalize Ikeda's conjecture to all near thresholds states, including for states related to unstable subsystems like di-neutron or di-proton. This idea might be surprising as one of the basis of Ikeda's conjecture to explain the diatomic-like structure of ^{8}Be was that alpha particles were viable as a subsystem due to their high binding energy. Indeed, this is obviously not the case for di-neutron or even di-proton subsystem. Still, experimental results tend to agree with this generalization of the near threshold clustering phenomenon.

One example is the previously shown ^{11}Li where similarly to the Hoyle state in ^{12}C, the borromean structure of its ground state is located $\sim$ 300 keV from the two neutron emission threshold (Fig. 1.7).

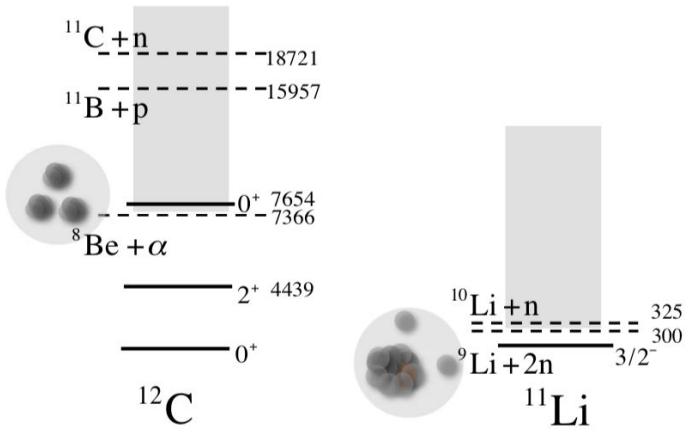

Figure 1.7: *Level scheme and molecular structure of two different borromean nuclei, ^{12}C and ^{11}Li showing similar clustering feature near the 2α decay threshold and the 2n decay threshold respectively.*

Okolowicz et al. [Oko12; Oko13] proposed to consider those nuclei as open quantum systems, where the properties of unbound states influence and mix with other states below the particle decay threshold. The opening of a new decay channel will induce a collective mixing of states near and below the decay threshold. Their model shows that it is in fact a single state, which they call the "aligned state", that concentrates most of the continuum-coupling correlation energy. This aligned state will strongly couple to the decay channel and thus carries many of its characteristics. The similarity between the aligned state and the decay channel is the key point of the clustering phenomenon. In other words, any state near a given decay threshold will couple strongly with the decay channel, thus mimicking its structure.

1.1.4 Three-body emission

In section 1.1.1 it was discussed that proton-rich nuclei near the drip-line can decay by emitting a proton from the ground state, or from one of their excited states. This type of emission is expected once the energy of the nuclear state is above the proton emission threshold (S_p). Similarly, if the energy of the nuclear state is higher than the two-proton

emission threshold (S_{2p}), the two-proton decay channel is open.

These two-proton emissions can be separated in:

- Simultaneous or direct two-proton emission where all three fragments are emitted at the same time;
- Sequential emission where the decay can be separated in two sequences of two-body decay.

Sequential emission

The Hoyle state is a good example of sequential decay [Cha16]. As previously discussed in section 1.1.3, the Hoyle state structure is described as a cluster of three-alpha particles. If the triple α capture occurs in stars, it is nearly impossible to study it experimentally. Three body resonances are then studied by measuring their three-body decay. In the case of ^{12}C, the Hoyle state decays by emitting a first α particle plus a ^{8}Be nucleus, then ^{8}Be itself decays into two α (Fig. 1.8).

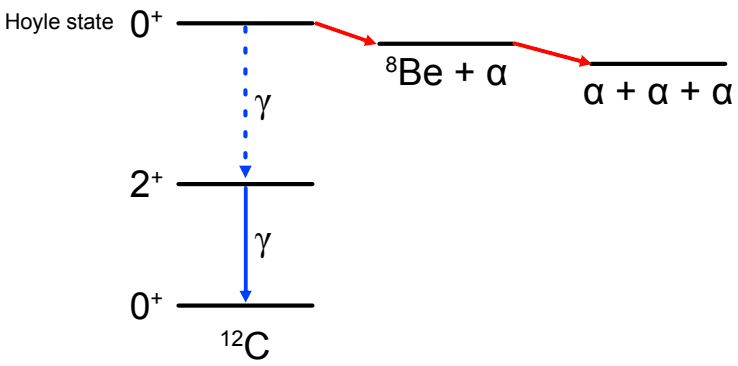

Figure 1.8: *Scheme of the open decay paths of the Hoyle state. The blue line corresponds to the radiative transitions in ^{12}C. The $0^+ \rightarrow v\ 2^+$ is represented in dash as the Hoyle state has a very small γ-decay branch to the first excited state of ^{12}C [Cha16].*

Simultaneous emission

The simultaneous emission of two nucleons from the ground state was predicted in 1960 by Goldanski [**goldanski**] for nuclei where the single-particle emission is not possible but the two-nucleon emission is. An example of such nuclei is ^{45}Fe for whom the ground state has an energy lower than S_p but higher than S_{2p} (Fig. 1.9) [Gio03]. Indeed, the ground state of ^{45}Fe is located below the one of ^{44}Mn then, as a consequence ^{45}Fe will decay directly to $^{43}Cr_{g.s.}$ by emitting two protons.

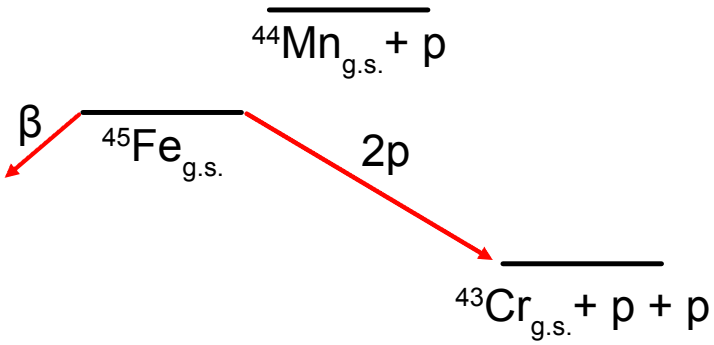

Figure 1.9: *Scheme of the decay paths of* ^{45}*Fe.*

Three-body correlations

Information about the decay mechanism and on the structure of the decaying state can be constrained by studying the correlations between the fragments. Let us consider the case where the state decays by emitting two-protons, plus a heavier fragment. Measuring the relative reduced energy between the protons, and between each of the protons and the fragment can give information on the decay mechanism. Simultaneous decay is often characterized by a small relative reduced energy between the two protons and a relative reduced energy sharing of $\sim 50\%$ between the fragment and the protons. On the other hand, sequential decay is often characterized by a random energy sharing between the two protons which translates to a flat distribution of the relative reduced energy 1.10a and two distinct maxima in the relative reduced energy sharing between the fragments and the protons. Figure 1.10b illustrate the differences in relative reduced energy that can be observed experimentally. Detailed description of the study of correlations and on how Fig. 1.10 was obtained can be found in section 3.3.2.

1.1.5 Radiative emission between unbound states

Experimental evidence of radiative emission between unbound states

The existence of narrow resonances makes conceivable the observation of gamma transitions between unbound states due to their long lifetime. Those gamma transitions have been rarely observed and their existence are still being debated today. An example of experimental work on gamma transitions between unbound states in a bound nucleus are the pioneering results obtained for ^{24}Mg (Fig. 1.11a) [Haa97] where the authors tried to observe the gamma transition between 10^+ to 8^+ resonant state: only 7 counts consistent with the expected gamma transition were observed.

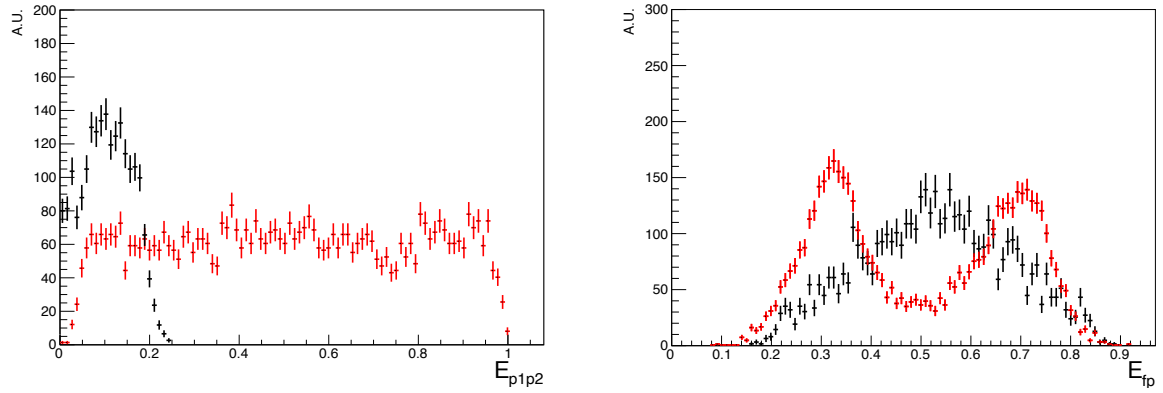

(a) (b)

Figure 1.10: *Two-proton decay for ^{15}F. (a): Comparison of the relative reduced energy between protons (E_{p1p2}), simulation of a sequential decay in red and simulation of a simultaneous decay in black. (b): Comparison of the relative reduced energy between ^{13}N and protons (E_{fp}), simulation of a sequential decay in red and simulation of a simultaneous decay in black.*

More surprisingly, it is for the unbound nucleus ^{8}Be (Fig. 1.11b) [Dat05; Dat13] that a gamma transition was clearly observed between the 4^+ and 2^+ state. The gamma transition was measured with a large B(E2) confirming that ^{8}Be was deformed and that this deformation was consistent with a 2α-cluster structure.

As previously discussed in the context of understanding the general and peculiar characteristics of near thresholds states, the search of such gamma transitions between unbound states should also be performed for unbound states with a structure featuring neutron or proton halo for example.

"Quasi-bound" unbound nucleus

For gamma-transitions between unbound states, the range of available energies for the gamma is quite broad. A possible impact of such "internal γ transition" could be an increased lifetime of the nuclei [Ste06; Ste07]. Let us assume (Fig. 1.12) a nucleus with a narrow excited state ($\Gamma_A < 50$ keV) populated with an energy E_A and a broad ground state of energy E_B and width $\Gamma_B > 200$ keV, 1 MeV above the proton emission threshold, then in the case where a gamma transition would occur between these states, the available energy for the γ would be $\sim E_\gamma \in [E_A, 0]$ (Fig.1.12). For the extreme case where E_γ is near

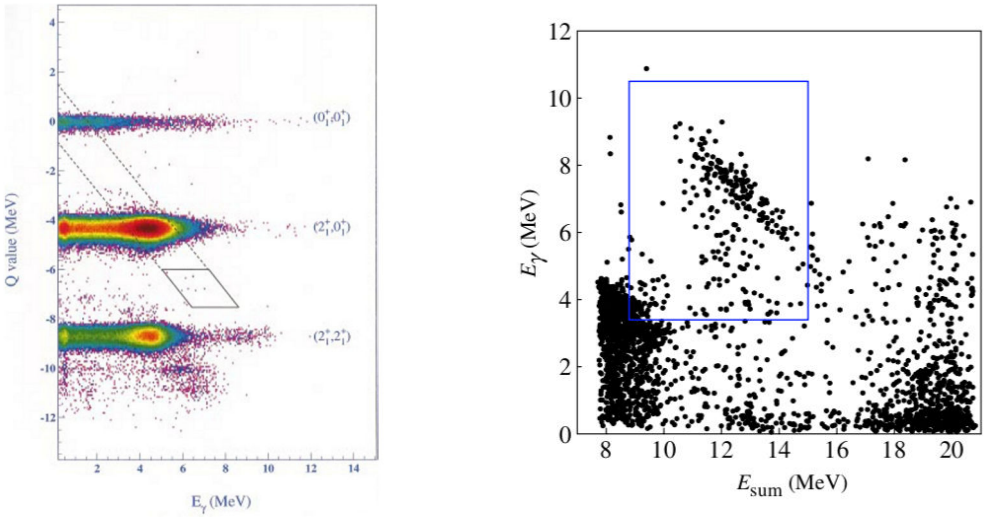

(a) (b)

Figure 1.11: *(a): Reaction Q-value as a function of the fragment γ-ray energies E_γ obtained for ^{24}Mg by Haas et al. [Haa97]. The parallelogram drawn in black corresponds to the region where gamma transition events between the 10^+ and 8^+ states are expected (only 7 counts were observed). (b): Gamma energy as a function of the sum of the two alphas energy obtained by Datar et al. [Dat13] for ^8Be. The blue rectangle corresponds to the region where gamma events are expected, a band of events is clearly identifiable in this region.*

E_A, the proton emission would be hindered as the proton would not have enough energy to go through the Coulomb + eventual centrifugal barrier. It could make the nucleus bound or, in less extreme cases, "quasi-bound". The more energy is taken by the gamma, the longer lived the nuclei should be. This change in lifetime could also be consistent with results from Ref. [Rot06; Kel04] who calculated and showed experimentally that the exponential decay law is a good approximation in most cases, but a poor one for broad resonances where it is expected that they should show a geometric decay law with much delayed decay time.

Possible astrophysical impact

In the case where unbound nucleus could become "quasi-bound", this could have an astrophysical impact [Ste06; Ste07], especially for proton-rich nuclei. The increased lifetime could open the possibility for such quasi-bound nuclei to decay competitively by β emission, or, in the context of astrophysical scenarios with high proton density (novae, X-Ray bursts...), capture another proton due to the increased lifetime. Thus creating new re-

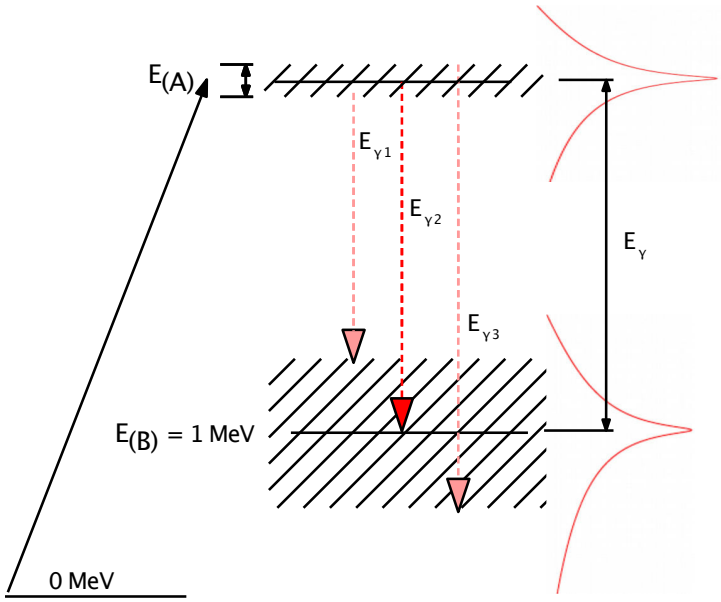

Figure 1.12: *Schematic representation of the gamma decay between two particle unbound states. In red are drawn the shape of resonances, following the Breit-Wigner formalism. Following the gamma decay $E\gamma_3$, the energy available for the proton will make the proton decay of the state very improbable as it is strongly hindered by the Coulomb barrier.*

action path which are not currently taken into account in the astrophysical models. If this is a common feature of the nucleus, and if the cross-section for such reaction is not too small, this could impact the computation of astrophysical reaction rates in stellar environment.

1.2 The unbound nucleus ^{15}F

1.2.1 Predictions of narrow resonances

Fluorine 15 is the isotope of fluorine located two neutrons beyond the proton drip-line. For such light nucleus, it is expected that it exists only as broad resonances in the continuum because of the small Coulomb barrier. It is the case for ^{15}F ground state ($J_\pi = 1/2^+$) which is unbound by $\sim$ 1.3 MeV and is seen as a broad s-wave resonance with Γ $\sim$500 keV [Gra16]. Same goes for its first excited state ($J_\pi = 5/2^+$) which is unbound by $\sim$ 2.8 MeV and is observed as broad resonance but with a narrower width: Γ = 300 keV [Gra16]. It is worth mentioning that this reduction in width for higher excitation energy contradicts the naive view that all nuclear levels should be broadened with increasing excitation energy. Both the structure of the ground state and first excited are interpreted as a proton orbiting around a ^{14}O core with l = 0 and l = 2 respectively (Fig. 1.4).

During the last 15 years multiple theoretical papers were published on the structure of ^{15}F [Can06; For06; For07; For11; Fra19]. Using the multi-channel algebraic system (MCAS) with Pauli-hindered method [Amo03], Canton et al. [Can06] predicted the existence of three extremely narrow odd-parity states in ^{15}F with widths of only few keV, namely $1/2^-$, $5/2^-$ and $3/2^-$. Those states were also predicted by Fortune and Sherr [For07] using a potential model to determine the single-particle widths which they scaled down to reproduce the measured widths in the mirror nucleus ^{15}C. In this last paper, the authors predicted the energies to be $\sim$ 1 MeV lower and the width to be ten times larger than the one of Canton et al. [Can06]. Despite their disagreement on the energy and width, both calculations predict the first two odd-parity states to be very narrow and thus to have half-lives an order of magnitude (or more) longer than the one of the ground state. Fortune and Sherr disagree on the width of the $3/2^-$ which they expect to be much broader. Both theoretical predictions agree that all three state should originate from a hole in the $0_{p1/2}$ shell coupled to the 0^+ state of ^{14}O for the $1/2^-$ state and to the 2^+ state of ^{14}O for the $5/2^-$ and $3/2^-$ state.

In the light of recent measurements of narrow states detailed in the next paragraph, new theoretical predictions were published in 2019 using the MCAS model by Fraser, Amos, Canton et al. [Fra19]. These results tend to agree more with the predictions of Fortune and Sherr [For07] for the $1/2^-$ state, but their model also predicts the existence of 30 states of various width and spin-parity between $\sim$ 1.3 MeV and $\sim$ 11.5 MeV. Most of those states are not observed in the mirror nuclei ^{15}C and 25 of them are currently unknown in ^{15}F.

1.2.2 Observation of narrow resonances

Following the theoretical predictions of Ref. [Can06] and Ref. [For07], three papers were published on the structure of ^{15}F by Mukha et al. [Muk08; Muk09; Muk10]. Those measurements, based on one experiment, of the two-proton decay of ^{16}Ne aimed to study the unbound nucleus of ^{15}F through the measurement of the ^{14}O + proton + proton and ^{13}N + proton + proton + proton correlations. In their paper it has been observed that by making projections on a given set of relative angles between the proton and the heavier fragments, multiple peaks were observed. Those peaks could only be reproduced by simulating the sequential decay of ^{16}Ne through 4 different resonances in ^{15}F (Fig. 1.13), the known ground state and first excited state, as well as two other unknown excited states. The energy and width of those resonances were constrained by varying them for each of the states in the simulation until the best fit with the experimental data was obtained. The spins and parities were assigned by comparison to the ^{15}F mirror nucleus (^{15}C). Results from this experiment are visible in Fig. 1.13. Due to the low statistics and the constraints of their experimental setup and technique, the energies were measured with large uncertainties and only an upper limit for the width of these two new uknown states, $\Gamma = 200$ (200) keV, was deduced and considered to be "very narrow" by the authors. They also discussed in their article the possibility for the predicted $5/2^-$ and $3/2^-$ states to decay sequentially by two-proton emission, but they did not observe any of those events. Their interpretation was that these states decay mostly to $^{14}O_{g.s.}(0^+)$ + p with partials widths of $\sim$ 50 keV for $5/2^-$ and more than 100 keV for $3/2^-$ compared to the widths for the decay to the first excited state $^{14}O(1^-)$ being respectively 4 keV for $5/2^-$ and 7 keV for $3/2^-$ (these partial widths were obtained using the shell model code: NuShellX [Bro14]).

Following the exploratory work of Ref. [Muk09], recent results were obtained by F. de Grancey et al. [Gra16] concerning the second excited state of ^{15}F. Using the resonant elastic scattering reaction ^{14}O(p,p)^{14}O and fitting the obtained differential cross-section using the R-Matrix formalism (see section 1.3.1), they found that $\sim$130 keV above the two-proton emission threshold (S_{2p}) a $1/2^-$ state exists with a 36 keV width more than 10 times narrower than the one of the ground state ($\sim$ 500 keV). The observation of such a narrow resonance was interpreted as the results of the collectivization of shell-model states near the particle emission threshold.

Detailed theoretical studies of the structure of ^{15}F second excited state ($1/2^-$) using the Gamow Shell Model [Mic02], in the coupled channel representation, with a ^{12}C core plus three valence proton showed that the $1/2^-$ state has an almost pure wave function of two protons in the $s_{1/2}$ shells. The spectroscopic factor of the state to the $^{14}O_{g.s.}$ + p

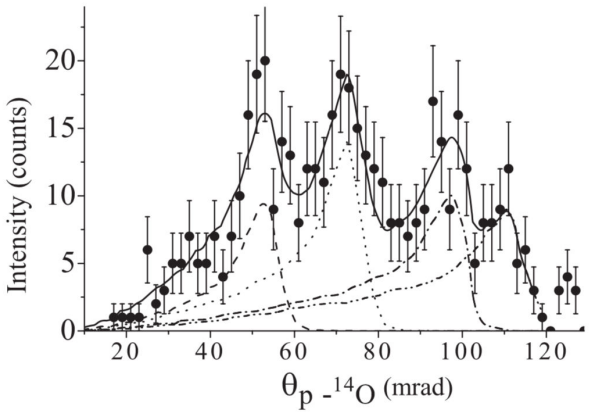

Figure 1.13: *Angular p-^{14}O distribution obtained in Ref. [Muk10] by performing projections in the proton-^{14}O relative angles. The dashed and dotted curves result from Monte Carlo simulations. The dash-dotted and dash-dot-dotted curves show the fit of two other peaks by suggesting two unknown excited states in 15F with 1p-decay energies of 4.9(2) and 6.4(2) MeV, respectively. The solid line is the sum fit.*

is very small, it is calculated at 97 % as a $^{13}N_{g.s.}$ core surrounded by two protons (Fig.1.15).

Such narrow resonances were observed in the previously discussed ^{8}Be whose ground state (0^+) structure is similar to the structure of the nearby 2α decay channel with a narrow resonance width of 5.57(25) eV. This 2α structure is kept for the first (2^+_1) and second (4^+_1) excited states of ^{8}Be and as those states are far from the 2α decay threshold they are observed as broad resonances. For higher excitation energies near the one-proton and one-neutron decay thresholds, the structure of ^{8}Be changes to the one of respectively ^{7}Li + p and ^{7}Be + n. Hence, for those resonances, the 2α component is suppressed and narrow resonances are observed. Comparing the results obtained for near-thresholds states and narrow states in drip-line nuclei to the one of ^{8}Be could be interesting to better understand which features of the near threshold clustering phenomenon are universal and which one are specific to each subsystem (α, 2n, ^{2}He...).

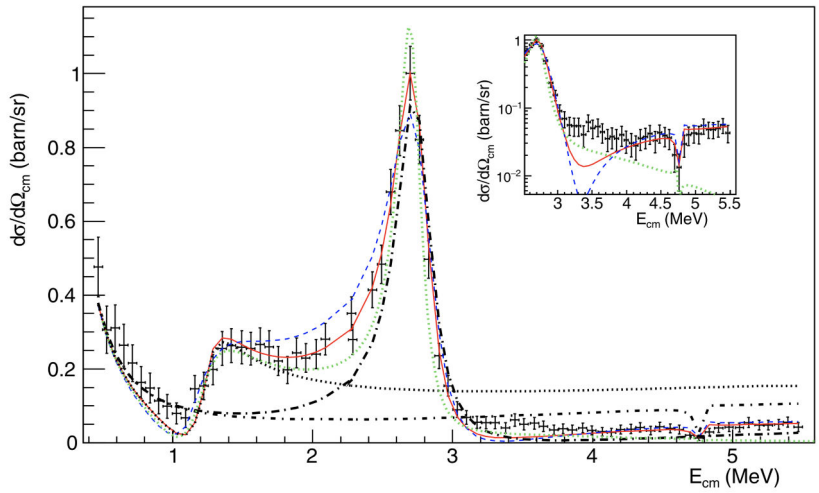

Figure 1.14: *Differential cross-section of the* $^{14}O(p,p)^{14}O$ *reaction studied in Ref. [Gra16] the ground state and first excited state of* ^{15}F *are measured as broad resonances while its second excited state is observed as a narrow resonances* $\sim$*130 keV above the* S_{2p}*. The GSM-CC calculation is shown in green, data are compared to the best R-Matrix fit in red as well as to the R-Matrix calculation made with* $\Gamma = 737$ *keV for the ground state in blue. R-Matrix calculations corresponding to the ground state alone (dotted line), first excited state (thick-dot–dash line), second excited state (thin-dot–dash line) are also shown.*

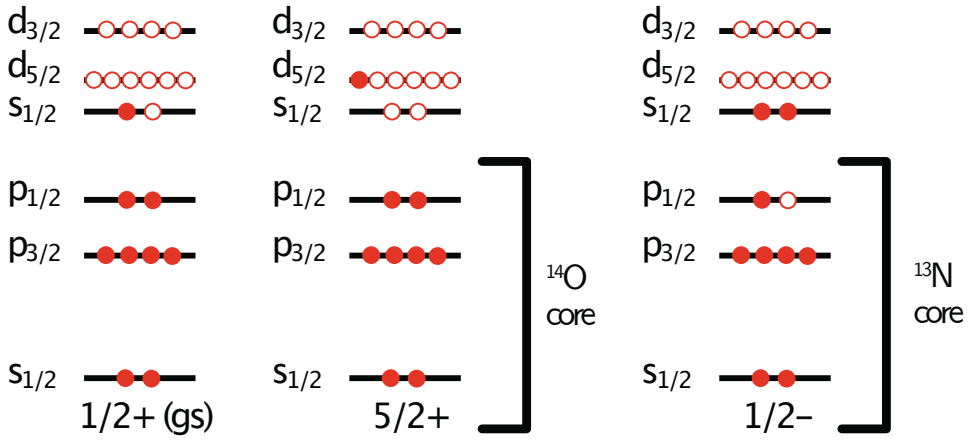

Figure 1.15: *Scheme of the shell model configurations of the ground state and first two excited state of* ^{15}F*. The second excited state was found to have a configuration with a large fraction of* $^{13}N_{g.s.}$ *core surrounded by two-proton in the 1s1/2 shell*

1.2.3 Status of ^{15}F

A summary of the best results obtained experimentally and theoretically on the spectroscopy of ^{15}F can be found in Table 1.1 and Fig. 1.16.

	Measured			Predicted		
J^π	Er (MeV)	Γ (keV)	Ref.	Er (MeV)	Γ (keV)	Ref.
$1/2^+$	1.270(20)	376(70)	[Gra16]	1.282	715	[Fra19]
$5/2^+$	2.794(16)	300(16)	[Gra16]	2.757	337	[Fra19]
$1/2^-$	4.757(16)	36(19)	[Gra16]	4.63	38	[For11]
$5/2^-$	6.4(2)	200(200)	[Muk09]	5.92	6	[For11]
$3/2^-$				6.30	350	[For11]
$1/2^+$				7.21	1210	[Can06]
$5/2^+$	7.8(2)	400(400)	[Muk09]	7.75	400	[Can06]
$3/2^+$				7.99	3600	[Can06]

Table 1.1: *Summary of the best experimental and theoretical results on the spectroscopy of ^{15}F. Energies are relative to the one-proton emission threshold: S_p = 1.270 MeV.*

The narrow $1/2^-$ state could be a good candidate to study the possibility of gamma transition in an unbound nucleus. Particularly the E1 transition between the first $1/2^-$ state and $1/2^+$ ground state as such transitions are known to be very strong and very fast. For example, the $1/2^- \rightarrow 1/2^+$ gamma transition in ^{11}Be is the fastest known dipole transition between bound states [End93]. In the case of ^{11}Be, it is due to its structure interpreted as a $^{10}Be_{g.s.}$ core surrounded by a neutron halo for the ground state [Mil83] thus making the wave function of the neutron very spread out. In this regard, $^{15}F_{g.s.}$ is comparable to ^{11}Be $1/2^+$ state, as its structure is also interpreted as a $^{14}O_{g.s.}$ core plus a proton. Also, both transitions in ^{15}F and ^{11}Be are similar as they occur between a nucleon in the 1s1/2 and in the 1p1/2, for which the overlap are expected to be large thus accelerating the gamma transition.

Of interest are also the other low-lying negative parity states, $5/2^-$ and $3/2^-$, as their energy, total width and partial width to either ^{14}O ground state by one proton emission or to ^{13}N ground state by simultaneous or sequential two proton emission are still unknown. The theoretical predictions that those negative parity states [For07; Can06] should be narrow despite the fact that they are more than 1 MeV above the two-proton emission threshold (S_2p) is to be tested experimentally. The behavior of the excited states in ^{15}F

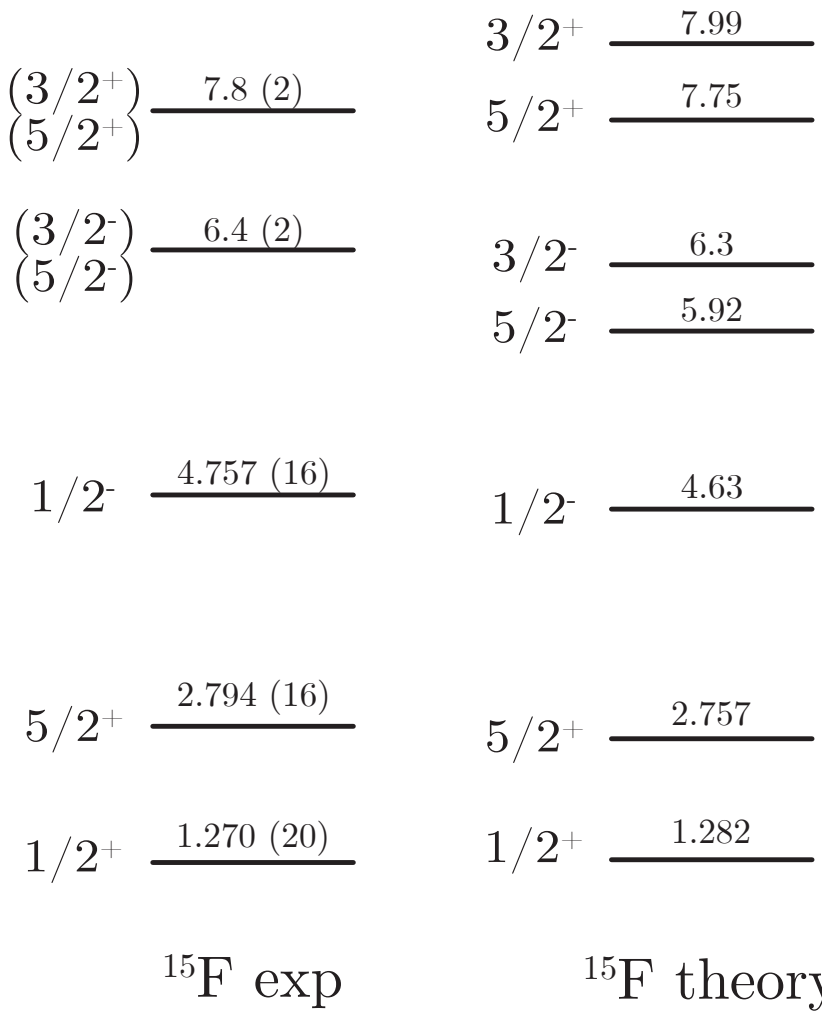

Figure 1.16: *Summary of the experimental and theoretical level scheme of* ^{15}F *from Table. 1.1, energies are given with respect to* S_p *= 1.270(20) MeV*

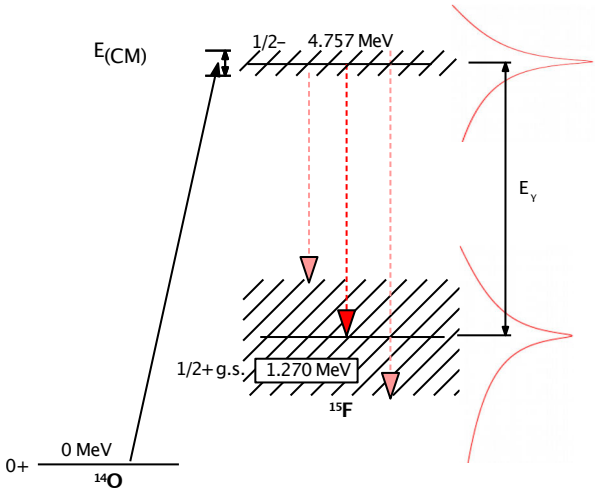

Figure 1.17: *A gamma transition is shown between the narrow second excited state ($1/2^-$) of ^{15}F and its broad $1/2^+$ ground state.*

is different to other unbound nuclei such as ^{8}Be for which, on the contrary, the excited states become broader as they get further from the 2α threshold.

1.3 Experimental project

1.3.1 Thick target technique

To populate the states of interest in ^{15}F, the thick target technique was employed. It is based on a type of reaction called the compound nucleus reaction which occurs when the incoming and target particles merge to form a compound nucleus (CN). In this type of reaction, the CN loses the memory of the initial structure of the particles in the entrance channel [Gho50]. CN can form when the center-of-mass (CM) energy (E_{CM} or resonance energy E_r) between particles in the entrance channel is equal to one of the states in the CN. When this occurs, strong enhancements in the cross section called resonances are observed.

In the case of the thick target technique, the idea is to use the energy lost by the beam inside the target to populate different states in the compound nucleus. Indeed, as the beam looses energy inside the target, the center-of-mass (CM) energy between the ions from the beam and the nuclei from the target will decrease, thus allowing the population of all the states between the maximum CM energy, at the entrance of the target, and the minimum CM energy, at the exit of the target. While the interest of the experiment lies in the formation of the compound nucleus of ^{15}F, both Rutherford scattering and compound nucleus reactions occur simultaneously. The interference between the two mechanisms results in the resonant elastic scattering reaction. The two contributions will first be described separately for better understanding.

Rutherford elastic scattering

The Rutherford elastic scattering involves the Coulomb force between the charged nuclei and not the nuclear force. In that case, the particles in the entrance channel and in the exit channel are identical :

$$A + B \rightarrow A + B, \tag{1.2}$$

For this reaction, the differential cross-section in the laboratory follows the Rutherford formula :

$$\frac{d\sigma}{d\Omega} = \left(\frac{Z_{beam} Z_{target} e^2}{4E_{beam}}\right)^2 \frac{1}{sin^4(\theta_{ejectile})/2} \tag{1.3}$$

Eq. 1.3 shows that the differential cross-section for elastic scattering is smaller for high energies and high scattering angles. This is true in the case of normal kinematics where the detected particle is the scattered beam. For inverse kinematics, in which the beam is

the heavy nucleus and the target the light nucleus, the detected particle is the scattered target ($\theta_{CM} = 180°$ corresponds to $\theta_{Lab} = 0°$), consequently, the differential cross-section becomes smaller for small scattering angles.

Formation of compound nucleus

Let us take the simple case where particles in the entrance and in the exit channel are different :

$$A + B \rightarrow CN \rightarrow D + E \tag{1.4}$$

Once the CM energy between the beam particle (A) and the target particle (B) is equal to the energy of a state in the CN, the CN can be formed. For the thick target technique, as the beam looses energy inside the target, the CM energy between the beam and the target particle will diminish as a function of the target depth, thus "scanning" all the available states. The range of accessible energies will consequently depend on both the energy of the beam, and the thickness of the target (fig.1.18).

Although being a dynamic process, the reaction from Eq. 1.4 can be described by two static processes (Eq. 1.5) :

$$\sigma = [\sigma_{geometry} \times CN_{formation\ probablity}] \times BR \tag{1.5}$$

The entrance channel (1) : $\sigma_{geometry} \times CN_{formation\ probablity}$ with $\sigma_{geometry} = \pi\lambda\!\!\!^{-2}\omega$, $\lambda\!\!\!^{-2}$ corresponds to the squared De Broglie reduced wavelength of the particle and $\omega = (2J+1)/((2J_1+1)(2J_2+1))$ is the statistical factor which depends on the spin of the states with J_1 and J_2 respectively the spin of the entrance channel particles and J the spin of the compound nucleus resonance. And with $CN_{formation\ probablity} = \frac{\Gamma_1(E)\Gamma(E)}{(E-Er)^2+\frac{\Gamma(E)^2}{4}}$, $\Gamma_1(E)$ is the width of the entrance channel and $\Gamma(E) = \sum_i^N \Gamma_i(E)$ the total width with N the number of open decay channels.

The exit channel (2): The branching ratio (BR) corresponds to the decay of the CN. It is the probability for this states to decay to a given channel. The branching ratio is equal to: $\Gamma_2(E)/\Gamma(E)$ where Γ_2 is the partial width of the decay channel. The determination of partial widths strongly depends on the type of decay channel (particle decay, gamma decay...). Detailed description on how to compute the partial widths relevant to this work is found in section 4.2.5 and 4.3.1. For the case of isolated resonances when particles in the entrance and exit channel are different, it is possible to obtain their cross-section using the Breit-Wigner formula (see Appendix 6.1) :

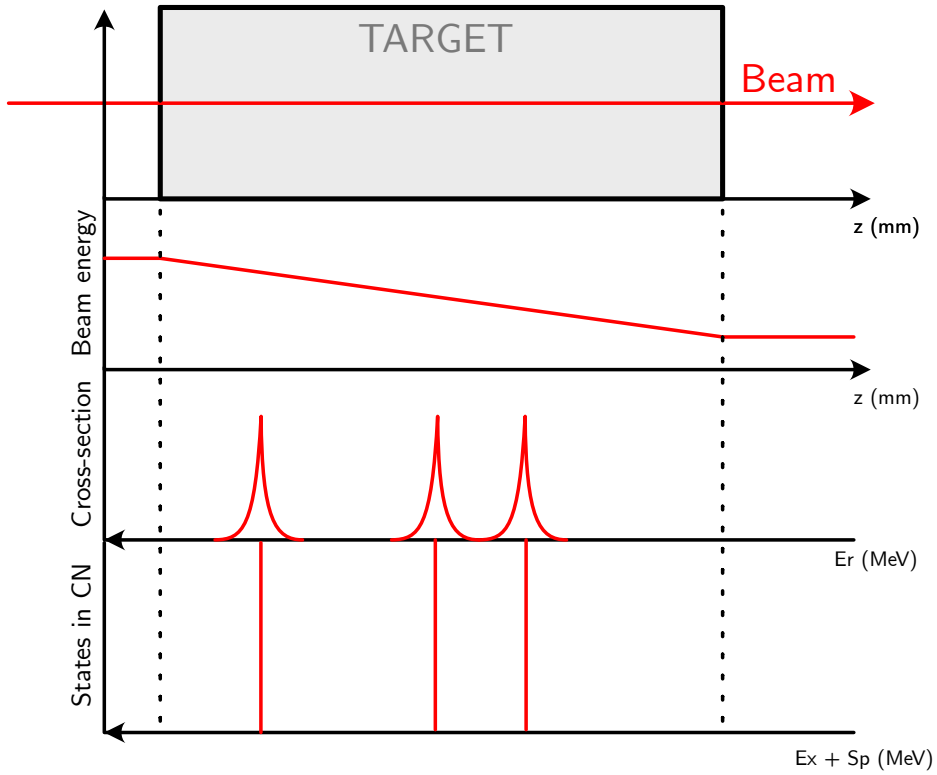

Figure 1.18: *Schematic representation of the working principle of the thick target technique. From top to bottom: (i) scheme of the beam trajectory inside the target. (ii) energy of the beam as a function of target depth. (iii) schematic representation of resonances in the excitation function for the formation of the CN vs the energy of the beam. (iv) illustration of the CN level scheme.*

$$\sigma_{BW} = \pi \lambda\!\!\!^{-2} \omega \frac{\Gamma_1(E)\Gamma_2(E)}{(E - Er)^2 + \frac{\Gamma(E)^2}{4}} \tag{1.6}$$

Resonant elastic scattering reactions (RES)

As its name implies, resonant elastic scattering is a process for which both elastic scattering and resonant capture occur simultaneously. Due to the quantum nature of nuclear reactions the two processes cannot be distinguished, this leads to interferences between the Rutherford scattering and the resonant compound nucleus scattering (Fig. 1.19a). This impacts the shape and amplitude of resonances and can create complicated resonance pattern with constructive and destructive characteristics (Fig. 1.19b). The shape

of the resonances depends on the spin and parity of the CN states. This make RES a very interesting nuclear reaction for nuclear spectroscopy, giving information on the energy, width, spin and parity of the studied resonances.

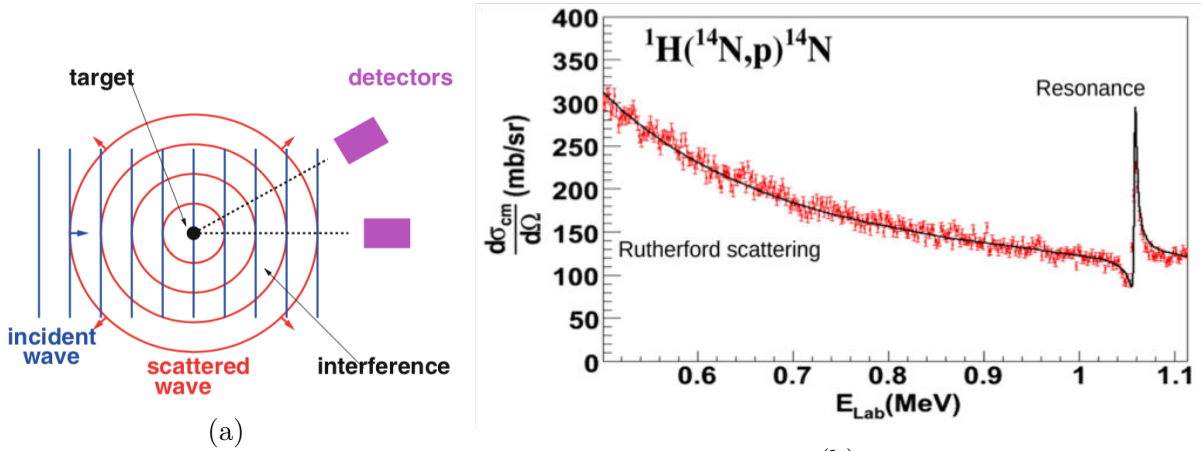

(a) (b)

Figure 1.19: *(a): Scheme of the interference phenomena [Cha16]. (b) example of a resonance obtained in the population of* ^{15}O *[Ste06].*

To describe resonances similar to the one of fig.1.19b, the R-Matrix formalism can be used. It is based on a division of the space in two distinct regions, the internal region (of radius a) described by a nuclear potential and an external region described by either a coulomb potential for charged particle or no potential for neutrons. Two main types of R-Matrix calculations exist, the calculable R-Matrix which aims at solving the Schrödinger equation mostly in the continuum to predict scattering cross-sections and the phenomenological R-Matrix whose goal is to parametrize scattering data to obtain information on the observed resonances. A detailed description of the second formalism is found in [Lan58a; Des10]. In this work we will only focus on the phenomenological R-Matrix.

To illustrate the origin of the interference, it is possible to simplify the problem by assuming that the potential between the projectile and the nucleus is a square well of depth V_0 and radius a (fig.1.20), here for simplicity the scattering of neutrons will be considered. Doing so, it is possible to demonstrate that the cross section can be written [Kra88]:

$$\sigma(E) = \frac{\pi}{k^2}|2sin(ka)e^{ika} - \frac{\Gamma}{(E-Er) - \frac{i\Gamma}{2}}|^2 \tag{1.7}$$

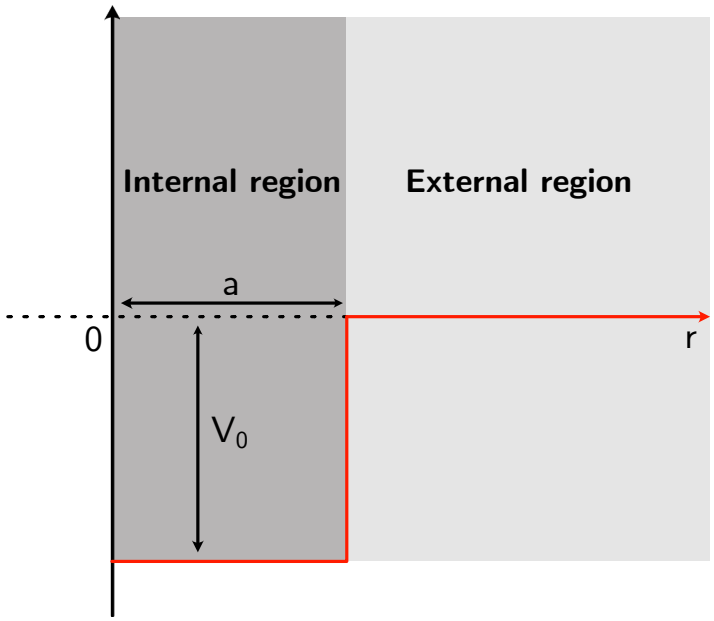

Figure 1.20: *Schematic representation of a square potential well of depth V_0 and radius a.*

In Eq. 1.7 the contribution from the elastic scattering and from the resonant capture are clearly visible. The two terms may interfere as they are added before calculating their square module. In Eq. 1.3 it is observed that in the case of inverse kinematics the Rutherford scattering cross section will be the smallest for small angle, thus in order to minimize the ratio between Rutherford scattering and resonant capture a detector covering small angles in the laboratory will be used. Moreover, as the energy resolution of the detected particles will depend on $\tan(\theta)$ having a detector covering small angles, ideally at 0°, will improve the measurement [de 18].

1.3.2 Goals of the project

Many questions concerning the odd-parity states of ^{15}F are still unanswered (see section 1.2.3). To try to answer some of them, the project described in this work will focus on three different experimental goals (Fig. 1.21):

- 1: Measure the energy and partial width of the $1/2^-$, $5/2^-$ and $3/2^-$ states in ^{15}F, to confirm the existence of the previously measured $1/2^-$ state and see if the narrow character of this state remains for excited states of higher energy, as predicted by

Ref. [Can06] and Ref. [For11]. Experimentally this will be studied via the resonant elastic scattering reaction ^{1}H(^{14}O,p)^{14}O.

- 2: If the $5/2^-$ and $3/2^-$ state can be populated, they should be well above the two-proton emission threshold and then should be two-protons emitter. In this case, the two-proton emission process and the correlations between those protons will be studied to determine if they decay by simultaneous emission: ^{1}H(^{14}O,2p)^{13}N or by sequential emission: ^{1}H(^{14}O,p)^{14}O(1^-)(p)^{13}N.

- 3: Constrain the possible gamma transition between two unbound states, the narrow $1/2^-$ state to the broad $1/2^+$ ground state: ^{1}H(^{14}O,p)^{15}F$(1/2^-)(\gamma$,p)^{14}O.

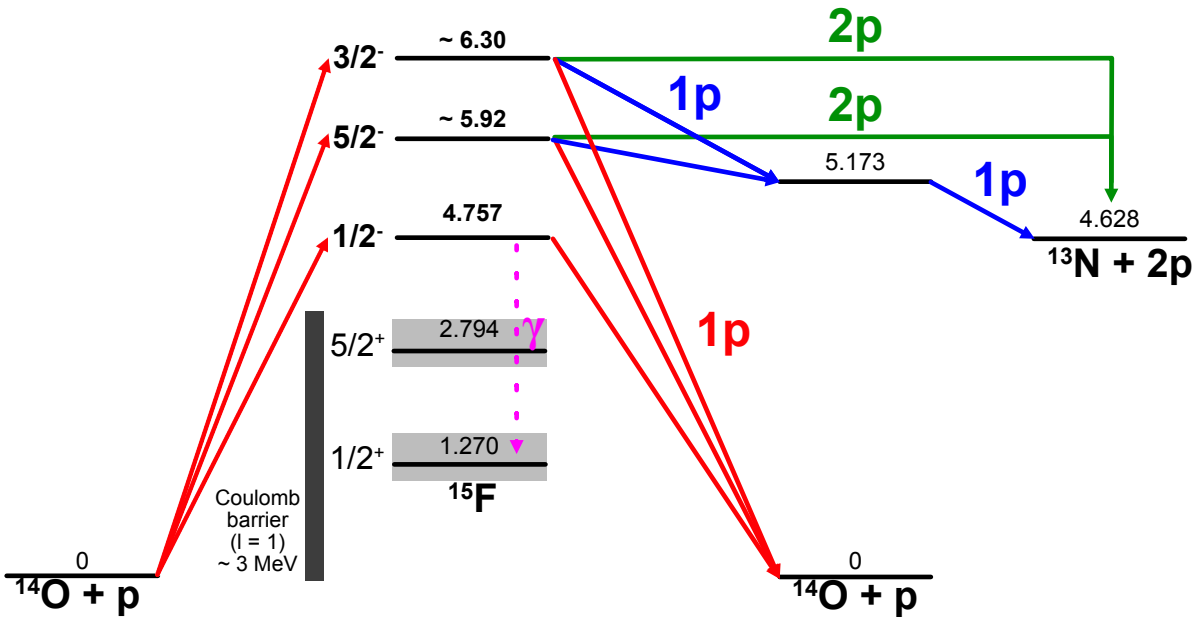

Figure 1.21: *Level scheme of the ^{15}F states studied in this work and their possible decay modes, energies are given in MeV.*

1.3.3 Experimental requirements

To reach our experimental goals, it was chosen to use solid targets made of polyethylene (C_2H_4). Using these targets induces background due to unwanted reactions between ^{14}O from the beam and ^{12}C in the target. At the required beam energy of $\sim$ 7.5 MeV/u, most of those background reactions are fusion-evaporation reactions. To measure the

background, and to remove it from the data, a carbon target was used.

To fulfill all three goals and to obtain the best experimental results possible, three polyethylene targets of different thicknesses were used :

- A "thick" target with a thickness of $\sim$ 200 μm, to populate states from the ground state to higher excitation energy states in ^{15}F, using the radioactive beam of ^{14}O. For calibration purposes, the same target should be used to obtain the excitation function ^{1}H(^{14}N,p)^{15}O using the stable beam of ^{14}N. This target is required for calibration or beam alignment purposes. With this target it was intented to populate the full excitation function of ^{15}F starting at E_{CM} = 7.05 MeV.
- An "on-resonance" target with a thickness of $\sim$ 100 μm, to populate states of higher excitation energy in ^{15}F ($5/2^-$ and $3/2^-$) as well as the already measured $1/2^-$ state. The thickness is carefully chosen to avoid the direct formation of the $^{15}F_{g.s.}$. In this way, if protons from $^{15}F_{g.s.}$ are identified, it means that gamma transitions have taken place. This is the main target of the experiment. This target aimed at populating states between E_{CM} = 4.18 MeV and E_{CM} = 7.05 MeV.
- An "off-resonance" target with a thickness of $\sim$ 70 μm, to populate only the $5/2^-$ and $3/2^-$ states without populating the $1/2^-$ state. This target is used to verify that if gamma particles are detected, they can only come from the internal gamma transition between the $1/2^-$ state and the $1/2^+$ ground state. The energies we expected to populate with this target were ranging from E_{CM} = 5.15 MeV and E_{CM} = 7.05 MeV.

As it can be understood from the description of the experimental goals, different detectors were useful: a charge particle detector for protons for the first and second goal, with at least a detector at 0° for the first goal and a gamma detector for the third goal.

1.3.4 Monte Carlo simulations

The use of Monte Carlo simulations has become the standard technique to simulate nuclear physics experiments. It is based on the repeated randomization of multiple parameters in order to reproduce the statistical and complex nature of real experiments. Even if Monte Carlo simulations can be done using "homemade" software it can be very complicated to reproduce all the detail and complications arising from the geometrical and physical characteristics of complex detectors. To this extent, the GEANT4[1] [Ago03] package developed at the CERN is the perfect toolbox to simulate nuclear physics experiment as

[1] GEometry ANd Tracking

it can give many information on the trajectory and energy lost by the particles inside a realistic three dimensional geometry (Fig. 1.22).

In this work, "homemade" software has been developed to simulate the different reactions of interest presented in the previous paragraphs. They were tested and then implemented in GEANT4 using the NPTool package which aims to unify the analysis and simulation of nuclear physics experiments [Mat16]. In other words, simulation generated using NPTool can be analyzed using the same analysis code developed to analyze real experimental data.

Two experiments will be detailed in chapters 2 and 3. The simulation performed for both experiments were similar with the main difference being the geometry of the light particles detectors (Fig. 1.22), adapted from the measurements performed by the optical surveyors. These simulations have been performed with two distinct purposes: (i) for the preparation of the two experiments by simulating the kinematics of the reaction products. It was useful to choose the detectors that were the most suited to detect the particles of interests, as well as optimizing their position, geometry, performance... (ii) as a tool used to interpret the experimental results obtained. It was especially helpful to simulate complex experimental effects such as the degradation of the experimental results by the resolution of the detectors or the angular and energy straggling of the detected particles in the target, the dead layers of the detector...

Simulation of the Rutherford scattering in a thick CH2 target

In this experiment the thick target technique was used, then, as the beam looses energy, elastic reactions occur continuously throughout the target. In the simulation, a random position of interaction in the target as well as random polar and azimuthal angles for the ejectiles were generated in spherical representation. The energy and angle of the protons can then be obtained from those variables (Fig. 1.23).

Using GEANT4, the angular coverage of the detectors can clearly be observed, as well as the impact of the Ta foil on the energy of the protons as there is a visible energy shift towards lower values of the protons for the 0° detector (Fig. 1.23b).

Simulation of the sequential and simultaneous two-proton emission from a narrow state

Contrary to the simulation of the elastic scattering reaction described in the section above, where reactions can happen throughout the target, the two-proton emission will happen

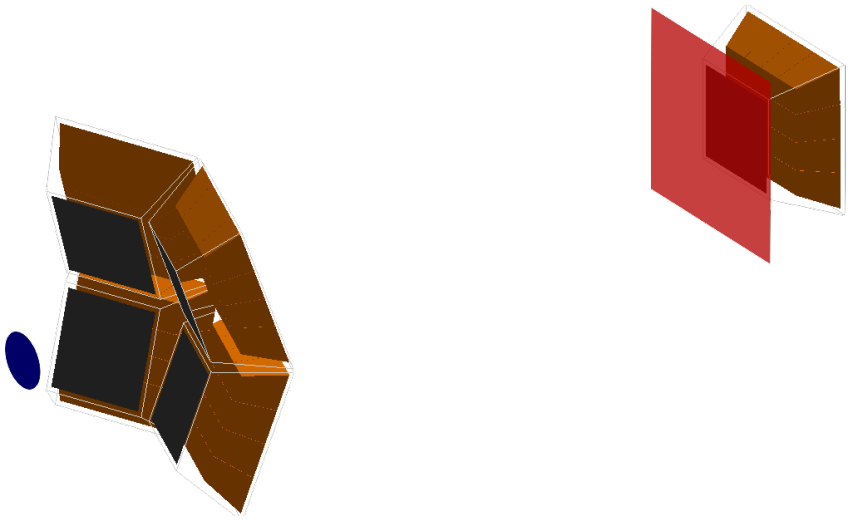

Figure 1.22: *Three-dimensional view of the experimental setup (only the charged particle detector) used in the first experiment generated using GEANT4 and NPTool . In black and orange are the MUST2 detectors (see section 2.2.4), in blue the target and in red the tantalum (Ta) foil used to stop the beam.*

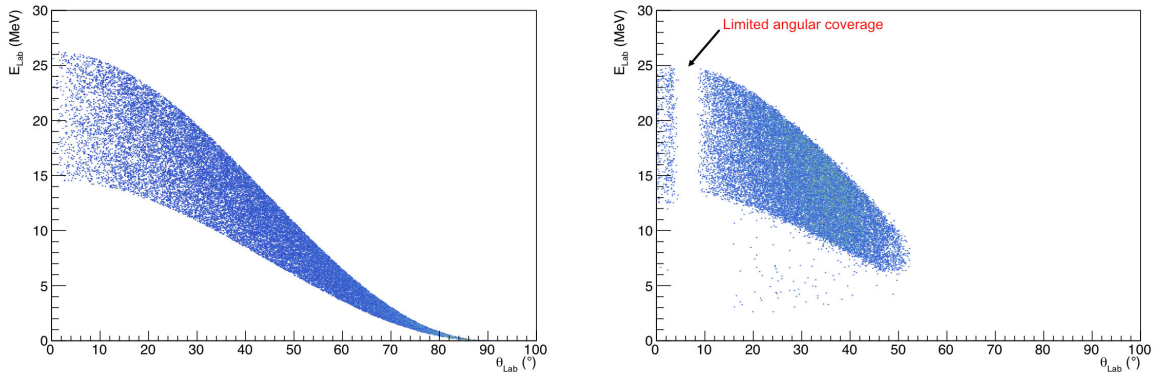

(a) (b)

Figure 1.23: *(a): Kinematics of the elastically scattered protons from a 7.5 MeV/u ^{14}O beam inside a 100µm CH_2 target. (b): Same as left but using GEANT4 to assess the performance of the experimental setup.*

in a precise target region, depending on the energy of ^{15}F resonances. For illustration, the decay from the $3/2^-$ state is considered in this section (Fig. 1.24).

To reproduce realistic experimental conditions the position of the interaction was shot randomly inside the 100 μm target and the center of mass energy between the beam particles and the target nuclei is obtained considering the energy lost by the beam before the interaction point. As, the two-proton decay should only occur when the compound nucleus ^{15}F is formed, the probability for the reaction to occur at a given target position was constrained using the Breit-Wigner formalism (see Appendix 6.1). It translates in the kinematics by the appearance of a broad line seen in Fig. 1.24a and Fig. 1.24c. Concerning the sequential decay, the 30 keV width of the intermediate state in ^{14}O was taken into account by constraining its profile similarly to the profile of the ^{15}F state using the Breit-Wigner formalism. In the case of the simultaneous emission, only the emission and decay of a ^{2}He-cluster was considered

The GEANT4 simulation shows that between the theoretical simulation and the reality there is a huge difference in resolution, it also highlights experimental feature such as the effect of the dead layers between detectors. A hole is visible in the energy distribution, which creates an extra line starting from 3 MeV at 0°, particularly visible for the ^{2}He decay (Fig. 1.24d), this line is due to punch-through events that crosses the first detection stage, but never reach the second stage (stop in the dead layer) thus creating a spurious line as only the energy detected by the first layer is registered. This is an example of effects that is very difficult to take into account and predict without simulating a realistic geometry of the experimental setup.

Simulation of the gamma emission from ^{15}F second excited state

The simulation of the gamma emission (Fig. 1.25) is a two step process. First, similarly to the two-proton emission, the energy at which the state was populated was constrained by a Breit-Wigner cross-section whose width was equal to the one of the $1/2^-$ state. Then, the gamma emission was generated considering the width of the $1/2^+$ ground state, and the energy at which the $1/2^-$ state was populated. As a consequence, the energy distribution of the gamma and subsequently the one of the proton in the CM was very broad, as the gamma can take almost all the available energy or none of it (Fig. 1.17). It translates to a very broad kinematics distribution.

1.3.5 Conclusion

In this chapter relevant characteristics of drip-line nuclei were reminded. The process of clustering was detailed with a strong emphasis on the effect of particle emission threshold on their formation, from the well known Hoyle state to more recent example of two-nucleon

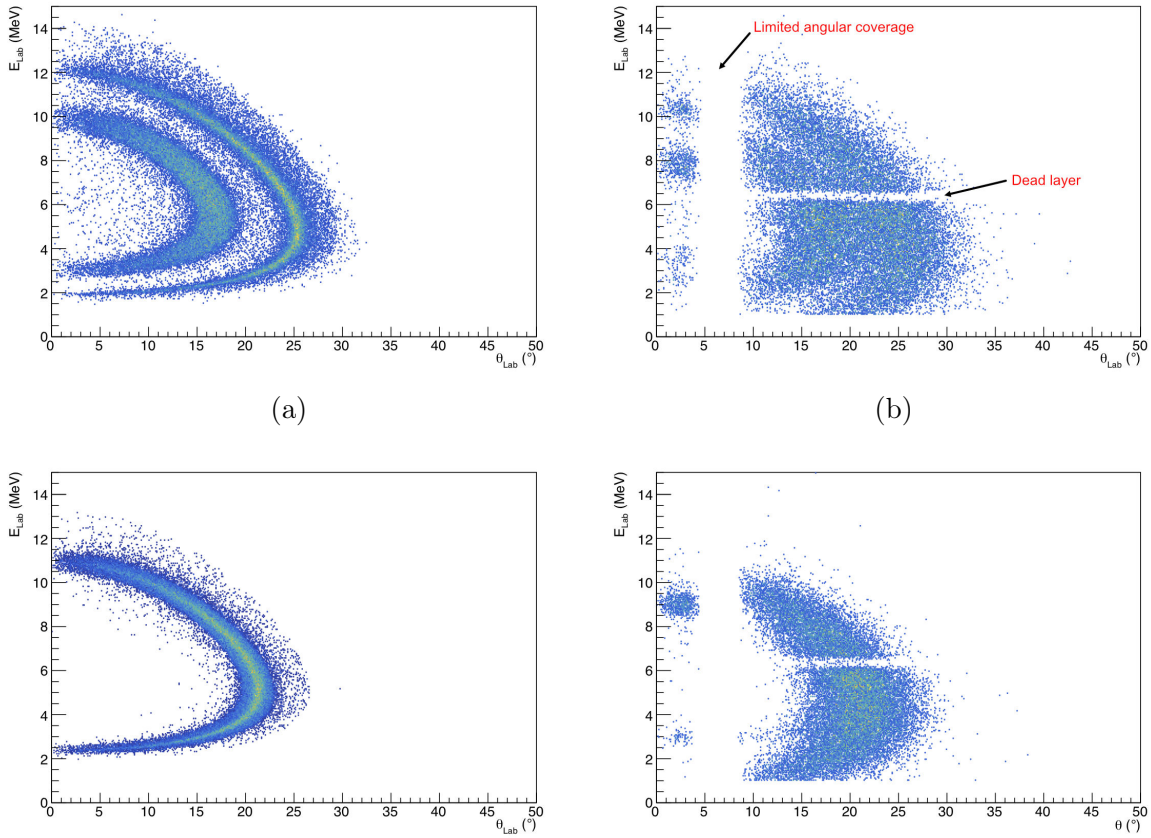

Figure 1.24: *(a): Simulation of the sequential two-proton emission from a 3/2⁻ state in ^{15}F (E_{CM} = 6.3 MeV and Γ = 40 keV). The kinematic line starting from 12 MeV at 0° corresponds to the emission of the first proton from the 3/2⁻ state in ^{15}F, the line starting at lower energy corresponds to the second proton emitted from ^{14}O first excited state (1⁻) the effect of the experimental setup is not considered. (b): Same as top left but using GEANT to assess the performance of the experimental setup. (c): Simultaneous two-proton emission from a 3/2⁻ state in ^{15}F (E_{CM} = 6.3 MeV and Γ = 40 keV). (d): Same as bottom left but using GEANT4 to assess the performance of the experimental setup.*

clusters. The process of gamma transitions between unbound states was also detailed and a few experimental results previously obtained were presented.

Fluorine 15 was proven to be a very good candidate to study both topics, due to

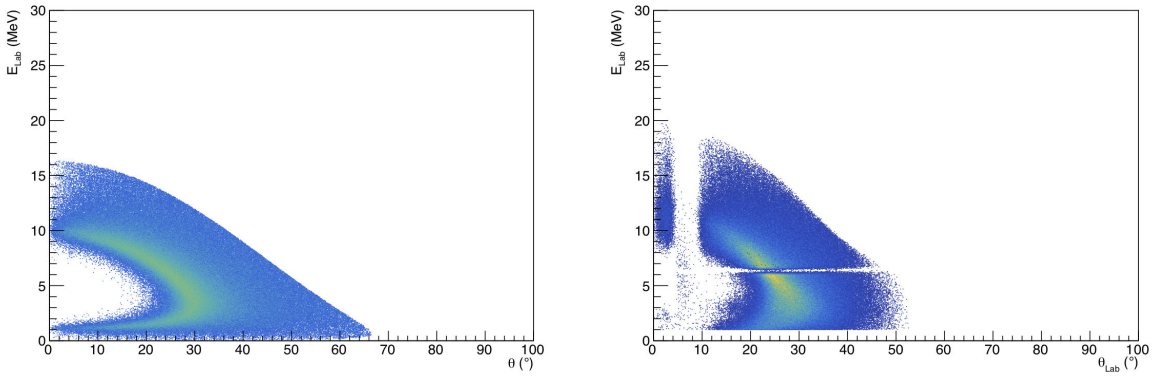

(a) (b)

Figure 1.25: *(a): Kinematic simulation of the protons emitted by the $1/2^+$ ground state of ^{15}F after the gamma emission from the $1/2^-$ state. (b): Same as left but using GEANT4 to assess the performance of the experimental setup.*

the unique structure of its odd-parity states motivating different studies of this nucleus. Consequently, three experimental goals of this study, namely the measurement of two new odd-parity states in ^{15}F, a $5/2^-$ and a $3/2^-$ states, their decay by two-proton emission and the possible gamma decay from ^{15}F second excited state to the ground state were detailed. The experimental requirements were also described and simulations were performed to verify the feasibility of such experiment. It is worth emphasizing that these simulations will prove to be an asset to help in the interpretation of the experimental results (see chapters 2 and 3).

2

Measurements of new states in ^{15}F

Contents

2.1 Introduction

In this chapter, a first experiment performed at GANIL is presented. This experiment was designed to study the structure of the ^{15}F unbound nucleus using the resonant elastic scattering reaction ^{1}H(^{14}O,p)^{14}O. This study used a radioactive ^{14}O SPIRAL1[1] beam impinging on a thick polyethylene (CH_2) target.

This work has three motivations that demanded the use of different type of detectors. Charged particles were detected using the MUST2[2] array (see section 2.2.4) and to detect gamma rays two different detectors were used: the EXL[3] demonstrator composed of 18 CsI crystals plus a LaBr3 detector, and to track the beam a CATS[4] (see section 2.2.3) detector was placed before the target.

In this first experiment, due to different malfunctions from GANIL's accelerators, only the first motivation, the measurement of new states in ^{15}F using the resonant elastic scattering reaction (^{1}H(^{14}O,p)^{14}O) will be detailed. The first part of the chapter (section 2.2) will focus on detailing the beam production as well as the different detectors used. In the second part of the chapter (section 2.3) the analysis of the resonant elastic scattering reaction will be described and results from this first experiment will be shown.

2.2 Experimental conditions

2.2.1 Beam production

To study new states in ^{15}F using the resonant elastic scattering reaction, a beam of ^{14}O at an energy of $\sim$7.5 MeV/u was produced by ISOL[5] method using GANIL SPIRAL1 facility. A primary beam of ^{16}O obtained from the ionization of stable oxygen gas from C01 source was accelerated by the two main GANIL cyclotrons (CSS1[6] and CSS2) before being sent on a thick carbon target (ECS[7]), which produces ^{14}O as well as other contaminants. Ions of ^{14}O are then selected and re-accelerated by the CIME[8] cyclotron (Fig. 2.1). With the $^{14}O^{4+}$ of interest, a beam of $^{14}N^{4+}$ was also transmitted for calibration purposes, by

[1] Système de Production d'Ions RAdioactifs en Ligne
[2] MUr a STrips 2
[3] EXotic Light Nuclei Studied at the NESR storage ring
[4] Chambre A Trajectoire de Saclay
[5] Isotopic Separation On Line
[6] Cyclotron à sécteurs séparés
[7] Ensemble Cible Source
[8] Cyclotron pour Ions de Moyenne Energie

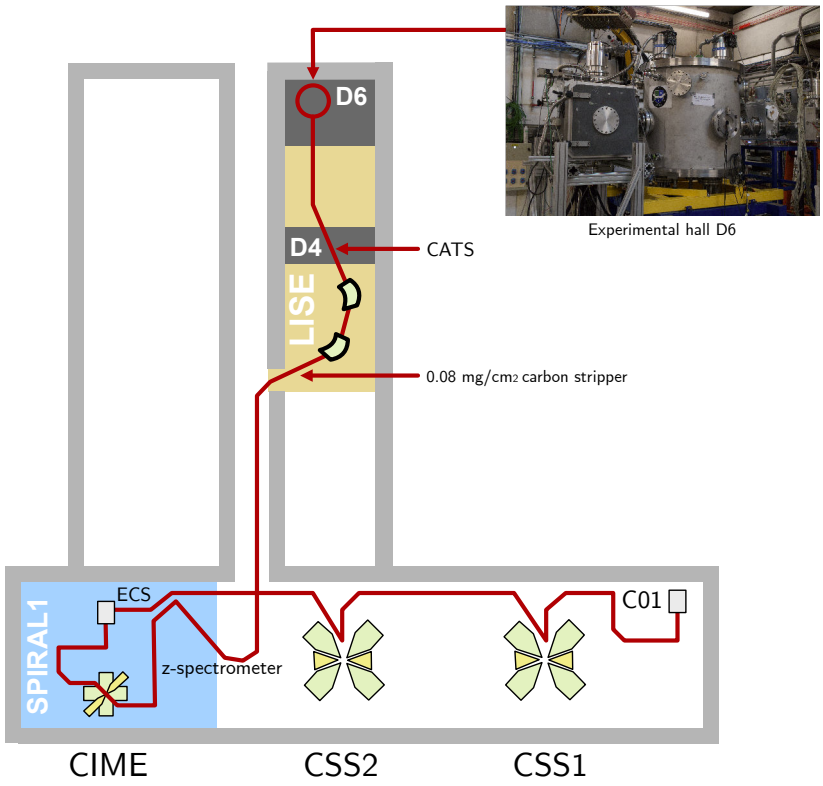

Figure 2.1: *Schematic representation of the relevant part of GANIL facility used to perform the E744 experiment. The ^{14}O radioactive beam was produced by the fragmentation of a ^{16}O beam and into the ECS target of SPIRAL1 (blue region). The beam was thereafter sent to the LISE spectrometer (yellow region) and finally to experimental hall D6 (dark grey region).*

populating well known states in ^{15}O [Guo05] using the resonant elastic scattering reaction. After being accelerated, the energy of the ions were obtained from the Bρ measured by the Z-spectrometer: Bρ = 1.40(1) T.m. This Bρ corresponds to: $E_{^{14}O^{4}}$ = 7.64(1) MeV/u and $E_{^{14}N^{4+}}$ = 7.64(1) MeV/u. It is worth pointing out that these energies were higher than the 7.5 MeV/u needed to perform the experiment, this was required to compensate for the energy lost by the beam hitting different materials placed before the target, such as the 0.08 mg/cm^2 carbon stripper used to fully strip the ions and the different layers of the CATS detector (see section 2.2.3).

The experiment was located at the end of the LISE spectrometer. A stripper foil was used at the entrance of the LISE spectrometer (D6 Fig. 2.1) to fully strip the ions,

		Attributed		Effectively obtained		
Beam	Target	UT	Intensity (pps)	UT	Intensity (pps)	Effective beam time
^{14}O	100μm CH_2	6	3x10^5	2.5	1.3x10^5	18%
^{14}O	70μm CH_2	4	3x10^5	-	-	0%
^{14}N	thick CH_2	2	3x10^5	0.625	2x10^5	20%
^{14}O	carbon target	4	3x10^5	0.75	1.3x10^5	8%

Table 2.1: *Summary of the beam intensity and beam time asked in the proposal compared to the one obtained. The effective beam time is equal to :* $\frac{UT_{Asked} \times Intensity_{Asked}}{UT_{Obtained} \times Intensity_{Obtained}}$

allowing the use of the spectrometer to select between $^{14}O^{8+}$ and $^{14}N^{7+}$.

During the experiment the facility had multiple issues. The main one being a water leak in one of the cavity of CSS1. This problem reduced by a factor 10 the expected statistics making the study of the two proton emission and gamma emission very challenging, as it requires higher statistics (see Table. 2.1). For this reason, only the analysis of the resonant elastic scattering reaction will be presented in this chapter.

2.2.2 Targets

This experiment used the thick target technique (section 1.3.1). To perform the measurement, multiple targets were required (section 1.3.3), being bought from GoodFellow [Goo] or built on site. The two most important thickness for the measurement namely the ∼100 μm CH_2 and the ∼70μm CH_2 were present twice on the target holder. A summary and a picture of the mounted target is found in Fig. 2.2.

(a)

Position	Material	thickness (μm)	
		Provided	Measured (appendix 6.2)
6	C_2H_4	187	-
5	C_2H_4	100(10)	92(9)
4	C_2H_4	104(10)	107(11)
3	C_2H_4	73(7)	-
2	C_2H_4	73(7)	77(8)
1	$^{(nat)}C$	75(8)	-

(b)

Figure 2.2: *(a) : Picture of the target holder, targets are numbered from bottom to top. (b) : Characteristic and position of the different target placed in the target holder. The thicknesses are the ones given by the manufacturer and the ones measured (appendix 6.2). The carbon target was made out of flexible graphite, for which the density given by the manufacturer ranges from 0.9 to 1.3 g/cm3.*

2.2.3 Beam tracking : CATS

The CATS detector [IRF] is a beam tracker, it can be used in conjunction with a second CATS detector to obtain a precise reconstruction of trajectories event by event. Its usefulness has been demonstrated multiple times in improving the angular resolution obtained with the MUST2 detector [Fla11]. It can also be used as a time reference with a precision of the order of the ns as well as being used to monitor the beam intensity with a very high efficiency. The detector itself is a low pressure multi-wire proportional chamber (Fig.2.3) filled with an isobutane gas (C4H10) with a pressure of 8 mbar. The gas is trapped between two 1.5 μm Mylar foils. Each detector is made of a plane of 71 anodes wires between two segmented cathode containing each 28 strips placed horizontally for one and vertically for the other. The active area of this detector is 70 $\times$ 70 mm^2.

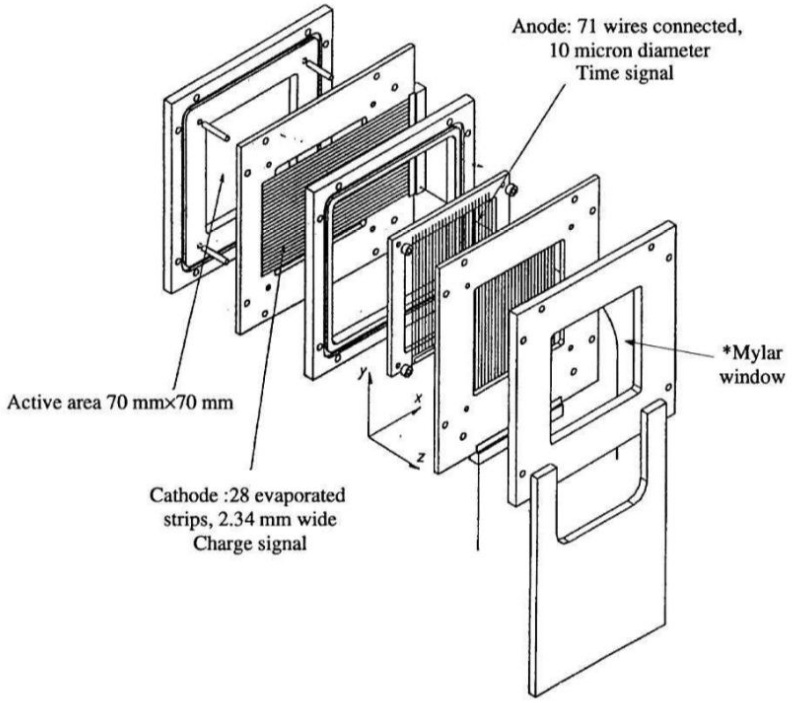

Figure 2.3: *Scattered view of the CATS detector. [IRF]*

In this experiment, a single CATS detector was mounted in experimental hall D4 (Fig.2.1). This was a simplified version of the CATS detector which did not feature strips as it was not used as a beam tracker but only as a monitor for the beam intensity and as

a time reference for time of flight identification. The choice of using a simplified CATS placed in another experimental hall was motivated by the fact that reactions between the beam and the different layers of the CATS detector would emit protons and subsequently add background. Its detection efficiency stayed stable throughout the experiment and measured to be of 99.5(5)%. To ensure minimum dead time, one out of thirty thousands CATS events were recorded by the acquisition.

Taking into account the beam energy loss in the stripper and in the CATS detector the energy of the two beams at the entrance of the experimental chamber were respectively : $E_{^{14}O^{8+}}$ = 7.46(1) MeV/u and $E_{^{14}N^{7+}}$ = 7.51(1) MeV/u

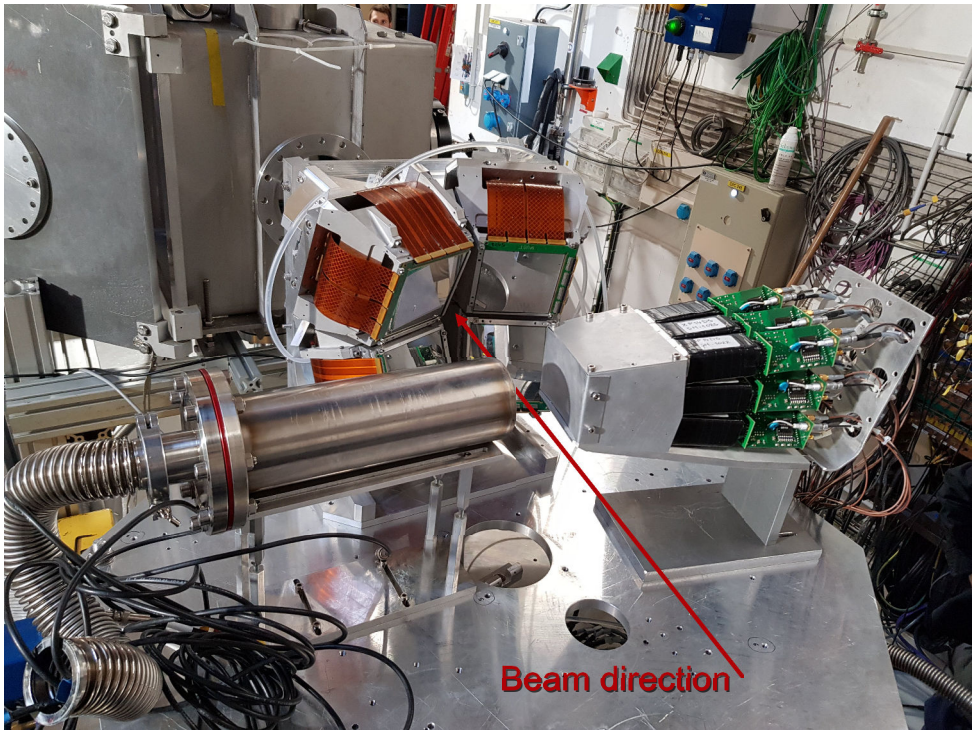

Figure 2.4: *Picture of the experimental setup used in the first experiment. On the back of the platform 4 MUST2 telescopes are found and on each side of the target (not on the picture) two gamma ray detectors. On the left a LaBr3 detector and on the right the EXL detector, which is a gamma ray detector composed of multiple CsI crystals.*

2.2.4 Charged particles detection : MUST2

Description of the detector

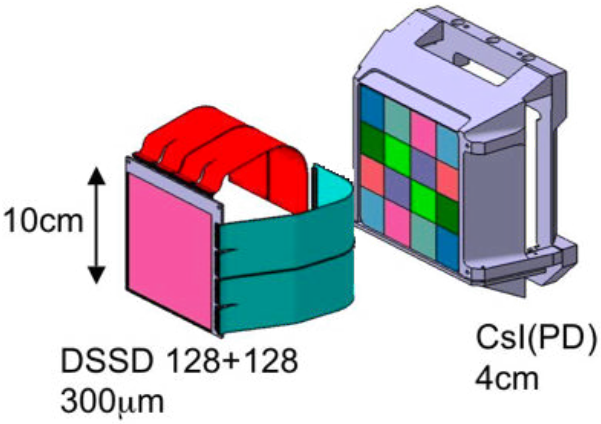

(a)

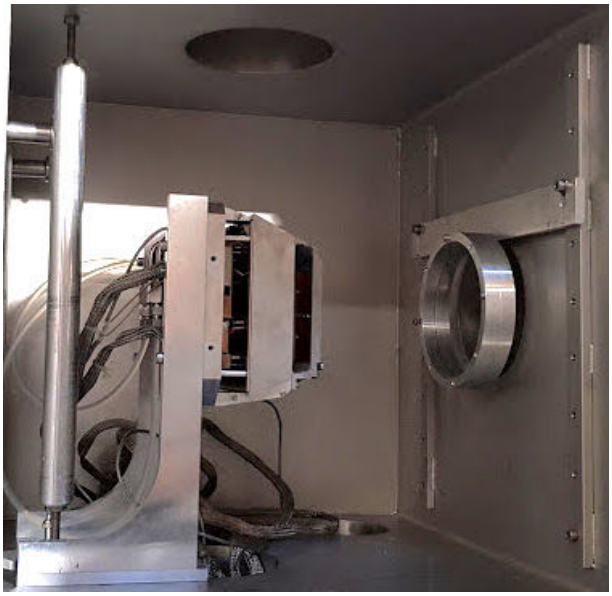

(b)

Figure 2.5: *(a) : Scattered view of the two stages used in this experiment. (b) : Picture of the chamber where the 0° detector was located.*

The MUST2 array is a set of up to eight modular telescopes (see Fig. 2.4) designed to measure light particles emitted through direct reactions in inverse kinematics. Each telescope is composed of three stages:

- The first stage is a 300 μm Double-Sided Silicon Strip Detector (DSSSD) with a 98 $\times$ 98 mm^2 active area. A layer of aluminum of 0.4 μm is evaporated on each side of the detector, this layer is then divided into 128 strips vertically on one side and horizontally on the other side. The strip pitch is 0.75 mm (the angular resolution of the detector is $\sim$0.15 degree at a distance of 15 cm) and the energy resolution for a strip is 40 keV, as obtained with an alpha source (Fig. 2.6a). This stage gives information on the energy loss, the time and the position of interaction of the particle. It was the main trigger of the data acquisition.

- The second stage of the telescope is made of two 4.5 mm SiLi (lithium-drifted silicon) detectors with an active area of 92 $\times$ 48 mm^2. They are segmented into 8 pads. This

stage has an energy resolution of 130 keV, as obtained with an alpha source (Fig. 2.6a). It allows a good energy measurement as well as a good particle identification paired with the first stage. Its drawback is that it geometrically covers only about 65% of the surface of the DSSSD. This stage is not used in the experiment.

- The third and last stage is a calorimeter made of 4 x 4 CsI crystals. Each crystal has a trapezoidal shape with a thickness of 40 mm and an active area of 30 x 30 mm^2 read by a photo-diode. They have a full coverage of the DSSSD stage, but their energy resolution is rather low. Its energy resolution depends on the energy of the detected particle and can be obtained with the formula: $\sigma_{CsI_{Energy}} = 0.08 \times \sqrt{CsI_{Energy}}$ MeV. Another drawback with the use of CsI is that their calibration is very dependent on the type of particles detected, making them more complicated to calibrate. The role of this last stage is to measure the residual energy of light particles that cross the first stage. It can be used for particle identification as well as for measuring the total energy of the light particles.

In this experiment five telescopes were used (Fig. 2.4). They were all composed of only the first and third stage. Four were located in the front and looking directly at the target with a mean distance of 15(1) cm and a fifth is placed in a different chamber at 0° with a distance to the target of 86(1) cm (Fig. 2.5b). To protect this detector, the beam was stopped in a 34(7) μm tantalum (Ta) foil placed at the entrance of the 0° chamber. Ta was chosen because it is a heavy element with a high coulomb barrier. For this reason, the beam is stopped in the foil without inducing background from unwanted reactions. It was also chosen to put the 0° detector in a different chamber as the ^{14}O ions are unstable and decay by beta emission. Stopping the beam inside a second chamber far from the target limits the background seen by the gamma detectors. During the experiment 4 out of 5 MUST2 telescopes worked as expected, one of the MUST2 telescopes located at 15(1) cm from the target had a DSSSD that did not work (electric current spikes during the whole experiment).

DSSSD energy calibration

The DSSSD energy calibration was performed using a three-alpha source composed of ^{239}Pu, ^{241}Am and ^{244}Cm. Energies from this source are listed in Fig. 2.6a. In the case of the MUST2 array, the energy detected by the 256 strips is coded with a 14 bit ADC between 0 and 16383. The strips from the junction side (X-strips) of positive polarity are coded from 8192 to 16383 and the strips from the ohmic side (Y-strips) of negative parity are coded between 0 and 8191. Before performing any calibration, the pedestals of all the strips were aligned electronically using the back-end electronic board.

Nuclei	Energy (MeV)	Intensity	Half-life (years)
^{239}Pu	5.15659(14)	70.77(14)	2.411 10^4
	5.11443(8)	17.11(14)	
	5.1055(8)	11.94(14)	
^{241}Am	5.48556(12)	84.8(5)	432.2
	5.44280(13)	13.1(3)	
	5.38823(13)	1.66(2)	
^{244}Cm	5.80477(5)	76.40(12)	18.1
	5.76264(3)	23.60(12)	

(a)

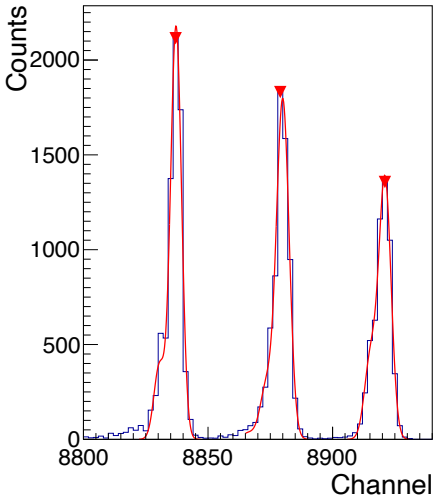

(b)

Figure 2.6: *(a) : Energies of the three alpha source used. (b) : Example of energy spectra obtained with the three alpha source for the strip 70 of detector n°5. The smooth line in red corresponds to the fit.*

The calibration program used was the standard one from the MUST2 collaboration ([Mat12], [Mor14]). The main and satellites peaks of each nuclei were fitted using gaussian functions, a linear fit was then performed to obtain the calibration of each strips. A "zero-extrapolation" method was also used to determine the aluminum dead layer taken into account in the calibration [Mat12]. An example of fit is shown in Fig. 2.6b and comparison between the raw data and the calibrated data is shown in Fig. 2.7.

DSSSD time calibration

Time calibration was performed for each strip using a time calibrator which randomly generated start and stop sent to TDC integrated in the electronic card of MUST2. The time between each start and stop was equal to : $N \times \tau$ where N is a random integer and τ the chosen period (here τ =20 ns) this was done to cover the full range (here 640 ns). Each strip was then calibrated using a second order polynomial taking the first peak as a reference. This calibration determines the slope but not the offset of the calibration, it was used only to identify particles if their energy was not sufficient to go through the first detection layer. In this experiment the time reference was the CATS detector and it was useful for protons with an energy lower than 6 MeV. See an example of calibrated data

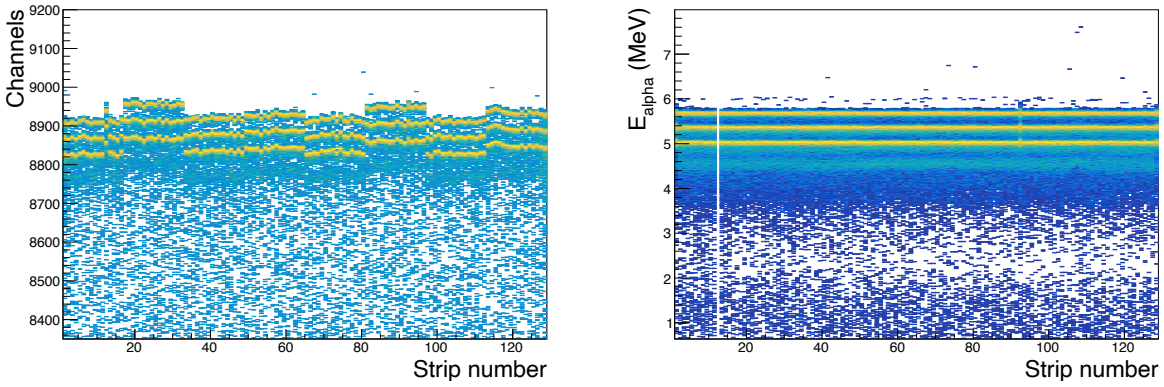

(a) (b)

Figure 2.7: *(a) : Non-calibrated alpha particles energy as a function of the strip number for X strips of telescope n° 5. (b) : Calibrated alpha particles energy in MeV as a function of the strip number for X strips of telescope n° 5.*

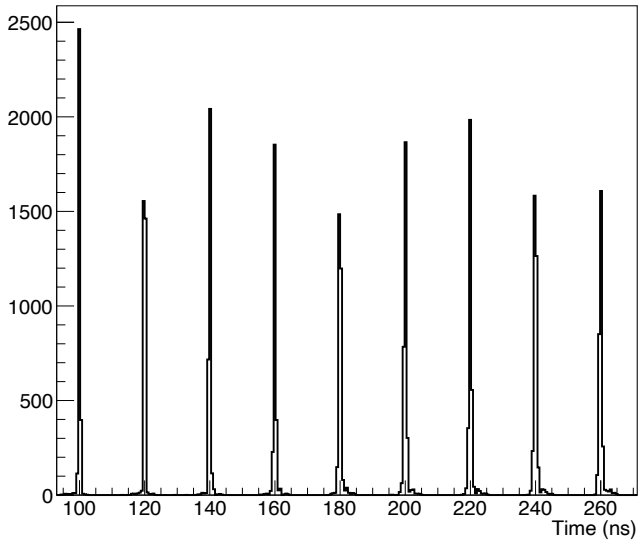

Figure 2.8: *Time calibration spectrum measured for telescope n°3. The period between two peaks is 20 ns.*

in Fig.2.8.

CsI energy calibration

The calibration of the CsI crystals was not done using a source. It would first of all be complicated and risky to dismount the DSSSD each time a calibration is needed and secondly, it would not be very useful, using an α source for example, as the calibration obtained would only work for alpha particles and be very limited in energy. Indeed, for charged particles interacting with CsI crystals, it has been shown that their calibration depends on the mass and charge of the detected particles [Mou08].

To calibrate the CsI, the energy lost by the particles in the first layer (ΔE) was used. It is known that charged particles loose energy in a given material depending on their energy and charge. For each crystals, once the calibration of the first layer was done, it was possible to draw the CsI energy in channel as a function of the DSSSD energy (Fig. 2.9a). Doing so (for each crystal), multiple curved lines corresponding to different types of detected particles can be observed. In this experiment, only the calibration of the protons was needed (which corresponds to the first curved line). Selection were then made around the proton for each crystals (Fig. 2.9a). Then, it was possible [Mou08] to

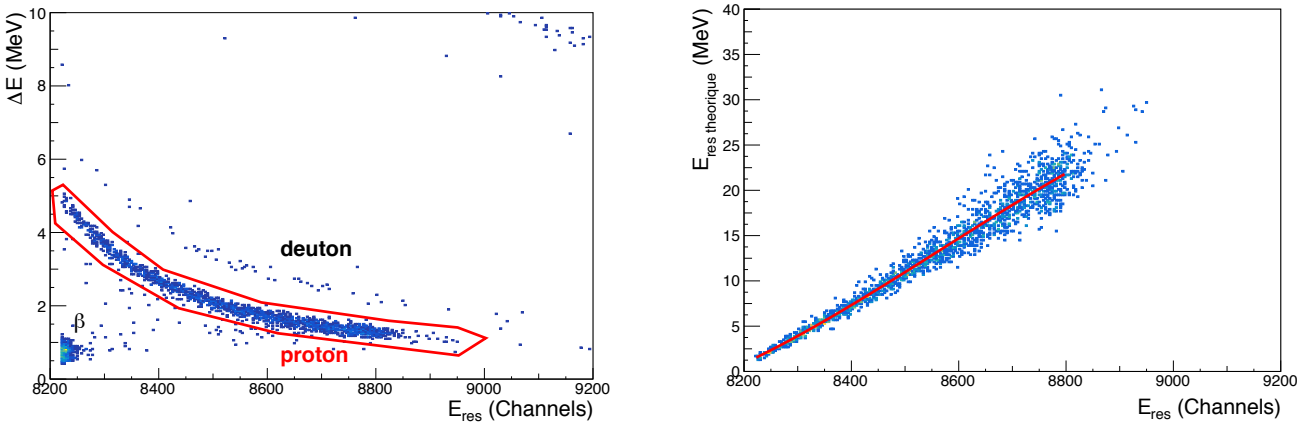

(a) (b)

Figure 2.9: *(a): Calibrated energy in the DSSSD as a function of the CsI energy (residual energy) in channels for crystal 10 of the 0° telescope, a red selection is drawn around the proton. (b): Calculated residual energy (from the DSSSD) as a function of the residual energy in channels for crystal 10 of the 0° telescope.*

compute the theoretical energy of the protons in the CsI crystals depending on the energy lost in the DSSSD through the use of energy loss tables, see Fig.2.9b. This theoretical energy as a function of the measured CsI energy (in channel) was then fitted, by using a third order polynomial function to obtain the calibration parameters for each crystals. By using this method there was no need to correct for the energy lost by the protons in any dead layer between the exit of the DSSSD and the entrance of the CsI, as the crystals were calibrated as if they detected all the residual energy (E_{res}) [Mou08].

To measure the total energy of the protons, another solution could have been to only use the CsI crystals for particle identification and directly use the energy measured by the DSSSD to compute the total energy of the particles. The issue with this method is that, as it can be seen on Fig.2.9b, the determination of the residual energy gets worst as the energy increases. This is due to the fact that the energy deposited in the DSSSD becomes smaller for higher proton energy (see Fig.2.9a). An error of a few keV would imply a much larger error in the computed residual energy.

Position dependent CsI energy calibration

During this experimental campaign it was observed that the crystals showed differences in the energy calibration depending on the position of interaction of the particles in the CsI (Fig.2.10). To correct this effect, it was possible to perform the calibration described

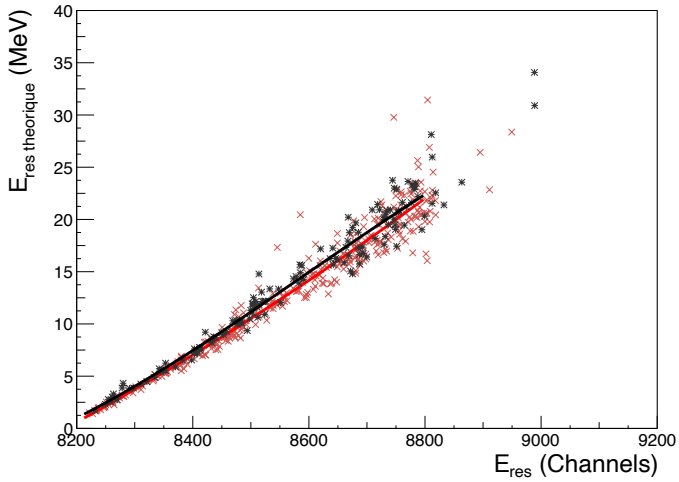

Figure 2.10: *Example of non-uniformity between two different pixels of the same CsI crystal.*

in the previous paragraph but for only a given set of X and Y strips of the DSSSD. This type of calibration will be called "pixel calibration" (Fig. 2.11). In this first experiment each crystal was divided in 3x3 = 9 pixels. The improvement was small, but still visible. An example of the improvement obtained using the pixel calibration is seen in Fig.2.12 where the center of mass (CM) energy spectra obtained with the ^{14}N beam is compared with and without using a pixel calibration (details on how to obtain this spectra are given in the next paragraph).

Validation of the energy calibration

To verify that the detectors are well calibrated it was possible to look at the data obtained with the ^{14}N beam. Indeed, the resonant elastic scattering reactions $^{14}\mathrm{N} + \mathrm{p} \rightarrow {}^{14}\mathrm{N} + \mathrm{p}$ has already been measured multiple times, either in direct kinematics [Oln58; Wes69] or similarly to this work in inverse kinematics [Guo05]. Here, the excitation function obtained by F. Q. Guo [Guo05] was used as a reference. To match the current experimental data to the reference, it was necessary to take into account the energy lost by the protons, both in the 34 μm tantalum foil located in front of the 0° detector and in the 187 μm CH_2 target itself. For this purpose, it was possible to use the energy loss table from GEANT4 to simulate the experiment. To perform such a simulation, the energy of the beam as well as the thickness of both the target and Ta foil were used. The simulation works as follows: a beam of ^{14}N interacts with the target and looses energy step by step; at each step protons are generated and loose energy, first in the remaining target, and then into

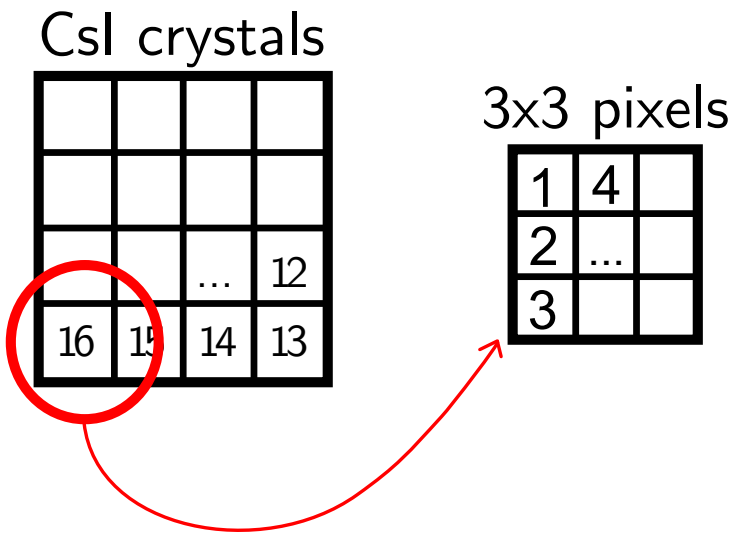

Figure 2.11: *Principle of the pixelization, each crystal is divided in pixel by using only a few strips for the calibration. Here as an example the crystal is divided in 8x8 = 64 pixels each using 4 strips in X and 4 strips in Y.*

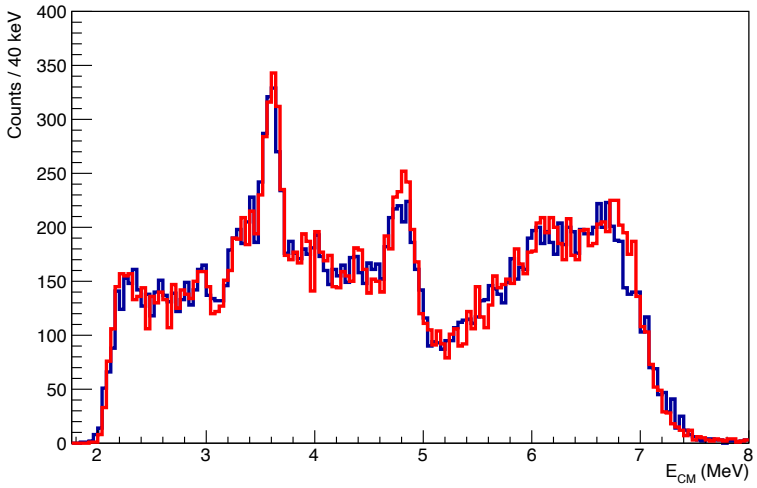

Figure 2.12: *Example of improvement obtained using a pixel calibration. In blue the spectra obtained without pixel calibration. In red the spectra obtained using the pixel calibration. The improvement in resolution is visible for the second most intense peak of the spectra (E_{CM} = 4.8 MeV). The states in ^{15}O were populated with a ^{14}N beam with $E_{^{14}N^{7+}}$ = 7.51(1) MeV/u impinging on target n°6.*

the tantalum foil, before being detected. From this simulation, the energy of the protons at the reaction point and at the detection point were computed. By drawing one as a function of the other a linear fit giving the real energy of the protons as a function of the measured proton energy was done. Using this function, the measured data were corrected for energy loss before being converted from the laboratory frame to the CM frame using the following formula :

$$E_{CM} = \frac{m_{beam}}{m_{light} + m_{beam}} \times T_{beam} = \frac{m_{light} + m_{beam}}{4 \times m_{beam} \times cos^2(\theta_{light})} \times T_{light} \tag{2.1}$$

Where T is the kinetic energy and "beam" and "light" corresponds respectively to the ^{14}N (or ^{14}O) and the proton. The result of this conversion is found in Fig. 2.13. By looking at the two most visible peaks in the cross section, an offset between the results from F. Q. Guo [Guo05] and the experimental data is clearly visible. This can be explained by an error in the thickness for both the thick CH_2 target (target n°6) and the tantalum foil.

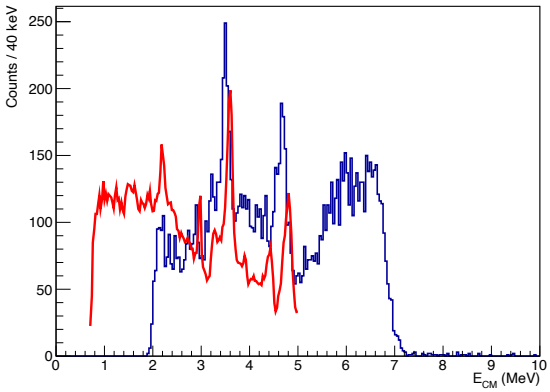

Figure 2.13: *Experimental spectra obtained for the $^1H(^{14}N,p)^{14}N$ reaction using the thick target (target 6). In red are previous experimental results [Guo05] for this reaction scaled in vertical to better match the raw experimental results. The shift in energy observed is understood as a consequence of an error in the estimated thickness of target n°6 and the fact that not one, but two Ta foil were used.*

To validate this hypothesis, and to obtain the thickness of target n°6 and the Ta foil, the energy of the two peaks with the highest cross section from Guo et al. [Guo05], as well as the maximum energy for elastically scattered protons at 0°, were used as a reference (Fig.2.14a). By varying the thickness of target n°6 and the Ta foil numerically, until the experimental energy matches the reference peaks it was found that the thickness of target

n°6 was 253(5) μm (to be compared to the 187 μm that was given by the manufacturer, this target was built on site with unknown uncertainty on its thickness) and the thickness of the Ta foil was 57(5) μm (to be compared with the 34(7) μm given by the manufacturer, it is concluded that not one, but two Ta foil on top of each other were used). After using the good thicknesses, the ^{15}O excitation function matches very well the results of Guo et al. [Guo05] (Fig. 2.15).

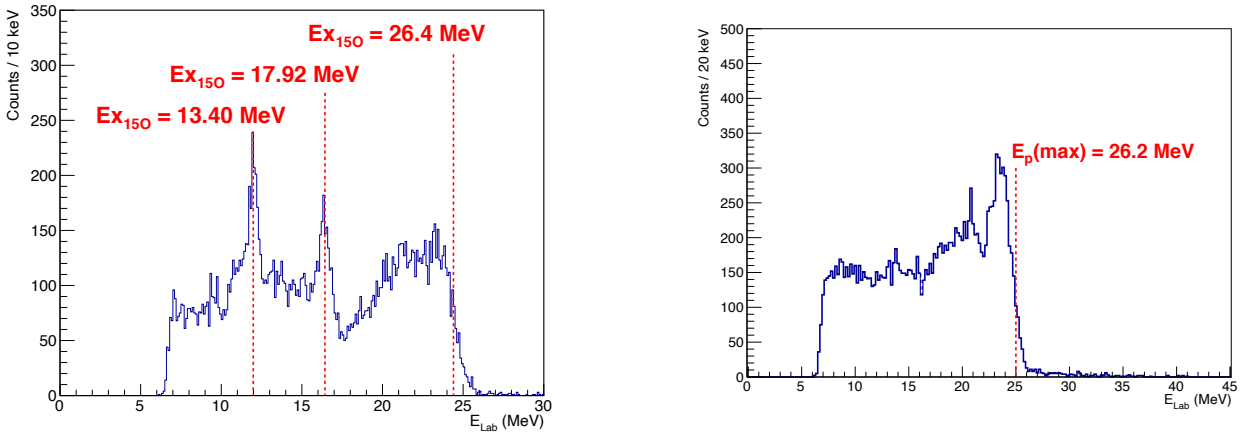

(a) (b)

Figure 2.14: *(a): Raw laboratory energy of the 0° telescope for the ^{14}N beam impinging on target n° 6 before the calibration. The values in red are the reference used to determine the thickness of the target n° 6 and of the Ta foil. (b): Raw laboratory energy of the 0° telescope for the ^{14}O beam impinging on target 4. The value in red corresponds to the maximum energy of the proton for a 7.46(1) Mev/u ^{14}O beam impinging on target n°4.*

A final verification was required to make sure that the Ta foil thickness computed was consistent with the excitation function measured with the ^{14}O beam. To this purpose the edge of the excitation function was used. It corresponds to the maximum energy of the proton for a 7.46(1) Mev/u ^{14}O beam impinging on target n°4 (see Fig.2.14b) whose thickness was measured in the second experiment (appendix 6.2). After applying the energy loss correction in the same manner than for the ^{14}N beam, it was found that a 57(5) μm Ta foil was consistent with the maximum energy measured by the 0° telescope.

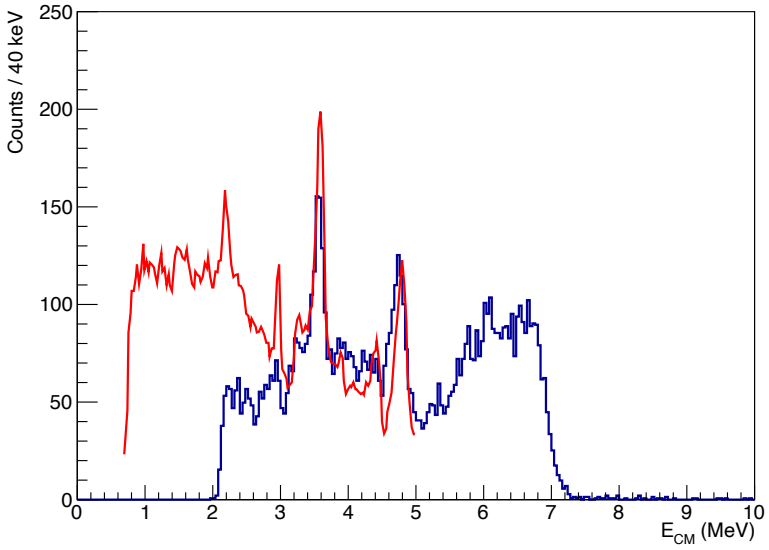

Figure 2.15: *Experimental spectra after target thickness corrections obtained for the $^{1}H(^{14}N,p)^{14}N$ reaction using the thick target (target 6). In red are experimental results obtained by F.Q Guo [Guo05] for this reaction.*

2.3 Analysis

2.3.1 From counts to cross section

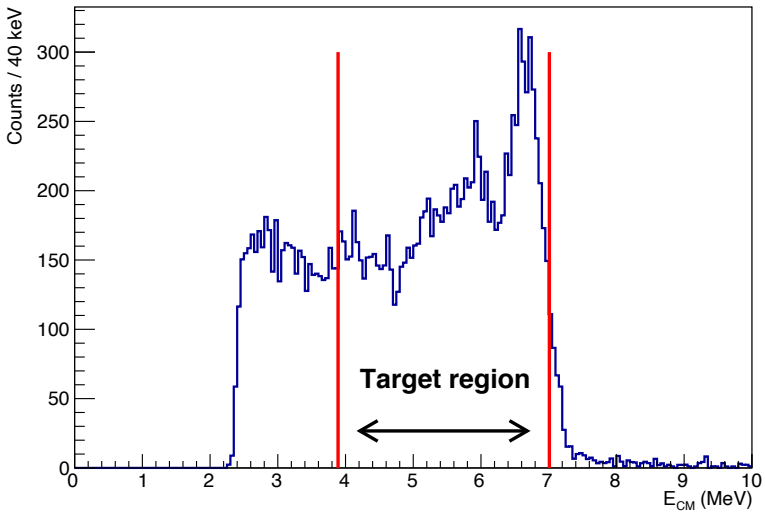

Figure 2.16: *Fluorine 15 excitation function of the 0° detector for proton events with laboratory angles between 0° and 3.5°. The two red line are placed to show the energy region available within the target.*

The first goal of the experiment was the measurement of new resonances in ^{15}F, their energy, width, spin and parity. To this aim, it is possible to use the resonant elastic scattering excitation function which can be obtained by measuring the total energy of the scattered protons of multiplicity one at small angles. Protons were identified by using the DSSSD energy as a function of residual energy (Fig. 2.9a) as here all events of interest go through the first detection stage ($E_{protons} > 6$ MeV). Once those conditions were applied, the CM excitation function of Fig. 2.16 was obtained. To convert this excitation function to a differential cross section, the following equation was used:

$$\frac{d\sigma}{d\Omega} = \frac{dN_{emitted}/d\Omega}{N_{incident} \times N_{Hydrogen/b}} \tag{2.2}$$

with $dN_{emitted}/d\Omega$ the number of events emitted in the solid angle $d\Omega$, $N_{incident}$ the number of beam particles impinging on the target and $N_{Hydrogen/b}$ the number of hydrogen atoms per barn.

Evaluating the background

On Fig. 2.16, protons with a CM energy as low as 2 MeV can be observed. Knowing the thickness of the target and considering only the elastic scattering reactions, it should not be possible to measure protons with CM energy lower than 4 MeV (3.89 MeV if there was no straggling). Those low energy protons come from the fusion evaporation reactions between ^{14}O ions of the beam and ^{12}C from the target. To evaluate this background, the standard method consists in measuring it with a carbon target (target 1) and, either directly subtract this spectrum to the experimental spectrum of interest, or, if the statistics is low, fit this ^{12}C spectrum and fill an histogram with this function to subtract a smooth background that will limit statistical fluctuations.

One issue with using a carbon target is that the energy lost by the protons inside it is different than the energy lost by the protons inside the polyethylene target. Correcting for this effect is not easy, especially as the thickness of the carbon target is difficult to evaluate (its density given by the manufacturer vary from 0.9 to 1.3 g/cm^3) Here, it is proposed, for the first time, to use the events of multiplicity 2 detected using the CH_2 target used for the ^{1}H(^{14}O,p)^{14}O measurement. The hypothesis is that two protons events are mainly from fusion-evaporation reactions, and so, marginally from ^{14}O + p reactions. This hypothesis is reinforced by using the fusion evaporation code PACE4 [Gav80; Tar08] with which we obtain that, in this case, the average multiplicity of protons emitted through fusion evaporation reactions is 2.16. A comparison of the multiplicity two events spectrum and the carbon spectrum, after applying an offset in energy to correct for the energy loss difference between the carbon and the polyethylene target, is given in Fig. 2.17a. Doing so and scaling the two vertically to have the same relative amplitude, a perfect match is observed in the target region with discrepancy at lower energy attributed to events coming from the predicted two proton emission from ^{15}F (section 1.3.2). As, there is no structure observed, the multiplicity 2 events were fitted using an exponential function Fig.2.17b. From this fit an histogram was filled and subtracted to the multiplicity 1 events of interest, see Fig. 2.18.

Normalizing with the beam intensity

Once the fusion-evaporation background was subtracted, the excitation function data has to be divided by the number of incident beam particles hitting the target. It can be obtained by using the CATS detector located in D4. In this experiment to limit the dead time, the CATS detector trigger was divided by 30000, meaning that only one out of thirty thousand triggers was written on disk. The number of beam particles interacting with the target was: $N_i = 6.8(1) \times 10^9$. Here, as explained previously, the efficiency of the CATS detector was measured to be equal to 99.5(5) %.

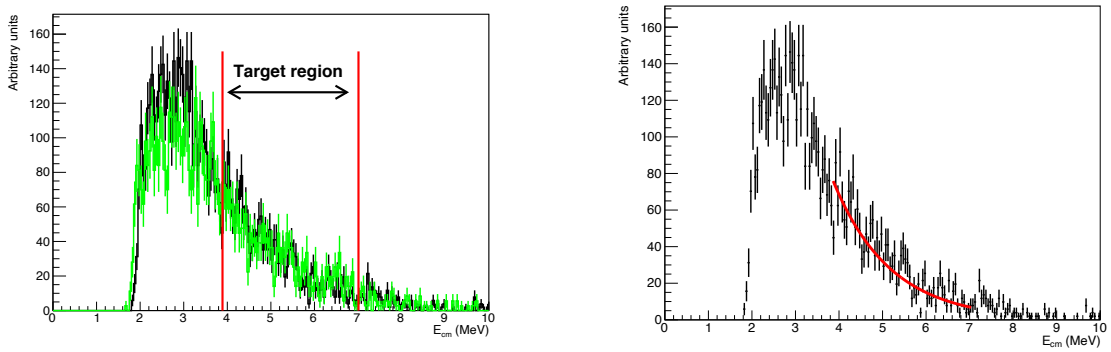

(a) (b)

Figure 2.17: *(a): Comparison between the spectra obtained with the carbon target in green and the multiplicity 2 events in black, a perfect match between the two can be observed in the target region with small differences at lower energy attributed to the predicted two proton emission from ^{15}F. (b): The multiplicity two event in black and the fit performed in the target region in red.*

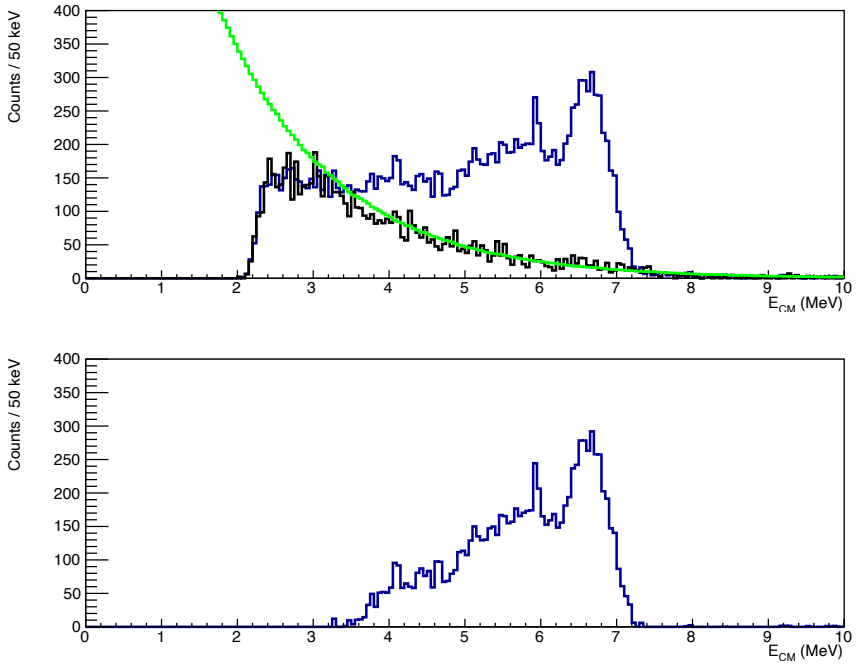

Figure 2.18: *Top: Raw spectra from Fig.2.16 in blue, with the multiplicity 2 spectra in black and in green the histogram filled by using the fit of Fig.2.17b. Bottom: The raw spectra from Fig.2.16 from which the background (green histogram) is subtracted.*

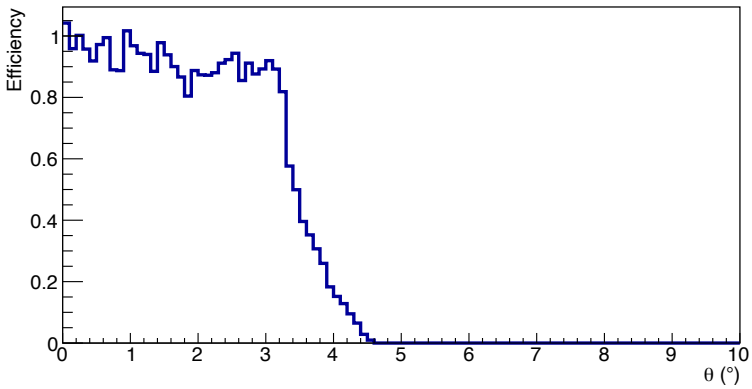

Figure 2.19: *Detection efficiency obtained from a GEANT4 simulation as a function of the angle of detection. This simulation takes into account the real geometry of the detector as well as the inefficiency coming from missing strips and interstrips.*

Detectors efficiency

The geometry of the detector has to be taken into account to obtain the cross section. In this experiment, the detector detection surface is a square, events detected with a laboratory angle between 0° and 3° were nearly fully detected while for large angles, the efficiency is decreasing Fig. 2.19. As a consequence, for certain angles the number of counts has to be compensated by the number of missed events. For this purpose, but also to correct for inefficiency from missing strips or from interstrips, a realistic GEANT4 simulation (see section 1.3.4) was performed. It featured a MUST2 telescope placed using the measurements provided by the surveyors, and an isotropic source emitting 1 MeV protons located at the target center.

The geometric efficiency was obtained from the number of protons detected divided by the number of protons emitted, and was done with a 0.1° step between 0° and 10° in the laboratory frame (Fig. 2.19). The number of events detected in each bin of energy was then divided by the efficiency. Here, it is chosen to limit the analysis to events with laboratory angles between 0° and 3.5° because for events with angles $> 3.5°$ the detector's efficiency drops under 50% which would decrease the resolution (see section 1.3.1) as well as increase the statistical uncertainty.

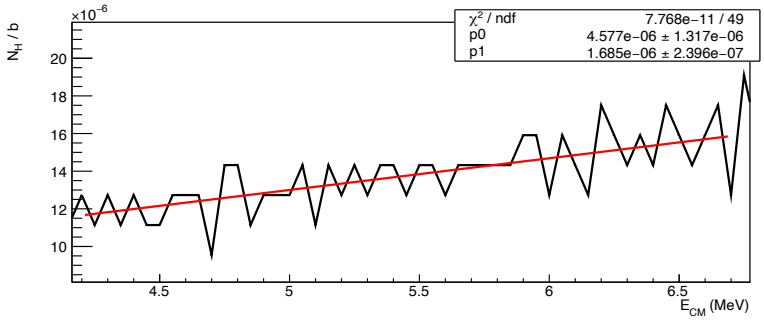

Figure 2.20: *Number of hydrogen atoms per barn as a function of the CM energy at which the elastic reaction took place.*

Getting the absolute cross sections

Finally, to obtain the absolute cross section, it was required to divide the excitation function by the number of target atoms per unit area. In the case of the resonant elastic scattering, compound nucleus formation occurs at precise CM energies which are reached as the beam looses energy inside the target. Naturally, this process happens continuously throughout the target, but experimentally the excitation function is drawn with a given binning, here 50 keV. Each bin of energy corresponds to a certain target thickness. To determine those depths, a GEANT4 simulation was used. This simulation featured a 7.46(1) MeV/u beam impinging on a 107(11) μm CH_2 solid target in which elastic scattering reactions were simulated. Then, the position of the reaction along the beam axis was drawn for each energy bin to obtain the effective thickness as a function of energy.

From the known target thicknesses and by knowing that the number of hydrogen atoms per cm^2 in 107(11) μm of CH_2 is : $\frac{2}{3}\times 1.32\times 10^{21} = 8.8\times 10^{20}$ hydrogen atoms per cm^2 which corresponds to 8.8×10^{-4} hydrogen atoms per barns (H/b), the effective number of hydrogen atoms per barns is then given by the following expression:

$$effective\ N_{Hydrogen}/b(E_{cm}) = \frac{effective\ thickness(E_{cm})}{total\ thickness} \times 8.8 \times 10^{-4}\mathrm{H/b} \qquad (2.3)$$

It was finally possible to draw the number of hydrogen atoms per barn as a function of the CM energy (Fig.2.20). It shows that the number of hydrogen per barns increases as a function of the CM energy. The result was fitted linearly. The absolute cross section was then obtained by dividing the experimental data by this linear function (Fig.2.21).

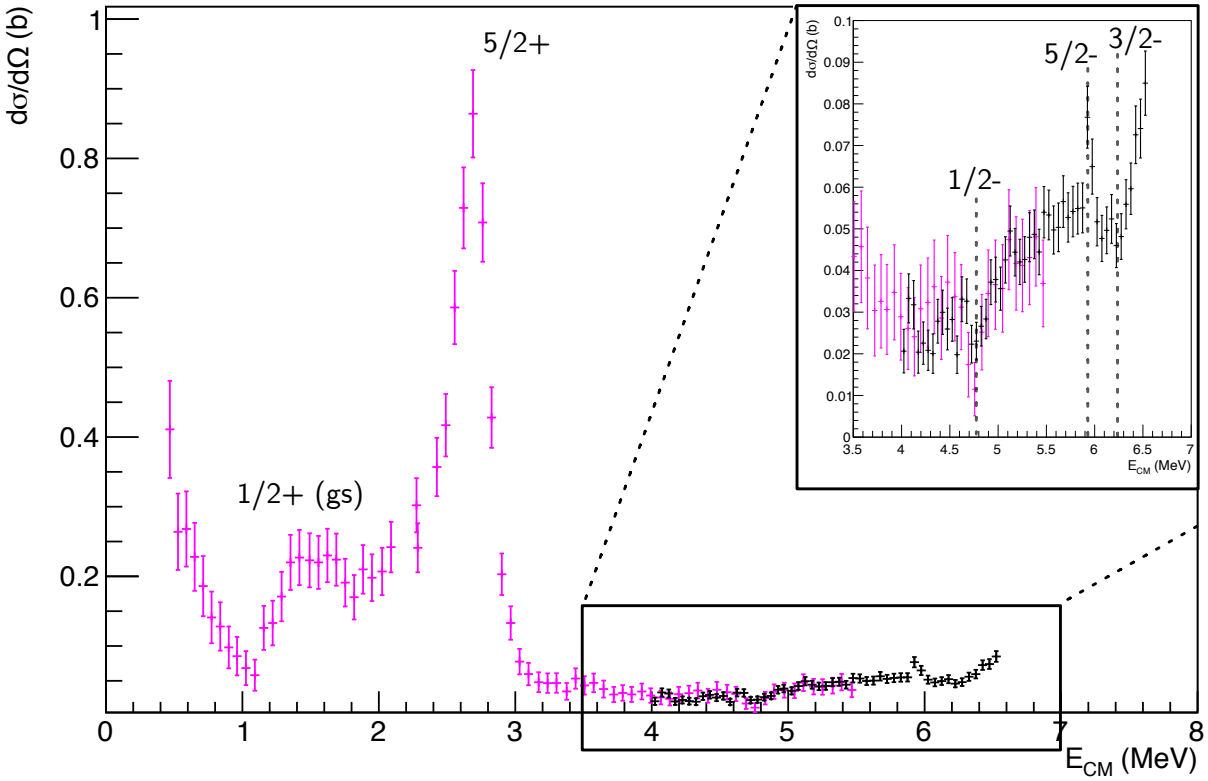

Figure 2.21: *Differential cross section of the resonant elastic reaction as a function of the CM energy obtained by F. De Grancey [Gra16] in magenta compared to the one obtained in this work in black.*

2.3.2 R-Matrix analysis

Once the cross section was obtained (Fig. 2.21) the R-Matrix formalism (section 1.3.1) was used by means of the AZURE2 software [Azu10] to obtain the energy, width, spin and parity of the measured states. The fit of the excitation function was done for CM energies between 4 and 6.5 MeV using a nominal value of the radius parameter a = 5.1 fm. In this energy range two new narrow states were predicted [For07] [Can06], a $5/2^-$ and a $3/2^-$ state, both included in the fit (Fig. 2.22). States located at lower and higher energy were also included, they are needed to reproduce the experimental data as they affect the amplitude and shapes of other resonances. To this aim, the known states measured by F. De Grancey [Gra16] namely the ground state ($1/2^+$), first ($5/2^+$) and second excited state ($1/2^-$) were introduced in the fit (see Table. 2.2 and Fig.2.21). At higher energy, based on theoretical predictions from [Can06] and by comparison to the known states in the mirror nucleus (^{15}C) two states were included: $5/2^+$ and $3/2^+$ (see Table.2.2).

Ref.	J^π	E (MeV)	Γ (keV)
[Gra16]	$1/2^+$ (g.s.)	1.270(20)	500(100)
[Gra16]	$5/2^+$	2.794(16)	300(16)
[Gra16]	$1/2^-$	4.757(16)	36(19)
[For07]	$5/2^-$	5.92	6
[For07]	$3/2^-$	6.30	350
[Can06]	$5/2^+$	7.750	100
[Can06]	$3/2^+$	7.990	100

Table 2.2: *Summary of the known and predicted states included in the fit. To fit the experimental data in AZURE2, the ground state and first excited states were fixed while all other states were free.*

The results of Table 2.3a and the figure 2.22a were obtained with a $\chi_2/N = 0.89$. As it can be seen on the figure, the $5/2^-$ state is not clearly visible and as the fit gives for this state a very narrow width of 2 keV, it was important to see if the experimental data can be fitted without the presence of this state. Results from this second fit can be found in Table 2.3b and the figure 2.22b. This second fit gave a $\chi^2/N = 1.04$, larger than the one obtained using the two states, but the difference in χ^2/N between the two fit is not significant enough to draw any final conclusion on the presence of a $5/2^-$ state. The energy and width of the $5/2^+$ and $3/2^+$ states given by the fit are only indications that higher energy states do exist as their presence were necessary to fit the experimental data. To estimate the uncertainties, each parameter were varied slightly while the other parameters were fixed to test the stability of the fit. The uncertainties on the energy of

the states also takes into account the error on the residual energy from the calibration method used to calibrate the CsI crystals. The results obtained are in good agreement with previous results from Ref. [Gra16] and Ref. [Muk09]. The $1/2^-$ state is measured with an energy 123 keV above the measurement from Ref. [Gra16] but is still within the margin of error of the two experiments. The measured $3/2^-$ is consistent with the one deduced in Ref. [Muk09] and there are indications that a new $5/2^-$ state is present in the excitation function.

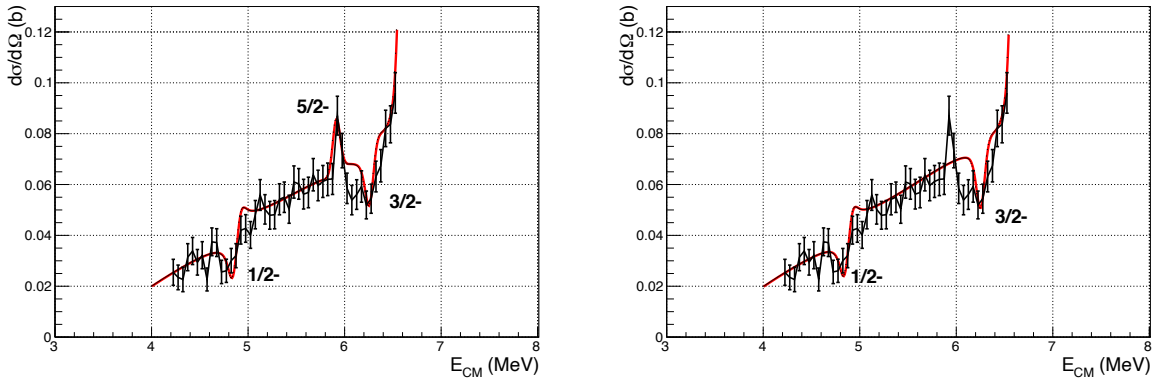

(a) (b)

Figure 2.22: *(a): Differential cross section in black fitted using AZURE2 by using both a $5/2^-$ and a $3/2^-$ state ($\chi^2/N = 0.89$). (b): Differential cross section in black fitted with a $3/2^-$ state but without including a $5/2^-$ state ($\chi^2/N = 1.04$).*

J^π	E_{cm} (MeV)	Γ (keV)
$1/2^-$	**4.88(14)**	**23(10)**
$5/2^-$	**5.91(14)**	**2(2)**
$3/2^-$	**6.29(14)**	**24(10)**
$5/2^+$	6.57(14)	5(20)
$3/2^+$	7.06(14)	1200(200)

(a)

J^π	E_{cm} (MeV)	Γ (keV)
$1/2^-$	**4.88(14)**	**23(10)**
$5/2^-$	**-**	**-**
$3/2^-$	**6.28(14)**	**30(10)**
$5/2^+$	6.61(20)	14(20)
$3/2^+$	6.90(30)	1100(200)

(b)

Table 2.3: *(a): Summary of the results obtained after performing the R-Matrix fit using both a $5/2^-$ and a $3/2^-$ state. (b): Summary of the results obtained after performing the R-Matrix fit with a $3/2^-$ state but without including a $5/2^-$ state. In both tables $E_{cm} = E_x + S_p$ with $S_p = 1.27$ MeV*

2.4 Conclusion

In this chapter, the analysis of a 0° MUST2 telescope was performed. The structure of ^{15}F was studied using the resonant elastic scattering cross section by sending a 7.46(1) MeV/u ^{14}O radioactive beam on a thick CH_2 target. Information on the structure of ^{15}F were extracted by fitting the cross section using the R-Matrix formalism. Despite the lack of statistics, a $3/2^-$ state has been observed. It was measured to be at a CM energy of 6.29(14) MeV with a width of 24(10) keV. The results obtained are also consistent with the presence of a $5/2^-$ state with a CM energy of 5.91(14) MeV and a width smaller than 2(2) keV.

3
Study of decay modes in ^{15}F

Contents

3.1 Introduction

In this chapter the second experiment performed at GANIL is detailed. Similarly to the first experiment, discussed in the previous chapter, this experiment was designed to detect new narrow states in ^{15}F and study their decay modes.

In the first experiment, despite important malfunctions from GANIL's accelerators, the first of the three aims of the measurement, namely the measurement of two predicted odd-parity states was realized. A new $3/2^-$ state was measured and we have indications for the presence of a $5/2^-$ state. The two other motivations, namely the measurement of the two-proton emission and the study of the possible gamma emission, remained out of reach due to the poor statistics.

Thanks to the very promising results obtained in the first experiment, the GANIL's direction agreed to schedule the measurement again in 2019. The experiment took place in a new experimental campaign coupling multiple state of the art detectors: MUGAST[1] array to detect light charged particles, VAMOS[2] spectrometer for the detection of heavy residues and AGATA[3] detector for gamma rays. It was the first experiment (after the commissioning) that used all those detectors coupled together, as well as the first experiment using the new MUGAST array.

Based on the preliminary results of the first experiment, having a different experimental setup, two possibilities were considered :

- The first option was to follow the original proposal and try to perform all three experimental goals in a single experiment. This would have required the use of either a MUST2 telescope at 0° or the use of VAMOS to detect protons. The advantage of this choice is that it makes possible the measurement of the $5/2^-$ state that was not clearly observed in the first experiment, if the widths allows it to be measurable.
- The second option was to shift the focus on two-proton and gamma emission. It implies setting VAMOS detectors to be sensible to ^{13}N and ^{14}O and not to protons. This can be done by choosing appropriate pressures for the drift and ionization chambers. The great advantage of this option is the removal of the fusion evaporation reactions between the ions of the beam and the carbon atoms from the target.

[1] MUST2 GASPARD and TRACE
[2] VAriable MOde Spectrometer
[3] Advanced Gamma Tracking array

The second option was selected. This choice was motivated by the advantage given by the removal of the fusion evaporation background, considering that we had good quality data on 1p from 2018 data and by the fact that even with a greater statistics, the possible observation of a new $5/2^-$ state seemed unlikely. If this $5/2^-$ state does exist, its width is very narrow (less than 2 keV). Increasing the statistics might help determining its existence, but its measurement would most probably be hindered by the energy resolution of either the MUGAST array or the VAMOS spectrometer.

This chapter will focus on the newly observed $3/2^-$ and $5/2^-$ and their possible decay by two-proton emission as well as on the possible gamma emission of the $1/2^-$ state to the ground state. The first part of the chapter will detail the experimental conditions such as the beam production, the targets and the detectors used. In the second part of the chapter, the analysis of the two-proton emission and the gamma emission will be detailed.

3.2 Experimental conditions

3.2.1 Beam production

For this measurement, the radioactive beam of ^{14}O was produced as in the first experiment (see 2.2.1). The main differences between the two experiments was that the experimental chamber was located in a different experimental hall (G1) (Fig. 3.1) and that the stripper foil was placed before the Z spectrometer instead of the LISE spectrometer. As a consequence, the selection of the secondary beam (^{14}O or ^{14}N) was performed at the exit of the CIME cyclotron (Fig. 3.1).

During the experiment the beam intensity was mostly stable, with a lower intensity than expected at the beginning which improved throughout the experiment. The maximum intensity provided by CIME was $\sim 3.10^5$ pps, but at such intensities VAMOS focal-plane detection system, particularly the ionization chambers, weren't able to work properly. Indeed, most of the beam particles were measured in the VAMOS focal-plane. The intensity was then reduced to $\sim 1.10^5$ pps, mostly to avoid destroying the different gazeous detectors of VAMOS as well as to limit pile up events in VAMOS.

In this experiment, the use of the VAMOS spectrometer after the target made possible the direct measurement of beams energies. The Bρ and energy of both the ^{14}O and ^{14}N beams were respectively : $B\rho_{^{14}O^{8+}}$ = 0.688(1) T.m / $E_{^{14}O^{8+}}$ = 7.42(1) MeV/u and $B\rho_{^{14}N^{6+}}$ = 0.915(1) T.m / $E_{^{14}N^{6+}}$ = 7.39(1) MeV/u.

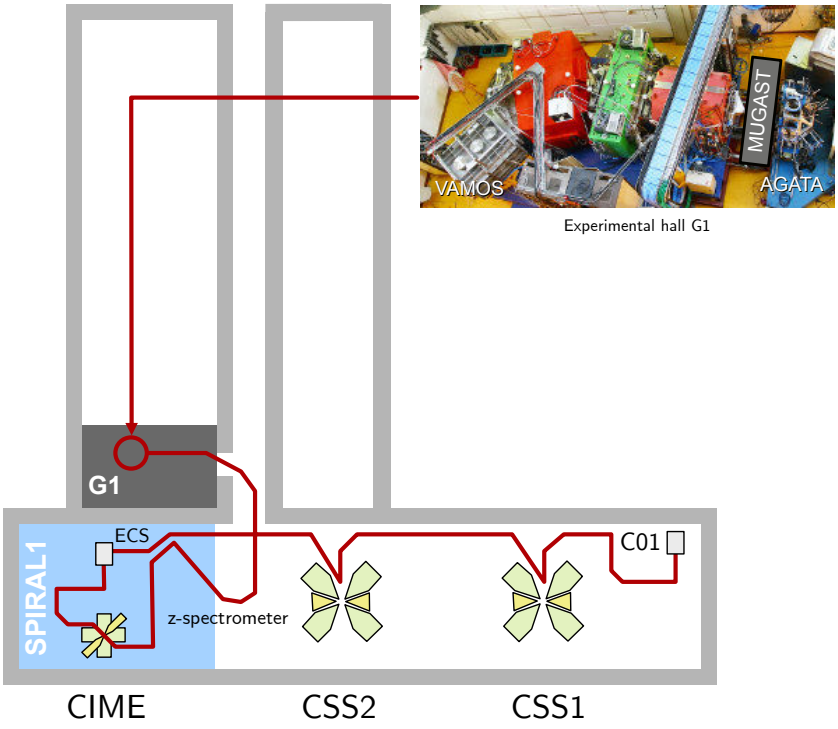

Figure 3.1: *Schematic representation of the relevant part of GANIL facility used to perform the experiment. The beam was produced by the fragmentation of a stable beam of* ^{16}O *into the ECS target of SPIRAL1 (blue region) to produce a radioactive beam of* ^{14}O*. The beam was then accelerated with CIME to 7.42(1) MeV/u and delivered to experimental hall G1 (dark grey region).*

3.2.2 Targets

This second experiment used a similar set of targets as for the first experiment. Differences were: the removal of the thick target, the inclusion of a 7 mm hole to perform the alignment of the beam and the mounting of three "on-resonance" targets. A summary is found in Fig. 3.2.

(a)

Position	Material	thickness (μm)	
		Provided	Measured (appendix 6.2)
1	hole ⌀ 7 mm	-	-
2	C_2H_4	104(10)	107(11)
3	C_2H_4	100(10)	92.3(9)
4	$^{(nat)}C$	75(8)	-
5	C_2H_4	73(7)	77.3(8)
6	C_2H_4	104(10)	-

(b)

Figure 3.2: *(a): Picture of the target holder. Targets are numbered from top to bottom. (b): Characteristic and position of the different targets placed in the target holder. The thicknesses are the ones given by the manufacturer and the measured thickness (appendix 6.2). The carbon target was made out of flexible graphite, for which the density given by the manufacturer ranges from 0.9 to 1.3 g/cm^3.*

3.2.3 Beam tracking : CATS

In this campaign, it was originally planned to use two CATS detectors for beam trajectory reconstruction, beam intensity monitoring, and as a time reference. To this purpose, two CATS detectors were placed before the target at respectively 2.05(1) m and 2.66(1) m.

Before this experiment, a commissioning of the MUGAST array was performed using a similar beam (^{16}O) at similar energies ($\sim$ 81 MeV). During this commissioning, it was observed that the CATS detectors induced an important angular straggling of the beam which lead to a beam spot on target of several centimeter (Fig. **??**) making the use of two CATS detectors not only ineffective but detrimental.

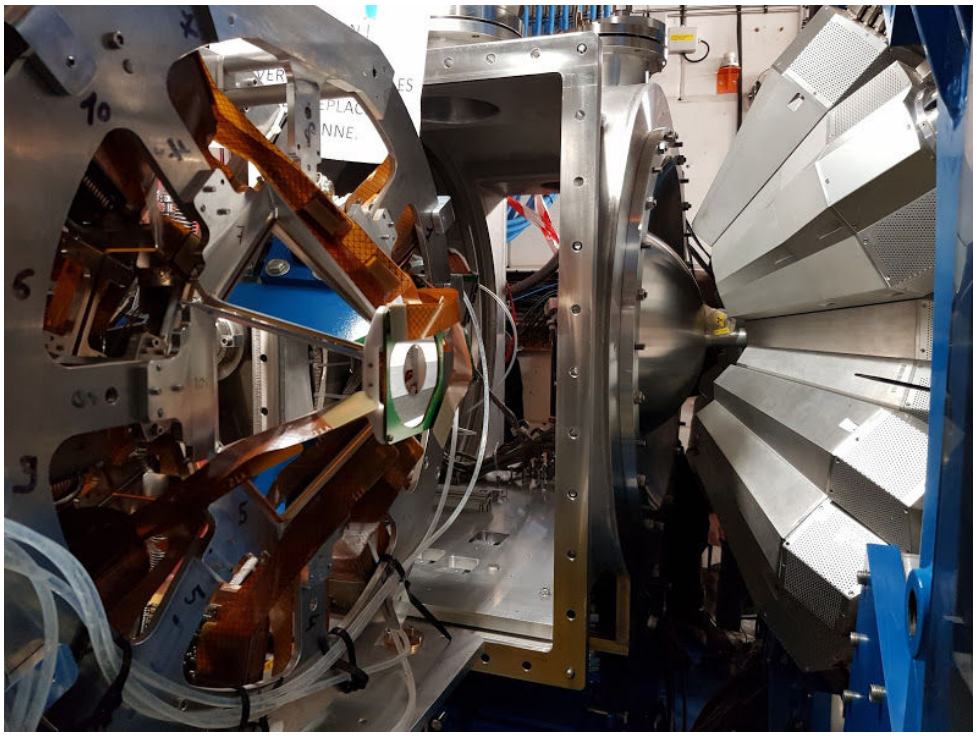

Figure 3.3: *Picture of the experimental setup used in this second experiment. On the right HPGe crystals of the AGATA detector can be seen and in the foreground on the left the back detectors of the MUGAST array are visible.*

During the experiment described in this work, a beam of ^{14}N was used to setup the different detectors. To make sure that it was not possible to use two CATS detectors, the beam spot was measured using the VAMOS spectrometer without any target. It was observed that with no CATS detector, the diameter of the beam spot was 3(2) mm (FWHM) at VAMOS focal-plane. Once the CATS detector was inserted, the beam spot became 10 times larger : 30(2) mm (FWHM). Based on this observation it was decided to only use a single CATS detector as adding a second CATS would only increase even more the angular straggling of the beam making the reconstruction of trajectories impossible.

The CATS detector used was the one located the furthest from the target (2.66(1) m). It was simply chosen for practical reason as it was easier to insert than the one nearer the target.

3.2.4 Light particles detection : MUGAST

Description of the detector

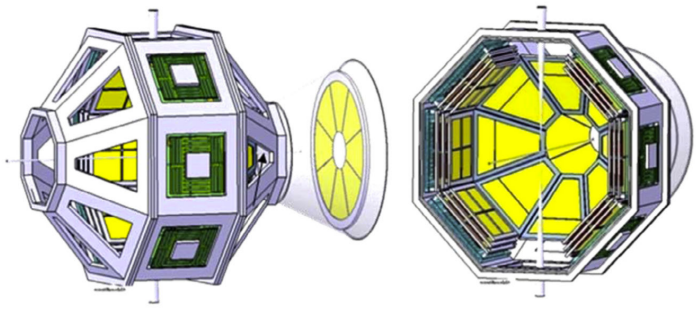

Figure 3.4: *Schematic view of the current design of the GRIT Array [Bea13].*

The MUGAST detector array (Fig. 3.3) is an ensemble of twelve detectors. It is the intermediate step towards a new silicon based array called GRIT (Fig. 3.4). The GRIT[4] array will consist in a new type of compact, high granularity, 4π acceptance silicon detector array designed to be integrated inside the AGATA or the PARIS array. It will be composed of multiple stages of DSSSD, with trapezoidal shapes covering both backward and forward angles and more common square shaped detectors at 90^{circ}. The detector will be capable of performing pulse shape analysis and discrimination for particle identifications [Ass15]. More information about the GRIT project can be found in Ref. [Bea13].

The MUGAST array was composed of the following detectors (Fig. 3.5a and Fig. 3.5b):

- Five trapezoid-shape 500 μm nTD[5] DSSSD at backward angles and placed at about 15 cm from the target.
- An annular DSSSD placed at 180° to cover most of the backward angles.
- Two square-shape 500 μm DSSSD were placed at 90° with respect to the beam direction and located 8 cm from the target, one of the 500 μm detector was complemented by a 1.5 mm thick square detector.
- Four MUST2 detectors were placed at forward angles using the same configuration described in the first experiment, they were placed at 17(1) cm from the target.

[4]Granularity, Resolution, Identification, Transparency
[5]Neutron Transmutation Doped

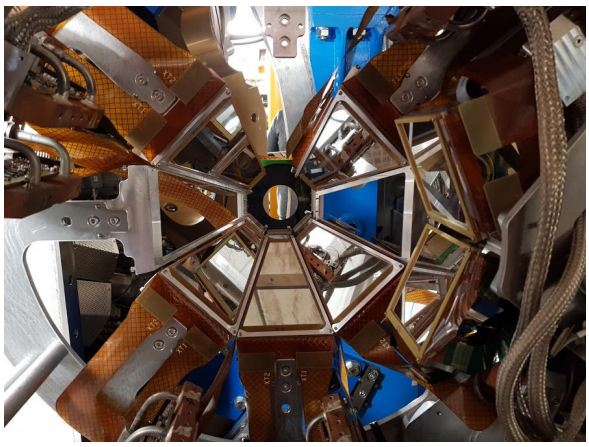

(a)

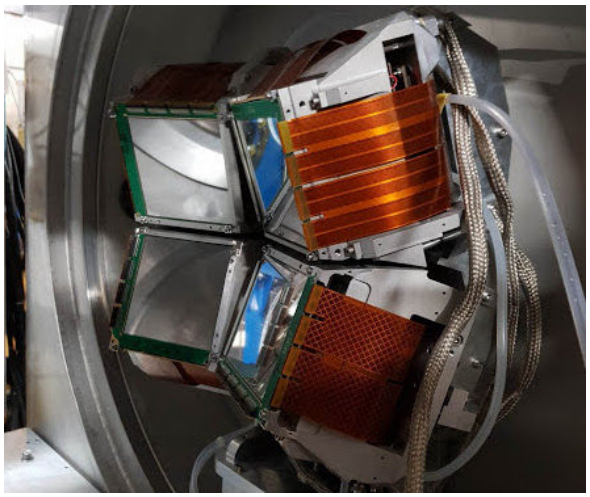

(b)

Figure 3.5: *(a): Picture of the backward detectors of the MUGAST array. (b): Picture of the MUST2 detectors inside the experimental chamber of G1*

In this measurement the different reactions of interest only emit charged particles at forward angles, thus only the MUST2 telescopes were analyzed (Fig. 3.5b). During the experiment MUST2 telescopes worked correctly except for crystal 12 and 15 of telescope 3 for which no signal was recovered.

Telescopes Calibrations

The calibration of the MUST2 telescope was performed using the same methods detailed in the first chapter (see section 2.2.4). The only difference between the two experiments concerned the CsI crystals pixel calibration, for which the non-linearity correction was performed with a much higher division of the CsI. They were divided in 8×8 = 64 pixels (8 strips in X and 8 strips in Y) compared to the 3×3 = 9 pixels used in the first experiment. It was made possible thanks to the much higher statistics obtained in this experiment compared to the first one.

Validation of the energy calibration

In this experiment, there were no thick ($\sim$ 200 μm) CH_2 target placed on the target holder. For this reason, the quality of the calibration was verified using the elastic scattering reaction. Indeed, both the maximum and minimum energy accessible to the protons as a function of their angle of emission in the lab are known. By superimposing on the

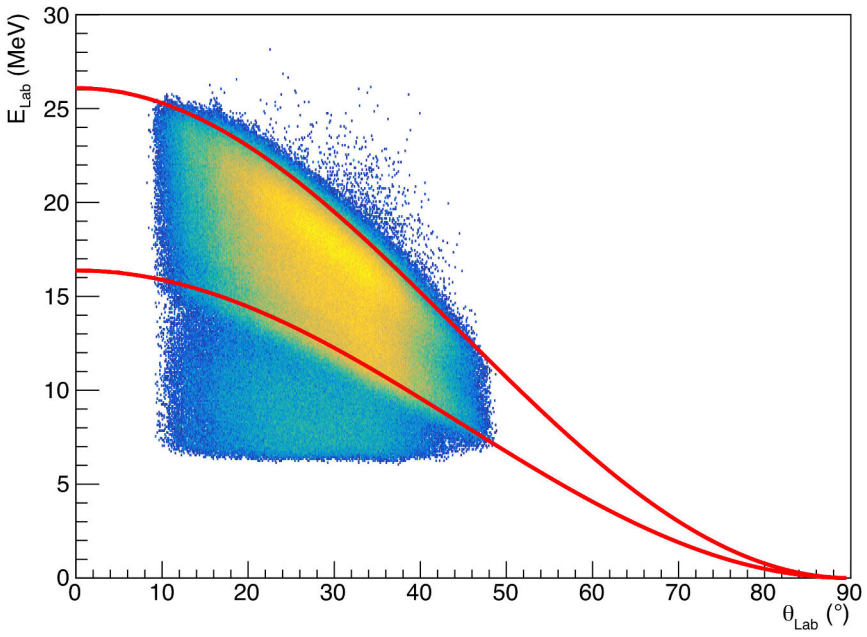

Figure 3.6: *Measured laboratory energy vs laboratory angle considering a beam hitting the target in the center. In red are the theoretical kinematic lines for the maximum and minimum energy accessible in the experiment (without angular or energy straggling).*

experimental kinematics the theoretical kinematic lines corresponding to reactions occurring both at the entrance and at the exit of the target, it was possible to validate the calibration. As it can be observed on Fig. 3.6, by summing events from all telescopes a good agreement between the theoretical kinematic lines and the experimental is obtained.

However, by performing the same analysis telescope by telescope small discrepancies were observed between the expected kinematic lines and the experimental data (see Fig. 3.7). Some telescopes seemed to reach energy above the lines while some were well under them. This might be explained by an offset in the impact position of the beam. Indeed, in both Fig. 3.6 and Fig. 3.7 laboratory angles (θ_{lab}) were obtained considering that the beam was hitting the target in its center. By applying an offset to the beam impact position both in the horizontal and vertical axis, the beam impact position for which the telescopes were aligned was X = -4 mm and Y = -1 mm, it was obtained by the mean of a χ_2 minimization described in details in Appendix. 6.3. After using the correct beam impact position and by summing events from all four telescopes, Fig. 3.8 was obtained. On this figure it can be observed that the agreement between the theoretical kinematic

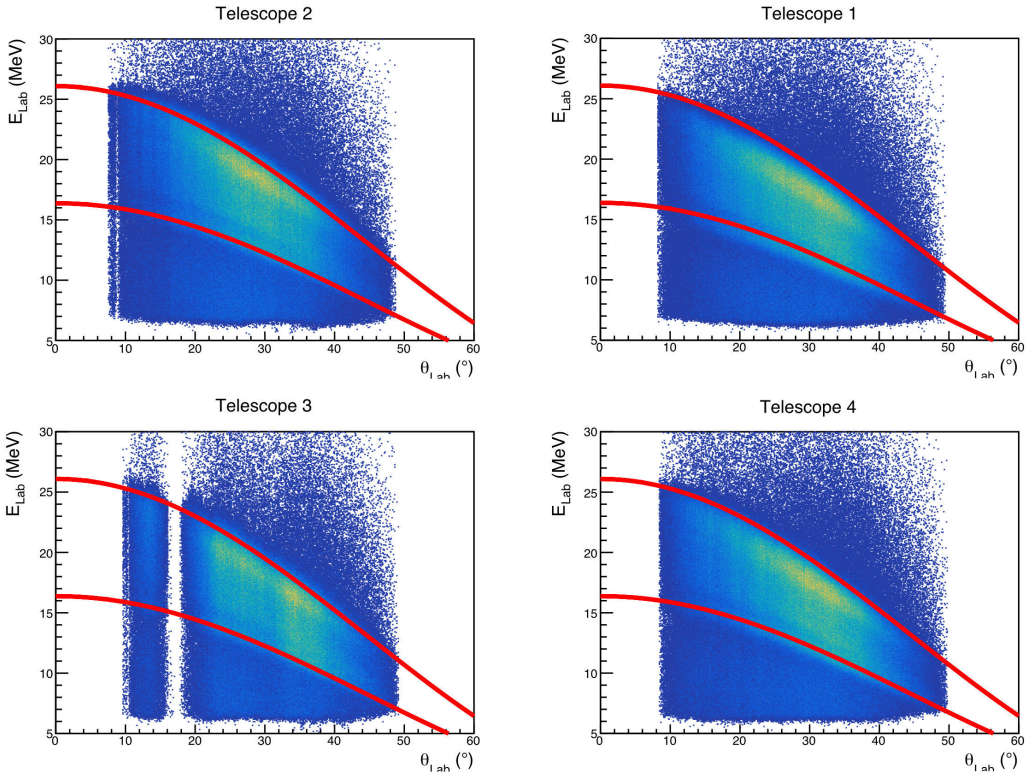

Figure 3.7: *Measured laboratory energy vs laboratory angle considering a beam hitting the target in the center for each telescopes. The gaps observed in the distribution for telescope n° 3 corresponds to the two missing crystals. In red are the theoretical kinematic lines for the maximum and minimum energy accessible in the experiment (without taking into account angular or energy straggling).*

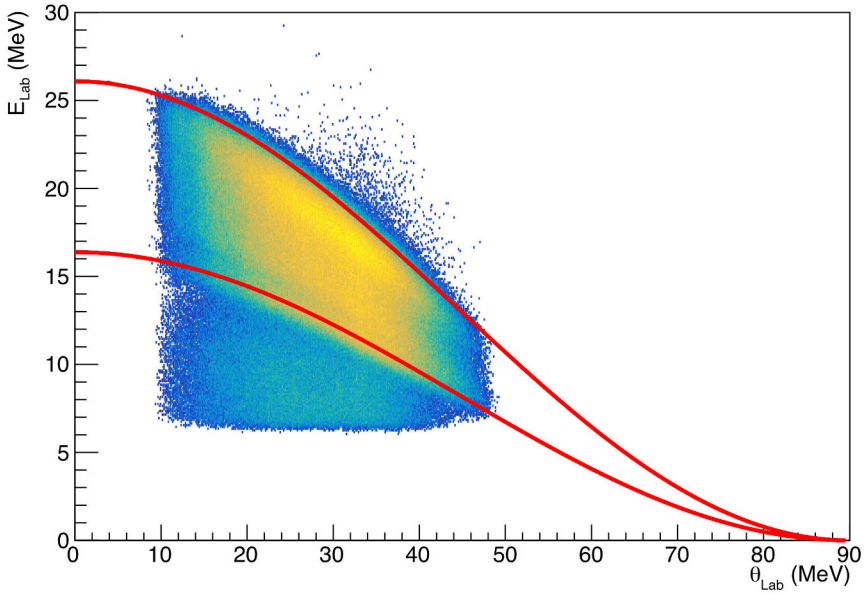

Figure 3.8: *Measured laboratory energy vs laboratory angle considering a beam hitting the target with X = -4 mm and Y = -1 mm. In red are drawn the theoretical kinematic lines for the maximum and minimum energy accessible in the experiment (without taking into account angular or energy straggling)*

lines and the maximum and minimum proton energy measured was improved compared to Fig. 3.6.

Multiparticle detection

To study the two-proton emission, it was important to understand how multiparticle events were treated, especially when two particles hit the same telescope. It was also important to make sure that good events were not rejected especially in the case of highly correlated protons for which the relative angle between the two protons might be very small. To do so, a strict and reliable way of matching events in the DSSSD when it detects more than one particle, had to be developed, for the first time, for MUST2 detectors.

Once a particle hit the DSSSD it triggers most of the time two different strips, one in X and one in Y (if the two particles hit the same strips they were rejected). In this case its position of interaction is determined by the intersection of the two strips. Now, if two particles hit different strips of the same DSSSD, they should trigger most of the

time four strips, two X strips and two Y strips. In this case, there are, for each particle, two possible intersections, but only one real physical position. To find out which particle corresponds to which position a strip matching based on the energy deposited in the X and Y strips was used. In this experiment X and Y strips were matched if their difference in energy was smaller than 100 keV. In the case where more than one particle hit the same DSSSD and deposited similar amount of energy, events were rejected. Some good events can be rejected by this matching, especially ^{2}He-like events which are expected to have similar energies and small relative angles. In the case where ^{2}He-like decay would occur, simulations from section 1.3.4 show that they should have similar polar angle ($\theta_{p1} \sim \theta_{p2}$) but they are not expected to have the same azimuthal angle ($\phi_{p1} \neq \phi_{p2}$), thus they will not be all rejected by this matching. Experimentally, it was observed that only 6.4(1) % of events were removed by the matching.

To illustrate the method used, let's assume that a 16×16-strip DSSSD (Fig. 3.9) was used, and that two particles were detected by this DSSSD, in this case there are two main scenarios :

- Fig. 3.9a : One proton deposit an energy of 2 MeV in the X strip 4, and 2.1 MeV in the Y strip 12, and the other proton deposit an energy of 1 MeV in the X strip 14, and 0.9 MeV in the Y strip 7, then, it is easy to conclude that the two protons have respectively the following strips coordinate : p_1(4, 12) and p_2(14,7). This type of events was kept and used in the analysis.
- Fig. 3.9b : The first proton deposit an energy of 0.8 MeV in the X strip 4, and 0.7 MeV in the Y strip 12, and the second proton deposit an energy of 0.7 MeV in the X strips 14 and 0.8 MeV in the Y strips 7, then, there are not two, but four solutions : p_1(4,12), p_1(4,7), p_2(14,12), p_2(14,7). And it is not possible to verify which solutions are the real ones. Those events were rejected and not used in the analysis as it was not possible to distinguish between the two events.

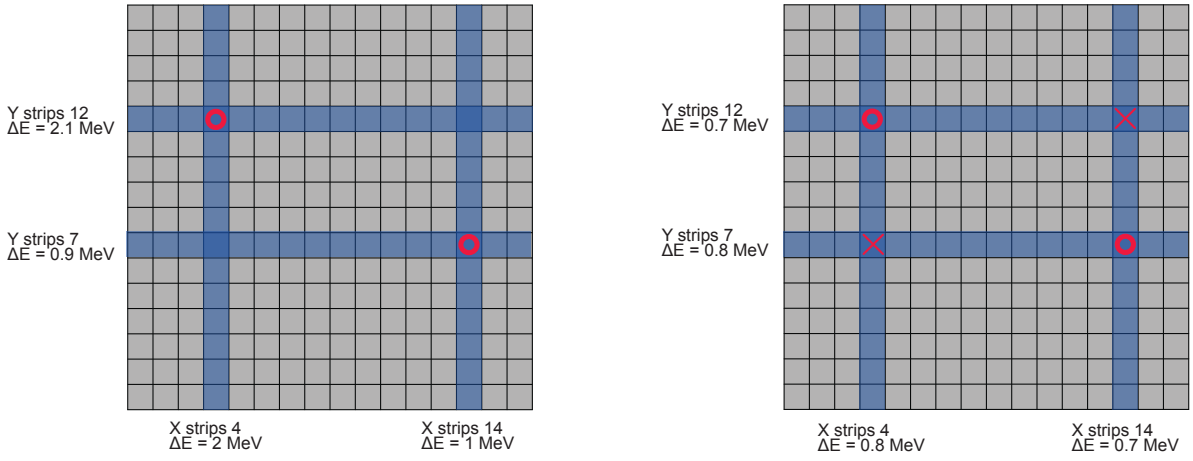

(a) (b)

Figure 3.9: *(a): Schematic view of a 16*16 strips DSSSD when two particles hit the DSSSD a sufficient energy difference to differentiate between the two particles. (b): Same as left but for particles hitting the DSSSD with similar energies, in this case the event was rejected and not used in the analysis.*

3.2.5 Detection of the recoils: VAMOS

Description of the detector

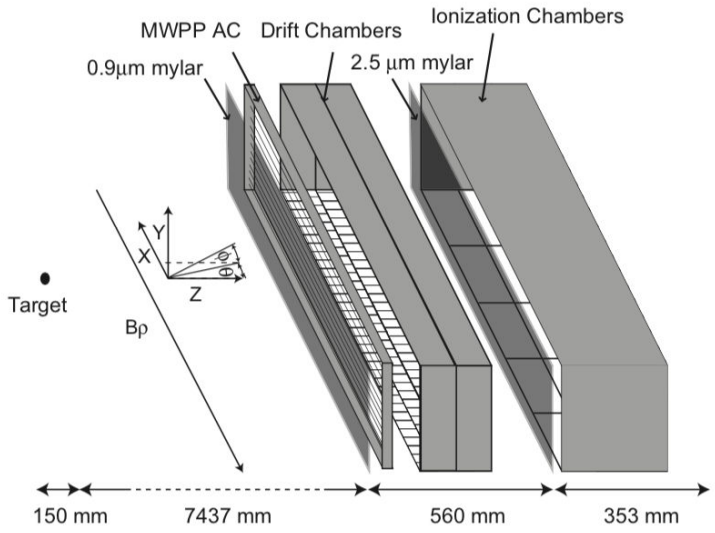

Figure 3.10: *Schematic view of the VAMOS focal-plane detection system. The coordinate system used for the determination of trajectories is shown [Rej11].*

VAMOS is a large acceptance spectrometer capable of reconstructing particles trajectories as well as performing complete identification of reaction products. Its angular acceptance reaches 80 msr, while its Bρ acceptance is : $dB\rho/B\rho_{ref} = 25\%$ where Bρ_{ref} is the reference Bρ. In this experiment VAMOS was used to measure the heavy ejectiles such as ^{14}O and ^{13}N.

One of the advantage of such a spectrometer is that its focal-plane can be equipped with many different type of detectors (Fig. 3.10). The following ones were used in this experiment:

- **Multi-Wire Parallel Plate Avalanche Counter (MWPPAC):** this detector is designed for fast timing measurement. It is made of a central cathode and two anodes. The vertical wires (cathode) are polarized whereas the horizontal wires (anode) are grounded. When a particle crosses the detector, ionization electrons are created between the two gaps and are accelerated towards the anodes.
- **Two segmented Drift Chambers (DC):** Each DC is separated into two smaller drift chambers. Their role was to detect the focal-plane position as well as the angle

of the trajectories of each ejectiles and to measure the Bρ of the heavy ejectiles. They were filled with isobutane gas at a pressure of 6 mb. Each DC is composed of two region, a drift region where ionization occurs and an amplification region separated by a grounded Frisch grid. The drift region is composed of a cathode negatively polarized. The amplification region is composed of amplification wires positively polarized underneath which 64 grounded cathode pads are positioned. When an ion crosses the drift chambers it ionizes the gas, electrons then drift towards the Frisch grid and generate an avalanche of electrons towards the pad. The X position of interaction is determined by the charge distribution on the pads using the hyperbolic secant function (Fig. 3.11), while the Y position is obtained from the drift time of the electron by measuring the time between the detection in the MWPPAC and the time of detection in the DC. An event was accepted if there were at least 3 out of 4 drift chambers signals triggered.

- **Eleven ionization chambers (IC):** They were filled with CF4 with a pressure of 125(2) mbar, their pressure were set to stop the recoils in the middle of the fifth chamber. Those ionization chambers can be used in conjunction to perform particles identification and energy measurement. Each IC is composed of cathode and anode pads separated by a Frisch grid. When ions cross the ionization chambers they loose energy and ionize the gas. The drift electrons are then amplified by the Frisch grid and collected by the anode pad. The amplitude of the signal being proportional to the number of drift electrons collected, the energy lost by the ions in the chamber is measured.

More detailed information about these detectors can be found in VAMOS technical paper [Rej11].

The full kinematics of the reaction can be obtain from the DC only, as they measure the Bρ and the angle at the focal-plane. The angle of emission at the reaction point was obtained from the angle at the focal-plane using the ion optical code ZGOUBI [Méo99]. IC were used for particles identification when they were required (see section 3.3.2).

Figure 3.12 shows the link between the observable of interest and the detector from which they were obtained.

MWPPAC calibration

To obtain the time of flight of the ejectile between the target and the MWPPAC, a Time to Amplitude Converter (TAC) was used. The start of the TAC was the MWPPAC while

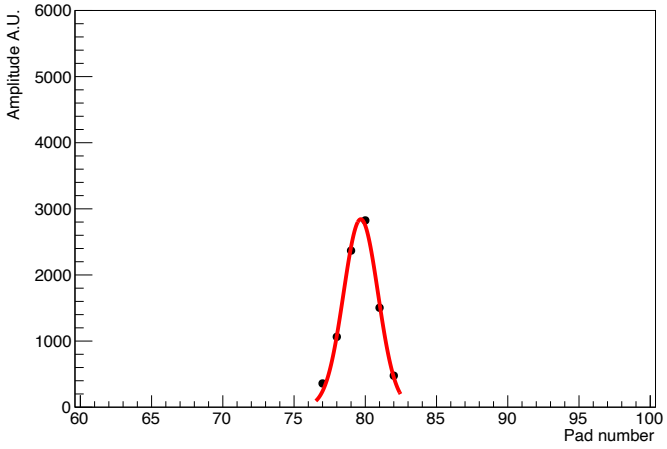

Figure 3.11: *Example of signal for a single events collected by the pads of the first drift chamber.*

the CATS detector was the stop. The TAC was calibrated using a time calibrator module which sent random pulses until it spanned the full time range. Using Fig. 3.13 a linear calibration was performed.

This first alignment gave the slope of the calibration, but to obtain the real time of flight of the ions between the target and VAMOS, an offset was added in the calibration. This offset was obtained using the reconstruction in M/Q. As M/Q $= v/B\rho =$ cst for a given ion, by looking at the measured M/Q of the beam an offset was applied until the measurement matched its physical value M/Q: $M/Q(^{14}O^{8+}) = 1.75$. Then as M/Q should be constant for each channels of the MWPPAC, the stability of M/Q was controlled by applying offsets to each channels, until they were aligned on the same M/Q. In summary, the time of flight was defined as :

$$ToF = offset + (single\ channel\ corrections) - t_{TAC} \tag{3.1}$$

The time calibration measured by the TAC was subtracted from the offsets because the start (MWWPPAC) was located after the stop (CATS) on the beam line (Fig. 3.14).

Drift chambers calibration

As previously explained, the drift chambers give information on the horizontal and vertical position of interaction of the ions. The pads give the horizontal position (X) and the

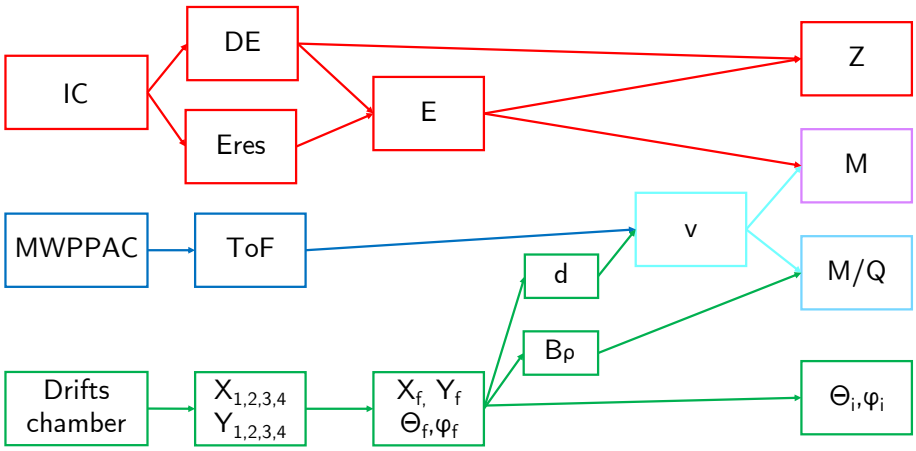

Figure 3.12: *Diagram showing how variables are obtained using VAMOS focal-plane detectors. With X_{1234} and Y_{1234} respectively the horizontal and vertical positions measured in the drift chambers, X_f and Y_f respectively the reconstructed horizontal and vertical position at the focal-plane, d is the distance traveled by the ions in the spectrometer v is the speed of the ions, ToF is the time of flight of the ions and θ_i and ϕ_i respectively the reconstructed polar and azimuthal angles of the ions relative to the measured beam impact position. More details on the procedure to obtain the different variables can be found in Ref.[Ram16]*

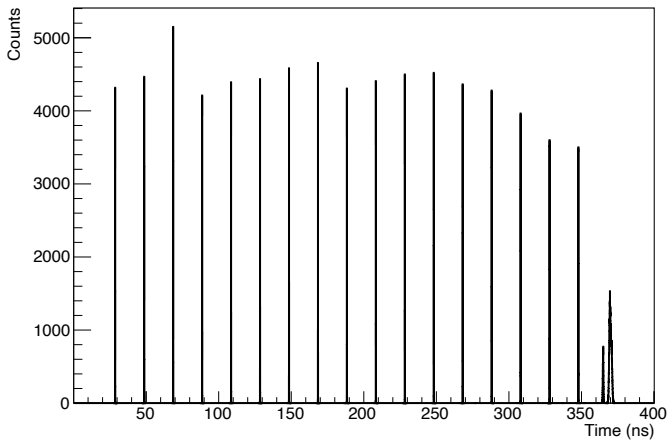

Figure 3.13: *Example of spectra obtained for the MWPPAC calibration using the time calibrator. The period between two peaks is 20 ns.*

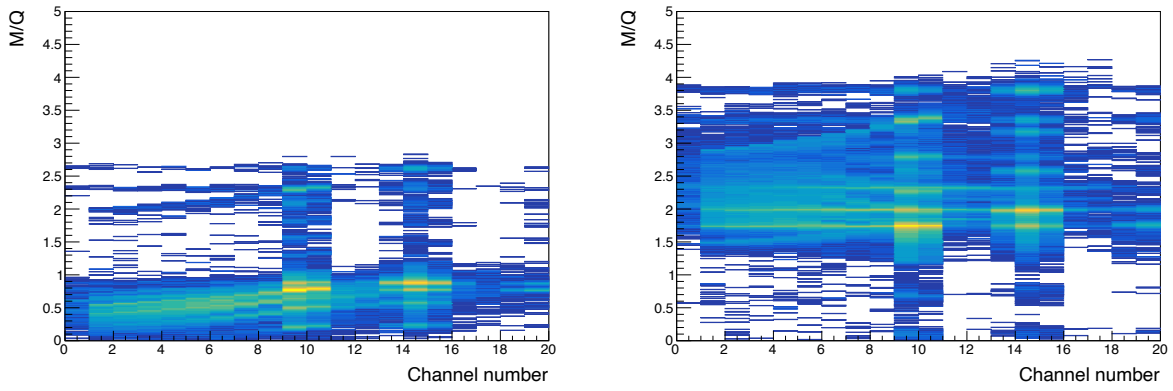

(a) (b)

Figure 3.14: *(a): M/Q vs MWPPAC electronic channel after applying the TAC calibration. In this spectrum the time of flight is inverted compared to the real time of flight and dependency of the time of flight as function of channel number is visible for the different ions. (b): same spectrum, but after applying the offset and single channel corrections.*

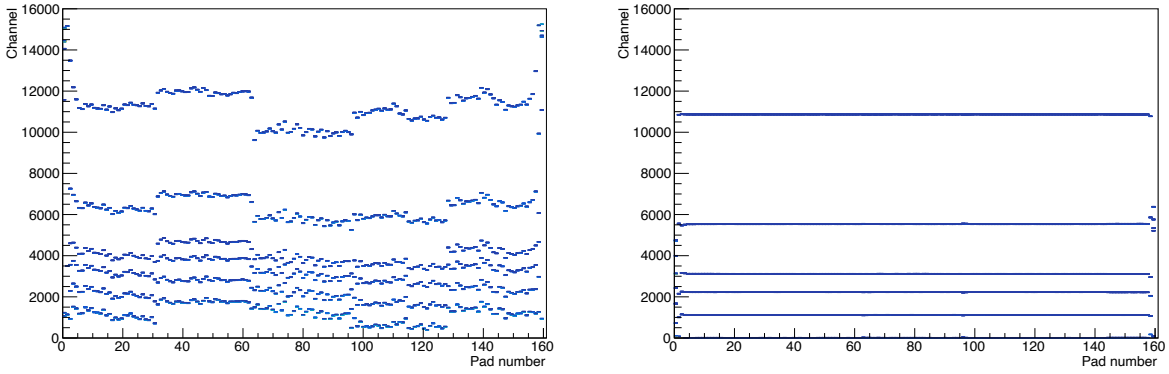

(a) (b)

Figure 3.15: *(a): drift chambers calibration spectrum using a pulse generator for the fourth drift chamber before alignment. (b): same spectrum but after the alignment.*

drift time in the chamber gives the vertical position (Y).

To perform the gain matching of the drift chambers pads, a pulse generator sending signals of different amplitudes into each pads was used. A gaussian function was used to fit each peak and then all peaks were aligned on a reference pad. The pad of reference was arbitrarily chosen (Fig. 3.17).

This necessary primary alignment was not sufficient to calibrate the detectors. A second alignment of the pads was required using real data. Indeed, the electronic chip that read different set of pads have different gains. To correct it, an offset for each set of pads of a given electronic chip was applied (Fig. 3.16).

The vertical position of interaction (Y) for the ions is deduced from the drift time of electrons. The drift time is measured using a TAC whose start comes from the MWPPAC and stop comes from the drift chambers themselves. The TACS for each drift chambers were calibrated by sending random pulses from a time calibrator module as described in the time of flight calibration of the MWPPAC. This calibration was tested by drawing the Y distribution of each drift chambers and by looking at their alignment (Fig. 3.17), as well as by looking at the angle between the beam and the vertical axis (Φ_f) which should be centered on 0. Offset on Y were then applied until all drift chambers were aligned and Φ_f was centered.

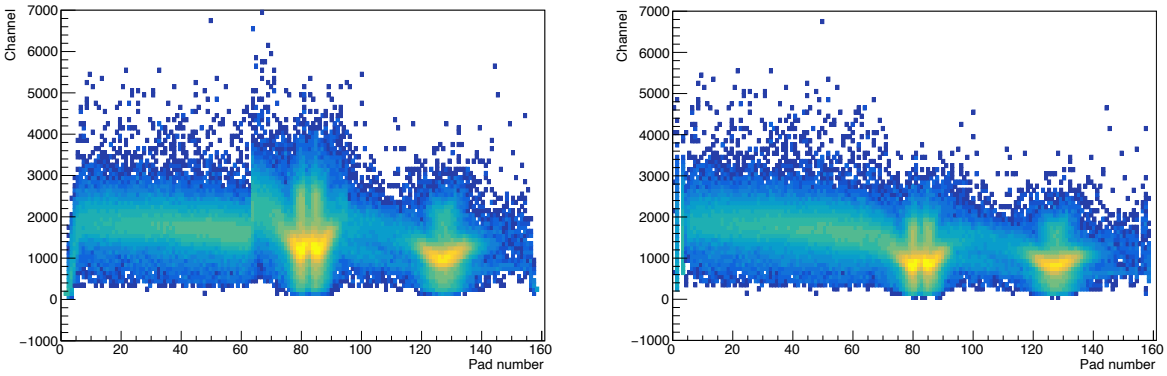

(a) (b)

Figure 3.16: *(a): Amplitude of the signal of the pad vs drift chambers pads number. For experimental data before the gain matching, clear discontinuity were visible especially between pad 64 and pad 65 (which are on two different electronic chip) as well as a gain that decreases on the edge of the drift chamber. (b): same spectra but after the gain matching.*

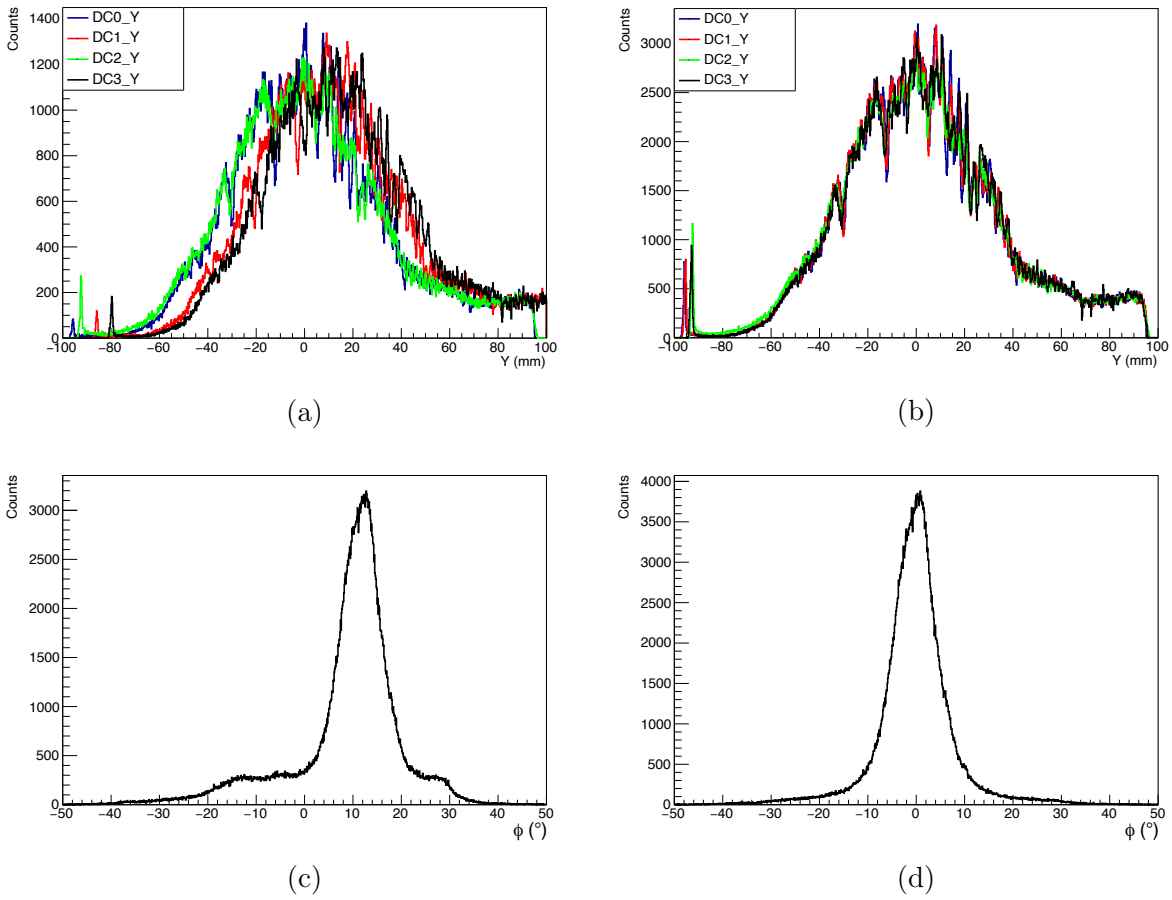

Figure 3.17: *(a): Y position in mm deduced from electrons drift time before applying the offsets. (b): Same as top left after aligning the drift chambers Y. (c): Reconstructed ϕ_f before the drift chambers alignment. (d): same as bottom left after alignment.*

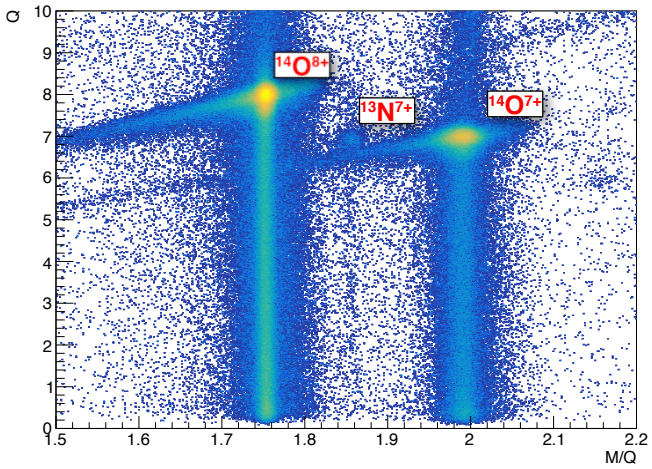

Figure 3.18: *Deduced Q as a function of M/Q. The horizontal lines are due to the pile-up events and the vertical one are spurious and are created by an error in the base line restoration algorithm of GANIL's acquistion.*

Ionization chambers calibration

Similarly to the drift chambers, the calibration of the ionization chambers (IC) has been done in a two steps process. A first calibration using a pulser was performed to align the different pads of each chamber. Then they were aligned using experimental data, by taking into account the energy lost by the ions before entering the IC and inside the IC. This calibration was performed online by the VAMOS collaboration and was verified by looking at different spectra, such as the identification in charge state reconstructed parameter Q vs M/Q for example (Fig. 3.18).

During the experiment, the gain of the preamplifier for all the ionization chambers has been changed. This led to a change in the calibration of the ionization chambers (Fig. 3.19b). To correct for this gain change, the previous calibration was modified by looking at the evolution of the ionization amplitude as a function of time. Doing so made possible to see the exact moment where the gain change was applied. It was corrected using a linear function (Fig. 3.19d).

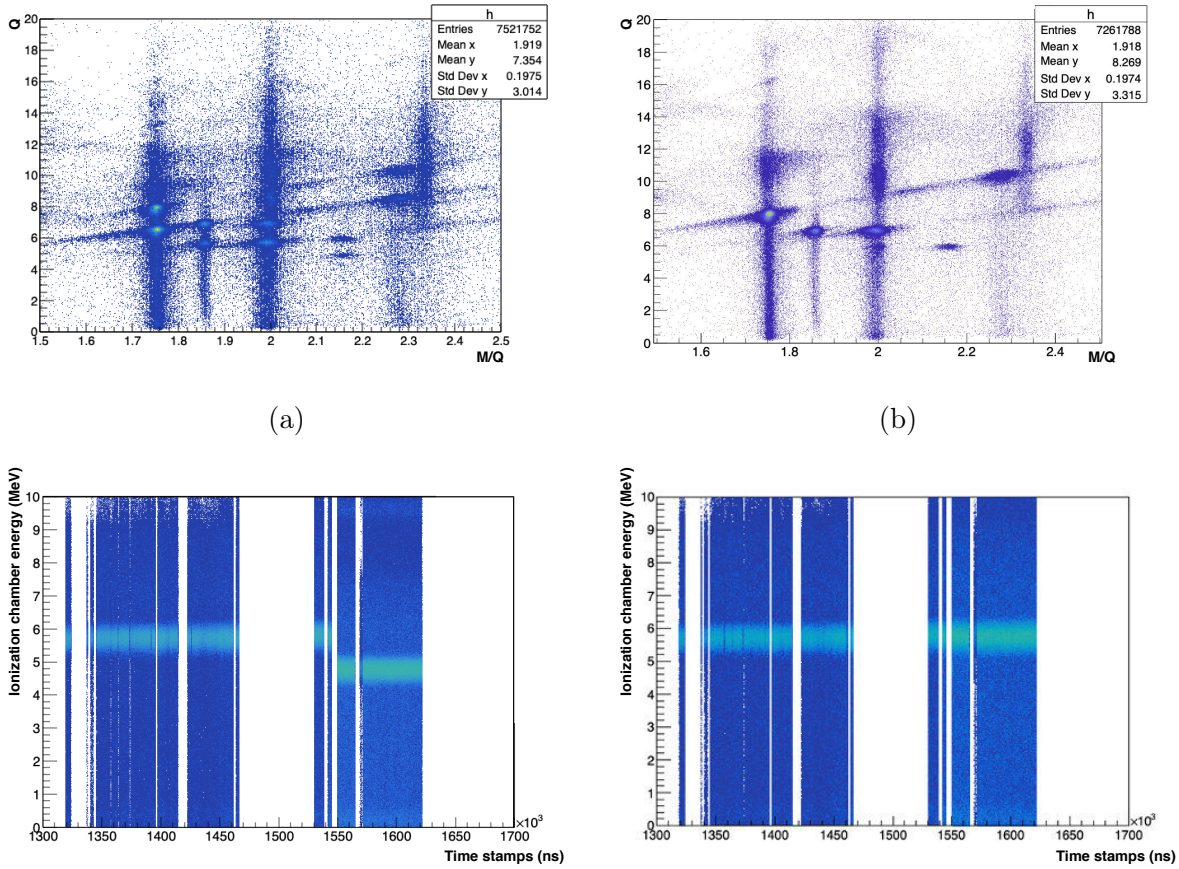

Figure 3.19: *(a): Q vs M/Q before adjusting for the calibration change done during the second half of the experiment. Ions identification shows duplicates spots of similar intensity in charge states. (a): same as top left, but after the re-calibration. No more duplicate spots of similar intensity can be seen, the only duplicates appear at higher Q from the pile-up. (c): Energy in one of the ionization chamber vs event time stamp in ns. (d): Same as bottom left but after applying the gain correction.*

3.2.6 Gamma detection : AGATA

Description of the detector

The AGATA[6] detector is a high purity segmented germanium based gamma ray detector array using the principle of gamma-ray tracking through the use of pulse shape analysis. AGATA is capable of performing precise energy measurement as well as precise 3D determination of the position of each of the interaction points of the gamma rays. It is composed of multiple clusters (Fig. 3.20a) which are made of three germanium crystals, each segmented in 36 parts. Detailed description of the detector can be found in AGATA technical paper [Akk12]. In this experiment 42 HPGe[7] crystals were used at backward angles with a coverage of 1π (Fig. 3.20b).

(a)

(b)

Figure 3.20: *(a): Picture of an AGATA cluster before being mounted. (b): Picture of multiple AGATA clusters next to the MUGAST chamber taken during the preparatory phase of the experiment.*

[6]Advanced Gamma Tracking Array
[7]High Purity Germanium

Nuclei	Energy (keV)
^{60}Co	1173.228(3)
	1332.492(4)
^{152}Eu	121.7817(3)
	244.69875(8)
	344.2785(12)
	443.96(4)
	778.9040(18)
	867.378(4)
	964.079(18)
	1112.074(4)
	1408.006(3)

Table 3.1: *The sources and the gamma rays energies used for the energy calibration procedure.*

Energy calibration

The energy calibration was performed using a ^{152}Eu and a ^{60}Co gamma sources spanning a large energy range from 122 keV to 1408 keV. Detailed description of those sources is found in Table. 3.1. The energy calibration of AGATA was performed before the experiment by the AGATA collaboration and validated experimentally, see Fig. 3.21a and Fig. 3.21b.

Use of AGATA

As the gamma emission branching ratio was expected to be very small, the most important aspect for this experiment was the efficiency of the gamma detector. To do so AGATA was used in add-back mode. In this detection mode, also called coincidence detection mode, if two or more crystals register a hit in temporal coincidence the energies detected by those crystals are added. Those events correspond mostly to gamma that undergo compton scattering from one crystal to its close neighbor [Duc99]. If a gamma enters in a first crystal and is then scattered to a second crystal where it stops, its total energy is equal to the sum of the energies lost in those two crystals. Summing those energies increases singnificantly AGATA's efficiency (measured efficiency at 1.4 MeV: 6.3(1) % with add-back and 5.5(1) % without).

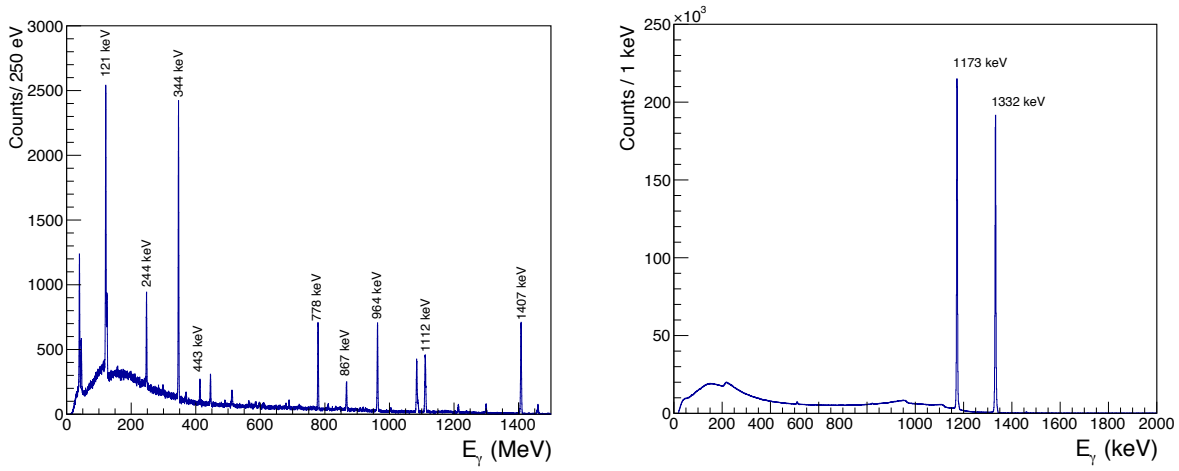

(a) (b)

Figure 3.21: *(a): Energy spectrum obtained with AGATA for the* ^{152}*Eu source. (b): Energy spectrum obtained with AGATA for the* ^{60}*Co source.*

3.3 Analysis

3.3.1 Measurement the reaction ^{1}H(^{14}O,p)^{14}O

The study of the resonant elastic scattering reaction as described in section 2.3.1 was also performed in this second experiment. Here, the MUST2 detectors were covering angles between 8° to 50 °. As explained in section 3.1, it was chosen to use a spectrometer at 0° instead of a light particles detector, thus angles between 0° and 8° of the protons couldn't be detected. Because of the kinematics, despite the higher statistics, it was not possible to obtain a better measurement than the one from the first experiment, especially concerning the possible existence of a $5/2^-$ states. Nevertheless, the $3/2^-$ state observed in the first experiment is still clearly visible for angles smaller than 12° confirming the result from the first experiment (Fig. 3.22).

To obtain the excitation function shown in Fig. 3.22 energies of multiplicity 1 events identified as protons obtained from all four MUST2 telescopes were combined with no selection in VAMOS due to VAMOS acceptance. The protons were selected by ΔE-E identification (Fig. 3.23a) and only angles smaller than 12° were considered. An excellent agreement between the two measurements is observed concerning both the $1/2^-$ and $3/2^-$ state. As expected, the $5/2^-$ state was not observed at such large angles since it is too narrow.

3.3.2 Two-proton analysis

Extracting the two-proton events from the background

The analysis of the resonant elastic scattering reaction led to the measurement of a narrow $3/2^-$ state, as well as the observation of a resonance compatible with the predicted $5/2^-$ state (see section 2.3.1). Both states are located, respectively, at 1.7 MeV and 1.3 MeV above the two-proton emission threshold (S_{2p} = 4.628 MeV). This means that the two-proton decay is possible, either by emitting the protons simultaneously, or sequentially. Protons were identified in two different ways depending on their energy :

- Protons with energy smaller than 6 MeV which do not have enough energy to cross the first stage of DSSSD were detected by time of flight identification. (Fig. 3.23b).
- Protons with energy higher than 6 MeV were detected by ΔE-E identification (Fig. 3.23a).

In the first experiment, it was observed that the main source for two-proton was the fusion evaporation reaction (Fig. 2.17a). Very good agreement between the two-proton

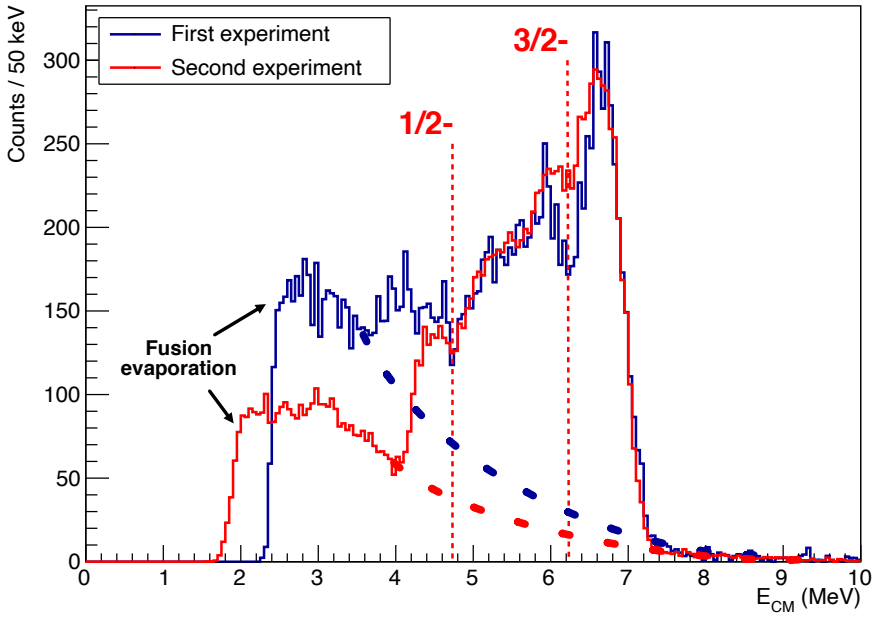

Figure 3.22: *In red : excitation function for angles smaller than 12° obtained in the second experiment by combining all four MUST2 detectors. In blue : excitation function for angles smaller than 3.5° obtained in the first experiment (see Fig. 2.21). The red excitation function is scaled vertically to match the blue one. A good agreement between the two excitation functions is observed concerning both the 1/2⁻ and 3/2⁻ state. As expected, the 5/2⁻ state is not visible, as such a narrow state will tend to disappear at larger angles. On this figure, it can also be observed that the carbon background is smaller at larger angles than at 0°*

data taken with the ^{nat}C target and data taken with the CH_2 target was observed for events with an energy larger than 14 MeV in the laboratory. Under 14 MeV, discrepancies were observed and attributed at that time to the two-proton events expected in this energy region. For this reason, it could have been expected, in this second experiment, to observe a kinematic line at low energy even without any selection in VAMOS, but looking at the kinematic spectrum obtained with the CH_2 target (Fig. 3.24a) and comparing it to the one obtained with the ^{nat}C target (Fig. 3.24b) no clear difference, except for the obvious difference in statistics, is observed.

In this experiment, it was decided to replace the 0° detector used in the first experiment by the VAMOS spectrometer. VAMOS made possible the detection of ^{13}N ions

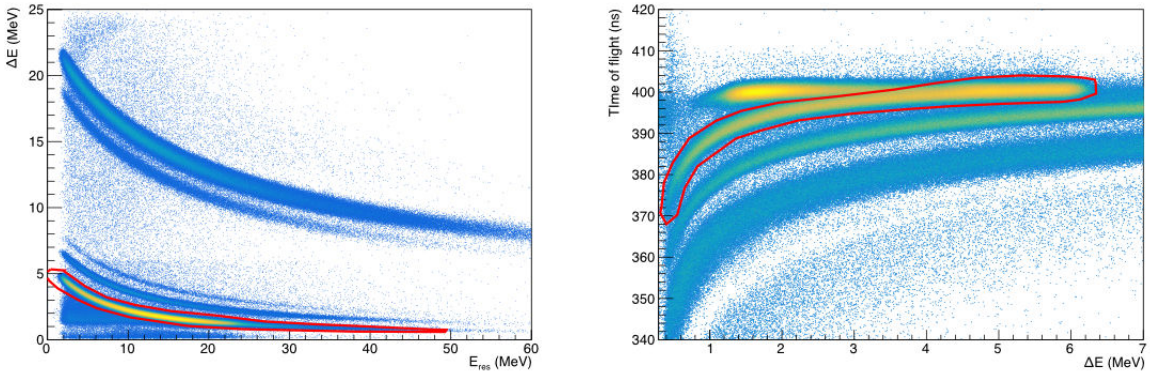

(a) (b)

Figure 3.23: (a): *DSSSD energy (ΔE) as a function of CsI energy (residual energy) for all MUST2 telescopes combined. The selection in red corresponds to the protons. (b): Time of flight as a function of DSSSD energy (ΔE) for all MUST2 telescopes combined. The selection in red corresponds to the protons.*

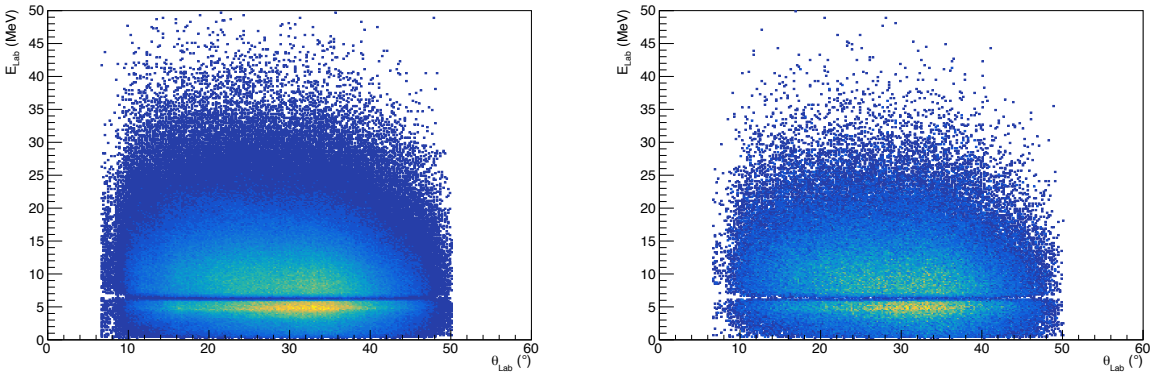

(a) (b)

Figure 3.24: *Measured energy of the two-proton events as a function of their measured angle in the laboratory. For a CH_2 target on the left (target n° 3) and for a ^{nat}C target on the right. As it can be observed, except for the difference of statistics, the two histograms are similar.*

emitted after the two-proton emission from the compound nucleus of ^{15}F. As observed on Fig. 3.25a there were no other ions with the same M/Q as ^{13}N for both of its charged states. It made the identification of ^{13}N easier and more efficient. Indeed, the M/Q de-

tection is obtained by combining information from the MWPPAC and the Drift chambers (see Fig. 3.12). Both showed relatively good efficiency throughout the experiment. On the other hand, to deduce the mass number M and the charge-state number Q for the measured ions the reconstruction efficiency depends on the IC efficiency. The measured efficiency for each ionization chamber was of 75(2) %. Deducing M or Q requires the information from three ionization chambers out of four, giving a reconstruction efficiency for the mass number M and charge state Q of 40(2) % (this procedure is described in ref. [Ram16]).

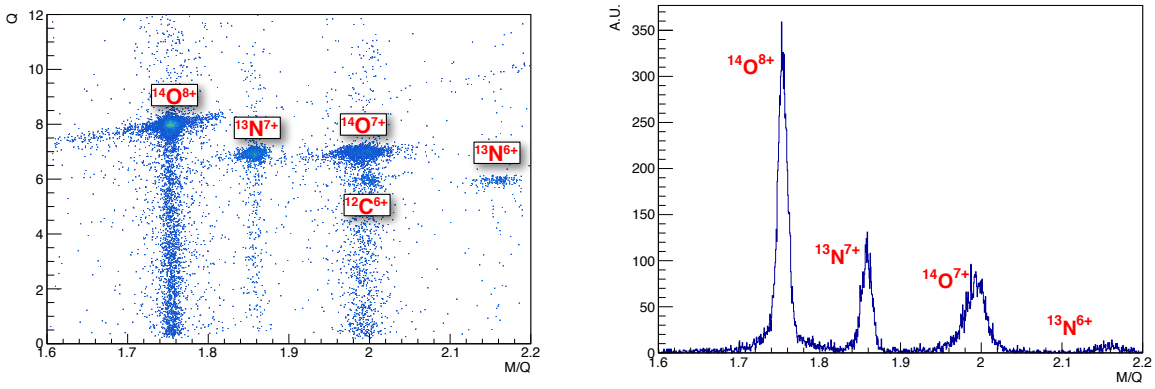

(a) (b)

Figure 3.25: *(a): Charge of the ions (Q) as a function of their mass divided by their charge (M/Q). As it can be observed, a simple selection in M/Q is sufficient to select both ^{13}N charged states because no other ion can be found at the same M/Q. This is not the case for $^{14}O^{7+}$, as $^{12}C^{6+}$ has the same M/Q. (b): Mass of the ions divided by their charge spectra used to select both ^{13}N charged states.*

By imposing the condition that ^{13}N ions were detected by VAMOS, Fig. 3.26a and Fig. 3.26b were obtained. As it can be observed on those figures, this condition removed most of the background and brought up two kinematics lines which resemble the one obtained by simulating the two-proton sequential emission in the introduction, see section 1.3.4.

The invariant mass method

To obtain the CM energy of the two-proton emitting state in the compound nucleus ^{15}F, the invariant mass method was used. This method requires the measurement of the full

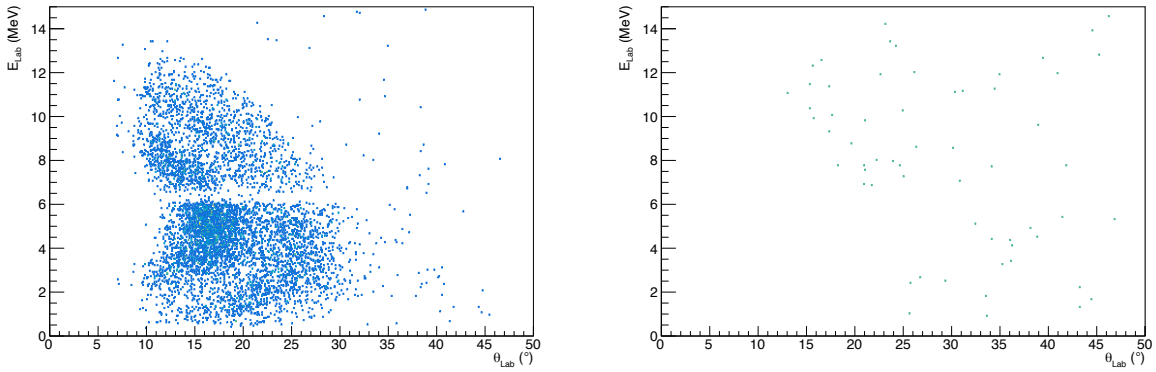

(a) (b)

Figure 3.26: *Energy of the protons corrected for energy loss as a function of their angle in the laboratory after applying M/Q selections on ^{13}N 7^+ and 6^+ charged states. CH_2 target (a) (target n°3) and ^{nat}C target (b). As it can be observed, two kinematic lines appear with the CH_2 target while almost all of the two-proton events generated by the ^{nat}C target are removed by the selection.*

kinematics of the reaction and it is derived as follows.

Let's consider the speed of light c = 1. In this case, the relation between mass and energy is:

$$E = \sqrt{p^2 + m^2} \tag{3.2}$$

In special relativity, the four-momentum is written:

$$P = \begin{bmatrix} \vec{p} \\ E \end{bmatrix} \tag{3.3}$$

And by definition:

$$P^2 = \begin{bmatrix} \vec{p} \\ E \end{bmatrix} = E^2 - p^2 = m^2 \tag{3.4}$$

From the energy-momentum conservation the four-momentum of ^{15}F in its excited state is written:

$$P_{^{15}F^*} = P_{^{13}N} + P_{p_1} + P_{p_2} \tag{3.5}$$

By squaring both sides of the equation, we obtain:

$$m_{^{15}F^*} = ||P_{^{15}F^*}|| \tag{3.6}$$

where $m_{^{15}F^*}$ is the invariant mass of the unbound system ^{15}F. The relative energy between the particles (E_{rel}) can be obtained by subtracting to the invariant mass, the mass of each particle in the rest frame. E_{rel} corresponds to the energy above the two-proton emission threshold :

$$E_{rel} = m_{^{15}F^*} - m_{^{13}N} - 2 \times m_p \tag{3.7}$$

The energy of the decaying state (CM energy) relatively to $^{14}O_{g.s.}$ can finally be obtained by adding the two-proton separation energy ($S_{2p} = 4.628$) to the relative energy :

$$E_{CM} = S_{2p} + E_{rel} \tag{3.8}$$

Compound nucleus formation

In all the equations previously detailed, the energy of the particles are at the reaction point. To obtain this energy from the energy of the detected particles, it was necessary to take into account the energy lost by those particles inside the target, and thus determine the target depth at which the reaction occurred. The two-proton emission happens only if the compound nucleus (CN) ^{15}F is formed. This CN formation will occur at a given target depth corresponding to the center of mass energy of one of the states in ^{15}F. Moreover, this can only take place for center of mass energy greater than $S_{2p} = 4.628$ MeV, which corresponds to a target depth (meaning that the beam has passed through this thickness before forming the compound nucleus ^{15}F at that energy) of 83.3 μm.

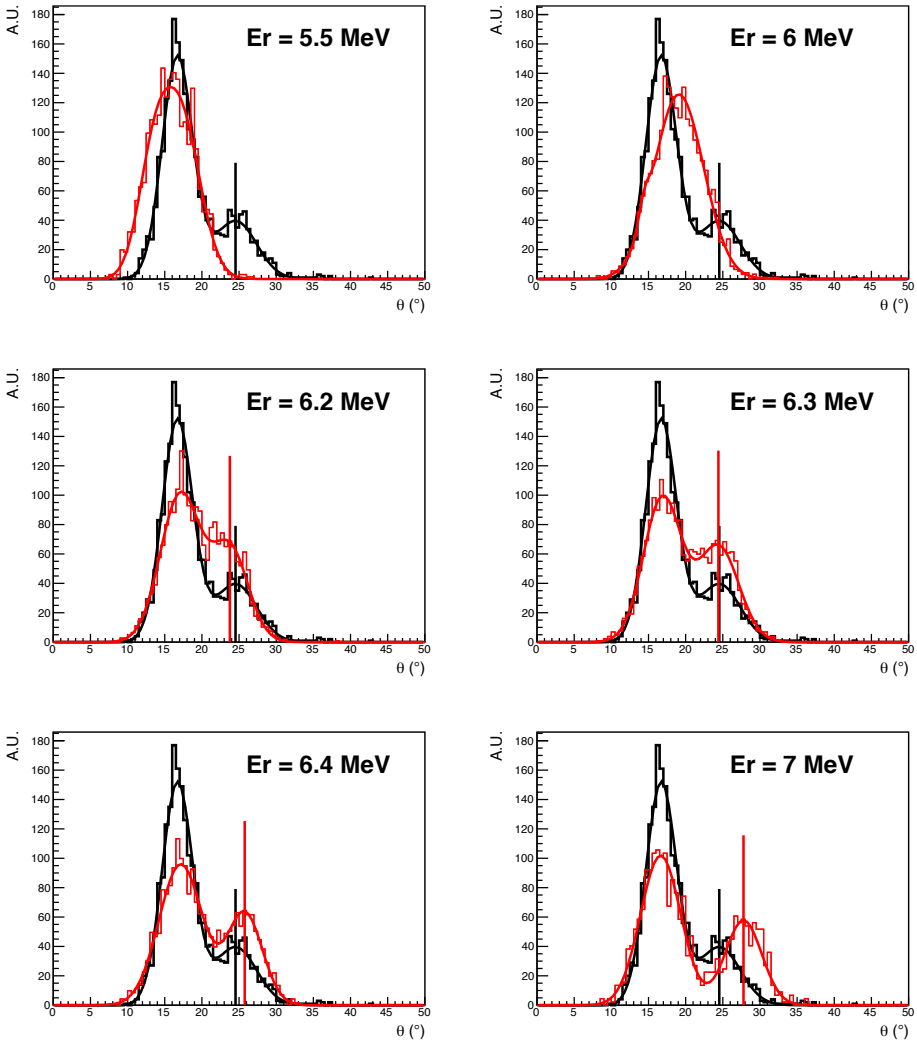

Figure 3.27: *In black: Experimental angular distributions for E_{Lab} ranging from 4 to 6 MeV, In red: simulation results at different resonances energy. The peak at higher energy corresponds to the emission of the first proton from the excited state in ^{15}F, thus its angular distribution depends on the resonance energy. The other peak at lower energy corresponds to the emission of the second proton emitted from the first excited state (1-) of ^{14}O. The black and red lines correspond to the mean value of the higher energy peak obtained by using a gaussian fit (black for the experimental data and red for the simulated results). The best agreement between the experimental data and the simulation is found for E_r = 6.3(5) MeV which is compatible with results from the first experiment (E_r = 6.29(14) MeV).*

In the experiment, two kinematic lines were observed. Based on the simulations presented in the introduction (see section 1.3.4) we expect that the $3/2^-$, or the $5/2^-$ state, decay at least by sequential emission. The formation energy of the compound nucleus has to be greater than the intermediate state in ^{14}O: $E_{^{14}O^{1-}} = 5.1732$ MeV, which corresponds to a depth of 66.3 μm. By taking all those constrains into account, the sequential two-proton emission could only occur between the entrance of the target and the maximum target depth of 66.3 μm.

As shown in section 2.3.1 and section 3.3.2 a new $3/2^-$ state at $E_{cm} \sim 1.7$ MeV above the S_{2p} was clearly observed. This energy corresponds to a target depth of 27(1) μm. The obvious hypothesis would be to consider that the two-proton emission occurred at this target depth and simply apply the corresponding energy loss correction. While it could be considered sufficient, it can also be independently validated in this measurement. To do so, a realistic GEANT4 simulation using the energy dependent Breit-Wigner formalism presented in section 1.3.4 was performed at different resonances energy and the resulted angular distribution was compared to the experimental one (see Fig. 3.27).

A first information obtained from those simulations is that MUGAST setup is sensible only to decays from excited states in ^{15}F situated above 5.5 MeV. Indeed at those energies the maximum proton emission angle is smaller than 10° in the laboratory frame (LAB). The minimum angle that could be detected by the MUST2 telescopes being 8.0(2) ° (Fig. 1.24c) no kinematical line could be observed for excited states lower than 5.5 MeV. Simulated and experimental angular distributions of the decaying protons (Fig. 3.27) showed a good agreement for a state with $E_r = 6.30(5)$ MeV consistent with the $3/2^-$ measured in the 2018 experiment ($E_r = 6.29(14)$ MeV).

Two-proton emitting states in ^{15}F

The two-proton excitation function was then derived using Eq. 3.8 and correcting the energy lost by the ^{13}N and the protons, considering that the reaction took place at a target depth of 27(1) μm, consistent with the formation of ^{15}F at a center of mass energy of 6.3 MeV (Fig. 3.27). Doing so, the two-proton excitation function displayed in Fig. 3.28 was obtained.

In Fig. 3.28 a good agreement with the two-proton excitation function and the $3/2^-$ state measured in the first experiment is observed. The energy of the state can be estimated by fitting the excitation function by a Breit-Wigner like function (f_{BW}) convoluted by a gaussian (f_{gauss}) to take into account the experimental resolution :

$$fBW_{fit} = (f_{gauss} \otimes f_{BW})(E_{CM}) \tag{3.9}$$

$$= \int_0^\infty \frac{1}{\sigma\sqrt{2\pi}} e^{-(t-p_0)^2/2\sigma^2} \times p_1 \frac{p_2 p_3}{((E_{CM}-t)-p_0)^2 + (p_2 + p_3/2)^2} dt \tag{3.10}$$

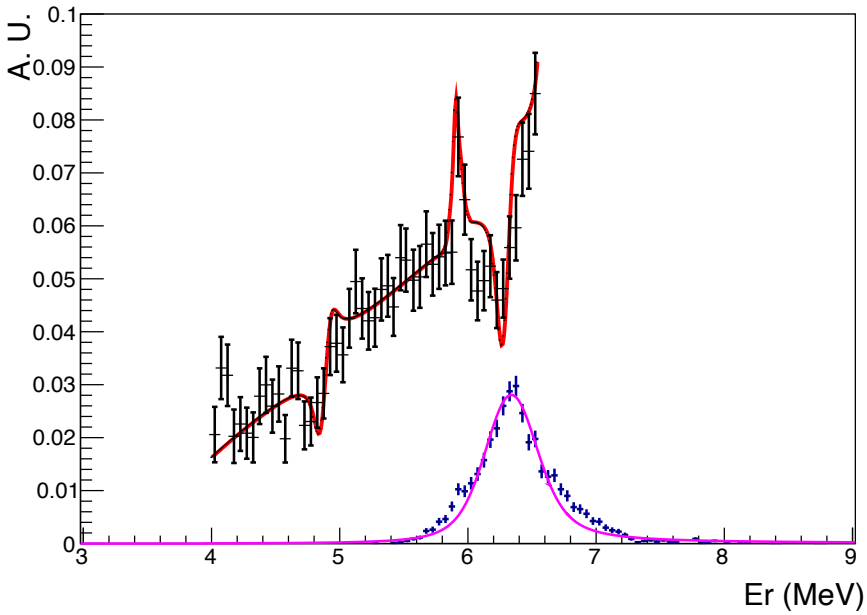

Figure 3.28: *In blue: Experimental two-proton excitation function. In black: Differential resonant elastic scattering cross-section from section 2.3.1. In magenta: gaussian convoluted fit (Eq. 3.10). In red: R-Matrix fit of the black spectrum.*

Where p_i are the free parameter of the fit, a fixed resolution of $\sigma = 150$ keV was used in the fit. Results from this fit can be seen in Fig. 3.28, a resonance energy: $E_r = 6.34(10)$ MeV is found.

By simulating the sequential two-proton emission of a $3/2^-$ state with CM energy 6.34 MeV, the best overall agreement was found for a state with a total width of 30(10) keV (see Fig. 3.29 and Fig. 3.30). This results is in agreement with the total width of the $3/2^-$ state measured in the first experiment ($\Gamma_{3/2^-} = 24(10)$ keV). The agreement between the simulation and the experimental data at low energy is poor and couldn't be well reproduced even by increasing the width of the state. We propose that this discrepancy between the simulation and the experiment at low energy is another hint toward the

existence of a $5/2^-$ state. By subtracting the simulated data to the experimental one, a peak at a CM energy of 6.0(1) MeV is observed (Fig. 3.29a). This peak is consistent with the $5/2^-$ state proposed in the first experiment. By simulating the sequential decay of both a $3/2^-$ state at 6.34 MeV with 30 keV width and a $5/2^-$ state at 6 MeV with a 2 keV width, the agreement between the simulation and the experiment increases (Fig. 3.29b) reinforcing the hypothesis that a $5/2^-$ state exist at 6.0(2) MeV.

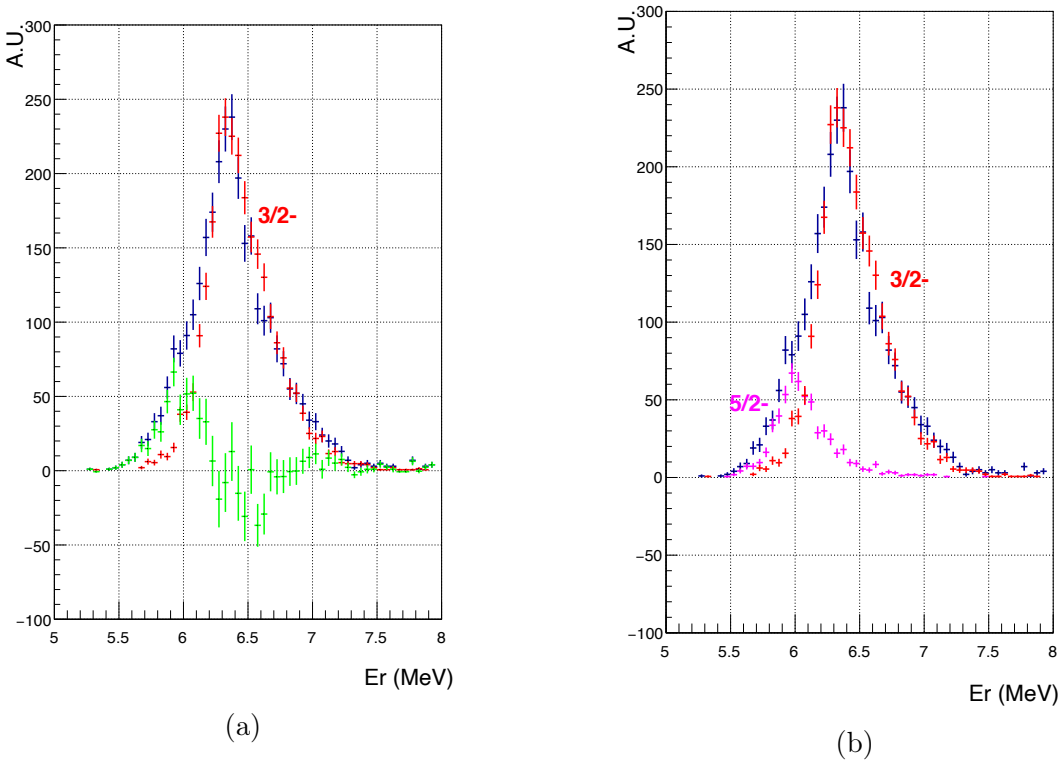

(a) (b)

Figure 3.29: *(a): Experimental data in blue compared to simulations of a sequential decay of a $3/2^-$ state at a CM energy of 6.34 MeV with a 30 keV width, in red. The green histogram corresponds to the result obtained from the subtraction of the red histogram from the blue one. The peak with CM energy of 6.0(1) MeV is in agreement with the previously deduced $5/2^-$ state. (b): Experimental data in blue compared to simulations of a sequential decay of a $3/2^-$ state at a CM energy of 6.34 MeV with a 30 keV width, in red, and sequential decay of a $5/2^-$ state at 6 MeV with a 2 keV width in magenta, the sum of the two simulations is found in Fig. 3.30*

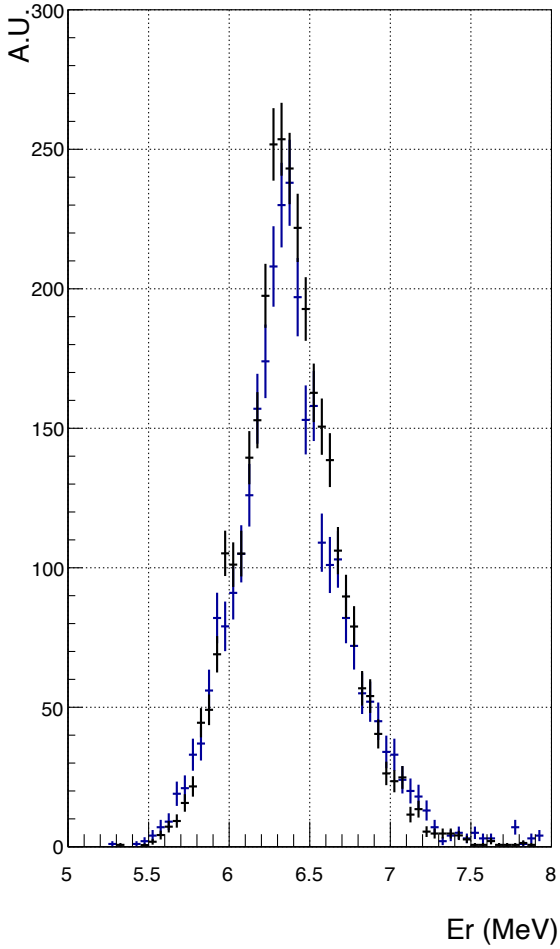

Figure 3.30: *Experimental data in blue compared to the sum of the two simulations from Fig. 3.29b in black. By simulating both the sequential decay of a 3/2⁻ and of a 5/2⁻ state a better agreement is obtained between the simulation and the experiment.*

Two-proton correlations

A question of great interest in this experiment is the decay mechanism of ^{15}F states above the two-proton emission threshold. In both the first and second experiment a new $3/2^-$ state was measured and hints of a $5/2^-$ state were observed both by the study of the resonant elastic scattering (see section 2.3.1) and by measuring the two-proton excitation function (Fig. 3.29 and Fig. 3.30).

As said in the previous paragraphs, the two-proton emission can either be a simultaneous emission, where the two protons are emitted together directly to the ^{13}N ground state, or they can be emitted sequentially. For the latter, the reaction is a two steps process that can be decomposed in two different two-body emission: a first one where the first proton is emitted from one of the excited states of ^{15}F (the $3/2^-$ state or the $5/2^-$ state) to the intermediate 1- state in ^{14}O, and a second one where this 1- state in ^{14}O decays to the ^{13}N ground state. As explained in the previous paragraphs, a simple visual comparison between the experimental two-proton kinematics and the simulations (section 1.3.4) shows that at least some, if not all, of the two-proton emissions are sequential.

To characterize the decay mechanism of the excited state(s) in ^{15}F the correlations between protons and ^{13}N were used. It was done using the Dalitz representation. Developed and commonly used in particle physics [Per00], Dalitz plots have already been used in nuclear physics to study particles correlations [Rev18a]. This representation is commonly obtained by drawing the normalized invariant mass of a first subsystem, here proton-proton, versus the one of the remaining subsystem, here proton-^{13}N [Rev18b]:

$$m_{ij}^2 = \frac{M_{ij}^2 - (m_i + m_j)^2}{(m_i + m_j + E_{rel})^2 - (m_i + m_j)} \tag{3.11}$$

where M_{ij} corresponds to the invariant mass of a given particles pair.

Considering the energy of the protons compared to their masses, it was shown that Dalitz plot can be obtained by using the relative reduced energy (E_{ij}) obtained from E_{rel} (Eq. 3.8) and their four-momentum vector (Eq. 3.3) [Mon19]:

- Relative reduced energy between the two protons :

$$P_{p1p2} = P_{p1} + P_{p2} \tag{3.12}$$

$$E_{p1p2} = \frac{P_{p1p2} - 2M_p}{E_{rel}} \tag{3.13}$$

- Relative reduced energy between the fragment and the first proton :

$$P_{fp1} = P_{p1} + P_{13N} \tag{3.14}$$

$$E_{fp1} = \frac{P_{fp1} - M_p - M_{13N}}{E_{rel}} \tag{3.15}$$

- Relative reduced energy between the fragment and the second proton :

$$P_{fp2} = P_{p2} + P_{13N} \tag{3.16}$$

$$E_{fp2} = \frac{P_{fp2} - M_p - M_{13N}}{E_{rel}} \tag{3.17}$$

In the raw data the first and second protons cannot be distinguished, as the order in which they were recorded by the data acquisition were purely due to MUGAST's electronic wiring. As a consequence, E_{fp1} and E_{fp2} cannot be discriminated and were called E_{fp}.

Calculating E_{fp} and E_{p1p2} using respectively Eq. 3.13, for the proton-proton subsystem and Eq. 3.15 and 3.17, for the ^{13}N + p subsystem produced Fig. 3.31a. On this figure two lines are observed. Those lines are characteristics of a sequential emission [Rev18a]. To understand the decay mechanism, realistic GEANT4 simulations were used. Based on the measurement of the two-proton excitation function from Fig. 3.29 and on the resonant elastic scattering measurements obtained in the first experiment, only a single $3/2^-$ state was first considered in the simulations.

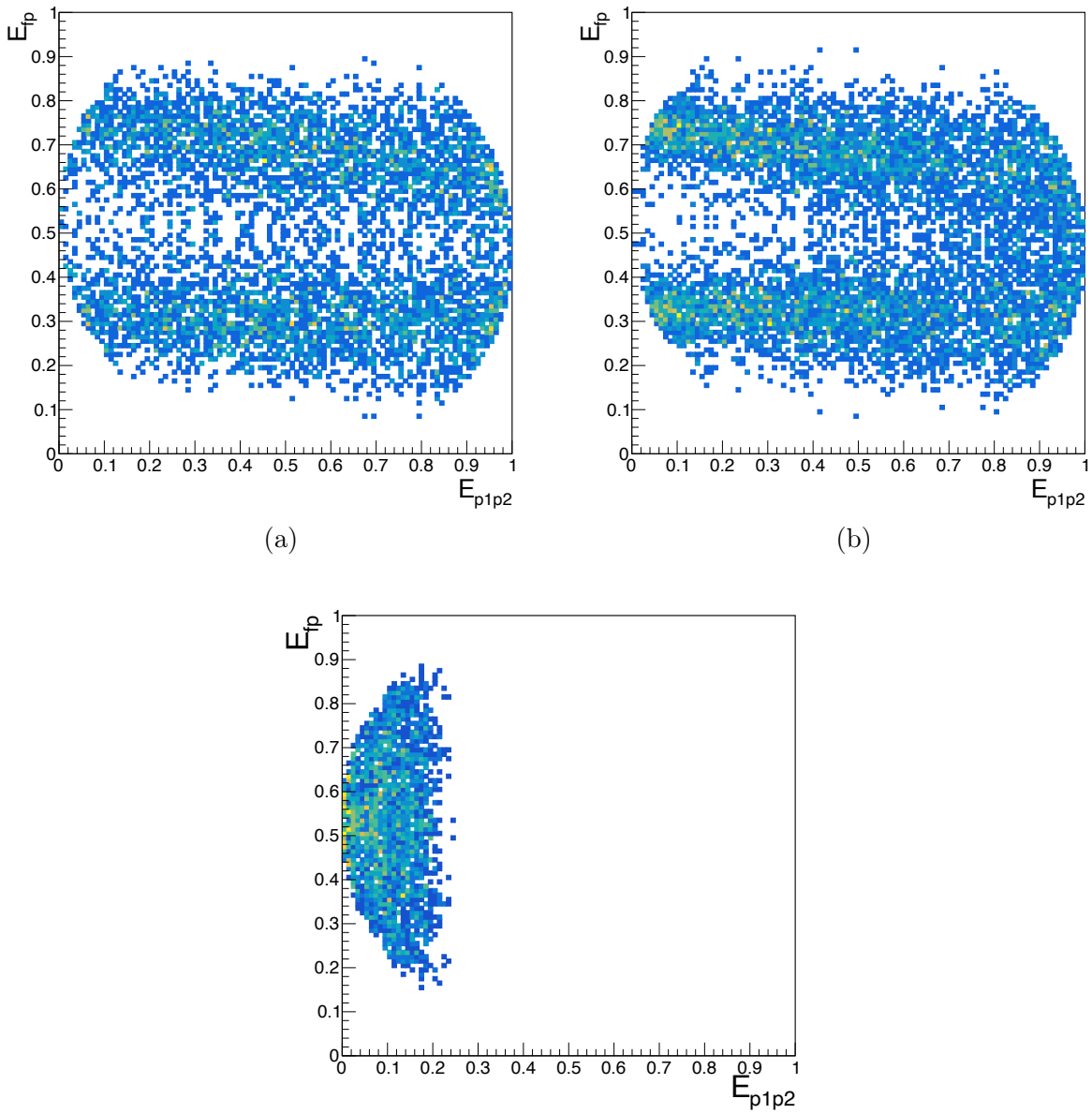

(a)

(b)

(c)

Figure 3.31: *(a): Experimental Dalitz plot for the $^{13}N + p + p$ decays. (b): Simulated Dalitz plot for the $^{13}N + p + p$ decays obtained by simulating the sequential decay through ^{14}O first excited state (1-) from the 3/2$^-$ state in ^{15}F (see section 1.3.4 and Fig. 1.24b). (c): Simulated Dalitz plot for the $^{13}N + p + p$ decays obtained by simulating the simultaneous two-proton decay from the 3/2$^-$ state in ^{15}F (see section 1.3.4 and Fig. 1.24d).*

By simulating first the two-proton sequential and simultaneous emission from the $3/2^-$ state in ^{15}F (section 1.3.4) with a CM energy of 6.34 MeV and a 30 keV width and by drawing the corresponding Dalitz plots, Fig. 3.31b and Fig. 3.31c were obtained. Comparing the simulations to the experimental data, a good agreement is observed with the sequential emission. A more detailed comparison can be performed by looking at the projection onto the relative reduced energy between protons E_{p1p2} and the relative reduced energy between the fragment and the protons E_{fp} see Fig. 3.32a and Fig. 3.32b respectively. Similarly to what is observed with the Dalitz representation, a good agreement between the simulation of the sequential decay and the experimental data was found, and no sign of simultaneous emission was observed. In the case where simultaneous emission would occur, a strong signal corresponding to high proton-proton correlation around $E_{fp} = 0.5$ and around $E_{p1p2} = 0$ should be observed, but as it can be seen on Fig. 3.32a, the amplitude stays constant on the full range while Fig. 3.32b shows that there is not a single peak around $E_{fp} = 0.5$ but two well separated peaks, a first one at $E_{fp} = 0.3$ corresponding to the sequential decay of the second proton from ^{14}O intermediate state and a second one at $E_{fp} = 0.7$ corresponding to the decay of the first proton from ^{15}F excited state.

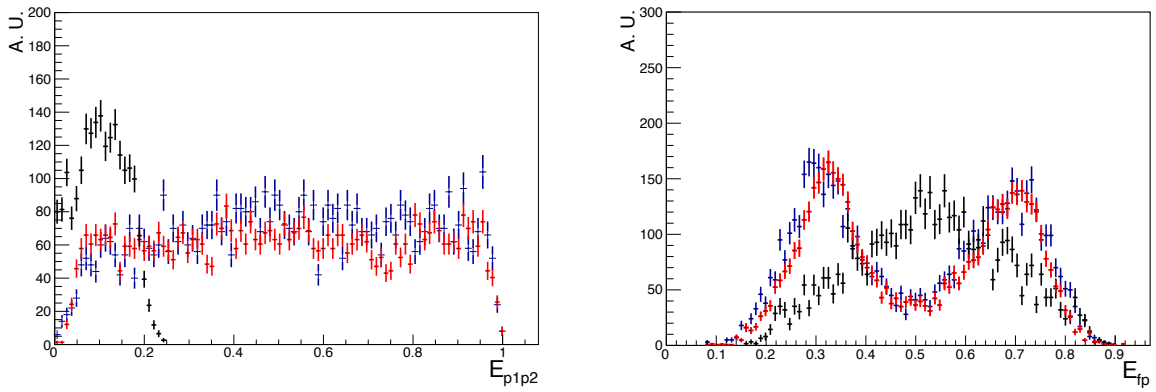

(a) (b)

Figure 3.32: *(a): Comparison of the relative reduced energy between protons, experimental data in blue, simulation of the sequential decay of the 3/2⁻ state in red and simulation of the simultaneous decay of the 3/2⁻ state in black. (b): Comparison of the relative reduced energy between ^{13}N and protons, experimental data in blue, simulation of the sequential decay of the 3/2⁻ state in red and simulation of the simultaneous decay of the 3/2⁻ state in black.*

The measurement of the two-proton excitation function (Fig. 3.29) gave an indication

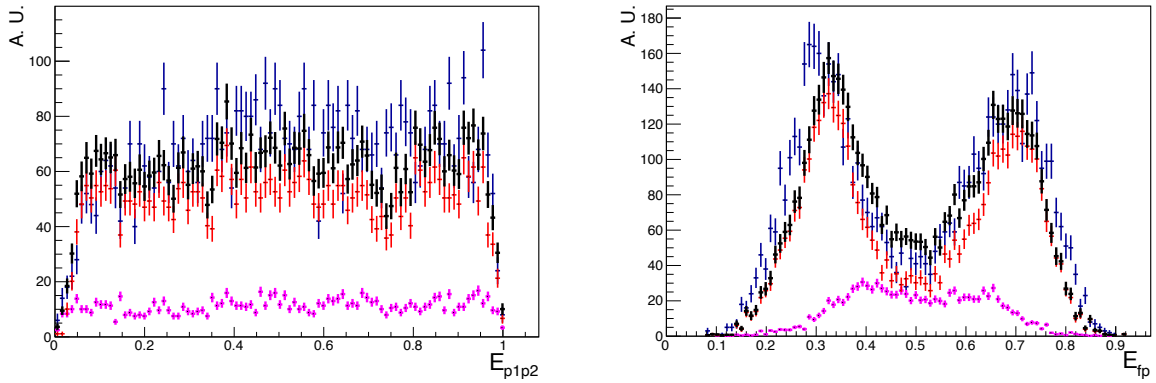

(a) (b)

Figure 3.33: *(a): Comparison of the relative reduced energy between protons, experimental data in blue, simulation of the sequential decay of the 3/2⁻ state in red and simulation of the sequential decay of the 5/2⁻ state in magenta. In black is the sum of the two simulations. (b): Comparison of the relative reduced energy between ^{13}N and protons, experimental data in blue, simulation of the sequential decay of the 3/2⁻ state in red and simulation of the sequential decay of the 5/2⁻ state in magenta. In black is the sum of the two simulations.*

that the $5/2^-$ state deduced in the first experiment existed. In the case this state do exists, adding the sequential decay of a $5/2^-$ state to the simulation in the same relative proportion as the one required to better match the excitation function from Fig. 3.29 should either, improve the good agreement obtained by simulating only the sequential decay of the $3/2^-$ state, or, at least, not drastically change this agreement. As it can be observed on Fig. 3.33b and Fig. 3.33a adding the sequential decay of a $5/2^-$ state doesn't seem to improve the agreement between the simulation and the experimental data, but it doesn't change it significantly. This results, in itself, is not sufficient to prove or disprove the existence of a $5/2^-$ state.

In the case where there are two distinct states decaying by two-proton emission, a common method is to look at the correlations for a given excitation energy range. By looking at E_{fp} for $E_x + S_p < 6$ MeV it can be observed (Fig. 3.34) that experimental data cannot be reproduced by simulating the sequential decay of a single $3/2^-$ state. By adding in the simulation the sequential decay of a $5/2^-$ state, a good agreement was found, thus validating the assumption that a very narrow $5/2^-$ state does exist in ^{15}F with a CM energy of 6.0(1) MeV and that this state also decays by emitting two protons sequentially.

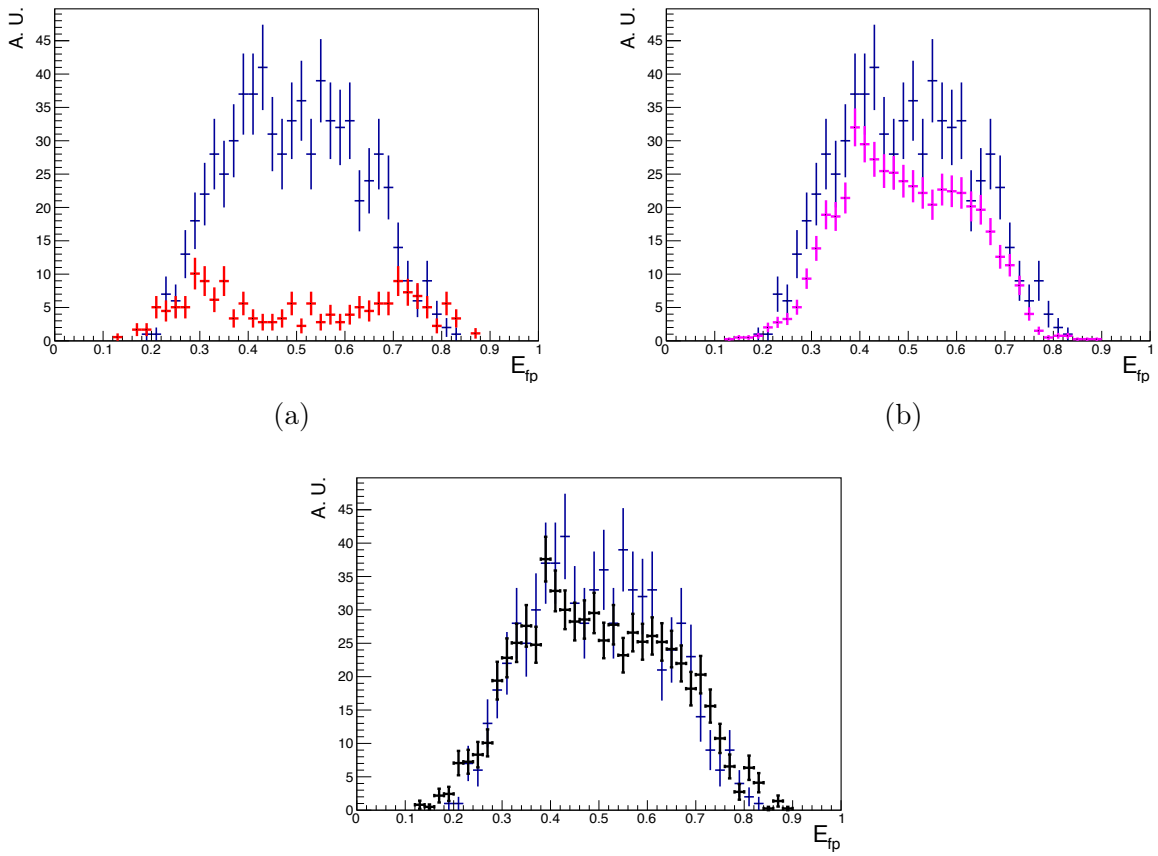

Figure 3.34: *(a) Experimental relative reduced energy of $^{13}N + p$ in blue, compared to the same observable obtained in the simulations of a sequential decay of a $3/2^-$ state at a CM energy of 6.34 MeV with a 30 keV width (in red) and of a sequential decay of a $5/2^-$ state at 6 MeV with a 2 keV width (b) (in magenta). The black histogram (c) corresponds to the addition of the magenta and the red. By simulating both the sequential decay of a $3/2^-$ and of a $5/2^-$ state a very good agreement is obtained between the simulation and the experiment.*

Intermediate state reconstruction

Both the $5/2^-$ and $3/2^-$ states were observed to decay only by sequential emission. Thanks to the measurement of the full kinematics of the reaction and due to the rather good separation observed in E_{fp} (Fig. 3.35a) between the two protons, it was possible to discriminate which one was emitted from ^{15}F excited state or from ^{14}O excited state. In

Fig. 3.35a two lines are visible, it can be observed that the bottom line is straight while the top line is not, it is due to a "wrong" reconstruction of the fragment + proton system. Indeed E_{fp} was computed considering the energy and angle of ^{13}N, but the fragment corresponding to the emission of the first proton is ^{14}O, not ^{13}N this lead to a small error in the calculation of E_{fp} and to a tilt of the line corresponding to the first proton emitted in the sequential emission. Once it was known which proton was the second proton emitted from ^{14}O, the energy of the intermediate state was obtained using the invariant-mass method described at the beginning of this section. The result of this reconstruction is shown in Fig. 3.35b. Fitting this state using the same gaussian convoluted Breit-Wigner function from Eq. 3.10, a value of $E_x(^{14}O) = 5.17(10)$ MeV in perfect agreement with the energy of the 1^- state from the literature is obtained.

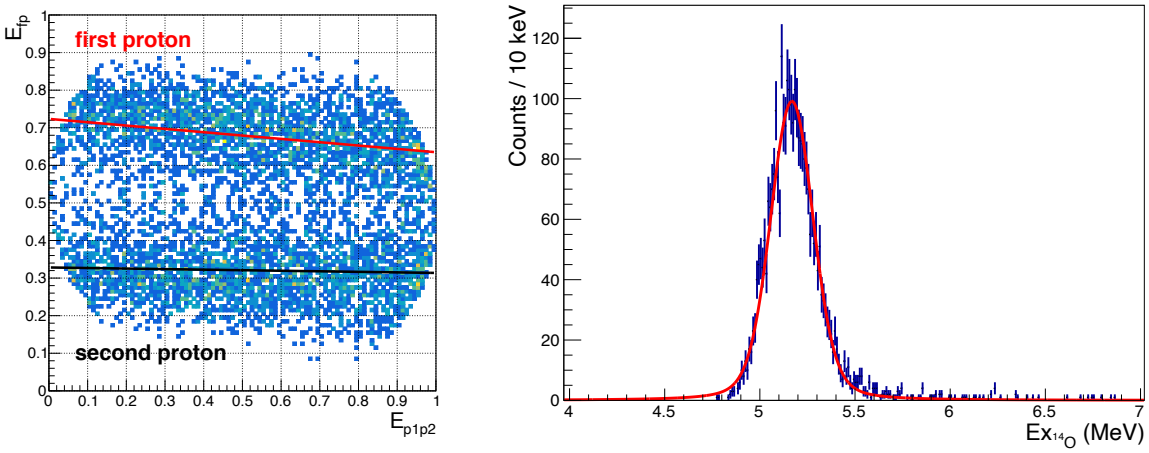

(a) (b)

Figure 3.35: *(a) Experimental Dalitz plot for the $^{13}N + p + p$ decays, the bottom line corresponds to the second proton emitted from the intermediate (1^-) state in ^{14}O, while the top line corresponds to the first proton emitted from ^{15}F excited state, the two lines were obtained by fitting linearly each lines, a clear tilt is observed for the top line compared to the bottom one. (b) ^{14}O intermediate state reconstructed using the invariant mass method.*

Determination of the cross-section

Simulations of the sequential two-proton emission used throughout this chapter show that (see section 1.3.4), except for protons emitted with a lab angle smaller than 8° (Fig. 3.36a), the MUST2 detectors covered the full angular distribution of the two protons. Even though differences in the angular distribution were observed between experimental

and simulated data (see Fig. 3.27), considering a constant angular distribution for protons emitted between 0° and 8° should be a relatively good approximation. Concerning ^{13}N, it can be observed that kinematically all ^{13}N events entered the spectrometer. Taking these information into account it is possible to obtain the total cross-section for the two-proton emission.

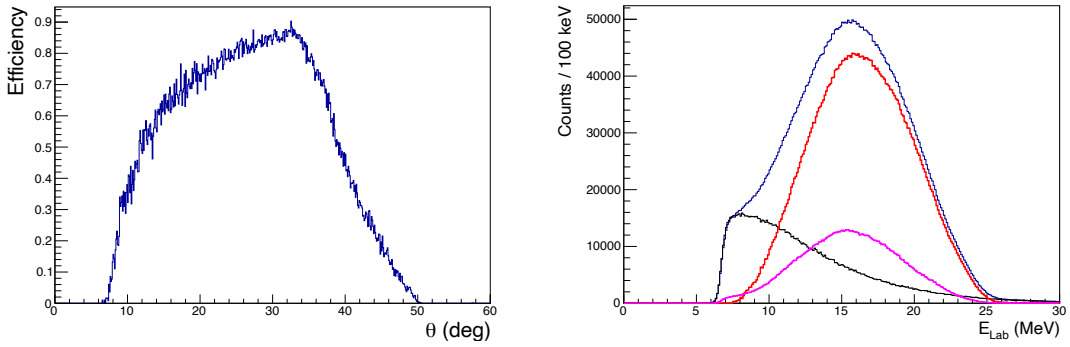

(a) (b)

Figure 3.36: *(a) MUST2 detection efficiency as a function of the laboratory angle obtained using GEANT4 (b) Laboratory energy of elastically scattered protons in MUST2. Blue: full distribution, black: background events from fusion evaporation, red: full distribution after subtracting the background, magenta: energy distribution with the condition that a M/Q was reconstructed in VAMOS.*

To this aim, it was required to determine the detection efficiency of both MUST2 and VAMOS. For MUST2 detector, the geometrical acceptance was obtained using simulated data similarly to the first experiment (see section 2.3.1). Determining the efficiency of the VAMOS spectrometer on the other hand was not an easy task, as in this experiment there was no detector before the magnet. We propose a new method making use of the elastic scattering reaction to determine its efficiency. Indeed, as for the ^{13}N ions emitted during the two-proton emission, elastically scattered ^{14}O ions are emitted with relatively small angles and should all enter the spectrometer. Therefore, if VAMOS detection's efficiency was 100%, for every elastically scattered proton detected by MUST2, a ^{14}O should be detected in coincidence in VAMOS. The condition that there is a reconstructed Bρ and a M/Q identification in VAMOS (Fig. 3.36b) shows that only $\sim$ 30 % of the elastic scattering events remain. This number is an indication that VAMOS is not fully efficient but it cannot be used, as is, to determine VAMOS's efficiency since the efficiency is strongly dependent on the Bρ of the detected particle.

Simulating the proton energy distribution as a function of the Bρ for different charged states (Fig. 3.37a) shows that for the elastic scattering reactions the full Bρ distribution is not accessible experimentally. Indeed, a clear cut is observed in Fig. 3.37a due to the Bρ acceptance of VAMOS which is $dB\rho/B\rho_{ref} = 25\%$ with B$\rho_{ref} = 0.52(1)$ T.m in this experiment. The simulation was performed using GEANT4 to simulate the detection of protons in the MUST2 detector, but the VAMOS geometry was not considered in the GEANT4 simulation. The three lines observed both in experimental and simulated data in Fig. 3.37a corresponds to the three detected charged states of ^{14}O. The distribution of charged states was simulated based on the experimental ones.

VAMOS efficiency as a function of Bρ in the experiment can be obtained from the simulation. Indeed, let's consider in the simulation only events where elastically scattered protons are detected by MUST2 (N_{simu}^{MUST2}). The number of events detected by VAMOS as a function of Bρ when a proton was detected in MUST2 is $N_{simu}^{VAMOS}(B\rho)$. Dividing this number by N_{simu}^{MUST2} gives the distribution of events as a function of Bρ:

$$n_{simu}(B\rho) = N_{simu}^{VAMOS}(B\rho)/N_{simu}^{MUST2}. \tag{3.18}$$

The same can then be done for experimental data, considering elastically scattered protons detected by MUST2 (N_{exp}^{MUST2}), and the number of events detected by VAMOS as a function of Bρ ($N_{exp}^{VAMOS}(B\rho)$) the distribution of events for a given Bρ is obtained:

$$n_{exp}(B\rho) = N_{exp}^{VAMOS}(B\rho)/N_{exp}^{MUST2}. \tag{3.19}$$

VAMOS efficiency is then equal to:

$$\epsilon_{VAMOS} = n_{exp}(B\rho)/n_{simu}(B\rho) \tag{3.20}$$

Even though the efficiency from Fig. 3.37b was obtained for elastic scattering reactions for which the angular distribution of ^{14}O is different from the one of ^{13}N after a two-proton emission, the fact that both reactions cover relatively small angles (between 0° to 6°) and that ^{13}N ions Bρ distribution covers a smaller range of Bρ than the one of ^{14}O (Fig. 3.38a) it was considered that this VAMOS detection efficiency was a sufficient approximation.

The cross section was then obtained using the following equation:

$$\sigma = \frac{N_{reaction}}{N_{incident} \times N_{target}/cm^2} \tag{3.21}$$

$N_{incident}$ was obtained from the CATS detector similarly to the first experiment and N_{target}/cm^2 was obtained considering a target thickness of ~ 10 μm based on the depth

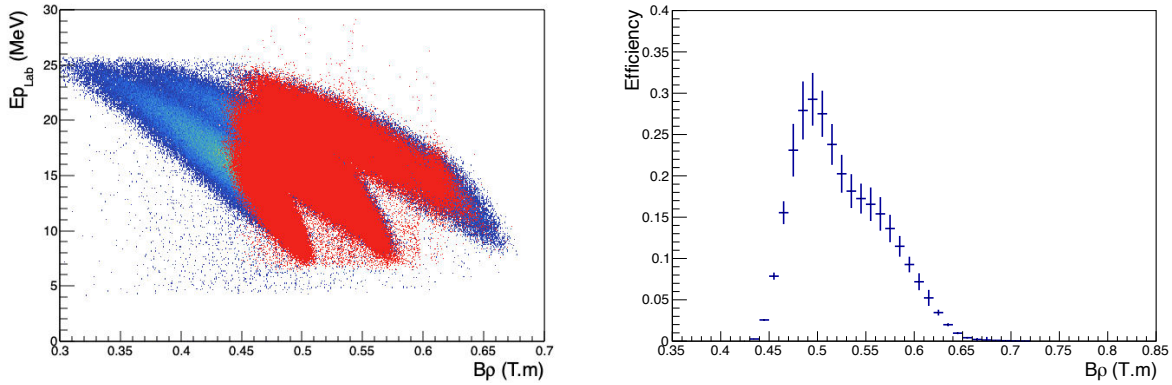

(a) (b)

Figure 3.37: *(a): Proton laboratory energy measured in MUST2 as a function of* ^{14}O *Bρ for the simulation in color and for the experimental data in red. (b): VAMOS efficiency as a function of Bρ (see text).*

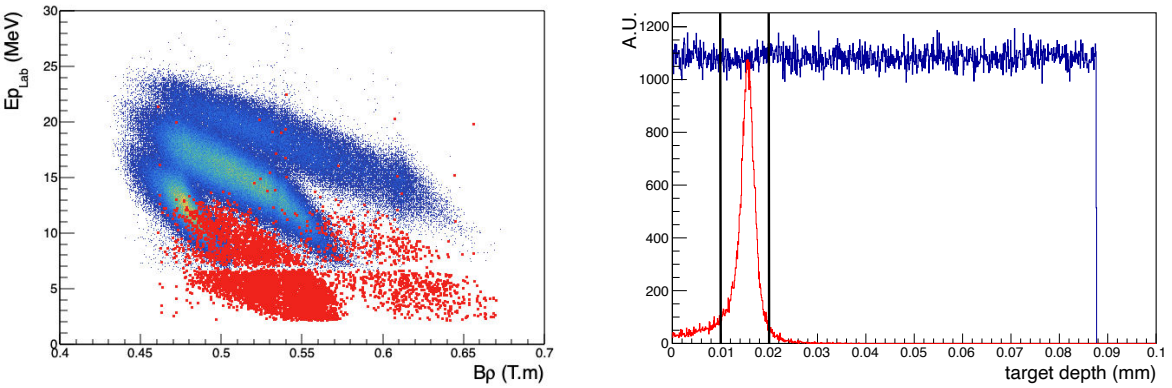

(a) (b)

Figure 3.38: *(a): Proton laboratory energy measured in MUST2 as a function of Bρ for the* ^{14}O *in color and for the* ^{13}N *in red. (b): Simulation of the two-proton reactions inside a 92.3µm target, all simulated events in blue, in red are the simulated events for which there was a two-proton emission. As it can be observed, the reactions are localized and most events occurred in a thickness of* $\sim$ *10 µm, the black lines corresponds to the target region considered.*

where the compound nucleus ^{15}F is formed in the target and on the width of the states ($\sim$ 30 keV). This thickness was determined using a simulation (Fig. 3.38b) similar to the

one used throughout this chapter. Figure **??** shows the final two-proton cross-section.

The two-proton cross-section obtained can be used together with to the results from the first experiment to obtain the partial width of each decay channels. To this aim, both results can be simultaneously fitted by AZURE2 software, similarly to the fit performed in section 2.3.1. Results from this fit can be found in Table 3.2, Fig. 3.39 and Fig. 7.8.

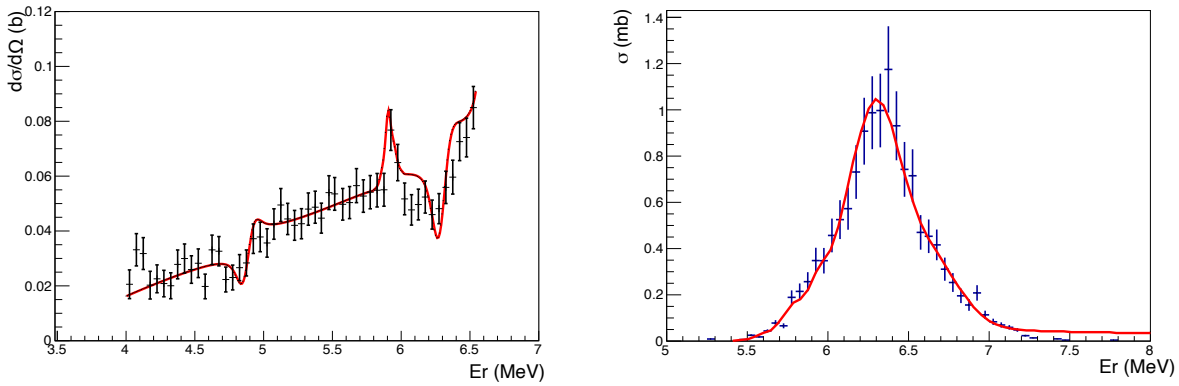

(a) (b)

Figure 3.39: *Simultaneous fit of the resonant elastic scattering reactions (a) and the two-proton emission (b).*

J^π	E_{CM} (MeV)	Γ_{1p} (keV)	Γ_{2p} (keV)	BR_{2p}
$1/2^+$	1.270(20)	376(70)	-	-
$5/2^+$	2.794(16)	300(16)	-	-
$1/2^-$	**4.88(14)**	**23(10)**	-	-
$5/2^-$	**5.91(14)**	**2(1)**	**0.03(2)**	**1.5(2) %**
$3/2^-$	**6.29(14)**	**40(10)**	**0.3(1)**	**0.7(1) %**
$5/2^+$	6.67(20)	27(20)	0.05(5)	0.2(2) %
$3/2^+$	6.94(30)	1000(500)	-	-

Table 3.2: Summary of the R-Matrix fit obtained by simultaneously fitting both results from the resonant elastic scattering reaction (section 2.3.1) and the two-proton emission ($E_{CM} = E_x + S_p$ with $S_p = 1.27$ MeV).

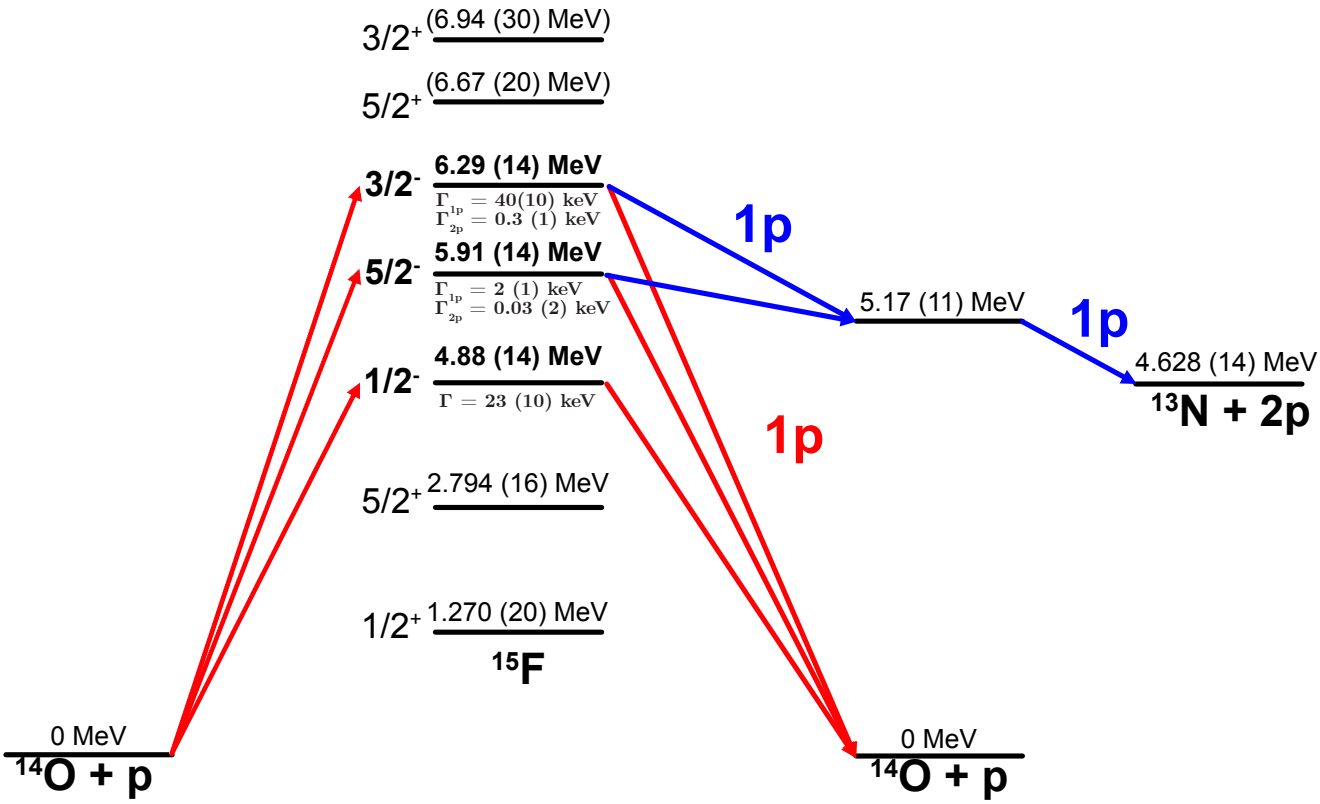

Figure 3.40: *Summary of the ^{15}F states populated and measured experimentally and their decay paths.*

Results from Table 3.2 are consistent with the previously obtained results from section 2.3.1. The fit shows that the branching ratio for the two-proton emission are quite small ($\sim 1\%$). It is also interesting to point out that the addition of a $5/2^+$ and a $3/2^+$ state is required to reproduce the experimental results (similarly to what was done in section 2.3.1).

3.3.3 Gamma analysis

A test case, the double excitation of ^{14}O and ^{12}C

Before studying unbound gamma transitions in ^{15}F the triple coincidence between MUGAST, VAMOS and AGATA had to be tested. A good test case is the double excitation of ^{14}O and ^{12}C. This reaction can be described as follow:

$$^{14}O +^{12} C \rightarrow^{14} O^* +^{12} C^* \rightarrow^{13} N + p +^{12} C + \gamma$$

By detecting a ^{13}N in VAMOS, a proton in MUST2 and a γ in AGATA, a peak at E_γ = 4439.82(21) keV [Kel17] corresponding to the deexcitation of ^{12}C first excited state should be observed in the gamma spectrum. Protons were selected both by ΔE-E (Fig. 3.23a) and by time of flight identification (Fig. 3.23b) and only events where a single proton was detected were considered. The ^{13}N ions were selected using the M/Q identification of section 3.3.2 (Fig. 3.25a). As both the VAMOS and AGATA acquisition were triggerless, it was possible to choose a time window to remove most of the background that could results from random coincidences in the gamma spectrum (Fig. 3.41) and select only the events in coincidence (prompt events).

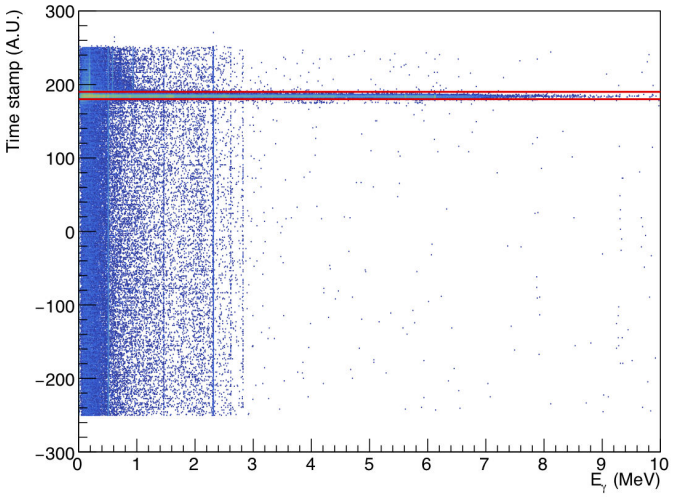

Figure 3.41: *Time stamp difference between AGATA and VAMOS vs gamma energy, the visible line corresponds to the selected prompt events.*

Applying those selections, Fig. 3.42 is obtained, where a peak is clearly visible at 4400(10) keV in relatively good agreement with the value of E_γ = 4439.82(12) found in the literature, the energy is slightly different due to the doppler effect which is not

corrected in this spectra. It proves that the triple coincidence is working and that the detection of high energy gamma is possible.

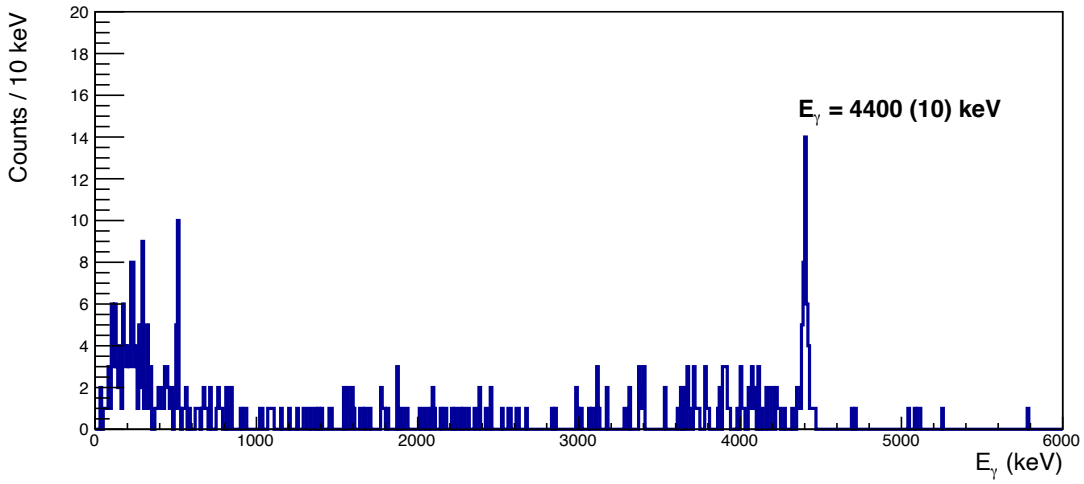

Figure 3.42: *Gamma spectrum obtained for the double excitation of* ^{14}O *and* ^{12}C

The case of ^{15}F

The narrow states of ^{15}F measured in this work might emit gamma rays. The gamma transition (E_γ ~3.5 MeV) between the $1/2^-$ and $1/2^+$ ground state of ^{15}F predicted in Ref. [Gra16] is an E1 transition of a proton in the 1s1/2 shell to the 0p1/2 shell. Similarly to the transition observed in ^{11}Be [Mil83; End93], it is expected to be very strong, because the transition involves the same spins $1/2^- \rightarrow 1/2^+$. To study this transition it was decided to measure the following reaction:

$$^{14}O + p \rightarrow^{15} F^* \rightarrow^{15} F_{g.s.} + \gamma \rightarrow^{14} O + p + \gamma$$

Gamma transitions between unbound states have rarely been observed and the cross-section for these reactions are expected to be very small. As a consequence, to observe such gamma transition the best compromise between detection efficiency and background to noise ratio had to be found. Considering that the efficiency of the gamma detector is going to be the lowest, it was interesting to first look at the experimental data only using VAMOS and MUST2. Indeed, AGATA detection efficiency for high energy gamma was estimated by AGATA's collaboration (Fig. 3.43), and was calculated using the efficiency obtained from a GEANT4 simulation scaled on the measured efficiency from an Europium source (Table 3.1). For a gamma with an energy of 3.5 MeV, an efficiency of

$\epsilon_{AGATA} = 4(2)$ % was obtained.

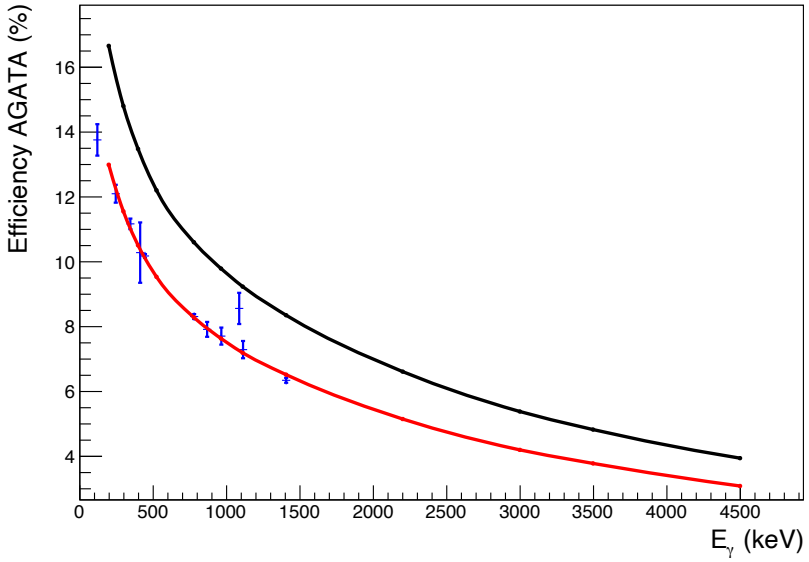

Figure 3.43: *Efficiency of AGATA (in red) estimated by scaling a GEANT4 simulation (in black) to match the measured efficiency obtained with a ^{152}Eu source (in blue).*

Protons were selected both by ΔE-E (Fig. 3.23a) and by time of flight identification (Fig. 3.23b) and only events where a single proton was detected were considered. Contrary to what was observed for the detection of ^{13}N ions in VAMOS it was not possible to use only a selection in M/Q as it was not selective enough. Indeed, $^{14}O^{7+}$ and $^{12}C^{6+}$ ions have the same M/Q = 2 (Fig. 3.25a). The standard method used to select all ^{14}O ions charged states would be to use the deduced M or Q, but as discussed in section 3.3.2, selections requiring M and Q implies the use of multiple ionization chambers which showed poor efficiencies during the experiment. We propose to use the velocity obtained by combining information from the MWPPAC and the drift chambers (Fig. 3.12) as a function of the energy deposited in the first ionization chamber only (see Fig. 3.44a). This selection was proven to be sufficient (Fig. 3.44b) to select the different charged states of ^{14}O while removing the $^{12}C^{6+}$ ions without reducing significantly the statistics.

Figure 3.45a shows the kinematics obtained after applying those conditions, the elastically scattered protons are clearly visible as well as events below the elastic scattering region. The energy and angle of those events seem consistent with the simulation of the gamma transition from section 1.3.4. To verify if those events are just background events or real events the thin target (target n° 5) designed to ensure no direct population of the

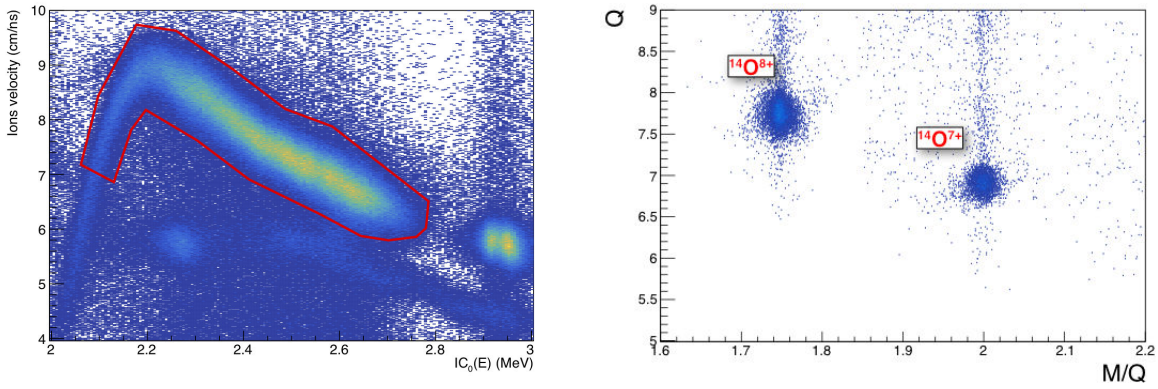

(a) (b)

Figure 3.44: *(a): Ions velocity as a function of the energy lost in the first IC with the selected events in red. Only part of the tail was selected to avoid contamination from other ions. (b): M/Q vs Q for events remaining after applying the red selections of the spectrum on the left.*

$1/2^-$ state was used. With this target in the same conditions, Fig. 3.45b was obtained. Similarly to what is obtained with the thick target, many events are visible under the elastic scattering reaction. It is worth mentioning that the number of events measured with the thin target was half of the one taken with the thick target. The line starting from 3 MeV at 20° to 5 MeV at 50°, more visible with the thick target, is spurious (it is also observed by simulating the elastic scattering reaction), it corresponds to "punch-through" events. They are events who had enough energy to cross the first detection layer of MUST2 (DSSSD), but for which no energy was registered in the second layer (CsI). These background events mimic the expected $^{14}O + p \rightarrow^{15} F^* \rightarrow^{15} F_{g.s.} + \gamma \rightarrow^{14} O + p + \gamma$ events.

The fact that, using the thin target, there are still events consistent with the one expected after a gamma transition shows that, even after applying all the necessary conditions, a background still remains. Then, to indisputably prove the existence of the gamma transition in ^{15}F, triple coincidences is required. It consisted of the observation of a single proton in MUGAST's front detectors, an ^{14}O in VAMOS and a gamma in AGATA. Only events below the elastic scattering region in Fig. 3.45a were selected to limit random coincidences with the elastic scattering reaction and as for the measurement of the double excitation only gamma prompt events were considered (Fig. 3.41). Once those conditions were applied, Fig. 3.46 was obtained. From the $1/2^-$ gamma transition, a gamma with an energy of: $E_\gamma = 3.5 \pm 0.5$ MeV is expected. The 500 keV range is

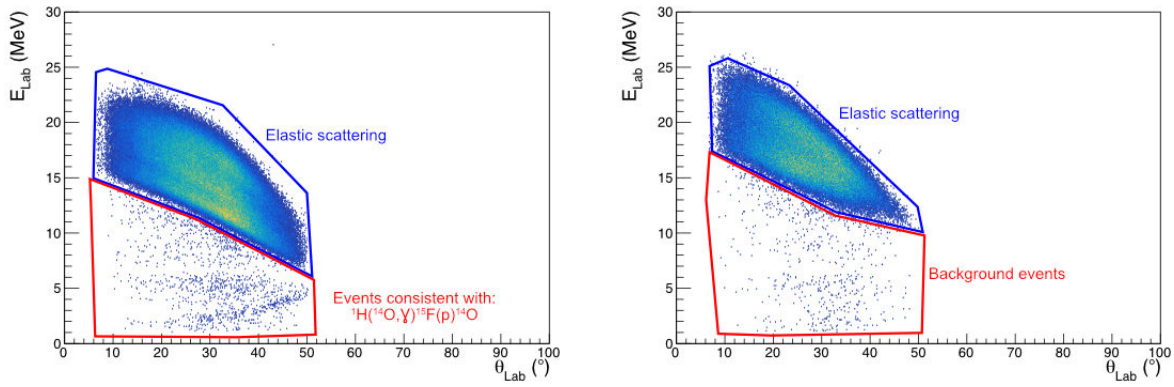

(a) (b)

Figure 3.45: *(a) Measured proton energy as a function of their measured angle in the laboratory, using the thick target (target n° 2). (b) Measured proton energy as a function of their measured angle in the laboratory, using the thin target (target n° 5). It corresponds to the background measurement.*

explained by the width of both states, especially the one of the ground state ($\Gamma_{1/2^+} \sim 500$ keV), meaning this transition could span an energy range of the order of 1 MeV. Looking at Fig. 3.46, there are no clear accumulation of events around those energies.

An interesting and expected feature of this gamma transition is that if the energy spectra of all emitted particles are expected to be broad, due to the width of the states, the sum of their energy in the center of mass should result in the apparition of a narrow peak with a CM energy equal to the one of the decaying state, namely the $1/2^-$ state. After correcting the energy lost by the charged particles inside the target, the CM energy can be computed. Figure 3.47 shows the CM energy as a function of the gamma energy. No event are compatible with the expected gamma transition, with a gamma energy of 3.5 $\pm$ 0.5 MeV and a CM energy equal to 4.8 $\pm$ 0.250 MeV The 500 keV intervals was chosen because the gamma energy is expected to have a width of the order of 1 MeV and considering that the resolution of AGATA is negligible compared to the width of the gamma peak. The 250 keV interval for the CM energy is chosen broad on purpose to account for the energy resolution of the charged particles detectors. Their resolutions were evaluated using the GEANT4 simulation from the previous section compared to the experimental data. A resolution of $\sigma_{M2} = 0.15(2)$ MeV and $\sigma_{VAMOS} = 1.0(5)$ MeV in the lab were obtained which translates to a resolution of $\sigma^{CM}_{total} = 0.25(1)$ MeV

Knowing the total number of incoming beam particles as well as the target thickness

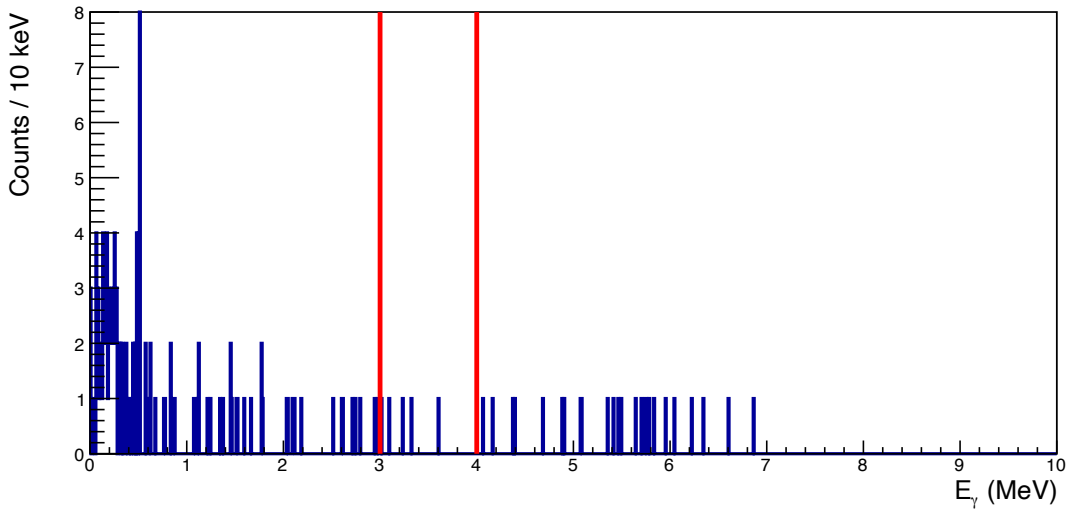

Figure 3.46: *Gamma energy spectrum obtained after applying all the necessary conditions. No peak or accumulation of events is visible in the expected energy range.*

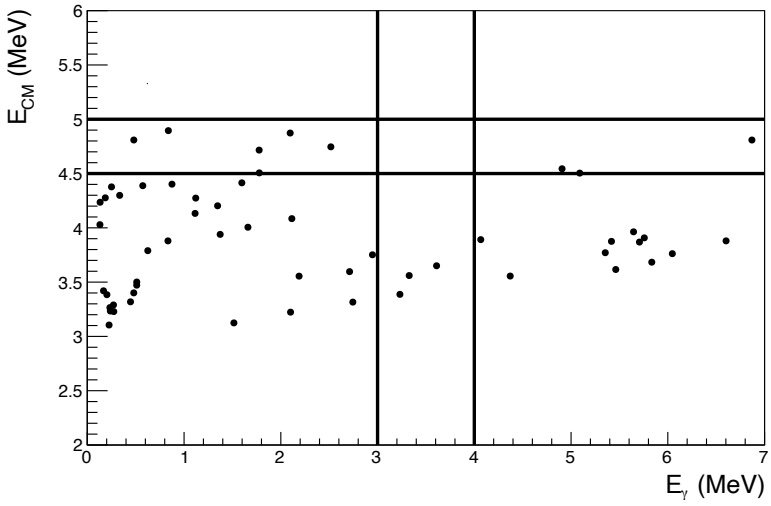

Figure 3.47: *Center-of-mass energy as a function of the gamma energy. In black all events remaining after applying all the relevant conditions. The black lines correspond to the area where events consistent with a 1/2$^-$ state with Ecm = 4.5 ± 0.250 MeV and a gamma of 3.5 ± 0.5 MeV were expected.*

required to form the compound nucleus of ^{15}F in its second excited state (similarly to what was used for the two-proton emission Fig. 3.38b) and, by estimating the detection efficiency of the three detectors required to detect such event, it is possible to give a limit for the cross-section ^{1}H(^{14}O,γ)^{15}F(p)^{14}O. The detection efficiency was estimated using a GEANT4 simulation for MUST2 which showed that the detectors covered 91(2) % of the expected angular distribution. Taking into account MUST2 efficiency (Fig. 3.36a), $\epsilon_{MUST2} = 59(2)$ % was found. For VAMOS the efficiency was estimated to be similar to the one obtained for the ^{13}N and ^{14}O detection with a total efficiency of: $\epsilon_{VAMOS} = 30(5)$ %. and for AGATA the efficiency of $\epsilon_{AGATA} = 4(2)$ % was used. Then, a limit of $\sigma_\gamma < 73(39)$ μb is obtained, it corresponds to a partial width $\Gamma_\gamma < 4.4(1.5)$ eV and thus a limit branching ratio for the gamma of: BR $< \Gamma_\gamma/\Gamma_{tot} < 4.4$ eV / 23 keV $< 0.019(10)$ %.

3.4 Conclusion

In this chapter, the decay channels of the odd-parity states of ^{15}F were studied using the new detector array MUGAST coupled to the VAMOS spectrometer and AGATA detector. The $3/2^-$ state already measured in the first experiment was confirmed, both by studying the resonant elastic scattering reaction, and by measuring its two-proton emission which was found to be 100% sequential. The assumption from the first experiment that a $5/2^-$ exists in ^{15}F was reinforced by studying the two-proton excitation function and finally confirmed by looking at the correlations between the fragments and the protons, its two-proton emission was also found to be 100% sequential. The possible gamma transition between ^{15}F $1/2^-$ second excited state and its $1/2^+$ ground state was studied, but no event consistent with this transition was observed. For this reason only a limit for the cross-section of the reaction ^{14}O(p,(γ))^{15}F(p)^{14}O was obtained: $\sigma_\gamma < 73(39)$ μb corresponding to a BR for the gamma transition of: BR $< 0.019(10)$ %.

4 Interpretations

Contents

4.1 Introduction

The measurement of the energy and width of the negative parity states in ^{15}F answers some of the questions discussed in the introduction of this thesis (chapter 1) but it also gives rise to multiple new questions on their structure and decay.

The first part of the chapter will focus on understanding the structure of these states using shell model (SM) calculations. The level scheme of ^{15}F and the one of its mirror nucleus ^{15}C will be compared and the spin-orbit interaction between analog states will be discussed. The SM prediction and the experimental results will be compared and the dominant SM configurations will be presented. A comparison between the structure of ^{15}C and ^{15}F states will be made and the mirror symmetry breaking for the $3/2^-$ state in ^{15}F and ^{15}C will be discussed. The experimental and theoretical spectroscopic factors will be compared.

In the second part of the chapter, gamma transitions between unbound states will be discussed and clues on what makes a good candidate to study gamma transitions between unbound states will be discussed.

4.2 ^{15}F structure

The measurement of two new narrow states, namely the $5/2^-$ and $3/2^-$ states, more than 5 MeV above the one proton emission threshold and well above the Coulomb and centrifugal barrier is not what is naively expected, as in most cases states tend to get broader with increasing excitation energy. What is noticible is the width of the $3/2^-$ state. Indeed, looking at ^{15}F mirror nucleus ^{15}C, the width of the mirror $3/2^-$ state is more than 4 times broader than the one of ^{15}F measured in this work ($\Gamma_{3/2^-}(^{15}C) = 176(15)$ keV [For11]).

Fortune and Sherr challenged the results of Canton et al. for several reasons including the width of the $3/2^-$ state. While both papers from Canton et al [Can06] and Fortune and Sherr [For07] predicted the first two negative parity states of ^{15}F to be narrow, they disagreed on the width of the $3/2^-$ state. Canton et al predicted the $3/2^-$ state to have a width of 40 keV when Fortune and Sherr predicted a width an order of magnitude larger (300 keV) with the argument that it was *"very difficult to understand how the width in ^{15}F could be less than in ^{15}C"* [For07]. Those papers also disagreed on the energy of those states with energy predicted by Fortune and Sherr $\sim$ 1 MeV lower than the one of Canton et al. Experimental results seem to fall in between those two theoretical predictions (Fig. 4.1). The negative-parity states were all measured with width smaller than 40

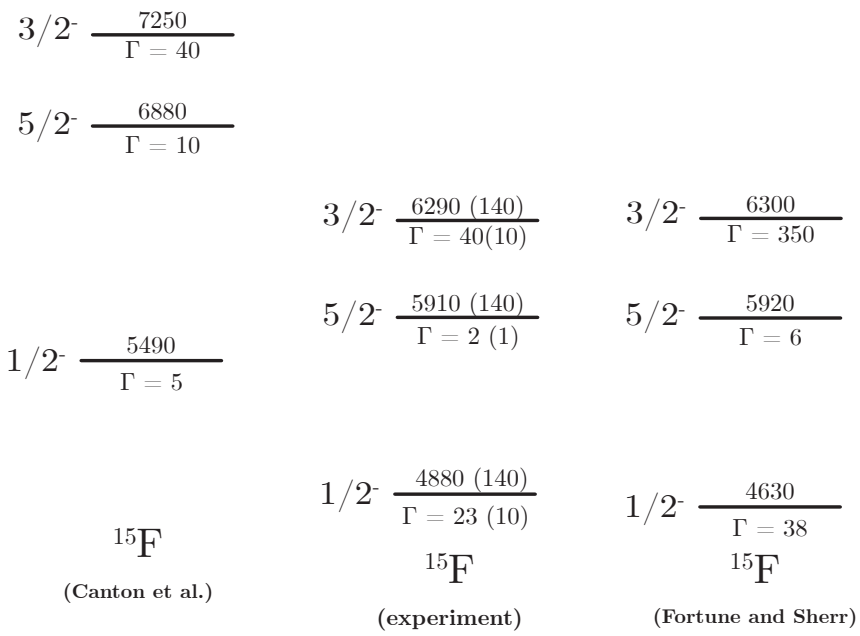

Figure 4.1: *Comparison of the experimental level schemes obtained in this work (center) to the one of Canton et al. [Can06] (on the left) and to the one of Fortune and Sherr [For07] (on the right).*

keV, as predicted by Canton et al. [Can06], but with a good agreement with the energies and widths predicted by Fortune and Sherr [For07], except for the width of the $3/2^-$ state.

Understanding the structure of the odd-parity states, and especially the one of the $3/2^-$ state might explain why its width is much narrower than the one measured in ^{15}C. Moreover, none of the two theoretical studies have taken into account the fact that all states can also emit 2 protons. The existence of nearby decay channels might impact the widths of the states. The structure of the negative-parity states is also of interest in discussing the effect of coupling to the continuum on the structure of nuclei. For example taking the case of ^{8}Be, its ground state is narrow due to its close proximity to the 2α emission threshold and while its two following excited states keep the 2α clustered structure of the ground state, they have a much broader width. On the other hand, the opposite is observed in ^{15}F, where the $1/2^-$ state close to the two-proton emission threshold is narrow and the following two excited states with probably a very similar structure have either much smaller width ($5/2^-$) or comparable one ($3/2^-$).

4.2.1 Comparison to the mirror nucleus ^{15}C

As discussed in section 1.1.2, due to the charge independence and charge symmetry of the nuclear force it is expected for mirror nuclei to have similar level scheme. Experimentally it is not always the case, especially for mirror pair of bound and unbound nuclei, where a shift in energy, called the Thomas-Ehrman shifts (section 1.1.2), can be observed.

In the case of ^{15}F and ^{15}C, the ground state and first excited state of ^{15}F are unbound, while the equivalent ones in ^{15}C are bound. Comparing the ground state of ^{15}F and ^{15}C, a large Thomas-Ehrman shift of 1.27 MeV was observed [Gra09], and attributed to the fact that ^{15}F ground state is understood as a $^{14}O_{g.s.}$ core plus an unbound proton in the 1s1/2 shell [Gra16], thus with no centrifugal barrier. Concerning the first excited state, a large Thomas-Ehrman shift was also calculated [Gra09], but this shift was much smaller due to the presence of the centrifugal barrier.

Comparing the newly measured negative-parity states in ^{15}F with the mirror states in ^{15}C, all three negative parity states in ^{15}F are shifted by $\sim$ 400 keV compared to the analog states in ^{15}C. It is explained because both the negative-parity states of ^{15}F and ^{15}C are unbound, which was not the case while comparing the positive-parity states. As a consequence, the Thomas-Ehrman shifts are expected to be much smaller.

4.2.2 Spin-orbit coupling in the continuum

In the early days of nuclear structure one of the main theoretical challenges was the reproduction of the experimentally observed magic numbers. They were finally reproduced using the shell model with the addition of the spin-orbit (SO) interaction. One of the consequences of this interaction is the splitting of the single-particle orbitals. The strength of the interaction will then play an obvious role on the ordering and the energy of those orbitals. It is then interesting to measure the isospin dependence of this interaction by looking at ^{15}F and its mirror, ^{15}C.

Here the orbital of interest is the l = 2 single-particle orbital which splits in the "d3/2" and the "d5/2" orbitals. The energy of the $3/2^+$ was not directly measured experimentally, but its energy was estimated from the R-Matrix fit of the negative-parity states: $E_r(3/2^+)$ = 5670 (300) keV, while on the other hand, the $5/2^+$ state was measured in previous experiments [Gra16] $E_r(5/2^+)$ = 1524 (16) keV. Calculating the energy difference between the two we obtain:

$$\Delta E(^{15}F) = E_r(3/2^+) - E_r(5/2^+) = 4146\ (300)\ keV \tag{4.1}$$

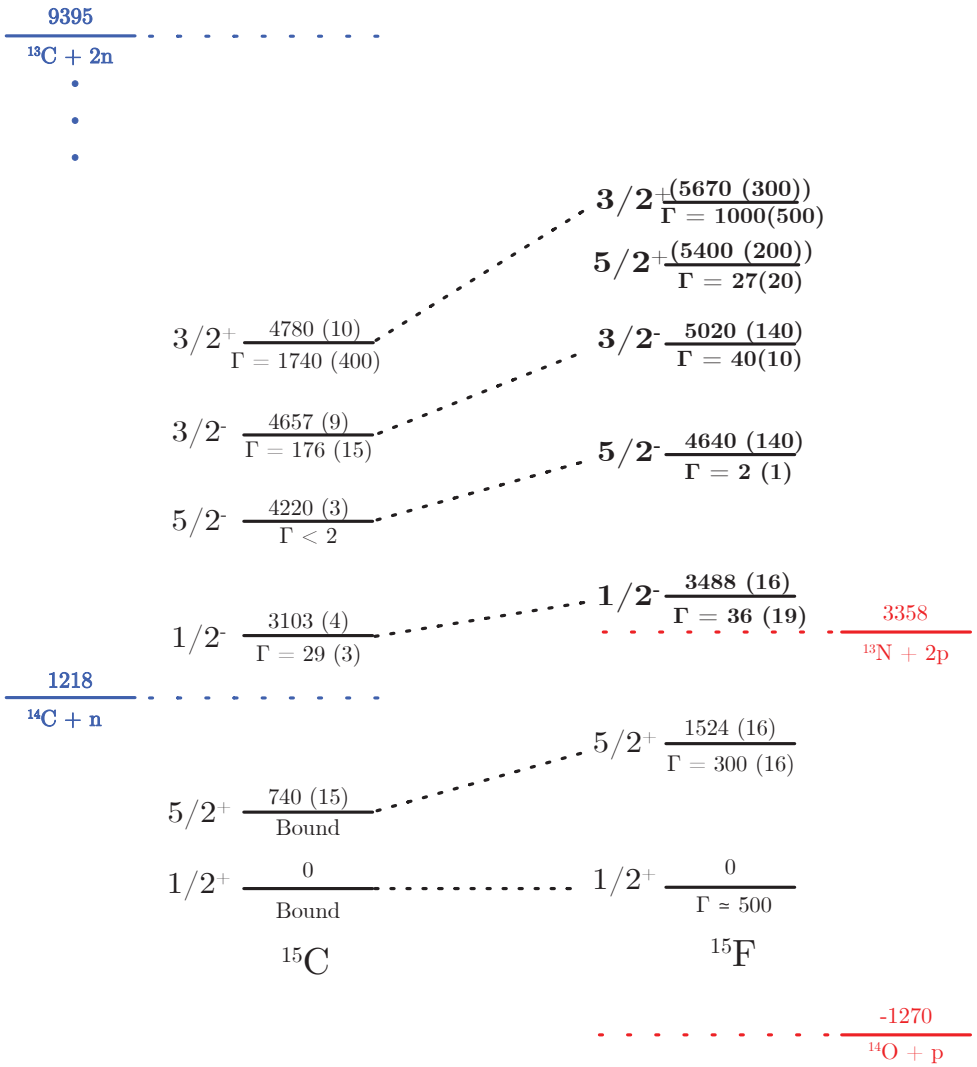

Figure 4.2: *Level scheme of ^{15}C compared to the one of ^{15}F. Energy and width are given in keV. In blue and red are the neutron and proton emission thresholds, respectively. The level sequence of ^{15}C and ^{15}F are similar but energy shifts are visible. As it can be observed, the measured width of the 3/2$^-$ state is unexpectedly narrow in ^{15}F compared to ^{15}C. The levels in boldface corresponds to the one measured or estimated in this work.*

Doing the same for the analog states of ^{15}C: the $3/2^+$ state with $E_r(3/2^+) = 4780(10)$ keV and the $5/2^+$ with $E_r(5/2^+) = 740(15)$ we obtain:

$$\Delta E(^{15}C) = E_r(3/2^+) - E_r(5/2^+) = 4040\ (18)\ keV \tag{4.2}$$

As it can be observed, an excellent agreement between the two values is obtained. Then we do not find, in this work, evidence that the spin-orbit interaction is isospin dependent.

4.2.3 Shell model configuration

To study the structure of ^{15}F negative-parity states, the level scheme can be obtained in the shell model (SM) with the help of the *nushellX* code [Bro14]. Shell model calculations presented in this work were performed considering the psd model-space which allows the population of the 0p3/2, 0p1/2, 1s1/2, 0d5/2 and 0d3/2 shells and uses the *psdmk* interaction based on the Cohen-Kurath (CK) [Coh65] interaction for the 0p-shell configurations, the Millener-Kurath (MK) [Mil75] interaction for the particle-hole interaction between the p-shell and the sd-shell and the G-Matrix from Kuo [Kuo94] for the two-body matrix elements of sd-shell configurations. From this SM calculation, Fig. 4.3 was obtained.

In Fig. 4.3, noteworthy differences between the SM calculation and the experimental results can be observed. First of all, the sequence of excited states is slightly different. Indeed, the SM predicts a $3/2^+$ state between the $1/2^-$ and $5/2^-$ states. Looking at the mirror nucleus ^{15}C, and the theoretical prediction of Canton et al. [Can06] a $3/2^+$ state is expected in ^{15}F but at much higher energy, which is consistent with our experimental results where the addition of both a $5/2^+$ and $3/2^+$ state at higher energy were required in the R-Matrix fit (section 2.3.1 and section 3.3.2) to better reproduce the experimental data. The $1/2^-$ state energy is close to the one calculated by the SM, but the energy of all other negative-parity states seem to disagree with the SM and have energy $\sim$ 1 MeV lower than in the SM calculation. This is similar to what was observed comparing the experimental results to Canton et al. calculations [Can06].

The shell model also informs us on the main single-particle proton shells configurations of ^{15}F states. Each state is a combination of different configurations. Here, only the configurations representing more than 10 % of the total state are presented, the results were obtained using the *nushellX* code (Table 4.1):

- **$1/2^+$(g.s.)**: 82 % $^{14}O_{g.s.}$ core and a proton in the 1s1/2 (Fig. 4.4). This results are in agreement with Ref. [Gra16].
- **$5/2^+$**: 84 % $^{14}O_{g.s.}$ core and a proton in the 1d5/2 (Fig. 4.4), in agreement with Ref. [Gra16].
- **$1/2^-$**: 30 % $^{13}N_{g.s.}$ core with two protons in the 1s1/2 + 38 % $^{13}N_{g.s.}$ core with two protons in the 1d5/2 (Fig. 4.5). These results agree with the prediction of Canton

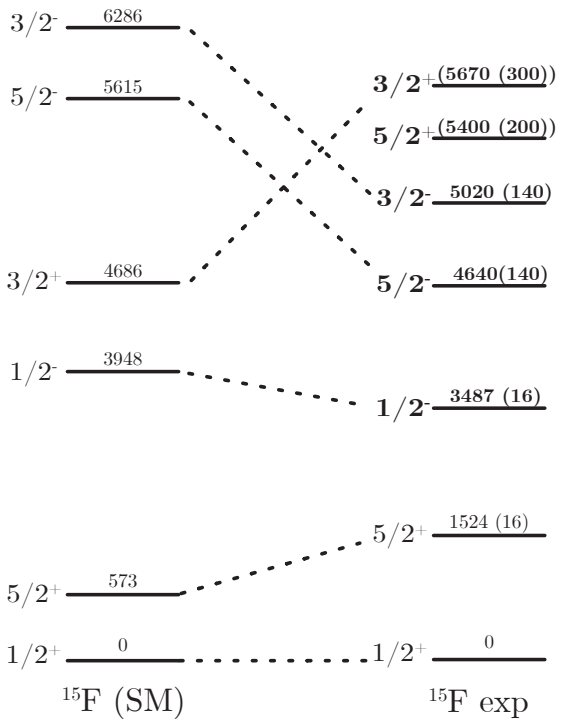

Figure 4.3: *Comparison between the SM level scheme and the experimental one, the levels in boldface corresponds to the one measured or estimated in this work. There are large differences between the two, especially concerning the prediction of a 3/2$^+$ state, which was not observed experimentally nor expected by comparison to the mirror nuclei (Fig. 4.2). The 5/2$^+$ and 3/2$^+$ states energies are written in parenthesis as they were included in the R-Matrix fit (Table 3.2) but were not directly measured.*

et al. [Can06] and Fortune and Sherr [For07; For11] who predicts that the three negative-parity states of ^{15}F should have the SM configuration $^{13}\mathrm{N}_{g.s.}\times(\mathrm{sd})^2_{J=0,2}$. This is also consistent with the structure of the mirror nucleus negative-parity states suggested by ^{13}C(t,p) reaction [For11], interpreted as a $^{13}\mathrm{C}_{gs}\times(\mathrm{sd})^2_{J=0,2}$.

- **5/2$^-$**: 38 % $^{13}\mathrm{N}_{g.s.}$ core with one proton in the 1s1/2 and a second proton in the 0d5/2 + 30 % a $^{13}\mathrm{N}_{g.s.}$ core with two protons in the 1d5/2 (Fig. 4.6). As for the 1/2$^-$ state, this agrees with the prediction from Canton et al. and Fortune and Sherr as well as with the structure of the mirror nucleus.

- **3/2$^-$**: The mixing of mainly three configurations is obtained (Fig. 4.7). Two already foreseen in Canton et al. and Fortune and Sherr. 18 % $^{13}\mathrm{N}_{g.s.}$ core with a proton in

the 1s1/2 and a second proton in the 0d5/2 + 27 % $^{13}N_{g.s.}$ core with two protons in the 0d5/2. As well as a third configuration not theoretically predicted before: 21 % with a hole in the 0p3/2 and two protons in the 0d5/2.

J^π	Proton configuration	Repartition (%)
$1/2^+$(g.s.)	$^{14}O_{g.s.} \times (1s1/2)^1$	82
$5/2^+$	$^{14}O_{g.s.} \times (0d5/2)^1$	84
$1/2^-$	$^{13}N_{g.s.} \times (1s1/2)^2$	29
	$^{13}N_{g.s.} \times (0d5/2)^2$	38
$5/2^-$	$^{13}N_{g.s.} \times (0d5/2)^2$	30
	$^{13}N_{g.s.} \times (1s1/2)^1 \times (0d5/2)^1$	38
$3/2^-$	$^{13}N_{g.s.} \times (1s1/2)^1 \times (0d5/2)^1$	18
	$^{13}N_{g.s.} \times (0d5/2)^2$	27
	$(0s1/2)^2 \times (0p3/2)^3 \times (0p1/2)^2 \times (0d5/2)^2$	21

Table 4.1: *Summary of the main shell model configurations obtained for the known states of ^{15}F using the nushellX code.*

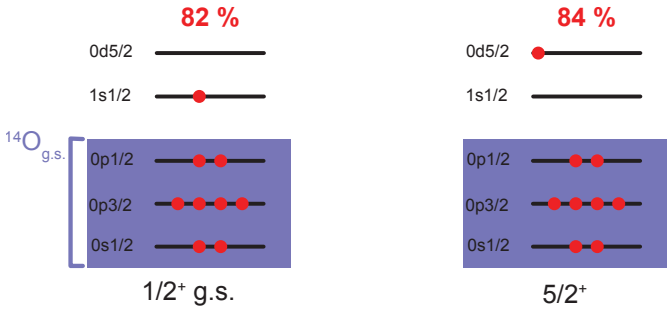

Figure 4.4: *Schematic representation of the dominant SM configurations for the $1/2^+$ (g.s.) and $5/2^+$ states of ^{15}F obtained with the nushellX code and psdmk interaction.*

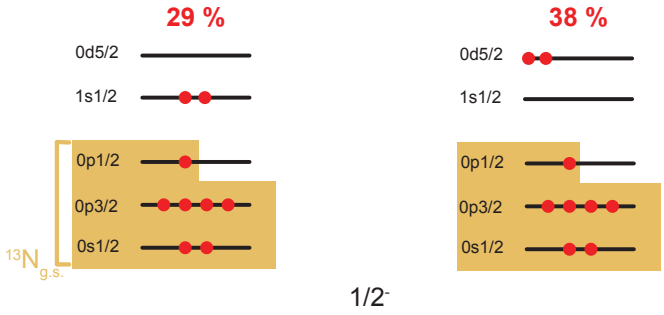

Figure 4.5: *Schematic representation of the dominant SM configurations for the 1/2⁻ state of ^{15}F obtained with the nushellX code and psdmk interaction.*

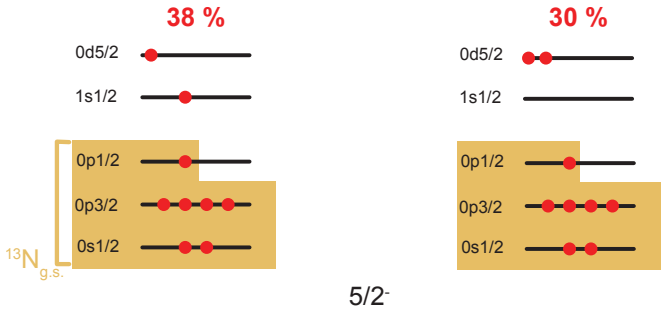

Figure 4.6: *Schematic representation of the dominant SM configurations for the 5/2⁻ state of ^{15}F obtained with the nushellX code and psdmk interaction.*

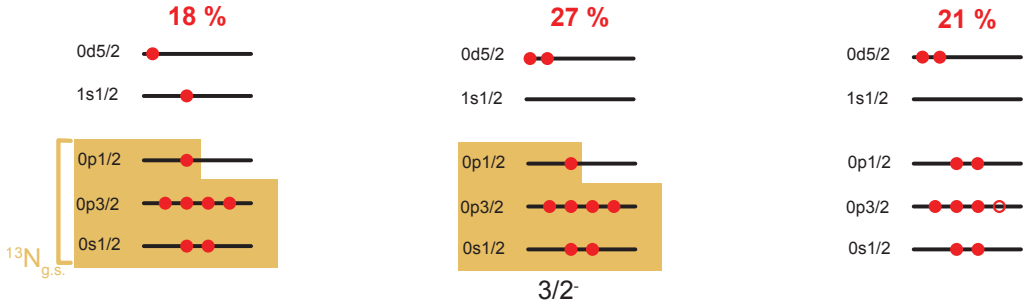

Figure 4.7: *Schematic representation of the dominant SM configurations for the 3/2⁻ state of ^{15}F obtained with the nushellX code and psdmk interaction.*

4.2.4 Discussion on the structure of the $5/2^-$ and $3/2^-$ states

The measured energy and width of the odd-parity states of ^{15}F might be better understood by comparing the ^{15}F level scheme to the one of ^{14}O + p and ^{13}N + 2p (Fig. 4.8). For example, the previously measured $1/2^-$ state is only 130(16) keV above the $^{13}N_{g.s.}$ + 2p (taking into account the measurement from this work and the one from Ref. [Gra16]). Its narrow width might be explained by the mixing of this state with the nearby decay channel ($^{13}N_{g.s.}$ + 2p) and was interpreted as mostly a $^{13}N_{g.s.}$ core plus two protons in the 1s1/2 orbital.

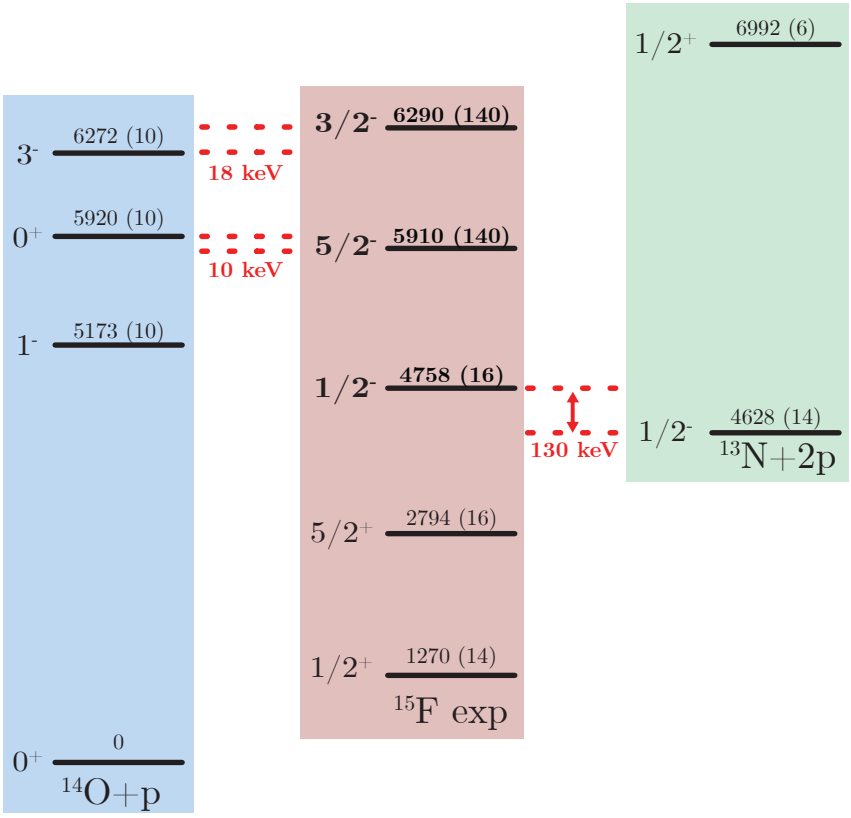

Figure 4.8: *Level scheme of ^{15}F, ^{14}O + p and ^{13}N + 2p. The energy are given in keV relatively to the ^{14}O ground state. In red are written the energy difference between ^{15}F states and the states of its neighbors. The levels in boldface are the one measured or estimated in this work.*

Looking at Fig. 4.8 it is clear that both the $5/2^-$ and $3/2^-$ states have energies that are close to the one of the second 0^+ and the 3^- state in ^{14}O + p respectively (considering

$E_r = E_x + S_p$, with $S_p = 1.27$ MeV).

Doing the same comparison between the $3/2^-$ of ^{15}C with the $^{14}C(3^-)$ + n a symmetry breaking is observed. Indeed, relative to the neutron emission threshold, the $3/2^-$ state of ^{15}C has an energy of $E(3/2^-) = E_x(3/2^-) + S_n = 4657 + 2178 = 5875(10)$ keV. Comparing this value to the 3^- state in ^{14}C: $E_x = 6728.2(13)$ keV, we find that the two states are 853 keV apart compared to the 18 keV difference observed between the $3/2^-$ state of ^{15}F and the 3^- state of ^{14}O + p.

As a consequence, it might be reasonable to assume that similarly to what was observed for the $1/2^-$ state, the width of the $3/2^-$ state is an order of magnitude narrower than its mirror $3/2^-$state in ^{15}C probably due to the mixing of this state with the nearby 3^- state of ^{14}O + p, especially as they are only 18 keV apart. This assumption might be validated looking at the overlap between $^{15}F(3/2^-)$ state and the $^{14}O(3^-)$ state + p.

While we can understand how the structure of $^{15}F(3/2^-)$ might be similar to the one of $^{14}O(3^-)$ state plus a proton (in the 1s1/2 for example) it does not seem trivial to understand how the structure of $^{15}F(5/2^-)$ could be similar to the one of $^{14}O(0_2^+)$ state plus a proton, even though they also have similar energies. Understanding the mixing of ^{15}F states with the nearby states of ^{14}O + p would then require detailed theoretical calculations, such as Shell Model Embedded in the Continuum (SMEC) [Ben99] or Gamow Shell Model (GSM) [Mic02] calculations both of which are beyond the scope of this work.

4.2.5 Theoretical spectroscopic factors

To quantify the overlap between the ^{15}F and ^{14}O states plus a proton, the shell model, with the help of the *nushellX* code, can be used to calculate the spectroscopic factors.

The spectroscopic factors are indicators of the structure of a nuclear state, they are defined as the overlap integral between the final state wave function Ψ_B and the initial wave function Ψ_{A+a}. Spectroscopic factors are a measure of the probability that a given compound state B can be described by a single-particle state A + a:

$$S = | < \Psi_{A+a} | \Psi_B > |^2 \tag{4.3}$$

in the case of ^{15}F, it corresponds to :

$$S = | < \Psi_{^{14}O+p} | \Psi_{^{15}F} > |^2 \tag{4.4}$$

They are often given with the included squared isospin Clebsch-Gordan coefficient to account for the possible isospin difference between the initial and final state:

$$C^2 = | < T_A T_{zA} T_a T_{zA} | T_B T_{zB} > |^2 \tag{4.5}$$

with T_X the total isospin and T_{zX} the isospin projection of system X. To differentiate the theoretical spectroscopic factors from the experimental ones, the theoretical spectroscopic factor will now be written: C^2S_{theory}.

C^2S_{theory} were calculated with *nushellX* for ^{15}F excited states with different states of ^{14}O + p (Table 4.2). It shows that, as previously calculated [Gra16], both the ground state and first excited state of ^{15}F have large overlaps with $^{14}O_{g.s.}$ + p while the $1/2^-$, $5/2^-$ $3/2^-$ states have little overlap with it.

Overlap integral	C^2S_{theory}
$<\Psi_{^{14}O(0^+)_{g.s.}+p}\|\Psi_{^{15}F(1/2^+)_{g.s.}}>$	0.96
$<\Psi_{^{14}O(0^+)_{g.s.}+p}\|\Psi_{^{15}F(5/2^+)}>$	0.89
$<\Psi_{^{14}O(0^+)_{g.s.}+p}\|\Psi_{^{15}F(1/2^-)}>$	0.025
$<\Psi_{^{14}O(0^+)_{g.s.}+p}\|\Psi_{^{15}F(5/2^-)}>$	0.0087*
$<\Psi_{^{14}O(0^+)_{g.s.}+p}\|\Psi_{^{15}F(3/2^-)}>$	0.0011

Table 4.2: *Spectroscopic factors relatives to the $^{14}O(0^+)_{g.s.}$ + p calculated, using the SM code nushellX, for the different known states of ^{15}F. The value for the $5/2^-$ couldn't be obtained with nushellX, it was obtained using Oxbash with the WBT interaction [War92] (Priv. Com. Nadya Smirnova)*

To support or contradict our assumption on the mixing of the $3/2^-$ states with the nearby ^{14}O states, it can be interesting to calculate his spectroscopic factors with the 3^- state of ^{14}O + p. It is important to keep in mind that the shell model might not be able to reproduce the mixing of ^{15}F states with the nearby ^{14}O states. Indeed, the shell model is not able to reproduce the effect of the particle emission thresholds on the structure of nearby states. Similarly it might not be able to account for the mixing of ^{15}F states with the nearby ^{14}O states. This is discussed in Ref. [Oko12; Oko13] where the author says that: *"SM, nucleons occupy bound single particle orbits of an infinite (harmonic oscillator) potential; hence, they are isolated from the environment of scattering states. Since the scattering continuum is not considered, the presence of decay thresholds and exceptional points is neglected. Hence, the essential aspect of the nuclear clustering mechanism is totally absent."* In other words, the SM doesn't take into account the effect of particle emission thresholds on the structure of nearby states. Thus, the results ob-

tained for the overlap of the $3/2^-$ state with the 3^- state should then be used with caution.

Overlap integral	C^2S_{theory}
$<\Psi_{^{14}O(3^-)} + p \vert \Psi_{^{15}F(3/2^-)}>$	0.11
$<\Psi_{^{14}O(1^-)} + p \vert \Psi_{^{15}F(5/2^-)}>$	0.34
$<\Psi_{^{14}O(1^-)} + p \vert \Psi_{^{15}F(3/2^-)}>$	0.24

Table 4.3: *Spectroscopic factors relatives to the relevant ^{14}O excited states + p calculated using the SM code nushellX.*

The calculation of the overlap of the $3/2^-$ state in ^{15}F with ^{14}O(3^-) + p gave a spectroscopic factor of: $C^2S_{theory} = 0.11$ (Table 4.3). This results is much lower than what we could naively expect by simply comparing the level scheme of Fig. 4.8. But it is still an order of magnitude higher than the overlap calculated with $^{14}O_{g.s.}$ + p. For reference, the spectroscopic factor of the $1/2^-$ state to the nearby $^{13}N_{g.s.}$ calculated using the GSM [Gra16] is: $C^2S_{theory} = 0.97$.

Experimentally the decay of both the $5/2^-$ and $3/2^-$ state were observed to be sequential through ^{14}O first excited state (1^-). The relevant spectroscopic factors can be calculated, see Table 4.3. Both states show relatively large overlap to ^{14}O(1^-) + p compared to the one calculated for $^{14}O_{g.s.}$ + p.

4.2.6 Experimental spectroscopic factor

The spectroscopic factors described in the previous section are not physical observable and thus are not accessible experimentally. Still, it is possible to derive an analogous quantity from the experimental data called the dimensionless reduced width (θ^2). C^2S and θ^2 are comparable in the sense that they are both a measure of the probability of a given compound state B to be described by a single-particle state A + a. In this work, θ^2 will be called the experimental spectroscopic factor: C^2S_{exp}.

Definition of the width

Let's consider the radial wave function of the compound system A + a: $R(r)$, The spectroscopic factor, *ie*, the probability to find the nucleus B in the structure A + a can be written in integral form:

$$\int_0^\infty R(r)^2 r^2 dr = \int_0^\infty u^2(r) dr = C^2 S \tag{4.6}$$

To obtain the experimental spectroscopic factor it is necessary to first derive the partial width of a decay channel λ (in this work, λ corresponds to either the decay by one-proton or two-proton emission). It is defined by Lane and Thomas [Lan58b] in their description of the R-Matrix formalism:

$$\Gamma_\lambda(E) = \frac{\hbar^2 s}{\mu} |R(s)^2| P_l(E) \tag{4.7}$$

Where s is the radius of the compound nucleus B, μ the reduced mass of the compound system, $|R(s)|^2$ the probability to find the particle at position r = s = radius of the nucleus and $P_l(E)$ the penetrability function corresponding to the probability for a particle to go through the coulomb + centrifugal barrier with l the azimuthal quantum number (Eq. 4.8). $P_l(E)$ is calculated using the regular (F_c) and irregular (G_c) coulomb functions.

$$P_l(E) = \frac{1}{F_c^2 + G_c^2} \tag{4.8}$$

The width can be rewritten in term of experimental spectroscopic factor [Cla88]:

$$\Gamma_\lambda(E) = \frac{3\hbar^2}{\mu s^2} P_l(E) C^2 S_{exp} \tag{4.9}$$

where C^2S_{exp} corresponds to the experimental spectroscopic factor :

$$C^2 S_{exp} = \frac{s^3}{3} |R(s)|^2 \tag{4.10}$$

The Wigner limit

The Wigner limit [Oli95] corresponds to the limit where $C^2 S^W_{exp} = 1$. Which then translates to:

$$C^2 S^W_{exp} = \frac{s^3}{3} |R_W(s)|^2 = 1 \tag{4.11}$$

And thus Eq. 4.9 becomes :

$$\Gamma_{W\lambda}(E) = \frac{3\hbar^2}{\mu s^2} P_l(E) \tag{4.12}$$

Equation 4.9 can be rewritten in term of $\Gamma_{W\lambda}(E)$:

$$\Gamma_\lambda(E) = C^2 S_{exp} \Gamma_{W\lambda}(E) \tag{4.13}$$

Consequently :

$$C^2 S_{exp} = \frac{\Gamma_\lambda(E)}{\Gamma_{W\lambda}(E)} \tag{4.14}$$

Calculating C^2S_{exp}

From the experimental results obtained in this work, it is possible to compute C^2S_{exp} for two different decay channels, the $^{15}F \rightarrow {}^{14}O_{g.s.} + p$ studied using the resonant elastic scattering reaction (section 2.3.1) and the $^{15}F \rightarrow {}^{14}O(1^-) + p$ obtained in section 3.3.2. The experimental spectroscopic factors were obtained using Eq. 4.14, and the Wigner width from Eq. 4.12 were obtained using the coulomb function from the GSL[1] [Gou09]. Results from these calculations are found in Table 4.4 and Table 4.5.

Single particle channel	l	E_r (MeV)	Γ (keV)	Γ_W (keV)	C^2S_{exp}
$^{15}F(1/2^+_{g.s.}) \rightarrow {}^{14}O_{g.s.} + p$	0	1.270(20)	~ 500	1500	~ 0.33
$^{15}F(5/2^+) \rightarrow {}^{14}O_{g.s.} + p$	2	2.794(16)	300(16)	810	0.37(2)
$^{15}F(1/2^-) \rightarrow {}^{14}O_{g.s.} + p$	1	4.757(16)	23(10)	7400	0.0031(14)
$^{15}F(5/2^-) \rightarrow {}^{14}O_{g.s.} + p$	3	5.91(14)	2(1)	1300	0.0015(8)
$^{15}F(3/2^-) \rightarrow {}^{14}O_{g.s.} + p$	1	6.29(14)	40(10)	10140	0.0039(10)

Table 4.4: *Experimental spectroscopic factors for* $^{15}F \rightarrow {}^{14}O_{g.s.} + p$

Single particle channel	l	E_r - $Ex^{14}O(1^-)$ (MeV)	Γ (keV)	Γ_W (keV)	C^2S_{exp}
$^{15}F(5/2^-) \rightarrow {}^{14}O(1^-) + p$	2	0.74(14)	0.03(2)	0.043	0.70(47)
$^{15}F(3/2^-) \rightarrow {}^{14}O(1^-) + p$	2	1.12(14)	0.3(1)	0.94	0.32(10)

Table 4.5: *Experimental spectroscopic factors for* $^{15}F \rightarrow {}^{14}O(1^-) + p$

A comparison of the trends of the experimental and theoretical spectroscopic factors in Fig. 4.9a shows relatively good agreement between the two, even though the absolute values are different. Both calculations find that the negative parity states are not well reproduced by the structure $^{14}O_{g.s.}$ plus a proton, in agreement with both the predictions of Ref. [Can06] and Ref. [For07]. Concerning the spectroscopic factors obtained for ^{15}F

[1] Gnu Scientific Library

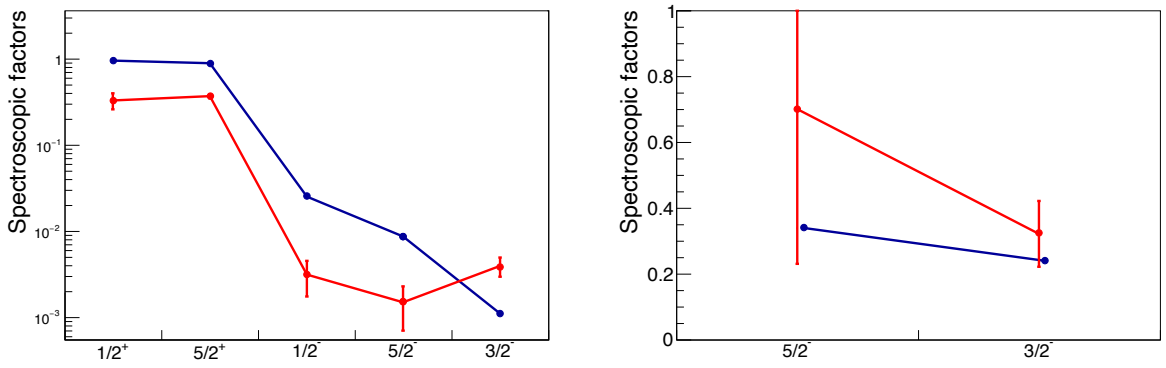

(a) (b)

Figure 4.9: *(a) Comparison between the theoretical spectroscopic factor from Table 4.2 in blue and the experimental one from Table 4.4 in red relative to* $^{14}O_{g.s.}$ *+ p. (b) Comparison between the theoretical spectroscopic factor from Table 4.3 in blue and the experimental one from Table 4.5 in red relative to* $^{14}O(1^-)$ *+ p.*

states with ^{14}O(1^-) + p the SM calculations are within the margin of error of the experimental results. Large overlap with ^{14}O(1^-) + p for the $5/2^-$ and $3/2^-$ are obtained, both in experimental and theoretical spectroscopic factors.

These results on the structure of ^{15}F states are interesting and give a better understanding of the structure of the newly measured negative-parity states, but as explained above, the shell model calculations performed in this work neglect the effect of nearby states and particle emission thresholds on the structure of these states. More realistic calculations should then be performed to take into account the mixing of ^{15}F states with the continuum. Such calculations are beyond the scope of this work, nevertheless, it would be very interesting to use the Gamow shell model (GSM) similarly to what has been done in Ref. [Gra16] to better understand the coupling of the ^{15}F states with the nearby states in ^{14}O + p and ^{13}N + 2p and maybe confirm our interpretation, especially concerning the width of the $3/2^-$ state.

4.3 Gamma transitions in unbound nuclei

As discussed in the introduction (see section 1.1.5), gamma transitions between unbound states have rarely been observed, as their branching ratio are expected to be very small, compared to particle emission. This experiment is no exception as no event consistent with the expected $1/2^- \rightarrow 1/2^+$ transition in ^{15}F was measured. Understanding those transitions is interesting as they could help understanding the structure of cluster states as well as have an impact in determining the reaction rates of certain astrophysical scenarii, especially sites where many proton captures occur, such as X-ray burst for example [Ste07].

As in the past extremely strong E1 transition has been observed in the halo nucleus ^{11}Be [Mil83] between $1/2^-$ and $1/2^+$ state and a similar transition could be expected in ^{15}F involving the same spins but for protons instead of neutrons. This transition was not observed experimentally. In this section the reasons why the transition was not observed will be detailed, and we will try to determine the conditions required to observed such transitions.

4.3.1 Determination of the 1s1/2 → 0p1/2 single particle width

To understand why the gamma transition was not observed in our experiment, it can be interesting to compute the partial width of the gamma decay channel (Γ_γ). It is done using equation 4.15 derived by Blatt and Weisskopf in 1952 [Joh52]:

$$\Gamma_W^{EL}(E_\gamma) = \hbar\lambda = \frac{8\pi(L+1)}{\hbar L[(2L+1)!!]^2}\left(\frac{E_\gamma}{\hbar c}\right)^{2L+1} B(E1) \tag{4.15}$$

In the case of E1 transition, L = 1 and equation 4.15 becomes :

$$\Gamma_W^{E1}(E_\gamma) = \hbar\lambda = \frac{16\pi}{9}\left(\frac{E_\gamma}{\hbar c}\right)^{3} B(E1) \tag{4.16}$$

Where B(E1) corresponds to the reduced transition probability which can be derived as in [Hey94] (page 158):

$$B(El) = \frac{(2J_f+1)(2l+1)}{4\pi} \times \left(\frac{\tilde{e}}{e}\right)^2 \times \begin{pmatrix} J_i & J_f & l \\ 1/2 & -1/2 & 0 \end{pmatrix}^2 \times \langle r^l \rangle^2 \tag{4.17}$$

With $J_i = 1/2$, $J_f = 1/2$ the spin of the initial and final states, l = 1 the angular momentum, $\tilde{e}$ the effective charge (Eq. 4.19) and $\langle r^l \rangle$ the radial integral, we obtain:

$$B(E1) = \frac{6}{4\pi} \times \left(\frac{\tilde{e}}{e}\right)^2 \times \frac{1}{6} \times \langle r \rangle^2 \tag{4.18}$$

In most cases for transitions involving protons, the effective charge is: $\tilde{e} \sim$ e [Hey94] (page 158). But, in Ref. [Suh07] (page 145) it is shown that for E1 transition involving protons $\tilde{e}$ is often much smaller due to spurious contribution from the center of mass motion. In their book, they advise to use the following equation to obtain a more realistic effective charge:

$$\tilde{e} = \frac{N}{A} e = 6/15e = 0.4e \tag{4.19}$$

With N the number of neutrons (N = 6) and A the number of nucleons (A = 15).

The radial integral $\langle r \rangle$ (Eq. 4.20) can then be obtained from the initial and final wave function, respectively corresponding to the wave function of a proton in the 1s1/2 and a proton in the 0p1/2 shells.

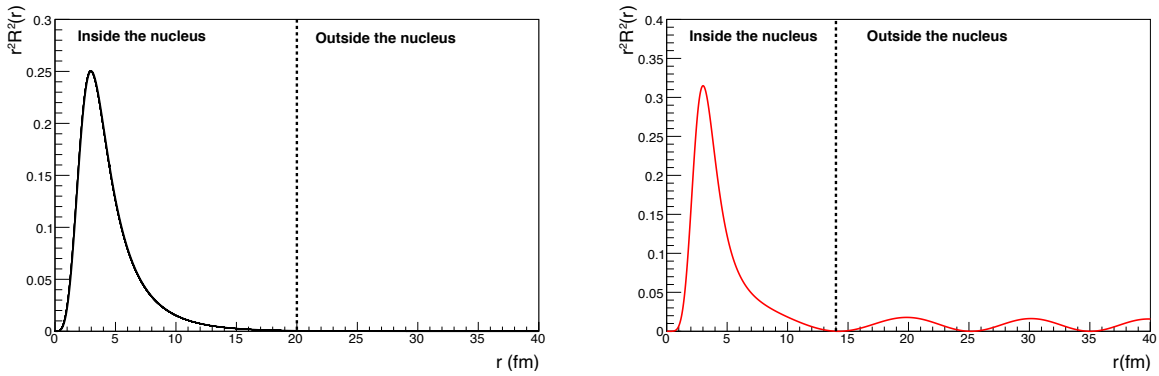

(a) (b)

Figure 4.10: *Different solutions of the Schrodinger equation. (a) The state is bound. (b) The state is unbound and outside the nucleus a plane wave can be recognized.*

Let's call "s" the first minimum of the wave function. Figure 4.10 shows an example of the wave function of a bound proton 4.10a and of an unbound proton 4.10b. For the bound one, the proton is trapped inside the nucleus, as a consequence the wave function will tend to 0 when r tends to infinity, r < s corresponds to the region inside the nucleus. On the other hand for the unbound one, two regions are visible, a first region similar to the bound wave function (r < s) which corresponds to the wave function inside the nucleus, and a second region corresponding to the wave function of the particle outside the nucleus

and which will repeat itself as r tends to infinity. As explained in E. Fermi's course [Fer49], at the time of the decay (t = 0), the nucleon is inside the nucleus, thus the integration will only be performed until r = s. The wave function (ψ_i) is then renormalized in the integration's interval to make sure that $|\psi_i|^2 = 1$ at t = 0 before the proton is emitted with $\psi(\vec{r}) = u(r)/rY_lm(theta, phi)$ and:

$$\langle r \rangle = \int_0^s r u_i(r) u_f(r)\, dr \tag{4.20}$$

The initial state is the $1/2^-$ state of ^{15}F, its structure is interpreted as a ^{13}N core and two protons in the 1s1/2. The wave function of a proton in the 1s1/2 (Fig. 4.11) was obtained assuming that protons in the 1s/2 had a binding energy equal to the energy of the $1/2^-$ state of ^{15}F minus the ground state of ^{13}N split in two between the two protons of the 1s1/2 shell:

$$E_p^{1s1/2} \sim \frac{E_{^{15}F}^{1/2^-} - E_{^{13}N}^{1/2^-_{g.s.}}}{2} = \frac{4.757 - 4.628}{2} = 64.5keV \tag{4.21}$$

The wave function of the proton in the 0p1/2 (Fig. 4.11) was obtained considering that its binding energy was equal to the energy required to put a proton from the 0p1/2 to the 1s1/2 shell. In ^{14}O, the 1^- first excited state with E_x = 5.173 MeV is obtained by promoting a proton from the 0p1/2 to the 1s1/2, thus, taking into account the energy of the ground state of ^{15}F, which is unbound by 1.27 MeV, the estimated binding of a proton in the 0p1/2 is:

$$E_p^{0p1/2} \sim E_{^{15}F}^{1/2^+_{g.s.}} - E_{^{14}O}^{1-} = 1.270 - 5.173 = -3903keV \tag{4.22}$$

Those binding energies show that the 1s1/2 proton is only unbound by a few keV while the proton in the 0p1/2 is in fact tightly bound. Those wave functions were then computed by solving the Schrödinger equation in a Wood-Saxon nuclear potential by the mean of the DWU software based on the code DWUCK4 [Koo93] (Fig. 4.12).

Using the wave function from Fig. 4.12, a value of $\langle r \rangle^2 = 8.3$ fm^2 is obtained. Incorporating this value in Eq. 4.18 gives B(E1) = 0.11 e^{2}fm^2 thus giving a predicted width (Eq. 4.16) of Γ_γ = 3.25 eV.

The estimated branching ratio (BR) for the gamma decay can then be obtained from the width the $1/2^-$ state in ^{15}F obtained in section 2.3: BR = $\frac{\Gamma_\gamma}{\Gamma_{1/2^-}} = \frac{3.25eV}{23keV} = 0.014$ %. This result is close to the experimental limit of BR < 0.019(10) %. The fact that the branching ratio is so small explains why the gamma transition was not observed experimentally. In term of cross-section using the Breit-Wigner formalism, it translates, at the

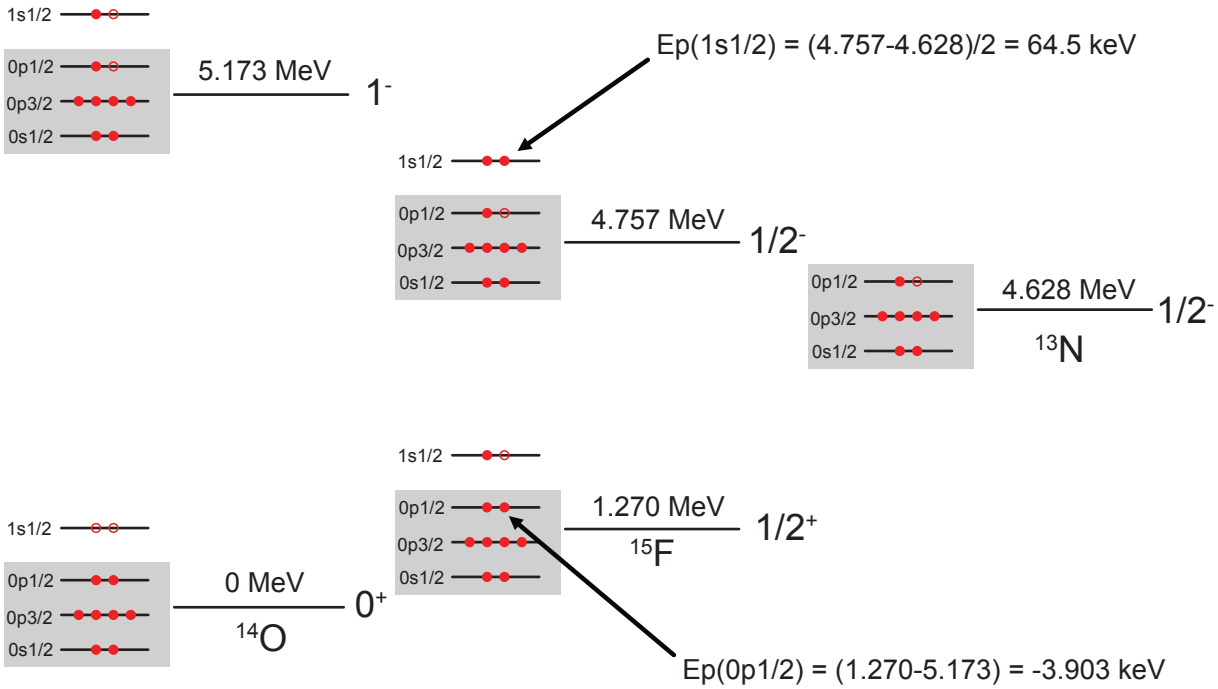

Figure 4.11: *Level scheme of the relevant states used to evaluate the gamma transition probability.*

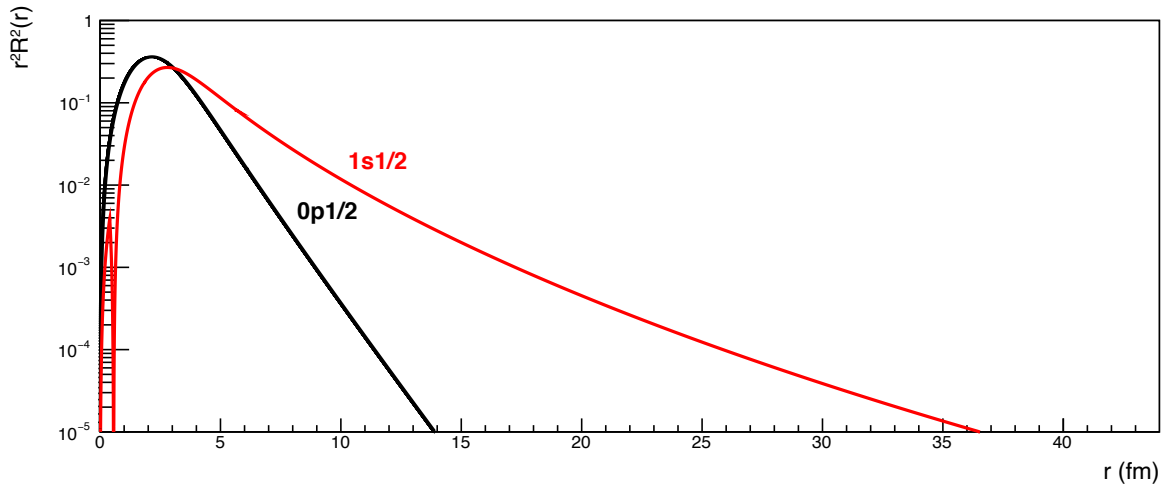

Figure 4.12: *Single-particle wave functions of the 1s1/2 shell in red and the 0p1/2 shell in black.*

resonance, to $\sigma_{BW} \sim 50$ μb, which is also close to the limit obtained experimentally of $\sigma_\gamma < 73(38)$ μb.

4.3.2 Understanding the strength of the E1 transition in ^{11}Be

The gamma transition observed in ^{11}Be is the strongest one of the nuclear chart [End93] with $\tau = 166(15)$ fs [Mil83]. This transition is similar to the one studied in ^{15}F as it concerns the transition of a neutron from the 1s1/2 to the 0p1/2 shell whereas in ^{15}F it is the transition of a proton between the same shells. One difference between ^{11}Be and ^{15}F is the spread of the 1s1/2 and 0p1/2 wave functions. It is due mostly to the absence of the coulomb barrier and to the neutron halo structure of ^{11}Be, interpreted to be a ^{10}Be with a loosely bound neutron [Mil83] both in its ground state ($1/2^+$) and, even more strongly, in its first excited state ($1/2^-$) whose energy is 320 keV, only 181 keV below the neutron emission threshold ($S_n = 501$ keV).

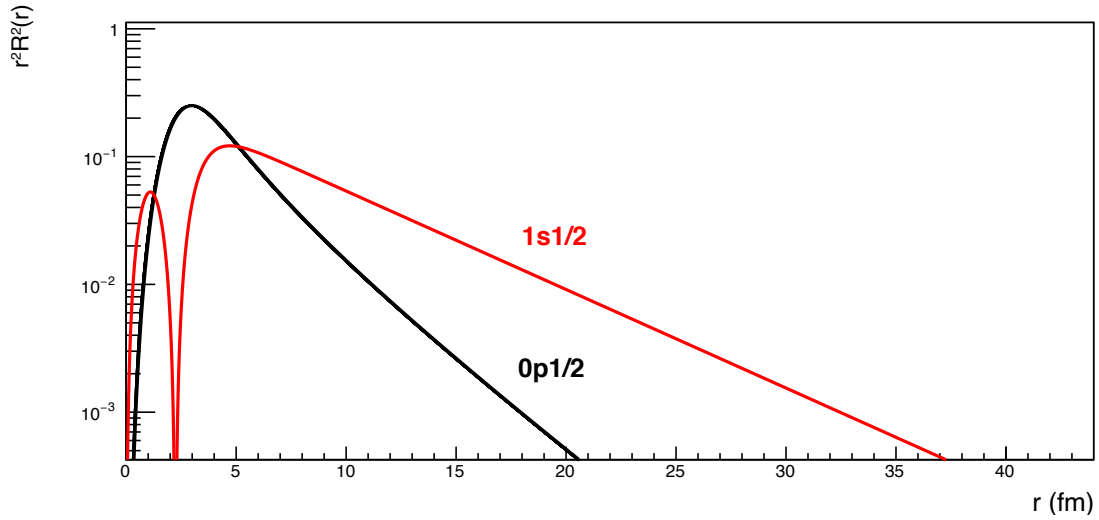

Figure 4.13: *Single particle wave functions of the 1s1/2 shell in red and the 0p1/2 shell in black calculated in the case of* ^{11}*Be.*

The wave functions of both configurations, a neutron in the 1s1/2 and a neutron in the 0p1/2 can be obtained in the same way as for ^{15}F by solving the Shrödinger equation in a Wood-Saxon potential using the DWU software and considering that ^{11}Be = ^{10}Be$_{g.s.}$ core + n (Fig. 4.13). The binding energy of the 1s1/2 neutron was estimated to be equal to :

$$E_n^{1s1/2} \sim E_x(1/2^-) - S_n = 320 - 501 = -181 \ keV. \tag{4.23}$$

For the ground state neutron in the 0p1/2 the binding energy is simply equal to the binding energy of ^{11}Be :

$$E_n^{0p1/2} = -S_n = -501 \ keV. \tag{4.24}$$

The radial integral $\langle r \rangle$ obtained for ^{11}Be is then : $\langle r \rangle^2 = 23.8$ fm^2 which is ~ 3 times the one of obtained for ^{15}F ($\langle r \rangle^2 = 8.3$ fm^2) .

To compare similar transitions, and to remove the energy dependence introduced in the calculation of the width, the strength of electromagnetic transitions are often given in Weisskopf unit (W.u.). They are obtained by dividing the partial width of the gamma decay channel and the estimated Weisskopf width (in eV), which is for E1 transition :

$$\Gamma_W^{E1} = 6.8 \times 10^{-2} \times A^{2/3} \times E_\gamma^3 \tag{4.25}$$

With A the number of nucleons, and E_γ the energy of the gamma emitted in the transition in MeV. For ^{11}Be, $\tau = 166(15)$ fs, which corresponds to a width :

$$\Gamma_\gamma(^{11}Be) = \frac{\hbar}{\tau} = 0.004 \ eV \tag{4.26}$$

Considering that the Weisskopf estimate is $\Gamma_W^{E1}(^{11}Be) = 0.011$, the reduced transition probability for the 1s1/2 $\rightarrow$ 0p1/2 transition in ^{11}Be is:

$$B(E1) = \Gamma_\gamma(^{11}Be)/\Gamma_W^{E1}(^{11}Be) = 0.36 \ W.u. \tag{4.27}$$

The same can be obtained for ^{15}F, knowing the calculated width: $\Gamma_\gamma^{calc}(^{15}F) = 3.25$ eV, and the Weisskopf estimate for $E_\gamma = 3.487$ MeV: $\Gamma_W^{E1}(^{15}F) = 17.5$ eV. The reduced transition probability for the 1s1/2 $\rightarrow$ 0p1/2 transition in ^{15}F is:

$$B(E1) = \Gamma_\gamma^{calc}(^{15}F)/\Gamma_W^{E1}(^{15}F) = 0.18 \ W.u. \tag{4.28}$$

Contrary to what was expected from prior calculations [Gra16], the ^{15}F B(E1) is not strong (B(E1) < 3) [End93], and it is only half of the one of ^{11}Be. Even though the two gamma transition involve the same shells, the characteristic of the gamma transition in ^{15}F cannot be deduced from the one of ^{11}Be.

4.3.3 Error in the predicted gamma width

Prior to the realization of the two experiments presented in this work, a gamma width more than 15 times larger than the limit was predicted [Gra16]. This can be explained for two different reasons.

Firstly, in their calculation they used the tabulated effective charge ($\tilde{e}$) of ^{17}F which was the closest nucleus to ^{15}F with a known value of $\tilde{e} = 1.2$ e. This value was considered to be a good approximation. Indeed, it would be expected for ^{15}F to have an even larger effective charge than ^{17}F as it has two neutrons less. But as explained in Ref. [Suh07] for E1 transitions, the effective charge is reduced due to spurious center of mass motion. They should have used the more realistic value obtained with Eq. 4.19 and used in this work : $\tilde{e} = 0.4$ e. This results in a reduction of the width by a factor 9.

Secondly, difference between the two values originates, also, from an error in the calculation of the radial integral. Indeed in their prediction they considered the transition between a proton in the 1s1/2 of ^{15}F second excited state to a proton in the 1s1/2 of ^{15}F ground state, instead of a proton in the 1s1/2 to a proton in the 0p1/2, in other words they computed the integral: <1s1/2|r|1s1/2> while they should have computed: <0p1/2|r|1s1/2>. This lead to a factor 1.6 difference in the determination of $\langle r \rangle^2$ as the proton in the 0p1/2 is tightly bound compared to the ground state proton of the 1s1/2.

4.3.4 Other possible candidates in ^{15}F

Studying ^{11}Be showed that an important parameter for the strength of the transition is the spreading of the wave function. In ^{15}F, the ground state is interpreted as mostly a $^{14}O_{gs}$ core and a proton in the 1s1/2. For this state, the proton wave function is extremely spread as there is no centrifugal barrier (l = 0) and the proton is unbound by 1.27 MeV (Fig. 4.14). The first excited state of ^{15}F structure is similar to the ground state, but with a proton in the 0d5/2, then, the spreading of the wave function is smaller due to the presence of the centrifugal barrier (l = 2), but it is still relatively spread as the proton is unbound by 2.794 MeV. The wave function can then be obtained similarly to the one of Fig. 4.12 and Fig. 4.13. The radial integral obtained is $\langle r^2 \rangle^2 = 1205.3$ fm^4 and the corresponding width is : $\Gamma_\gamma = 4.4\ 10^{-4}$ eV.

This is an E2 transition, for which transitions are considered to be strong for B(E2) > 20 W.u. [End93]. For an E2 transition, the Weisskopf estimate is:

$$\Gamma_W^{E2} = 4.9 \times 10^{-8} \times A^{4/3} \times E_\gamma^5 = 1.5 \times 10^{-5}\ eV \tag{4.29}$$

Then, for the 0d5/2 $\rightarrow$ 1s1/2 transition in ^{15}F a reduced transition probability of B(E2) = 28.3 W.u. is obtained. Thus making this transition a "strong" one worth looking into [End93]. However, E2 transition are much less probable and with the computed width of 4.4 e-4 eV, it means a branching ratio of: BR = Γ_γ / Γ_{tot} = 4.4 10^{-4} eV / 300 keV = 1.5 10^{-7} %, making its detection even less probable than the one experimentally studied in this

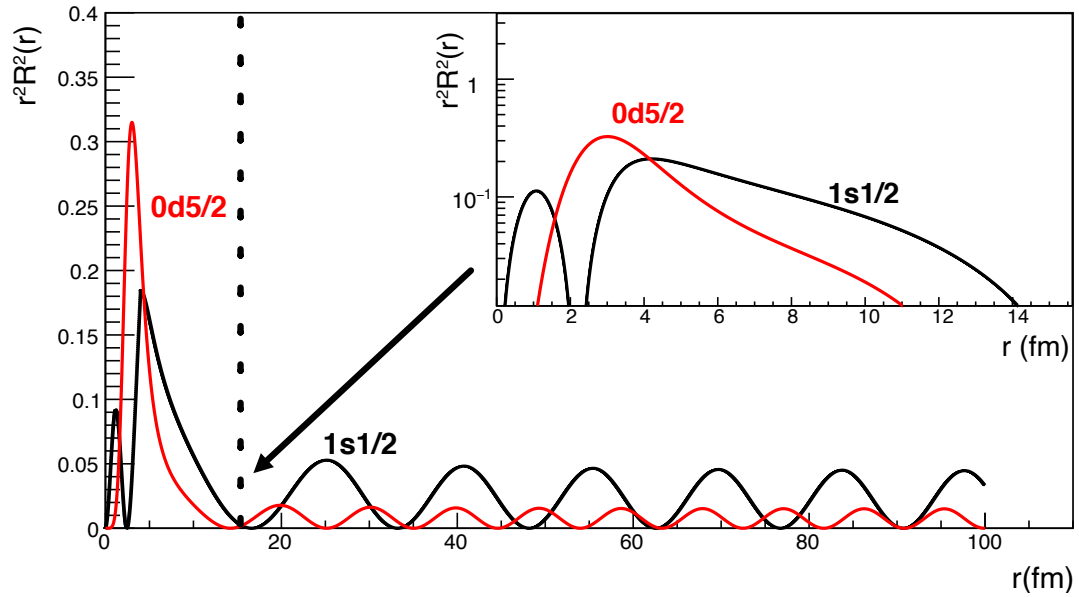

Figure 4.14: *Single particle wave functions of a proton in the 1s1/2 shell in black and in the 0d5/2 shell in red. The two states are unbound and thus extend to $r \to \infty$, the integration is then performed until the first minimum is reached.*

work.

4.3.5 Conditions required to find good candidates

What we learned from the study of ^{15}F and ^{11}Be is that to experimentally observe a strong gamma transition (B(E1) $>$ 0.3 W.u. or B(E2) $>$ 20 W.u.) in an unbound nucleus, it is required that the wave function of both the initial and final states are very spread out. The larger the spread, the stronger the transition. But, having a large wave function is not sufficient for this transition to be experimentally observable, indeed, the energy of the states, as well as the branching ratio of other decay channels play an important role in making the transition experimentally accessible or not. For example in ^{11}Be, the width of the $1/2^-$ state is very narrow ($\Gamma_\gamma = 0.04$ eV), even though the lifetime of the state is short (166 fs $\sim 10^{-13}$s), it is still quite "long" lived compare to the one of unbound states whose half-life are of the order of 10^{-21}s. As a consequence, observing transitions between unbound states requires either an extremely strong branching ratio to the gamma decay channel compared to the particle decay channel, or very high intensity (for example, to

measure the unbound transition in ^{8}Be [Dat05] a beam of $\sim$ 1 pnA was required.) and/or extremely long beam time.

4.4 Conclusion

In this chapter the detailed study of the structure of the negative-parity states of ^{15}F was performed in the shell model with the help of the *nushellX* code. Similarities in term of energies between the level scheme of ^{14}O + p and ^{15}F were highlighted. From these similarities we propose that the $5/2^-$ and $3/2^-$ should strongly couple, respectively, to the second 0^+ and the 3^- state of ^{14}O. The symmetry breaking between ^{15}F and ^{15}C for the $3/2^-$ state seen in the widths of the state could be understood from the closeness of the ^{14}O(3^-) + p to the ^{15}F$(3/2^-)$ which are only 18 keV apart compared to the difference of 853 keV between ^{14}C(3^-) + n and ^{15}C$(3/2^-)$. The experimental and theoretical spectroscopic factors, are consistent with a very little overlap between the negative-parity states of ^{15}F with ^{14}O$_{g.s.}$ + p, and a larger overlap for ^{14}O(1^-) + p. In the future, more realistic calculations taking into account the mixing of ^{15}F states with the continuum should be performed, as they might explain why the width of ^{15}F$(3/2^-)$ is 4 times narrower than its analog state in ^{15}C. The expected gamma transition between the $1/2^-$ state and the ^{15}F$(1/2^+)_{g.s.}$ was not experimentally observed and deduced to have a cross section smaller than $\sigma_\gamma < 73(38)$ μb . This chapter also explained why the transition was not seen and gave clues on what could make a better candidate to study gamma transitions between unbound states. Neutron loosely bound or unbound nuclei seems better candidates to see gamma transitions, due to the absence of Coulomb barrier, their larger effective charge and more spread wave function.

5
Conclusion and outlook

In this work the unbound nucleus ^{15}F was studied by performing and analyzing two distinct GANIL experiments aiming at three goals. (i) The measurement of the odd-parity states of ^{15}F predicted to be much narrower than the ground state and first excited state of ^{15}F, contradicting the naive expectation that unbound states in the continuum should get broader as the excitation energy increases. (ii) Those states were predicted to be more than 1 MeV above the two-proton emission threshold and as a consequence the measurement of their decay by two-proton emission was expected. (iii) The second excited state of ^{15}F, the $1/2^-$ state, already measured with a width $\Gamma_\gamma = 36(19)$ keV was predicted to decay by gamma emission to the $1/2^+$ ground state.

The first experiment was originally designed to cover all three goals, but due to malfunctions from GANIL accelerators only the first goal was reached. In this experiment, the resonant elastic scattering reaction ^{1}H(^{14}O,p)^{14}O was used and studied for the first time using a MUST2 telescope covering laboratory angles smaller than 5°. The measurement of the resonant elastic scattering differential cross-section led to the observation of two new narrow states, the $5/2^-$ and $3/2^-$ states whose spin and parity were assigned by the mean of the R-Matrix formalism. Those states were observed to be very narrow ($\Gamma_{5/2^-} = 2(1)$ keV and $\Gamma_{3/2^-} = 40(10)$ keV)), at resonances energies more than 5 MeV above the one-proton emission threshold ($S_p = 1.27$ MeV) and ~ 1 MeV above the two-proton emission threshold ($S_{2p} = 4.628$ MeV): $E_{r3/2^-} = 6.29(14)$ MeV $E_{r5/2^-} = 5.91(14)$ MeV. What was particularly interesting was the width of the $3/2^-$ states which was debated

among theoreticians [Can06; For07; For11] and expected to be similar to the one of its mirror state in ^{15}C.

The second experiment was the first experiment performed using the new MUGAST array coupled to VAMOS spectrometer and AGATA gamma-ray spectrometer. This experiment focused on the two remaining goals. The two-proton emission cross-section was measured and the $5/2^-$ state, deduced in the first experiment, was confirmed by measuring the two-proton excitation function as well as by measuring the relative reduced energy between ^{13}N and the protons. The $3/2^-$ state was clearly observed in both experiments by measuring the resonant elastic scattering reaction and in the second experiment by measuring its decay to $^{13}N_{g.s.}$ by two-proton emission. Both states were observed to decay only by the sequential emission of two protons. From those measurements, the total width and partial width of the states were obtained (Fig. 3.2 and Table 3.39). The measurement of the branching ratio showed that the one proton emission was the main decay channel for those states.

Both R-Matrix fits performed in section 2.3.1 and section 3.3.2 required the addition of two other states at higher energy, a $5/2^+$ and a $3/2^+$ states, their energy and width deduced in the fit can only be taken as hints of their existence. It would be interesting in future experiments to measure those states in a similar fashion, to measure their width, which are expected to be broad ([Can06]) and their decay by either one-proton or two protons emission. This would be particularly interesting to test the isospin dependence of the spin-orbit interaction and to confirm the preliminary results obtained in this work.

Calculations of both the experimental and theoretical spectroscopic factors agreed that negative-parity states of ^{15}F had little overlap with $^{14}O_{g.s.}$ + p, while large overlaps were calculated between ^{15}F negative-parity states and $^{14}O(1^-)$ + p. The comparison to the nearby states in ^{14}O + p and ^{13}N + 2p showed strong similarities in energy, especially between the ^{14}O second 0^+ state with $^{15}F(5/2^-)$ and ^{14}O first 3^- state with $^{15}F(3/2^-)$ state. It would be very interesting to perform more realistic calculations taking into account the coupling of ^{15}F states to the continuum to see if it reinforces our interpretation. Such calculations are beyond the scope of this work, but should be performed in the future.

The expected gamma emission from the $1/2^-$ state to the ground state of ^{15}F was studied, but not observed experimentally (Fig. 3.47). An experimental limit for the partial width of the γ-transition was obtained ($\Gamma_\gamma < 4.4(1.5)$ eV). Theoretical calculations were performed to explain the reasons why the cross-section was smaller than what was expected, and results were found to be consistent with the limit obtained experimentally. Different characteristics of the gamma transitions between unbound nucleus were dis-

cussed and calculations were performed providing clues to help finding better candidates to study these transitions. If experimentally no indication of a strong E1 transition in ^{15}F was observed, nor another state in ^{15}F was considered to be a good candidate to study the phenomenon of gamma transitions in unbound nucleus, it would be interesting to use what we learned both experimentally and theoretically, to find a more suitable candidate to study this type of transitions in drip-line nuclei in the future.

6 Appendix

6.1 Derivation of the Breit-Wigner formula

For resonances reaction, the cross-section can be obtained using the so-called Breit-Wigner formalism developed by G. Breit and E. Wigner in 1936. First, let's remind the reader that the geometrical cross-section corresponds to the surface in which the interaction between the projectile and the target occur. In term of impact parameter (b), the angular momentum is $L = bp$, with $p = \hbar/\lambda$, thus $L = b\hbar/\lambda$. At the quasi-classical limit, the angular momentum is quantified following: $L = l\hbar$. Where the maximum cross-section for a given l corresponds to the surface between two successive concentric rings of impact parameter: b_{l+1} and b_l:

$$\sigma_l^{max} = \pi b_{l+1}^2 - \pi b_l^2 = (2l+1)\pi\lambda^2 \tag{6.1}$$

The statistical factor (2l + 1) can be replaced by the more general factor taking into account the spins of the nucleus:

$$\omega = \frac{2J+1}{(2J_1+1)(2J_2+1)} \tag{6.2}$$

where J = J_1 + J_2 is the total spin and J_1 and J_2 are respectively the spin of the colliding nuclei [Cla88].

Let's now consider the simpler case of a reaction where particle in the entrance and exit channel are identical. Let's also use the natural system of unit with $\hbar = c = 1$. In that case, the wave function of a decaying states can be written:

$$\Psi(t) = \Psi(0)e^{-i\Omega_r t}e^{-t/2\tau} \tag{6.3}$$
$$= \Psi(0)e^{-t(iE_r+\Gamma/2)} \tag{6.4}$$

where $\Gamma = \hbar/\tau$ is the partial width and E_r is the resonance energy. Let's call $\chi(E)$ the Fourrier transform of the wave function, $\Psi(t)$ [Per00]:

$$\chi(E) = \int_{-\infty}^{\infty} \Psi(t)e^{i\Omega t}dt \tag{6.5}$$

with Ω = E, we obtain:

$$\chi(E) = \int_{-\infty}^{\infty} \Psi(t)e^{iEt}dt \tag{6.6}$$
$$= \Psi(0)\int_{0}^{\infty} e^{-t(iE_r+\Gamma/2-iE)}dt \tag{6.7}$$
$$= \frac{K}{(E_r - E) - i\frac{\Gamma}{2}} \tag{6.8}$$

The cross-section will be proportional to the decay probability, knowing that the maximum cross-section corresponds to the geometrical cross-section: $\sigma_{max} = 4\pi\lambda\!\!\!^{-2}\omega$, and as $(\chi(E)\chi(E)^*)_{max} = (\chi(E_r)\chi(E_r)^*)_{max} = 4K^2/\Gamma^2$, we obtain by identification:

$$\sigma_{BW} = \pi\lambda\!\!\!^{-2}\omega\frac{\Gamma^2}{(E - E_r)^2 + \frac{\Gamma^2}{4}} \tag{6.9}$$

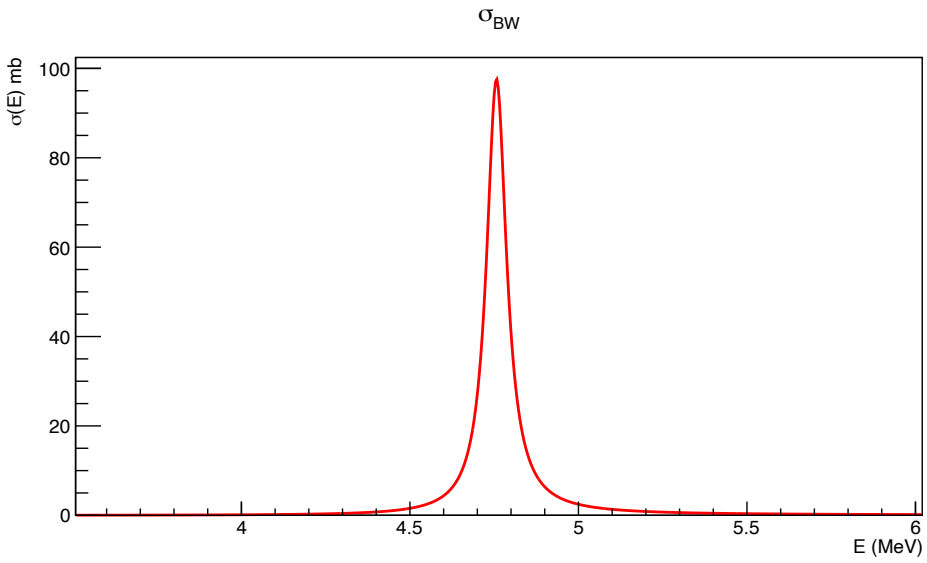

Figure 6.1: Example of a Breit-Wigner cross-section

For some reactions presented in this work, the entrance and exit channel can be different. In that case, the Breit-Wigner formula becomes:

$$\sigma_{BW} = \pi \lambda\!\!\!^{-2} \omega \frac{\Gamma_1 \Gamma}{(E - E_r)^2 + \frac{\Gamma^2}{4}} \times \frac{\Gamma_2}{\Gamma} \tag{6.10}$$

$$\sigma_{BW} = \pi \lambda\!\!\!^{-2} \omega \frac{\Gamma_1 \Gamma_2}{(E - E_r)^2 + \frac{\Gamma^2}{4}} \tag{6.11}$$

with $\Gamma = \Gamma_1 + \Gamma_2 + ...$ the total width taking into account all the of the opened decay channels. Γ_1 and Γ_2 the partial widths of the entrance and exit channels respectively. Γ_2/Γ is called the branching ratio (BR).

6.2 Target thickness measurements

In the second experiment presented in section 3.3.2 the use of a spectrometer placed after the target made possible a precise measurement of the target thickness. To this extent, the Bρ was measured with and without inserting the different targets. The energy loss of the beam being different depending on the target thickness, measuring the Bρ will change depending on the thickness of the inserted target. The relation between the energy and the Bρ can be obtained from the mass (M_{ion}) and the charge (Q_{ion}) of the ion:

$$E_{ion} = \sqrt{M_{ion}^2 + (B\rho_{ion} \times c \times Q_{ion})^2} \tag{6.12}$$

The measurement of the thicknesses was performed using the $^{14}N^{7+}$ beam. The incident beam energy was determined by measuring the Bρ of the beam using the 7 mm hole : Bρ = 0.9148 Tm. Targets were inserted and their Bρ measured. Their thicknesses were then deduced using energy loss tables. Results can be found in table.6.1.

Target	Bρ (Tm)	Charged state	Thickness
2	0.7473	$^{14}N^{6+}$	107 (11)
3	0.7754	$^{14}N^{6+}$	92.2 (9)
	0.8294	$^{14}N^{5+}$	92.4 (9)
		Mean thickness :	92.3 (9)
5	0.8023	$^{14}N^{6+}$	77.3 (8)

Table 6.1: *Summary of the measured target thicknesses.*

Those measurements also showed strong inhomogeneity, especially for target 2 which was the main target of the first experiment. As a consequence, target 3 was used in the second experiment (Fig. 6.2).

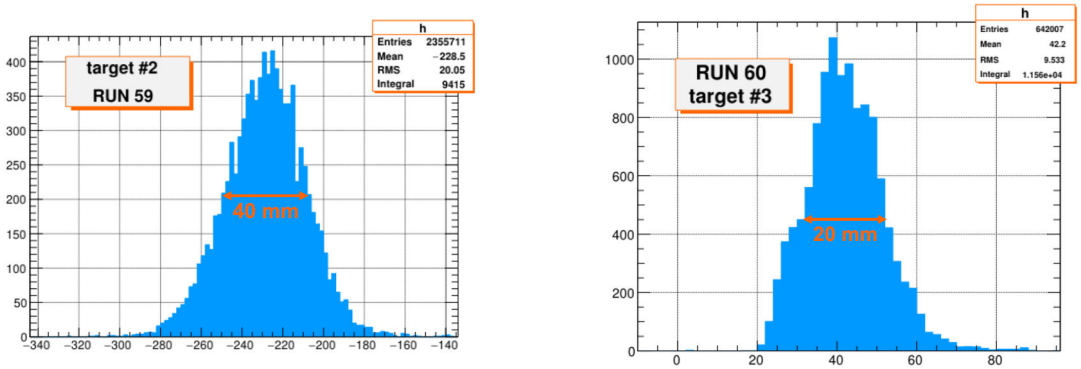

(a) (b)

Figure 6.2: *On-line spectra of the beam dispersion seen on X with target 2 on the left compared to the dispersion with target 3, the spread observed is twice larger using target 2.*

6.3 Mean beam position on target

6.3.1 Proof of principle using simulated data

To determine the mean position at which the beam is hitting the target it is possible to use the reaction kinematics. Indeed, in the case of elastic scattering in a thick target, the maximum scattered proton energy is unique for a given angle. In MUST2, the scattering angles are reconstructed considering a certain beam position. The beam position can be obtained iteratively by varying the assumed beam position and by doing projections on the laboratory angles for different energies (Fig. 6.3) using a χ^2 minimization (Eq. 6.13):

$$\begin{aligned}\chi^2(E_{Lab}) = (\theta_{T1} - \theta_{T2})^2 + (\theta_{T1} - \theta_{T3})^2 + (\theta_{T1} - \theta_{T4})^2 \\ + (\theta_{T2} - \theta_{T4})^2 + (\theta_{T2} - \theta_{T3})^2 + (\theta_{T3} - \theta_{T4})^2\end{aligned} \tag{6.13}$$

with θ_{Ti} the maximum angle for telescope i, measured at a given energy (Fig. 6.3). Projections on the laboratory angles were made for E_{Lab} = 24, 22, 18, 15, and 12 MeV with a 0.1 MeV range. The χ^2 minimization was performed for each projection, the incident beam position on the target was obtained from the minimum $\chi^2_{total} = \sum \chi^2(E_{Lab})$.

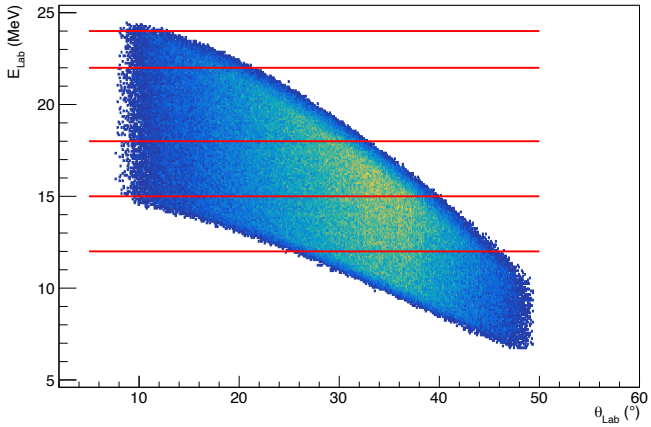

Figure 6.3: A representation of the different slices made to perform the χ^2 minimization. Those slices were : 24 ± 0.1 MeV, 22 ± 0.1, 18 ± 0.1 MeV, 15 ± 0.1 and 12 ± 0.1 MeV

This method was first tested on simulated data generated using GEANT4 through the nptool framework. To have a controlled simulation, to test our code, a "perfect" beam was used, meaning that the simulated beam had no straggling in energy or position and

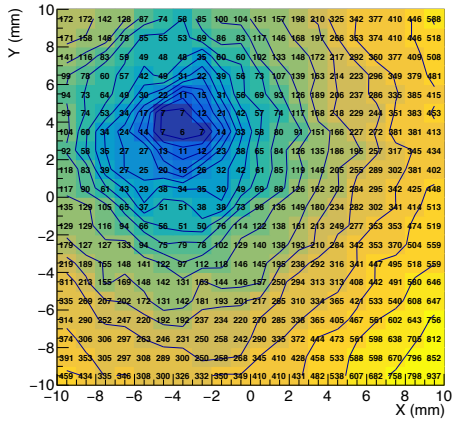

(a) Simulated :(-4, 3) mm. Found : (-4, 3) mm.

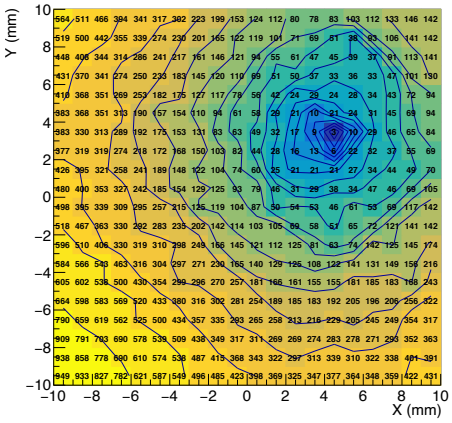

(b) Simulated :(4, 3) mm. Found : (4, 3) mm.

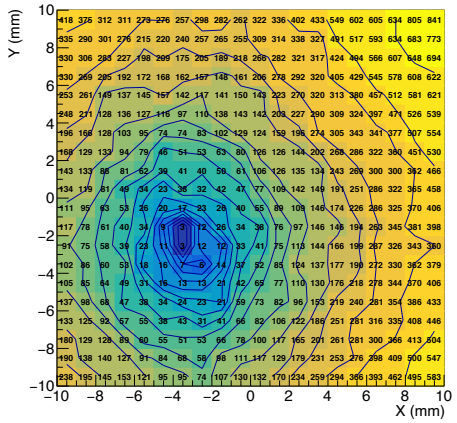

(c) Simulated :(-4, -3) mm. Found : (-4, -3) mm.

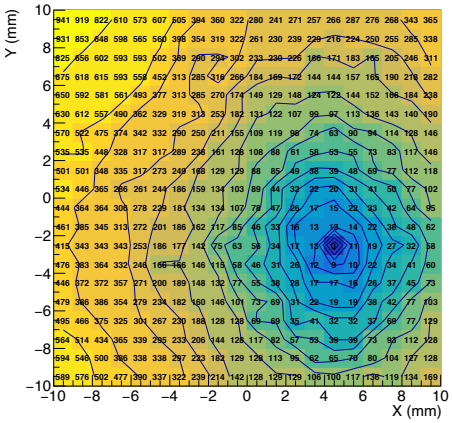

(d) Simulated :(4, -3) mm. Found : (4, -3) mm.

Figure 6.4: Different results obtained with the χ^2 method described in the text using a perfect beam (no straggling)

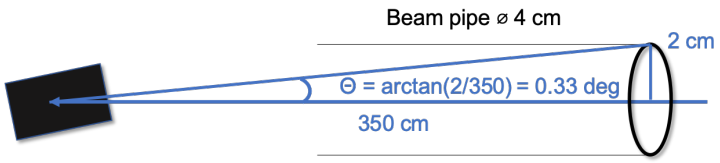

Figure 6.5: Scheme of the maximum beam angle.

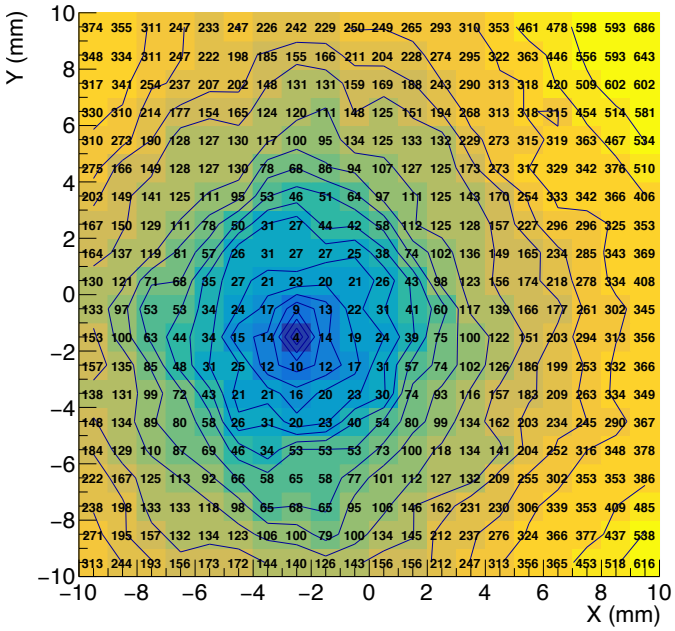

Figure 6.6: Simulation considering an incident beam angle on target of 0.33°. Simulated: (-4, -3) mm. Found : (-3, -2) mm.

no angle. The χ^2 was then computed for different beam positions using a 1 mm grid step.

Experimentally, the beam is not perfect. Fig. 6.5 shows that the maximum incident beam angle is 0.33°. It is worth mentioning that at such angle, the beam transmission through VAMOS would have been very small. Still using this angle in the simulation will give an idea of the sensitivity to the beam angle as it will reproduce the "Worst case scenario". Using this angle, it is found that there is an error of 1mm both in X and Y in the reconstructed beam position (Fig. 6.6). The reconstruction method described here is working with a precision better than 1 mm.

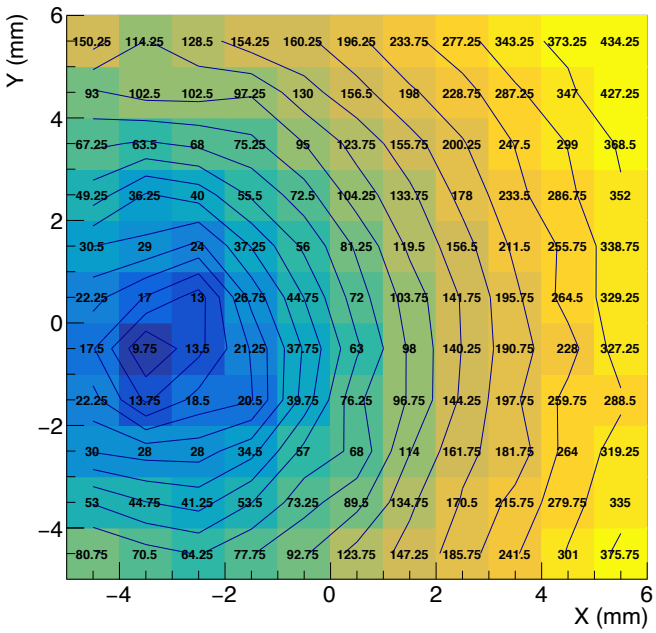

Figure 6.7: Using the χ^2 method on the entire set of experimental data, the beam position on target is found at (-4, -1) mm.

6.3.2 Application to experimental data

This code was then used on experimental data. The method converged on a beam position of X = -4 (1) mm and Y = -1 (1) mm.

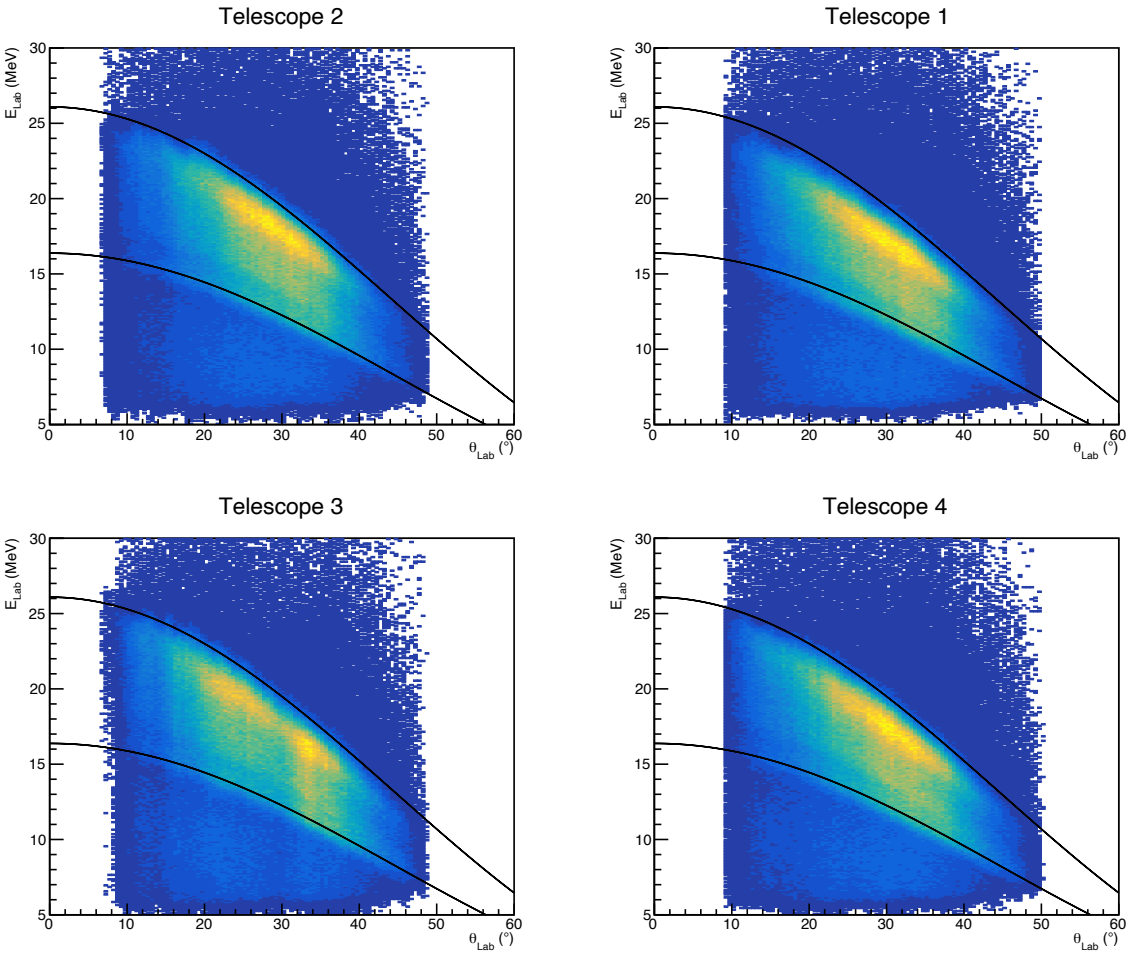

Figure 6.8: Energy in the laboratory frame as a function of the angle in the laboratory reconstructed for the beam positioned at X = -4 mm (1) and Y = -1 (1) mm. The black lines corresponds to the maximum and minimum theoretical kinematic lines for the elastic reaction considering the energy of the incoming beam and the thickness of the target used.

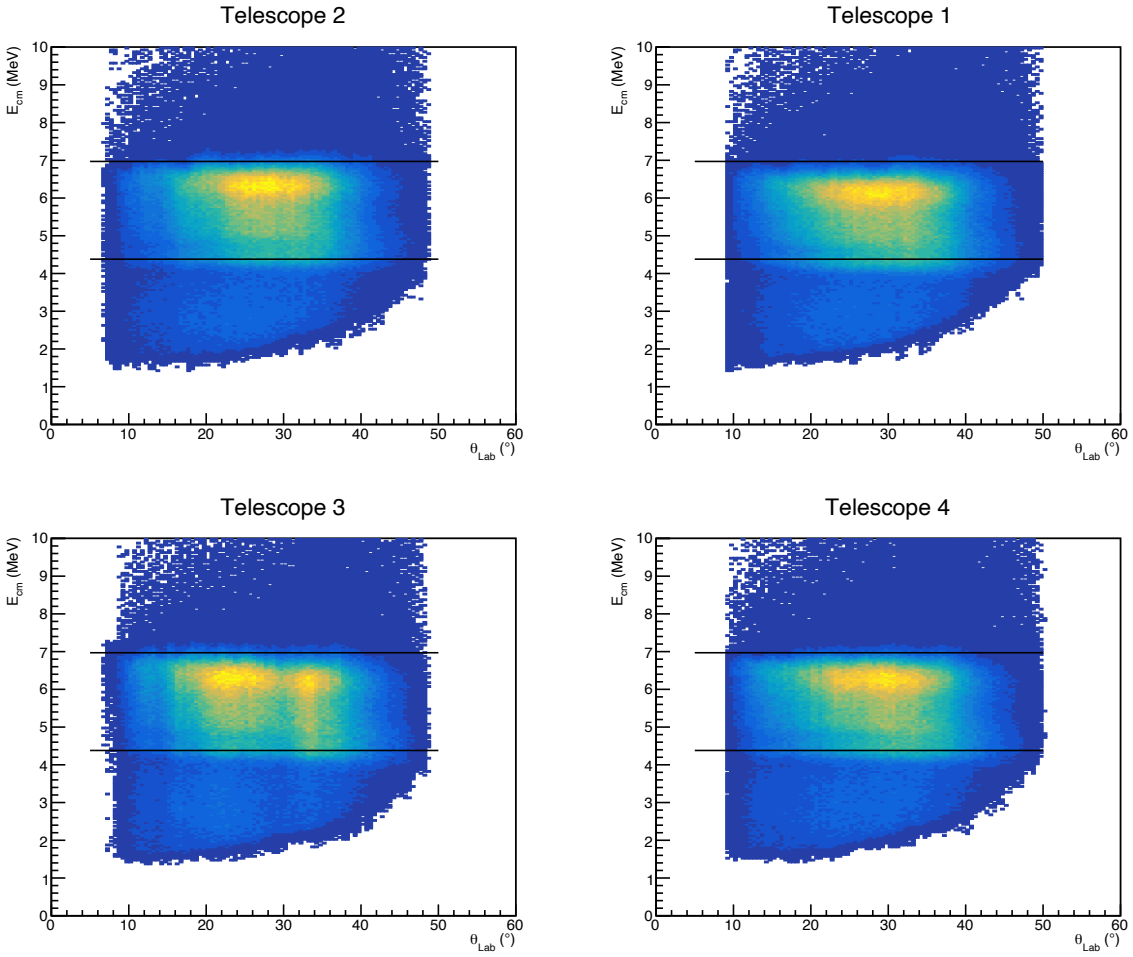

Figure 6.9: Energy in the center of mass as a function of the angle in the laboratory reconstructed for the beam positioned at X = -4 (1) mm and Y = -1 (1) mm. The black lines corresponds to the maximum and minimum theoretical kinematic lines for the elastic reaction considering the energy of the incoming beam and the thickness of the target used.

6.4 Electronic schemes

This appendix shows the different electronic schemes used in both experiments. These schemes are given as a reference for future experiments.

The notation used in this appendix are:

- NIM-ECL: Module converting NIM signals to ECL signals and conversely.
- FIFO: Fan In Fan Out.
- COINC: Coincidence module.
- DIV: Divider transmitting signals only when N events are registered.
- CFD: Constant Fraction Discriminator
- TDC: Time to Digital Converter
- TAC: Time to Amplitude Converter
- DT: Dead Time.
- GMT: GANIL Master Trigger.
- FAG: Fast Analysis Gate.
- U2M: Scaler
- NUMEXO2: NUMériseur pour EXOgam2, is a NIM digitizer
- MUVI: MUst2 VxI cards.
- ORD: Logic signal sent by the MUST2 detectors when it is triggered.

6.4.1 First experiment

MUVI

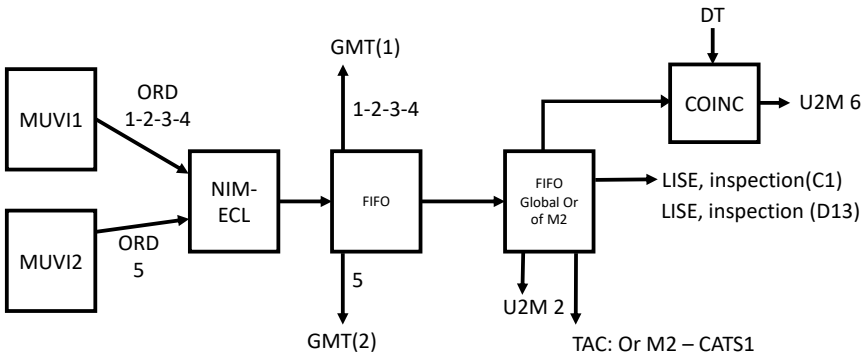

Dead Time

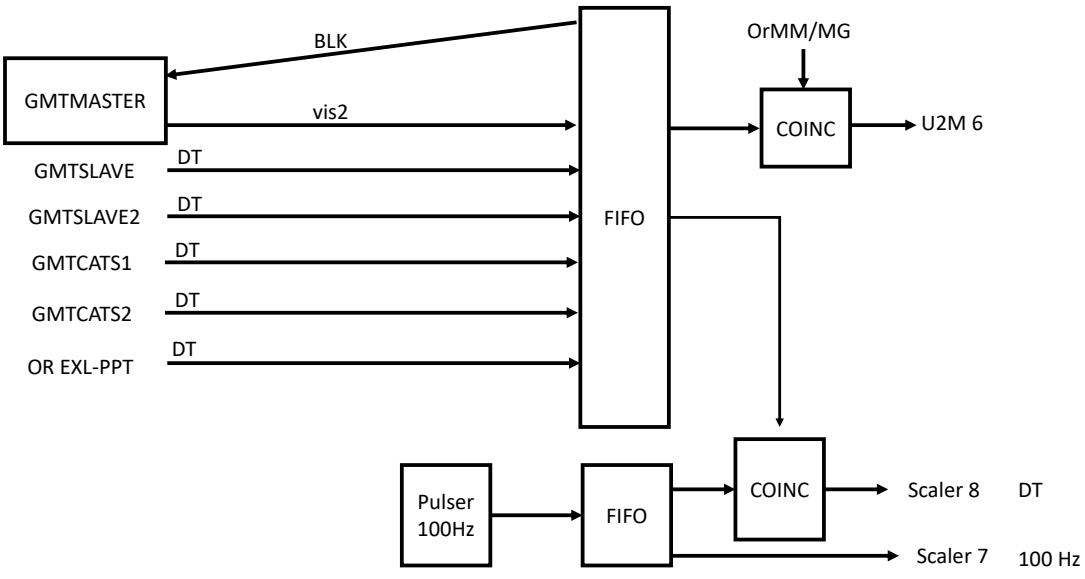

6.4.2 Second experiment

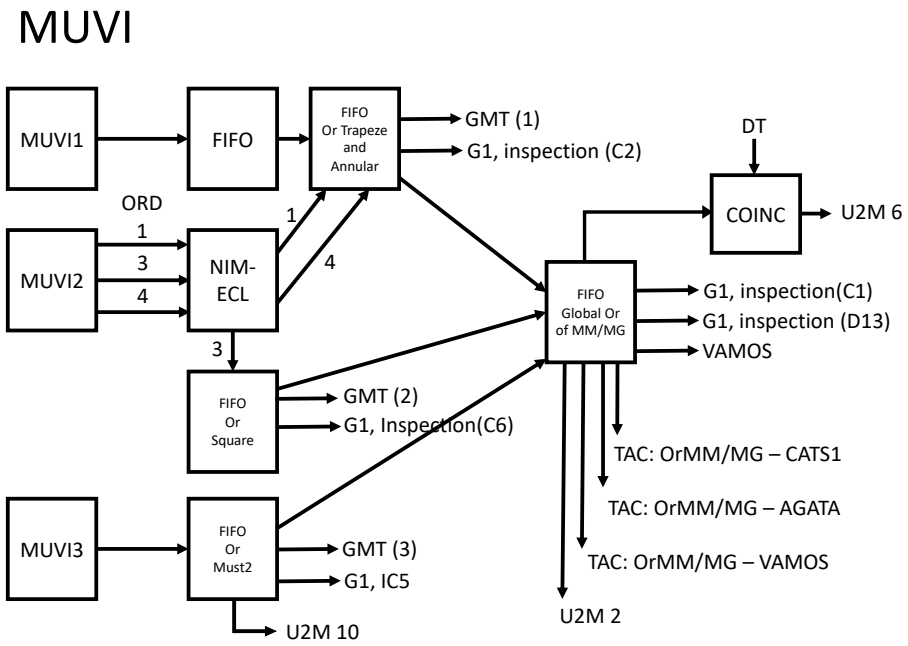

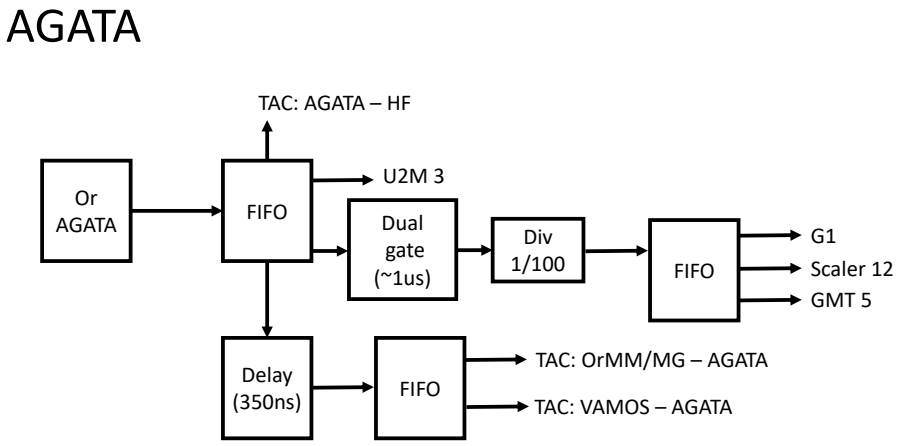

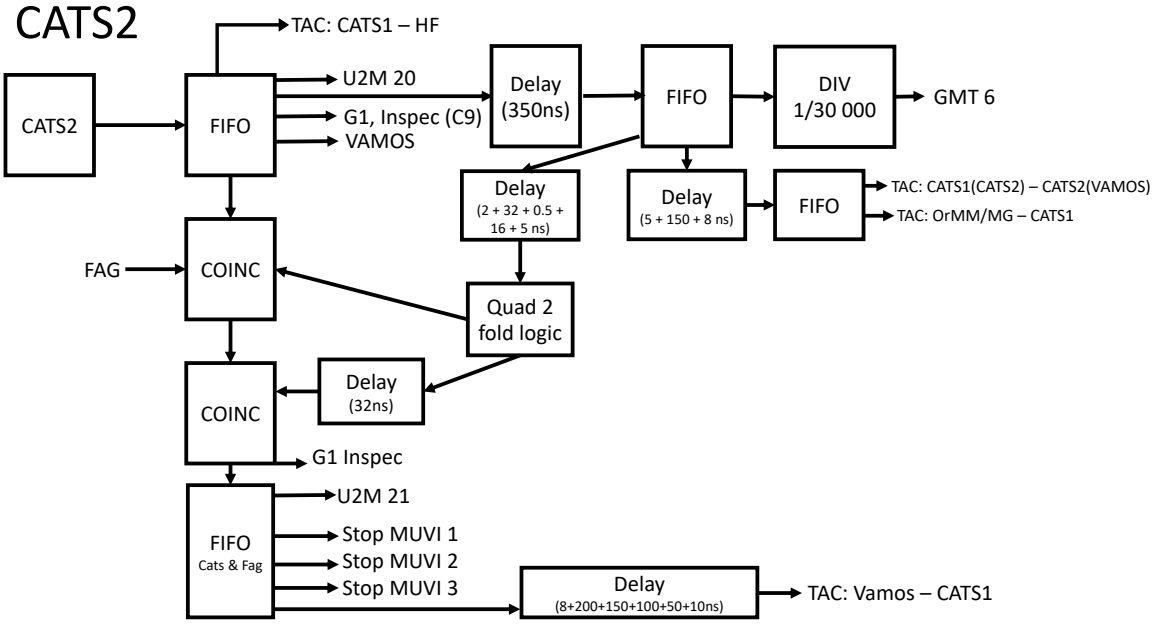
CATS2
CATS2
FIFO
TAC: CATS1 – HF
U2M 20
G1, Inspec (C9)
VAMOS
Delay
(350ns)
FIFO
DIV
1/30 000
GMT 6
Delay
(2 + 32 + 0.5 +
16 + 5 ns)
Delay
(5 + 150 + 8 ns)
FIFO
TAC: CATS1(CATS2) – CATS2(VAMOS)
TAC: OrMM/MG – CATS1
FAG
COINC
Quad 2
fold logic
COINC
Delay
(32ns)
G1 Inspec
FIFO
Cats & Fag
U2M 21
Stop MUVI 1
Stop MUVI 2
Stop MUVI 3
Delay
(8+200+150+100+50+10ns)
TAC: Vamos – CATS1

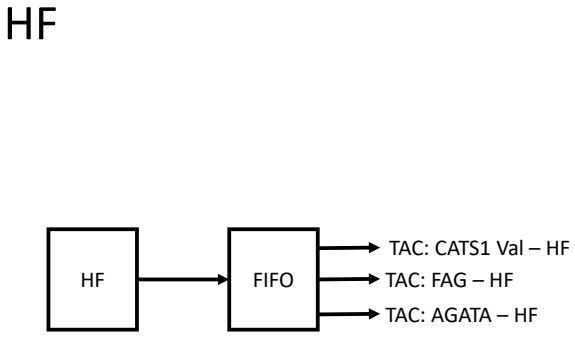
HF
HF
FIFO
TAC: CATS1 Val – HF
TAC: FAG – HF
TAC: AGATA – HF

Dead Time

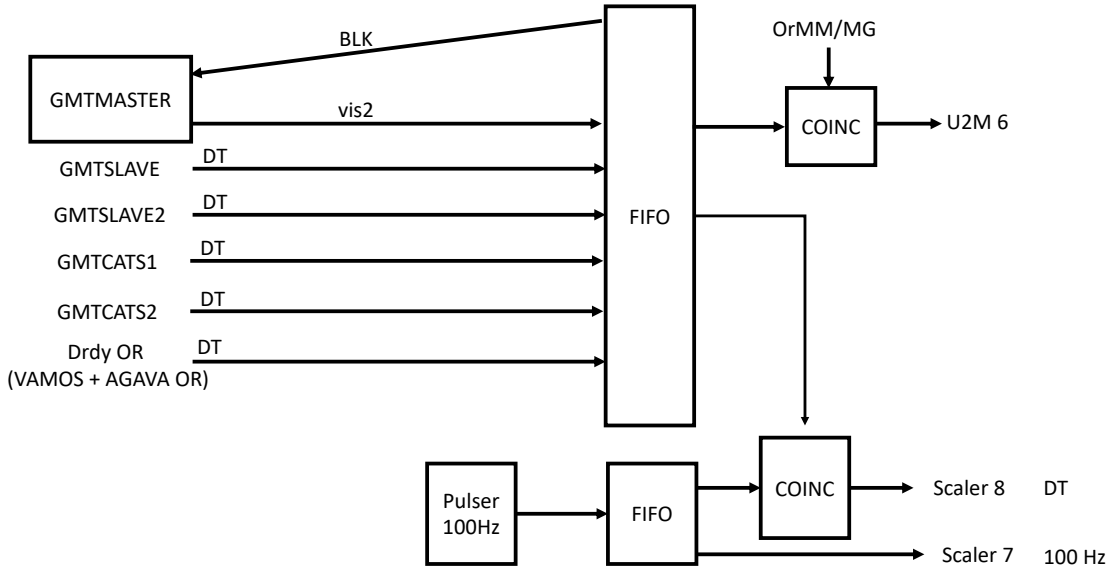

U2M

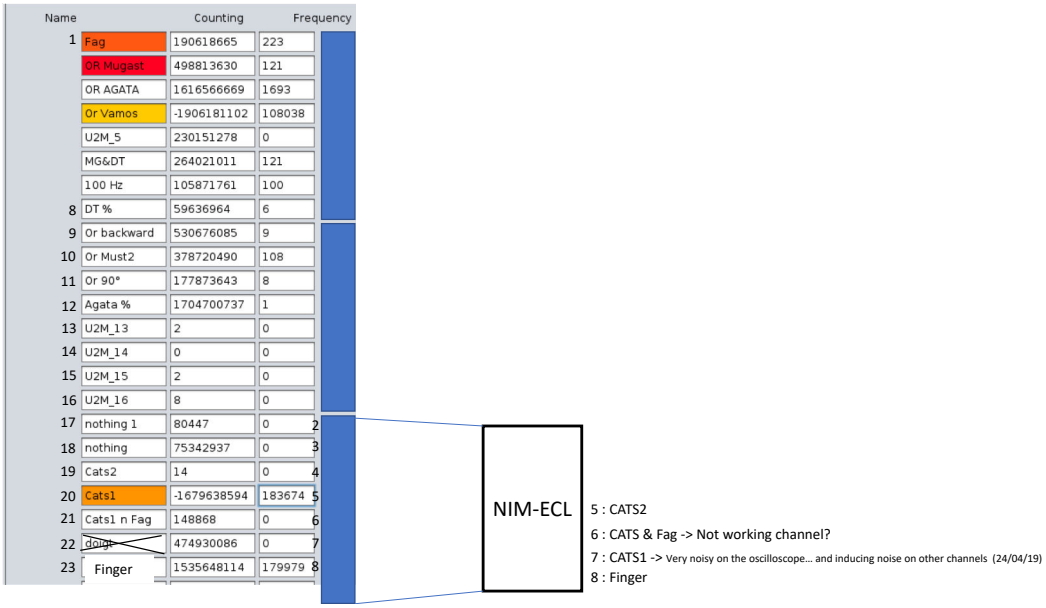

GMT

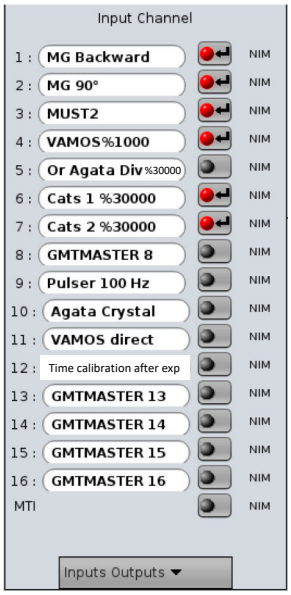
Input Channel
1 : MG Backward NIM
2 : MG 90° NIM
3 : MUST2 NIM
4 : VAMOS%1000 NIM
5 : Or Agata Div%30000 NIM
6 : Cats 1 %30000 NIM
7 : Cats 2 %30000 NIM
8 : GMTMASTER 8 NIM
9 : Pulser 100 Hz NIM
10 : Agata Crystal NIM
11 : VAMOS direct NIM
12 : Time calibration after exp NIM
13 : GMTMASTER 13 NIM
14 : GMTMASTER 14 NIM
15 : GMTMASTER 15 NIM
16 : GMTMASTER 16 NIM
MTI NIM
Inputs Outputs

MWPPAC

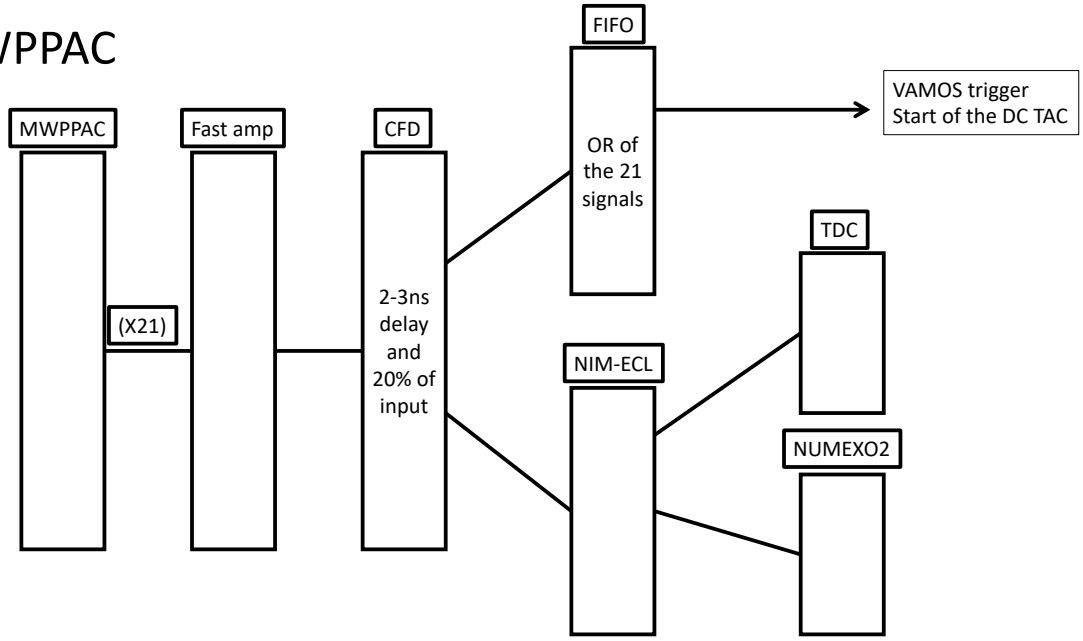
MWPPAC
(X21)
Fast amp
CFD
2-3ns delay and 20% of input
FIFO
OR of the 21 signals
VAMOS trigger
Start of the DC TAC
TDC
NIM-ECL
NUMEXO2

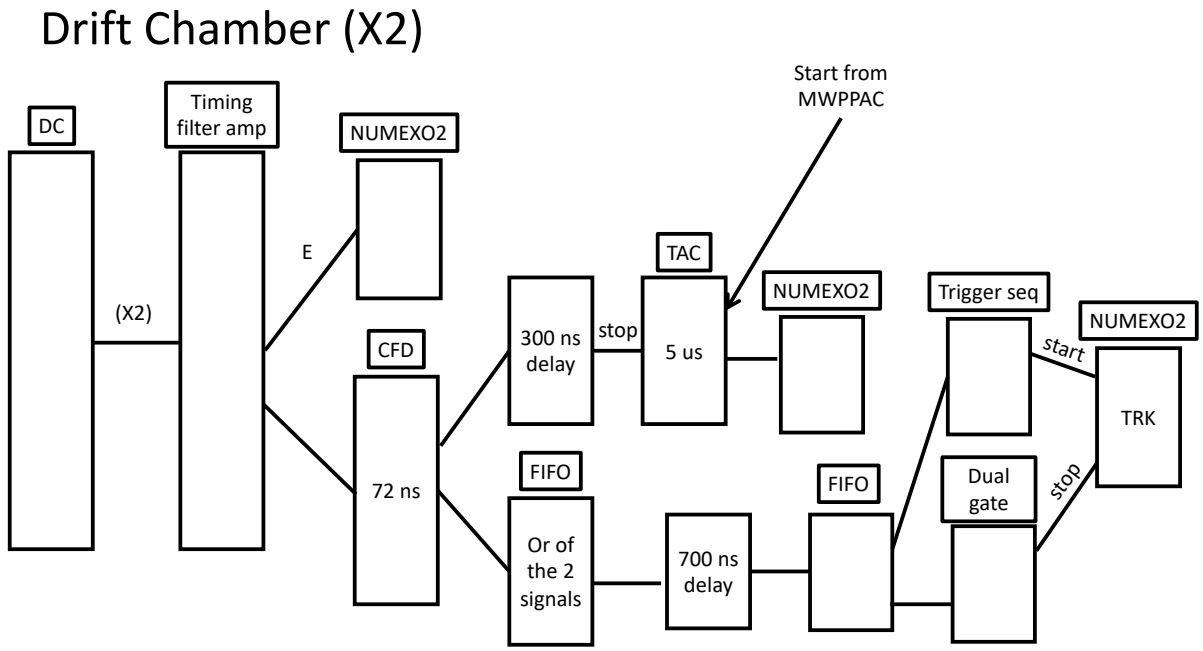
Drift Chamber (X2)
DC
Timing filter amp
NUMEXO2
Start from MWPPAC
(X2)
E
TAC
NUMEXO2
Trigger seq
NUMEXO2
CFD
300 ns delay
stop
5 us
start
TRK
72 ns
FIFO
FIFO
Dual gate
stop
Or of the 2 signals
700 ns delay

7
Résumé en Français

Ce chapitre a pour but de présenter mes travaux de thèse en français tout en essayant de les rendre le plus accessible possible au grand publique. Par conséquent, ce résumé n'a pas pour but de décrire en détail les aspects les plus complexes et techniques de ma thèse, pour cela j'invite les lecteurs anglophones à lire le manuscrit complet.

Introduction

Généralités

Depuis sa découverte en 1911 par Ernest Rutherford, le noyau de l'atome n'a cessé de fasciner les physiciens, qui ont cherché à l'étudier en détail, en particulier pour mieux comprendre les forces qui lui permettent de garder ses constituants, les protons et neutrons, liés ensemble. Pour cela, il est possible de faire entrer en collision des noyaux accélérés sur d'autres noyaux immobiles (cibles). Pendant des décennies ces réactions ont été faites à l'aide de noyaux stables. Ce sont environ 300 noyaux (composés de différents nombres de neutrons et de protons) qui furent étudiés grâce à ces expériences. Mais pour pouvoir tester la force nucléaire dans des conditions beaucoup plus extrêmes les chercheurs développèrent dans les années 90 des accélérateurs permettant d'accélérer des noyaux radioactifs, c'est à dire des noyaux qui possèdent une durée de vie limitée et se et qui se transforment spontanément en un autre noyau. Ces nouvelles expériences utilisant des noyaux radioactifs menèrent à la découvertes de nombreux nouveaux noyaux en accélérant

les découvertes. En effet, en quelques dizaines d'années, le nombre de noyaux connus à été multiplié par 10, passant de 300 noyaux connus avant les années 90 à plus de 3000 aujourd'hui.

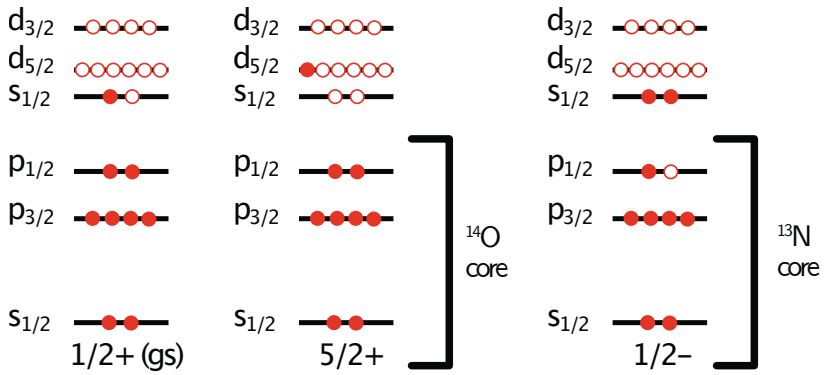

Figure 7.1: *Modèle en couche pour le fondamental, le premier et second états excités du* ^{15}F

Pour étudier les noyaux et pour étudier leur structure, les physiciens nucléaires utilisent des modèles théoriques, l'un des plus célèbres est le modèle en couches (Fig. 7.1). Dans cette représentation, les nucléons (= proton + neutron) se placent sur des couches caractérisées par une énergie et différents nombres quantiques. Exciter le noyau, c'est à dire déplacer un (ou plusieurs) proton(s) (ou neutron(s)) d'une couche vers une autre couche va coûter de l'énergie, le noyau excité aura alors une énergie supérieure à celle du noyau dans son état fondamental, énergie qui peut être mesurée expérimentalement. Ce noyau excité va ensuite chercher à se désexciter, soit par émission de γ (ou photon = particule de lumière), soit par émission d'une particule: électron, positron, proton, neutron, alpha. De part sa nature quantique, le noyau ne peut être excité que pour des valeurs précises d'énergies, une des missions du physicien est de mesurer ces niveaux d'énergies. La mesure de ces énergies quantifiées (=niveaux d'énergies) permet d'obtenir ce que l'on appelle un schéma de niveaux. L'unité utilisée pour mesurer ces énergies est l'électron Volt (eV), 1 eV = 1.6 10^{-19} Joules. Pour comprendre le principe d'excitation et d'énergie, prenons comme analogie celle d'un ballon de baudruche. Un ballon vide d'air correspondra à un noyau dans son état fondamental. Si on injecte de l'air dans le ballon, ce dernier va vouloir revenir à son état fondamental. Pour cela il va éjecter l'air, se désexciter. À la différence que pour le noyau, de part sa nature quantique, les niveaux d'énergie accessibles ne seront pas continus, mais quantifiés. Si on fait preuve d'imagination, un ballon "quantique" serait un ballon que l'on ne pourrait gonfler que pour certaines quantités précises d'air. Le modèle en couches développé en 1949 par Maria Goeppert Mayer, Eugene Paul

Wigner, and J. Hans D. Jensen eut beaucoup de succès puisqu'il était capable de reproduire avec précision une observation expérimentale incomprise jusqu'alors, l'existence de nombres magiques, c'est à dire de surstabilités observés lorsque les noyaux possèdent un nombre de neutrons ou de protons égal à 2, 8, 20, 28, 50, 82, 126.

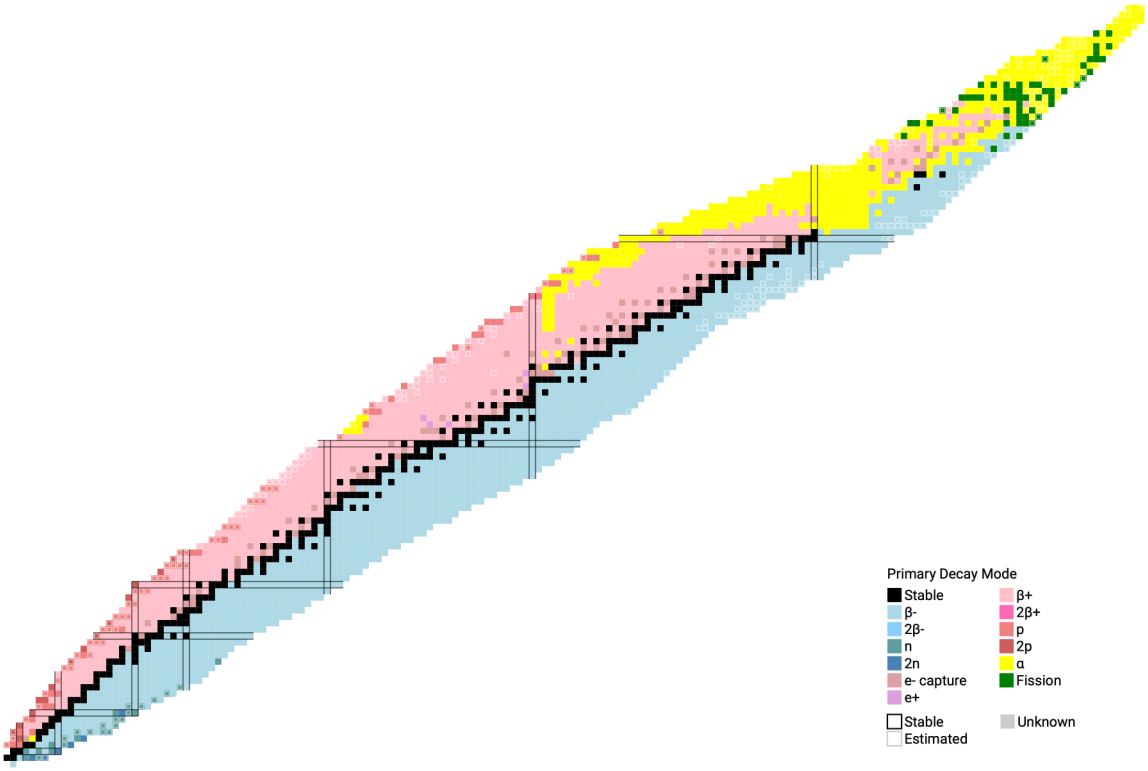

Figure 7.2: *Carte des noyaux. Chaque case correspond à un noyau ayant un nombre particulier de protons et de neutrons*

En classant les noyaux en fonction de leur nombre de neutrons et de protons, il est possible d'obtenir ce que l'on appelle la carte des noyaux (Fig. 7.2), en noir, on retrouve les noyaux stables, qui représentent la majorité des noyaux que l'on trouve sur Terre, on appelle cette "ligne" la vallée de stabilité. De chaque côté de cette vallée on retrouve les noyaux radioactifs qui vont se désintégrer en d'autres noyaux jusqu'à atteindre la vallée de stabilité, ces transformations auront principalement lieu par transformation d'un neutron en un proton ou inversement, par émission d'un électron ou d'un positron. Plus les noyaux étudiés sont loin de cette vallée de stabilité, plus ils ont une durée de vie courte et lorsque l'on atteint les "bords" de la carte des noyaux, ces derniers sont tellement instables qu'ils ne vont plus chercher à transformer un proton en un neutron (ou inversement) mais vont

émettre spontanément un proton (ou un neutron) on dit de ces noyaux qu'ils sont non-liés (par émission de particule) et on appelle ces régions les drip-lines. À l'approche des drip-lines, la structure des noyaux change, par exemple les nombres magiques peuvent disparaître et les noyaux considérés pour la plupart comme sphériques peuvent avoir des déformations extrêmes comme par exemple le noyau de Lithium 11 (Fig. 7.3) que l'on appelle un noyau à halo étant donné qu'il a une structure similaire à celle d'un noyau de Lithium 9 entouré de deux neutrons. Les noyaux à halo possédant une structure à trois corps sont appelés des noyaux borroméens, en référence aux anneaux borroméens où trois anneaux sont liés ensemble de façon à ce que si l'un des anneaux est retiré les deux autres anneaux ne seront plus liés. De la même façon, pour ces noyaux, retirer une particule va laisser le système à deux corps restant non lié, ce qui va mener à sa séparation.

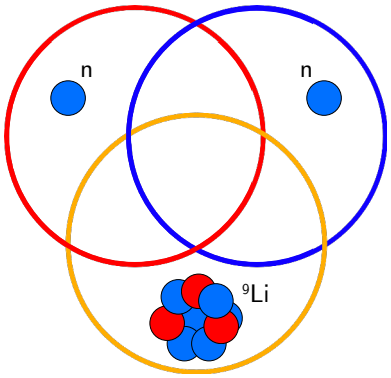

Figure 7.3: *Représentation schématique de la structure borroméene du* ^{11}Li

Le fluor 15

Dans cette thèse nous nous sommes intéressés au Fluor 15, ce noyau est placé deux neutrons au delà de la drip-line proton. Comme on peut le voir sur la figure 7.4, la drip-line proton est atteinte beaucoup plus rapidement que la drip-line neutron. Cela est principalement dû au fait que les protons sont chargés positivement et qu'ils vont donc se repousser. Ces derniers interagissent donc de façon nucléaire, mais aussi par interaction dite coulombienne alors que les neutrons eux n'interagissent que de façon nucléaire. Les nucléons sont piégés dans le noyau par ce que l'on appelle un potentiel, ce potentiel sera différent pour les protons et les neutrons, en effet les protons seront piégés à la fois par le potentiel nucléaire mais aussi paradoxalement par une barrière coulombienne. Si les protons et les neutrons ont une charge différentes ils possèdent néanmoins des caractéristiques très similaires, à tel point qu'on les étudie de façon souvent similaires en les appelant les nucléons. De son côté la force nucléaire n'est pas dépendante de la charge des particules.

On s'attend donc pour les noyaux miroir, c'est à dire les noyaux possédant le même nombre de nucléons mais avec un nombre échangé de protons et de neutrons, qu'ils aient des schémas de niveaux identiques.

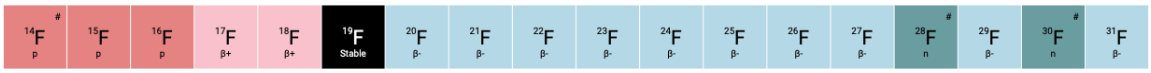

Figure 7.4: *Chaine isotopique du Fluor, en bleu les noyaux riches en neutrons et en rouge les noyaux riches en protons. Les couleurs foncés représentent les noyaux non-liés.*

Comme évoqué précédemment les caractéristiques des noyaux changent à l'approche de la drip-line. Ainsi, étudier deux noyaux miroirs dont un des noyaux est un noyau non-lié peut permettre d'obtenir des informations intéressantes. Le noyau miroir du ^{15}F est le Carbone 15, une comparaison des schémas de niveaux montre de larges différences en énergie entre les deux, ces différences montrent apparemment que la symétrie miroir est brisée. Cela est dû au fait que dans le ^{15}C le neutron est lié, alors que le proton du ^{15}F ne l'est pas, cela a pour effet de réduire la barrière coulombienne (Fig. 7.5) et par conséquent d'abaisser les niveaux d'énergie du noyau riche en proton. Cela est d'autant plus fort pour les niveaux n'ayant pas de barrière centrifuge (l = 0) ce qui est le cas pour l'état fondamental du fluor 15.

Pour les noyaux non-liés, les mesures des niveaux d'énergies ne sont pas des valeurs exactes, mais possèdent une certaine largeur (ou incertitude) proportionnelle à leur temps de vie, plus la durée de vie de l'état est faible, plus la largeur sera grande et inversement. Naïvement, on s'attendrait qu'à mesure que l'énergie d'excitation augmente, les états soient de plus en plus instables et donc de plus en plus larges, de la même façon que plus le ballon de baudruche est rempli, plus il va se vider rapidement. Pour le Fluor 15, c'est l'inverse qui est observé, et particulièrement pour son deuxième état excité (l'état $1/2^-$) qui a une largeur plus de dix fois plus faible que l'état fondamental. Cette mesure particulièrement intéressante est interprétée comme étant due à un changement de structure du noyau passant d'un cœur de ^{14}O et un proton pour le fondamental a un cœur d'azote 13 (^{13}N) et deux protons pour l'état $1/2^-$ (à 99%). Une des raisons de cette structure est un phénomène physique particulièrement intéressant, la clusterisation près des seuils. En effet, la structure d'un noyau peut changer lorsqu'un de leur niveaux d'énergies est proche de l'énergie à laquelle ils peuvent émettre spontanément une ou plusieurs particules. Un des exemples les plus célèbres de ce phénomène est l'état de Hoyle (Fig. 7.6). En effet, quand le carbone 12 est produit à une énergie d'excitation proche de la somme des énergies de trois noyaux d'hélium (appelés aussi particules α) le ^{12}C, qui est sphérique dans son état fondamental, a une structure qui va ressembler à celle de trois α (Fig. 7.6)

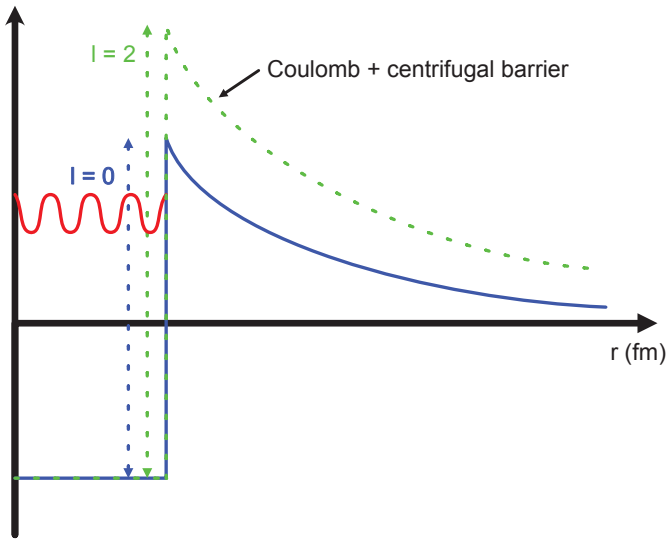

Figure 7.5: *Représentation schématique de la barrière coulombienne et centrifuge pour l=0 et l=2. Dans le noyau les protons et neutrons sont piégés dans ce que l'on appelle un puit de potentiel. L'onde sinusoïdale en rouge représente un nucleon piégé par la barrière coulombienne (et centrifuge pour l>0).*

dans l'état de Hoyle. De façon similaire pour le ^{15}F, l'état $1/2^-$ a une énergie proche de celle d'un ^{13}N plus deux protons et voit donc sa structure changer en celle d'un cœur de ^{13}N et deux protons.

Différentes prédictions théoriques portant sur les états de parité négative du ^{15}F (les états $1/2^-$, $5/2^-$ et $3/2^-$) s'accordent sur le fait que l'état $5/2^-$, pourtant au dessus du seuil d'émission deux protons, devrait être encore plus étroit que l'état $1/2^-$ précédemment mesuré. De plus, ces prédictions sont en désaccord sur la largeur de l'état $3/2^-$, l'une prédisant qu'il devrait être étroit alors que l'autre prédit un état beaucoup plus large (similairement à ce que l'on observe dans le ^{15}C). Il est donc intéressant de mesurer ces états de plus haute énergie, ainsi que d'observer leur décroissance par émission soit d'un, soit de deux protons. Il serait aussi intéressant de mesurer la décroissance γ de l'état $1/2^-$ qui pourrait être rendue possible par sa durée de vie accrue. Pour cela, dans cette thèse nous avons monter, réaliser et analyser deux expériences. Dans ce résumé, nous ne rentrerons pas dans les détails expérimentaux mais nous nous contenterons de présenter les résultats obtenus dans ces deux expériences indistinctement.

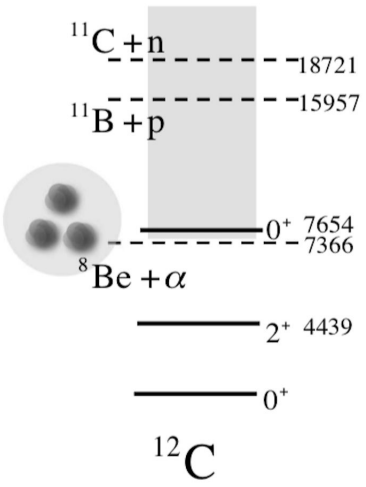

Figure 7.6: *Schéma de niveaux du carbon 12 et représentation schématique de sa structure en 3 α au niveau du seuil d'émission $^8Be + \alpha = 3\alpha$.*

Résultats expérimentaux

Nouveaux états

Dans cette thèse, deux expériences ont été réalisées dans le but d'étudier le noyau non-lié de ^{15}F. Ces expériences ont mis en œuvre les détecteurs de particules légères chargées, MUST2 et Mugast, le spectromètre VAMOS et le détecteur de rayonnements gamma AGATA. Dans ces deux expériences, l'état $1/2^-$ précédemment mesuré a été confirmé, avec une valeur compatible avec celle mesurée précédemment. Les deux états prédits à plus haute énergie d'excitation, l'état $5/2^-$ et $3/2^-$, furent eux aussi mesurés à des énergies en excellent accord avec les prédictions de Fortune et al. mais en désaccord avec sa prédiction sur la largeur de l'état $3/2^-$. On mesure cet état avec une largeur 10 fois inférieure à celle de sa prédiction. Cette largeur est par contre en relativement bon accord avec la prédiction faite par Canton et al. Ces états étant mesurés à plus de 1 MeV au dessus du seuil d'émission deux protons, on observe expérimentalement leur décroissance par émission 2p, et en étudiant les énergies relatives des fragments, c'est à dire les énergies emportées par les systèmes proton-proton et ^{13}N-protons on conclu que cette décroissance est séquentielle au travers de l'état 1^- du ^{14}O. Les résultats expérimentaux sont présentés sur la figure 7.7 et sont résumés dans le tableau 7.1

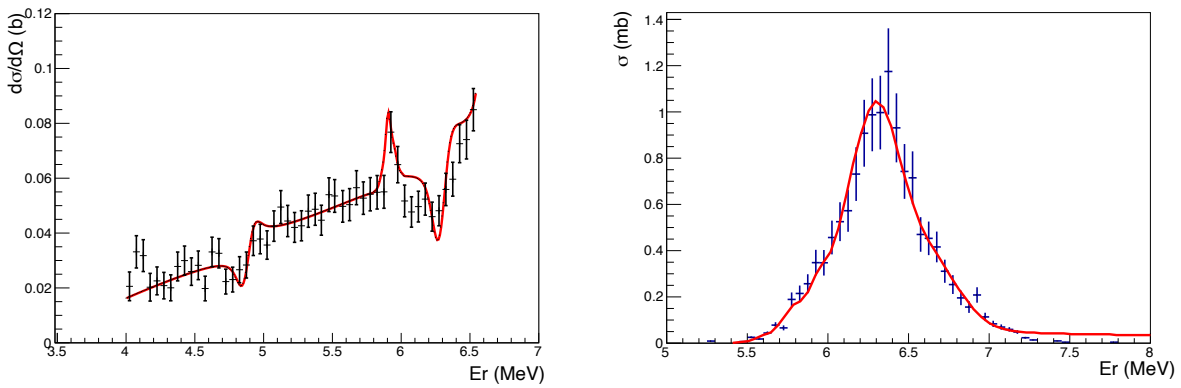

(a) (b)

Figure 7.7: *(a) Étude de la décroissance 1p du ^{15}F, résultats expérimentaux en noir et ajustement phénoménologique (R-Matrix) en rouge. (b) Étude de la décroissance 2p du ^{15}F, résultats expérimentaux en bleue et ajustement phénoménologique (R-Matrix) en rouge*

J^π	E_{CM} (MeV)	Γ_{1p} (keV)	Γ_{2p} (keV)	BR_{2p}
$1/2^+$	1.270 (20)	376 (70)	-	-
$5/2^+$	2.794 (16)	300 (16)	-	-
$1/2^-$	**4.88 (14)**	**23 (10)**	-	-
$5/2^-$	**5.91 (14)**	**2 (1)**	**0.03 (2)**	**1.5 (2) %**
$3/2^-$	**6.29 (14)**	**40 (10)**	**0.3 (1)**	**0.7 (1) %**
$5/2^+$	6.67 (20)	27 (20)	0.05 (5)	0.2 (2) %
$3/2^+$	6.94 (30)	1000 (500)	-	-

Table 7.1: Résumé des résultats obtenus via l'ajustement (R-Matrix) simultané des mesures Fig. 7.7. J^π correspond au spin-parité de létat, $E_{CM} = E_x + S_p$ avec $S_p = 1.27$ MeV correspond à l'énergie centre de masse de l'état, $\Gamma_{1p/2p}$ correspond aux largeurs des états et BR est le rapport d'embranchement vers la voie 2p.

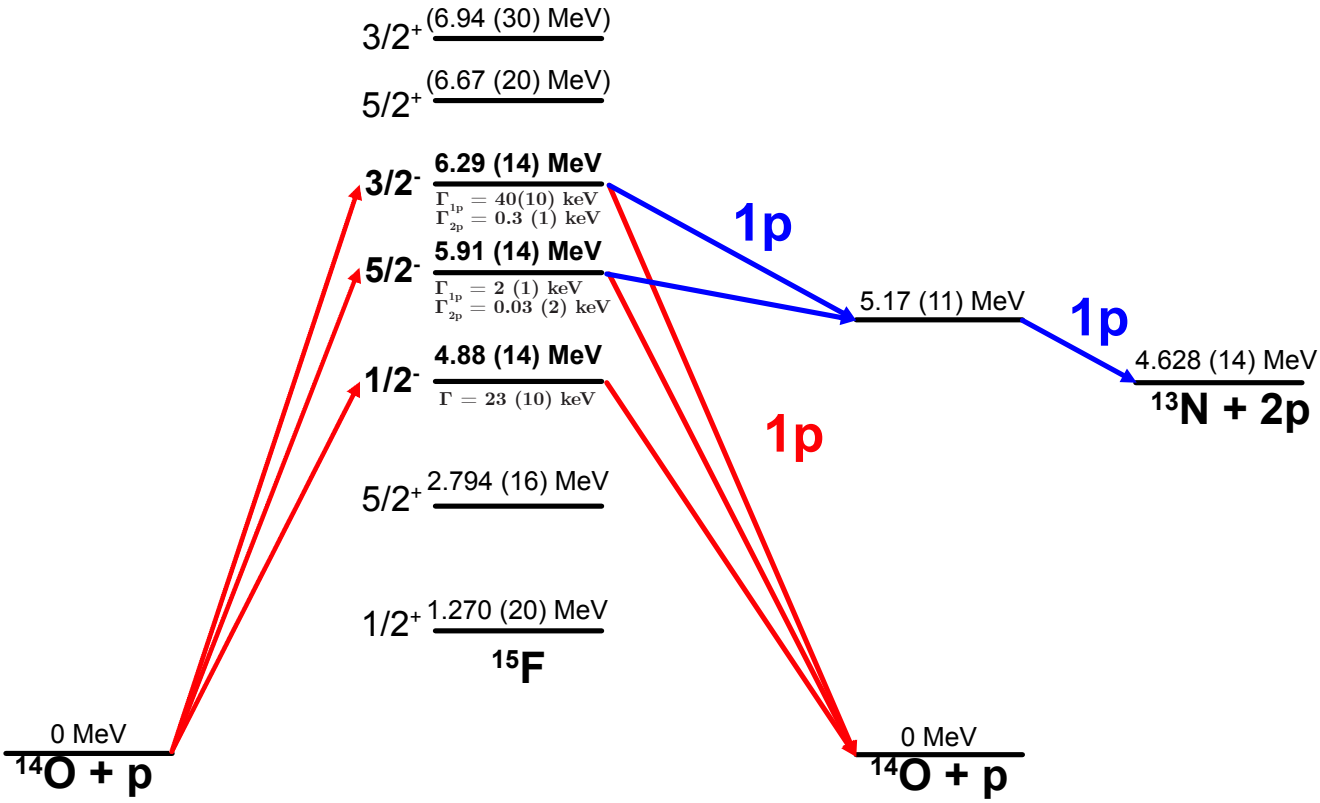

Figure 7.8: *Résumé des différents états mesurés et de leurs voies de décroissance.*

Mesure de la décroissance gamma

L'état $1/2^-$ observé précédemment ne semble pas décroître par émission gamma étant donné qu'expérimentalement on observe pas de gamma en coïncidence avec un ^{14}O et un proton dans la gamme d'énergie et d'angle attendue (Fig. 7.9).

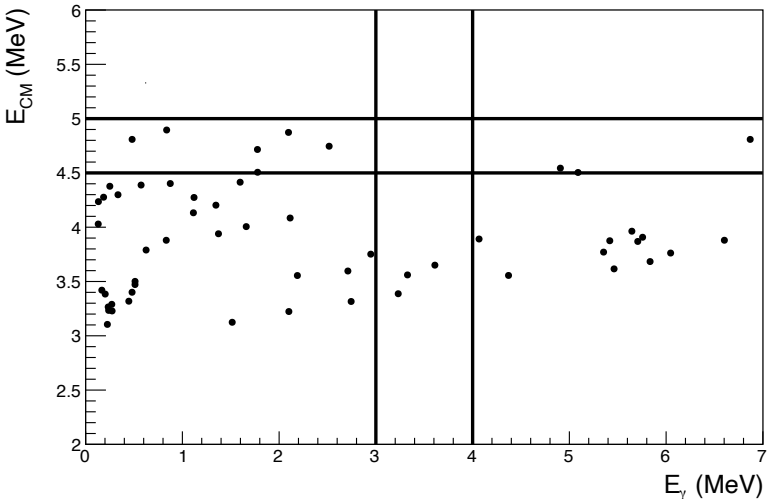

Figure 7.9: *Énergie centre de masse du fluor 15 en fonction de l'énergie gamma. Les lignes noirs correspondent aux domaines dans lesquels on s'attend à observer des évènements de décroissance gamma.*

Interprétation

Structure du ^{15}F

Les résultats obtenus, bien qu'en excellent accord avec la prédiction de Fortune et al. ne sont pas en accord avec sa prédiction de la largeur de l'état $3/2^-$ qui est mesurée comme étant beaucoup plus étroit que son analogue dans le noyau miroir (Fig. 7.10). Afin de mieux comprendre l'origine de cette différence il peut être intéressant de regarder les schémas de niveaux du ^{14}O + 1p et celui du ^{13}N + 2p. Comme on peut le voir sur la figure 7.10 il est clair que de la même façon que l'état $1/2^-$ était proche du seuil ^{13}N + 2p, les états $5/2^-$ et $3/2^-$ sont très proches des états 0^+ et 3^- respectivement. Il semble raisonnable de faire l'hypothèse que les états du ^{15}F se couplent avec les états du ^{14}O. Quand on regarde le noyau miroir, on voit que les états analogues du ^{15}C ne sont pas proches de ceux du système ^{14}C + n, cette différence pourrait expliquer la large différence de largeur entre le $3/2^-$ du ^{15}F et celui du ^{15}C.

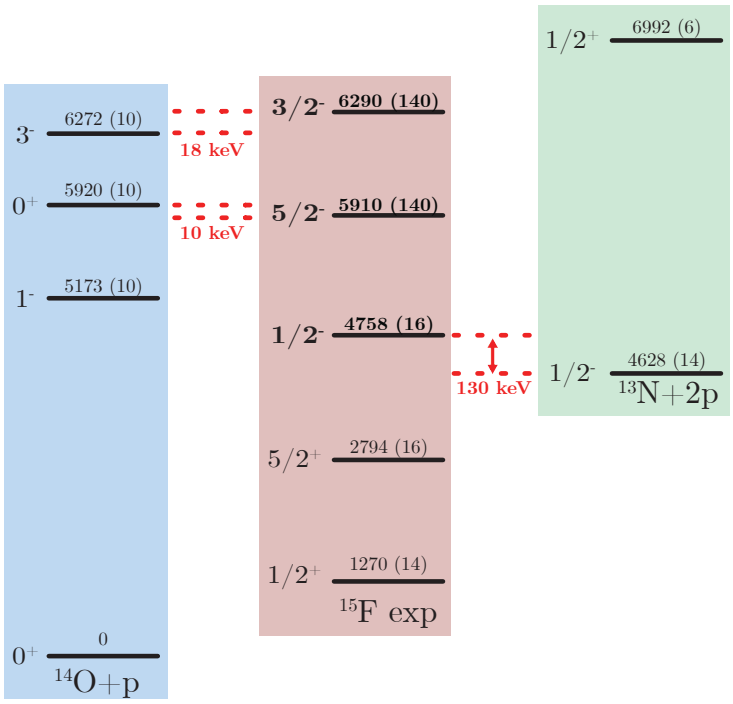

Figure 7.10: *Schéma de niveaux du ^{15}F relativement aux seuils ^{14}O + p et ^{13}N + 2p. Les énergies sont données en keV par rapport au fondamental du ^{14}O. En rouge sont écrit les différences d'énergies entre les états du ^{15}F et de ses voisins. Les valeurs en gras correspondent aux résultats obtenus dans ce travail.*

Décroissance gamma

Expérimentalement aucune décroissance gamma de l'état $1/2^-$ vers le fondamental du ^{15}F n'a été observée. Les raisons qui motivaient cette mesure était la similarité de cette transition avec celle observée dans le ^{11}Be, transition étant une des plus rapides jamais mesurée dans un noyau. Une telle mesure dans un noyau non-lié serait particulièrement intéressante. La raison pour laquelle cette décroissance n'a pas été mesurée expérimentalement est en fait due en grande partie au fait que contrairement au ^{11}Be dans lequel la transition implique des neutrons, ici la transition implique des protons qui sont donc soumis à une barrière coulombienne. La probabilité pour le neutron d'être "éloigné" du cœur de ^{10}Be est donc beaucoup plus grande que celle pour le proton d'être éloigné du cœur de ^{14}O. Aussi, la charge effective du proton dans le ^{15}F est de façon très surprenante la même que celle du neutron dans ^{11}Be. Par conséquent la probabilité de mesurer ce genre de transition dans le ^{15}F est en réalité beaucoup plus faible qu'attendu ($\sim$ 15 fois inférieur).

Bibliography

[Ago03] S. Agostinelli et al. "Geant4—a simulation toolkit". In: *Nuclear Instruments and Methods in Physics Research Section A: Accelerators, Spectrometers, Detectors and Associated Equipment* 506.3 (2003), pp. 250–303. ISSN: 0168-9002. DOI: https://doi.org/10.1016/S0168-9002(03)01368-8. URL: http://www.sciencedirect.com/science/article/pii/S0168900203013688.

[Akk12] S. Akkoyun et al. "AGATA—Advanced GAmma Tracking Array". In: *Nuclear Instruments and Methods in Physics Research Section A: Accelerators, Spectrometers, Detectors and Associated Equipment* 668 (2012), pp. 26–58. ISSN: 0168-9002. DOI: https://doi.org/10.1016/j.nima.2011.11.081. URL: http://www.sciencedirect.com/science/article/pii/S0168900211021516.

[Amo03] K. Amos et al. "An algebraic solution of the multichannel problem applied to low energy nucleon–nucleus scattering". In: *Nuclear Physics A* 728.1 (2003), pp. 65–95. ISSN: 0375-9474. DOI: https://doi.org/10.1016/j.nuclphysa.2003.08.019. URL: http://www.sciencedirect.com/science/article/pii/S0375947403016968.

[Aoy98] S. Aoyama et al. "Thomas-Ehrman effect on $s_{1/2}$ and $p_{1/2}$ resonance states in $^{10}\mathrm{C} + p$". In: *Phys. Rev. C* 57 (2 Feb. 1998), pp. 975–977. DOI: 10.1103/PhysRevC.57.975. URL: https://link.aps.org/doi/10.1103/PhysRevC.57.975.

[Ass15] M. Assié et al. In: *The European Physical Journal A* 51.1 (2015), p. 11. DOI: 10.1140/epja/i2015-15011-6. URL: https://doi.org/10.1140/epja/i2015-15011-6.

[Azu10] R. E. Azuma et al. "AZURE: An R-matrix code for nuclear astrophysics". In: *Phys. Rev. C* 81 (4 Apr. 2010), p. 045805. DOI: 10.1103/PhysRevC.81.045805. URL: https://link.aps.org/doi/10.1103/PhysRevC.81.045805.

[Bea13] D. Beaumel. "The GASPARD project". In: *Nuclear Instruments and Methods in Physics Research Section B: Beam Interactions with Materials and Atoms* 317 (2013). XVIth International Conference on ElectroMagnetic Isotope Separators and Techniques Related to their Applications, December 2–7, 2012 at Matsue, Japan, pp. 661–663. ISSN: 0168-583X. DOI: https://doi.org/10.1016/j.nimb.2013.05.047. URL: http://www.sciencedirect.com/science/article/pii/S0168583X13006113.

[Ben99] K. Bennaceur et al. "Study of the 7Be(p, *gamma*)8B and 7Li(n, *gamma*)8Li capture reactions using the shell model embedded in the continuum". In: *Nuclear Physics A* 651.3 (1999), pp. 289–319. ISSN: 0375-9474. DOI: https://doi.org/10.1016/S0375-9474(99)00133-5. URL: http://www.sciencedirect.com/science/article/pii/S0375947499001335.

[Bro14] B.A. Brown and W.D.M. Rae. "The Shell-Model Code NuShellX@MSU". In: *Nuclear Data Sheets* 120 (2014), pp. 115–118. ISSN: 0090-3752. DOI: https://doi.org/10.1016/j.nds.2014.07.022. URL: http://www.sciencedirect.com/science/article/pii/S0090375214004748.

[Can06] L. Canton et al. "Predicting Narrow States in the Spectrum of a Nucleus beyond the Proton Drip Line". In: *Phys. Rev. Lett.* 96 (7 Feb. 2006), p. 072502. DOI: 10.1103/PhysRevLett.96.072502. URL: https://link.aps.org/doi/10.1103/PhysRevLett.96.072502.

[Cha16] R. J. Charity. "Resonance phenomena: From compound nucleus decay to proton radioactivity". In: *The European Physical Journal Plus* 131.3 (2016), p. 63. DOI: 10.1140/epjp/i2016-16063-1. URL: https://doi.org/10.1140/epjp/i2016-16063-1.

[Cla88] William S. Rodney Claus E. Rolfs. *Cauldrons in the Cosmos*. University of Chicago Press, 1988.

[Coh65] S. Cohen and D. Kurath. "Effective interactions for the 1p shell". In: *Nuclear Physics* 73.1 (1965), pp. 1–24. ISSN: 0029-5582. DOI: https://doi.org/10.1016/0029-5582(65)90148-3. URL: http://www.sciencedirect.com/science/article/pii/0029558265901483.

[Dat05] V. M. Datar et al. "Publisher's Note: Direct Observation of the 4^+-to-2^+ Gamma Transition in ^{8}Be [Phys. Rev. Lett. 94, 122502 (2005)]". In: *Phys. Rev. Lett.* 94 (13 Apr. 2005), p. 139902. DOI: 10.1103/PhysRevLett.94.139902. URL: https://link.aps.org/doi/10.1103/PhysRevLett.94.139902.

[Dat13] V. M. Datar et al. "Electromagnetic Transition from the 4^+ to 2^+ Resonance in ^{8}Be Measured via the Radiative Capture in ^{4}He+^{4}He". In: *Phys. Rev. Lett.* 111 (6 Aug. 2013), p. 062502. DOI: 10.1103/PhysRevLett.111.062502. URL: https://link.aps.org/doi/10.1103/PhysRevLett.111.062502.

[de 18] de Oliveira Santos, Francois. "Resonant Elastic Scattering". In: *EPJ Web Conf.* 184 (2018), p. 01006. DOI: 10.1051/epjconf/201818401006. URL: https://doi.org/10.1051/epjconf/201818401006.

[Den54] David M. Dennison. "Energy Levels of the O^{16} Nucleus". In: *Phys. Rev.* 96 (2 Oct. 1954), pp. 378–380. DOI: 10.1103/PhysRev.96.378. URL: https://link.aps.org/doi/10.1103/PhysRev.96.378.

[Des10] P Descouvemont and D Baye. "TheR-matrix theory". In: *Reports on Progress in Physics* 73.3 (Feb. 2010), p. 036301. DOI: 10.1088/0034-4885/73/3/036301. URL: https://doi.org/10.1088%2F0034-4885%2F73%2F3%2F036301.

[Duc99] G. Duchêne et al. "The Clover: a new generation of composite Ge detectors". In: *Nuclear Instruments and Methods in Physics Research Section A: Accelerators, Spectrometers, Detectors and Associated Equipment* 432.1 (1999), pp. 90–110. ISSN: 0168-9002. DOI: https://doi.org/10.1016/S0168-9002(99)00277-6. URL: http://www.sciencedirect.com/science/article/pii/S0168900299002776.

[Dun53] D. N. F. Dunbar et al. "The 7.68-Mev State in C^{12}". In: *Phys. Rev.* 92 (3 Nov. 1953), pp. 649–650. DOI: 10.1103/PhysRev.92.649. URL: https://link.aps.org/doi/10.1103/PhysRev.92.649.

[Ehr51] Joachim B. Ehrman. "On the Displacement of Corresponding Energy Levels of C^{13} and N^{13}". In: *Phys. Rev.* 81 (3 Feb. 1951), pp. 412–416. DOI: 10.1103/PhysRev.81.412. URL: https://link.aps.org/doi/10.1103/PhysRev.81.412.

[End93] P.M. Endt. "Strengths of Gamma-Ray Transitions in A = 5-44 Nuclei, IV". In: *Atomic Data and Nuclear Data Tables* 55.1 (1993), pp. 171–197. ISSN: 0092-640X. DOI: https://doi.org/10.1006/adnd.1993.1020. URL: http://www.sciencedirect.com/science/article/pii/S0092640X8371020X.

[Fer49] Enrico Fermi. *Nuclear Physics, a course given by Enrico Fermi at the University of Chicago*. University of Chicago Press, 1949.

[Fla11] Freddy Flavigny. "Détermination de facteurs spectroscopiques absolus par réactions de knockout et de transfert". 2011PA112152. PhD thesis. 2011. URL: http://www.theses.fr/2011PA112152/document.

[For06] H. T. Fortune. "Constraints on energies of ^{15}F(g.s.), ^{15}O($\frac{1}{2}^+, T = \frac{3}{2}$), and ^{16}F($0^+, T = 2$)". In: *Phys. Rev. C* 74 (5 Nov. 2006), p. 054310. DOI: 10.1103/PhysRevC.74.054310. URL: https://link.aps.org/doi/10.1103/PhysRevC.74.054310.

[For07] H. T. Fortune and R. Sherr. "Comment on "Predicting Narrow States in the Spectrum of a Nucleus beyond the Proton Drip Line"". In: *Phys. Rev. Lett.* 99 (8 Aug. 2007), p. 089201. DOI: 10.1103/PhysRevLett.99.089201. URL: https://link.aps.org/doi/10.1103/PhysRevLett.99.089201.

[For11] H. T. Fortune. "Widths in ^{15}C and ^{15}F". In: *Phys. Rev. C* 83 (2 Feb. 2011), p. 024311. DOI: 10.1103/PhysRevC.83.024311. URL: https://link.aps.org/doi/10.1103/PhysRevC.83.024311.

[Fra19] P. R. Fraser et al. "Mass-15 nuclei and predicting narrow states beyond the proton drip line". In: *Phys. Rev. C* 100 (2 Aug. 2019), p. 024609. DOI: 10.1103/PhysRevC.100.024609. URL: https://link.aps.org/doi/10.1103/PhysRevC.100.024609.

[Fre14] M. Freer and H. O. U. Fynbo. "The Hoyle state in ^{12}C". In: *Progress in Particle and Nuclear Physics* 78 (Sept. 2014), pp. 1–23. DOI: 10.1016/j.ppnp.2014.06.001.

[FRS11] Professor E. Rutherford F.R.S. "LXXIX. The scattering of alpha and beta particles by matter and the structure of the atom". In: *The London, Edinburgh, and Dublin Philosophical Magazine and Journal of Science* 21.125 (1911), pp. 669–688. DOI: 10.1080/14786440508637080. eprint: https://doi.org/10.1080/14786440508637080. URL: https://doi.org/10.1080/14786440508637080.

[Gav80] A. Gavron. "Statistical model calculations in heavy ion reactions". In: *Phys. Rev. C* 21 (1 Jan. 1980), pp. 230–236. DOI: 10.1103/PhysRevC.21.230. URL: https://link.aps.org/doi/10.1103/PhysRevC.21.230.

[Gho50] S. N. Ghoshal. "An Experimental Verification of the Theory of Compound Nucleus". In: *Phys. Rev.* 80 (6 Dec. 1950), pp. 939–942. DOI: 10.1103/PhysRev.80.939. URL: https://link.aps.org/doi/10.1103/PhysRev.80.939.

[Gio03] J. Giovinazzo et al. "Two-proton decay of 45Fe: a new type of radioactivity". In: *Nuclear Physics A* 722 (2003), pp. C434–C438. ISSN: 0375-9474. DOI: https://doi.org/10.1016/S0375-9474(03)01403-9. URL: http://www.sciencedirect.com/science/article/pii/S0375947403014039.

[Goo] GoodFellow. *GoodFellow, Your global supplier for materials*. http://www.goodfellow.com.

[Gou09] Brian Gough. *GNU scientific library reference manual*. Network Theory Ltd., 2009.

[Gra09] Florence de Grancey. "Premiers états du 15F étudiés par diffusion élastique résonante". 2009CAEN2045. PhD thesis. 2009, 1 vol. (165 p.) URL: http://www.theses.fr/2009CAEN2045.

[Gra16] F. de Grancey et al. "An above-barrier narrow resonance in 15F". In: *Physics Letters B* 758 (2016), pp. 26–31. ISSN: 0370-2693. DOI: https://doi.org/10.1016/j.physletb.2016.04.051. URL: http://www.sciencedirect.com/science/article/pii/S0370269316301241.

[Gui84] D. Guillemaud-Mueller et al. "beta-Decay schemes of very neutron-rich sodium isotopes and their descendants". In: *Nuclear Physics A* 426.1 (1984), pp. 37–76. ISSN: 0375-9474. DOI: https://doi.org/10.1016/0375-9474(84)90064-2. URL: http://www.sciencedirect.com/science/article/pii/0375947484900642.

[Guo05] F. Q. Guo et al. "Reexamination of the energy levels of ^{15}F by ^{14}O + ^{1}H elastic resonance scattering". In: *Phys. Rev. C* 72 (3 Sept. 2005), p. 034312. DOI: 10.1103/PhysRevC.72.034312. URL: https://link.aps.org/doi/10.1103/PhysRevC.72.034312.

[Haa97] F. Haas et al. "Search for electromagnetic transitions between12C-12C cluster states in24Mg". In: *Il Nuovo Cimento A (1971-1996)* 110.9 (1997), pp. 989–999. DOI: 10.1007/BF03035936. URL: https://doi.org/10.1007/BF03035936.

[Hax49] Otto Haxel, J. Hans D. Jensen, and Hans E. Suess. "On the "Magic Numbers" in Nuclear Structure". In: *Phys. Rev.* 75 (11 June 1949), pp. 1766–1766. DOI: 10.1103/PhysRev.75.1766.2. URL: https://link.aps.org/doi/10.1103/PhysRev.75.1766.2.

[Hey94] Kris L. G. Heyde. *The Nuclear Shell Model*. Springer, 1994.

[Hoy54] F. Hoyle. "On Nuclear Reactions Occuring in Very Hot STARS.I. the Synthesis of Elements from Carbon to Nickel." In: *apjs* 1 (Sept. 1954), p. 121. DOI: 10.1086/190005.

[Huc85] A. Huck et al. "Beta decay of the new isotopes ^{52}K, ^{52}Ca, and ^{52}Sc; a test of the shell model far from stability". In: *Phys. Rev. C* 31 (6 June 1985), pp. 2226–2237. DOI: 10.1103/PhysRevC.31.2226. URL: https://link.aps.org/doi/10.1103/PhysRevC.31.2226.

[Ike68] Kiyomi Ikeda, Noboru Takigawa, and Hisashi Horiuchi. "The Systematic Structure-Change into the Molecule-like Structures in the Self-Conjugate 4n Nuclei". In: *Progress of Theoretical Physics Supplement* E68 (July 1968), pp. 464–475. ISSN: 0375-9687. DOI: 10.1143/PTPS.E68.464. eprint: https://academic.oup.com/ptps/article-pdf/doi/10.1143/PTPS.E68.464/5216547/E68-464.pdf. URL: https://doi.org/10.1143/PTPS.E68.464.

[IRF] IRFU. *Beam tracking detector*. http://irfu.cea.fr/Phocea/Vie_des_labos/Ast/ast_technique.php?id_ast=791.

[Joh52] Victor F. Weisskopf John M. Blatt. *Theoretical Nuclear Physics*. Wiley, 1952.

[Kam56] S. L. Kameny. "α-Particle Model of O^{16}". In: *Phys. Rev.* 103 (2 July 1956), pp. 358–364. DOI: 10.1103/PhysRev.103.358. URL: https://link.aps.org/doi/10.1103/PhysRev.103.358.

[Kel04] N. G. Kelkar, M. Nowakowski, and K. P. Khemchandani. "Hidden evidence of nonexponential nuclear decay". In: *Phys. Rev. C* 70 (2 Aug. 2004), p. 024601. DOI: 10.1103/PhysRevC.70.024601. URL: https://link.aps.org/doi/10.1103/PhysRevC.70.024601.

[Kel17] J.H. Kelley, J.E. Purcell, and C.G. Sheu. "Energy levels of light nuclei A=12". In: *Nuclear Physics A* 968 (2017), pp. 71–253. ISSN: 0375-9474. DOI: https://doi.org/10.1016/j.nuclphysa.2017.07.015. URL: http://www.sciencedirect.com/science/article/pii/S0375947417303330.

[Koo93] K. LangankeJ. A. MaruhnS. E. Koonin. *Computational Nuclear Physics 2*. Springer, 1993.

[Kra88] Kenneth S. Krane. *Introductory Nuclear Physics*. Wiley, 1988.

[Kuo94] T. T. S. Kuo and Jifa Hao. "Treatment of Pauli Exclusion Operator in G-Matrix Calculations for Hypernuclei*)". In: *Progress of Theoretical Physics Supplement* 117 (Mar. 1994), pp. 351–360. ISSN: 0375-9687. DOI: 10.1143/ptp.117.351. eprint: https://academic.oup.com/ptps/article-pdf/doi/10.1143/ptp.117.351/5423745/117-351.pdf. URL: https://doi.org/10.1143/ptp.117.351.

[Lan58a] A. M. Lane and R. G. Thomas. "R-Matrix Theory of Nuclear Reactions". In: *Rev. Mod. Phys.* 30 (2 Apr. 1958), pp. 257–353. DOI: 10.1103/RevModPhys.30.257. URL: https://link.aps.org/doi/10.1103/RevModPhys.30.257.

[Lan58b] A. M. Lane and R. G. Thomas. "R-Matrix Theory of Nuclear Reactions". In: *Rev. Mod. Phys.* 30 (2 Apr. 1958), pp. 257–353. DOI: 10.1103/RevModPhys.30.257. URL: https://link.aps.org/doi/10.1103/RevModPhys.30.257.

[Mat12] Adrien Matta. "Etude du noyau très riche en neutrons 10He par réaction de transfert d'un proton 11Li(d,3He)". 2012PA112032. PhD thesis. 2012. URL: http://www.theses.fr/2012PA112032/document.

[Mat16] A Matta et al. "NPTool: a simulation and analysis framework for low-energy nuclear physics experiments". In: *Journal of Physics G: Nuclear and Particle Physics* 43.4 (Mar. 2016), p. 045113. DOI: 10.1088/0954-3899/43/4/045113. URL: https://doi.org/10.1088%2F0954-3899%2F43%2F4%2F045113.

[May49] Maria Goeppert Mayer. "On Closed Shells in Nuclei. II". In: *Phys. Rev.* 75 (12 June 1949), pp. 1969–1970. DOI: 10.1103/PhysRev.75.1969. URL: https://link.aps.org/doi/10.1103/PhysRev.75.1969.

[Méo99] François Méot. "The ray-tracing code Zgoubi". In: *Nuclear Instruments and Methods in Physics Research Section A: Accelerators, Spectrometers, Detectors and Associated Equipment* 427.1 (1999), pp. 353–356. ISSN: 0168-9002. DOI: https://doi.org/10.1016/S0168-9002(98)01508-3. URL: http://www.sciencedirect.com/science/article/pii/S0168900298015083.

[Mic02] N. Michel et al. "Gamow Shell Model Description of Neutron-Rich Nuclei". In: *Phys. Rev. Lett.* 89 (4 July 2002), p. 042502. DOI: 10.1103/PhysRevLett.89.042502. URL: https://link.aps.org/doi/10.1103/PhysRevLett.89.042502.

[Mil75] D.J. Millener and D. Kurath. "The particle-hole interaction and the beta decay of 14B". In: *Nuclear Physics A* 255.2 (1975), pp. 315–338. ISSN: 0375-9474. DOI: https://doi.org/10.1016/0375-9474(75)90683-1. URL: http://www.sciencedirect.com/science/article/pii/0375947475906831.

[Mil83] D. J. Millener et al. "Strong $E1$ transitions in ^{9}Be, ^{11}Be, and ^{13}C". In: *Phys. Rev. C* 28 (2 Aug. 1983), pp. 497–505. DOI: 10.1103/PhysRevC.28.497. URL: https://link.aps.org/doi/10.1103/PhysRevC.28.497.

[Mon19] Belen Monteagudo Godoy. "Structure and neutron decay of the unbound Beryllium isotopes 15,16Be". Theses. Normandie Université, Nov. 2019. URL: https://tel.archives-ouvertes.fr/tel-02518505.

[Mor14] Pierre Morfouace. "Single-particle states in neutron-rich 69Cu and 71Cu by means of the (d,3He) transfer reaction". 2014PA112196. PhD thesis. 2014. URL: http://www.theses.fr/2014PA112196/document.

[Mot95] T. Motobayashi et al. “Large deformation of the very neutron-rich nucleus 32Mg from intermediate-energy Coulomb excitation”. In: *Physics Letters B* 346.1 (1995), pp. 9–14. ISSN: 0370-2693. DOI: https://doi.org/10.1016/0370-2693(95)00012-A. URL: http://www.sciencedirect.com/science/article/pii/037026939500012A.

[Mou08] Xavier Mougeot. “Spectroscopie des noyaux exotiques 6He, 7He avec les télescopes à pistes MUST2 et le faisceau SPIRAL d’8He”. 2008PA077137. PhD thesis. 2008, 1 vol. (166 p.) URL: http://www.theses.fr/2008PA077137.

[Muk08] I. Mukha et al. “Proton-proton correlations observed in two-proton decay of ^{19}Mg and ^{16}Ne”. In: *Phys. Rev. C* 77 (6 June 2008), p. 061303. DOI: 10.1103/PhysRevC.77.061303. URL: https://link.aps.org/doi/10.1103/PhysRevC.77.061303.

[Muk09] I. Mukha et al. “Observation of narrow states in nuclei beyond the proton drip line: ^{15}F and ^{16}Ne”. In: *Phys. Rev. C* 79 (6 June 2009), p. 061301. DOI: 10.1103/PhysRevC.79.061301. URL: https://link.aps.org/doi/10.1103/PhysRevC.79.061301.

[Muk10] I. Mukha et al. “Spectroscopy of proton-unbound nuclei by tracking their decay products in-flight: One- and two- proton decays of ^{15}F, ^{16}Ne, and ^{19}Na”. In: *Phys. Rev. C* 82 (5 Nov. 2010), p. 054315. DOI: 10.1103/PhysRevC.82.054315. URL: https://link.aps.org/doi/10.1103/PhysRevC.82.054315.

[Oko12] Jacek Okołowicz, Marek Płoszajczak, and Witold Nazarewicz. “On the Origin of Nuclear Clustering”. In: *Progress of Theoretical Physics Supplement* 196 (Oct. 2012), pp. 230–243. ISSN: 0375-9687. DOI: 10.1143/PTPS.196.230. eprint: https://academic.oup.com/ptps/article-pdf/doi/10.1143/PTPS.196.230/5342456/196-230.pdf. URL: https://doi.org/10.1143/PTPS.196.230.

[Oko13] J. Okołowicz, W. Nazarewicz, and M. Płoszajczak. “Toward understanding the microscopic origin of nuclear clustering”. In: *Fortschritte der Physik* 61.2-3 (2013), pp. 66–79. DOI: 10.1002/prop.201200127. eprint: https://onlinelibrary.wiley.com/doi/pdf/10.1002/prop.201200127. URL: https://onlinelibrary.wiley.com/doi/abs/10.1002/prop.201200127.

[Oli95] Francois De Oliveira. “Dtermination par raction de transfert de largeurs alpha dans le fluor 19. Applications l’astrophysique ”. PhD thesis. Universit Paris Sud - Paris XI, 1995.

[Oln58] J. W. Olness, J. Vorona, and H. W. Lewis. "Elastic and Inelastic Scattering of Protons by N^{14}". In: *Phys. Rev.* 112 (2 Oct. 1958), pp. 475–480. DOI: 10.1103/PhysRev.112.475. URL: https://link.aps.org/doi/10.1103/PhysRev.112.475.

[Oza00] A. Ozawa et al. "New Magic Number, $N = 16$, near the Neutron Drip Line". In: *Phys. Rev. Lett.* 84 (24 June 2000), pp. 5493–5495. DOI: 10.1103/PhysRevLett.84.5493. URL: https://link.aps.org/doi/10.1103/PhysRevLett.84.5493.

[Per00] Donald H. Perkins. *Introduction to High Energy Physics*. 4th ed. Cambridge University Press, 2000. DOI: 10.1017/CBO9780511809040.

[Ram16] Diego Ramos. " Fragment Distributions of Transfer- and Fusion-Induced Fission from 238U+12C Reactions Measured Through Inverse Kinematics ". PhD thesis. UNIVERSIDADE DE SANTIAGO DE COMPOSTELA, 2016.

[Rej11] M. Rejmund et al. "Performance of the improved larger acceptance spectrometer: VAMOS++". In: *Nuclear Instruments and Methods in Physics Research Section A: Accelerators, Spectrometers, Detectors and Associated Equipment* 646.1 (2011), pp. 184–191. ISSN: 0168-9002. DOI: https://doi.org/10.1016/j.nima.2011.05.007. URL: http://www.sciencedirect.com/science/article/pii/S0168900211008515.

[Rev18a] A. Revel et al. "Strong Neutron Pairing in core + $4n$ Nuclei". In: *Phys. Rev. Lett.* 120 (15 Apr. 2018), p. 152504. DOI: 10.1103/PhysRevLett.120.152504. URL: https://link.aps.org/doi/10.1103/PhysRevLett.120.152504.

[Rev18b] Aldric Revel. "Nuclear forces at the extremes". Theses. Normandie Université, Sept. 2018. URL: https://tel.archives-ouvertes.fr/tel-02082089.

[Rot06] C. Rothe, S. I. Hintschich, and A. P. Monkman. "Violation of the Exponential-Decay Law at Long Times". In: *Phys. Rev. Lett.* 96 (16 Apr. 2006), p. 163601. DOI: 10.1103/PhysRevLett.96.163601. URL: https://link.aps.org/doi/10.1103/PhysRevLett.96.163601.

[Sor08] O. Sorlin and M.-G. Porquet. "Nuclear magic numbers: New features far from stability". In: *Progress in Particle and Nuclear Physics* 61.2 (2008), pp. 602–673. ISSN: 0146-6410. DOI: https://doi.org/10.1016/j.ppnp.2008.05.001. URL: http://www.sciencedirect.com/science/article/pii/S0146641008000380.

[Sor93] O. Sorlin et al. "Decay properties of exotic N≃28 S and Cl nuclei and the ^{48}Ca/^{46}Ca abundance ratio". In: *Phys. Rev. C* 47 (6 June 1993), pp. 2941–2953. DOI: 10.1103/PhysRevC.47.2941. URL: https://link.aps.org/doi/10.1103/PhysRevC.47.2941.

[Ste06] Gheorghe Iulian Stefan. "Spectroscopic measurements via resonant elastic scattering of oxygen 15 and new pathway within the carbon-nitrogen-oxygen cycle". Theses. Université de Caen, Dec. 2006. URL: https://tel.archives-ouvertes.fr/tel-00141593.

[Ste07] I. Stefan et al. "New pathways to bypass the 15O waiting point". In: *AIP Conference Proceedings* 891.1 (2007), pp. 155–163. DOI: 10.1063/1.2713512. eprint: https://aip.scitation.org/doi/pdf/10.1063/1.2713512. URL: https://aip.scitation.org/doi/abs/10.1063/1.2713512.

[Ste14] I. Stefan et al. "Probing nuclear forces beyond the drip-line using the mirror nuclei ^{16}N and ^{16}F". In: *Phys. Rev. C* 90 (1 July 2014), p. 014307. DOI: 10.1103/PhysRevC.90.014307. URL: https://link.aps.org/doi/10.1103/PhysRevC.90.014307.

[Suh07] Jouni Suhonen. *From Nucleons to Nucleus*. Springer, 2007.

[Tan78] Y.C. Tang, M. LeMere, and D.R. Thompsom. "Resonating-group method for nuclear many-body problems". In: *Physics Reports* 47.3 (1978), pp. 167–223. ISSN: 0370-1573. DOI: https://doi.org/10.1016/0370-1573(78)90175-8. URL: http://www.sciencedirect.com/science/article/pii/0370157378901758.

[Tan85] I. Tanihata et al. "Measurements of Interaction Cross Sections and Nuclear Radii in the Light *p*-Shell Region". In: *Phys. Rev. Lett.* 55 (24 Dec. 1985), pp. 2676–2679. DOI: 10.1103/PhysRevLett.55.2676. URL: https://link.aps.org/doi/10.1103/PhysRevLett.55.2676.

[Tar08] O.B. Tarasov and D. Bazin. "LISE++: Radioactive beam production with in-flight separators". In: *Nuclear Instruments and Methods in Physics Research Section B: Beam Interactions with Materials and Atoms* 266.19 (2008). Proceedings of the XVth International Conference on Electromagnetic Isotope Separators and Techniques Related to their Applications, pp. 4657–4664. ISSN: 0168-583X. DOI: https://doi.org/10.1016/j.nimb.2008.05.110. URL: http://www.sciencedirect.com/science/article/pii/S0168583X08007969.

[Tho52] R. G. Thomas. "An Analysis of the Energy Levels of the Mirror Nuclei, C^{13} and N^{13}". In: *Phys. Rev.* 88 (5 Dec. 1952), pp. 1109–1125. DOI: 10.1103/PhysRev.88.1109. URL: https://link.aps.org/doi/10.1103/PhysRev.88.1109.

[Von02] Wolfram Von Oertzen. "Nuclear Clusters and Covalently Bound Nuclear Molecules". In: *Progress of Theoretical Physics Supplement* 146 (Mar. 2002), pp. 169–178. ISSN: 0375-9687. DOI: 10.1143/PTPS.146.169. eprint: https://academic.oup.com/ptps/article-pdf/doi/10.1143/PTPS.146.169/5264843/146-169.pdf. URL: https://doi.org/10.1143/PTPS.146.169.

[War92] E. K. Warburton and B. A. Brown. "Effective interactions for the 0p1s0d nuclear shell-model space". In: *Phys. Rev. C* 46 (3 Sept. 1992), pp. 923–944. DOI: 10.1103/PhysRevC.46.923. URL: https://link.aps.org/doi/10.1103/PhysRevC.46.923.

[Wes69] M. L. West et al. "Level Structure in ^{15}O from the Proton Bombardment of ^{14}N". In: *Phys. Rev.* 179 (4 Mar. 1969), pp. 1047–1059. DOI: 10.1103/PhysRev.179.1047. URL: https://link.aps.org/doi/10.1103/PhysRev.179.1047.

[Wig37] E. Wigner. "On the Consequences of the Symmetry of the Nuclear Hamiltonian on the Spectroscopy of Nuclei". In: *Phys. Rev.* 51 (2 Jan. 1937), pp. 106–119. DOI: 10.1103/PhysRev.51.106. URL: https://link.aps.org/doi/10.1103/PhysRev.51.106.

[Wil58] K. Wildermuth and Th. Kanellopoulos. "The "cluster model" of the atomic nuclei". In: *Nuclear Physics* 7 (1958), pp. 150–162. ISSN: 0029-5582. DOI: https://doi.org/10.1016/0029-5582(58)90245-1. URL: http://www.sciencedirect.com/science/article/pii/0029558258902451.

Above barrier narrow resonances in the unbound nucleus ^{15}F

The study of unbound nuclei beyond the drip-lines allows us to test our understanding of the atomic nucleus under extreme conditions. In this thesis, we have analyzed two separate GANIL experiments in which fluorine 15, located two proton beyond the proton drip-line, was studied. One of the interesting particularity of this nucleus is the presence of particularly narrow negative parity states, above the Coulomb and centrifugal barriers. In this work, we were interested in theses states. We have confirmed the existence of the second excited state 1/2- and have observed two new states, a 5/2- state and a 3/2- state by measuring their decay by emitting either one or two protons. The structure of these states has been discussed and we have tried to explain the origin of the asymmetry observed between the 3/2- state of fluorine 15 and its analogue state in carbon 15. We have also detailed the possibility of gamma transitions between unbound states.

Keywords: Nuclear physics, Nuclear structure, Unbound nuclei, Proton-rich nuclei, Drip-lines, Resonant elastic scattering, Two-proton emission, Gamma transitions between unbound states, GANIL, LISE, MUST2, VAMOS, MUGAST, AGATA, Data analysis, Numerical simulations

---

Résonances étroites au dessus de la barrière dans le noyau non-lié ^{15}F

L'étude des noyaux non liés permet de tester notre compréhension du noyau atomique dans des conditions extrêmes. Dans cette thèse nous avons analysé deux expériences distinctes réalisées au GANIL au cours desquels nous avons étudié le fluor 15 situé deux neutrons au delà de la drip-line proton. Une des particularités intéressante de ce noyau est la présence d'états de parité négative particulièrement étroits et situés au dessus des barrières Coulombiennes et centrifuges. Nous nous sommes intéressés dans ce travail à ces états, nous avons confirmé l'existence du second état excité 1/2- et avons observé deux nouveaux états, un état 5/2- et un état 3/2- en mesurant leur décroissance par émission d'un ou de deux protons. Nous avons discuté la structure de ces états et avons tenté d'expliquer l'asymétrie observée entre l'état 3/2- du fluor 15 et son analogue dans le carbone 15. Nous avons détaillé aussi la possibilité d'observer des décroissances gammas entre états non-liés.

Mots clés: Physique nucléaire, Structure nucléaire, Noyaux non-liés, Noyaux riches en protons, Drip-lines, Diffusion élastique résonnante, Émission deux protons, Transitions gamma entre états non-liés, GANIL, LISE, MUST2, VAMOS, MUGAST, AGATA, Analyse de données, Simulations numériques